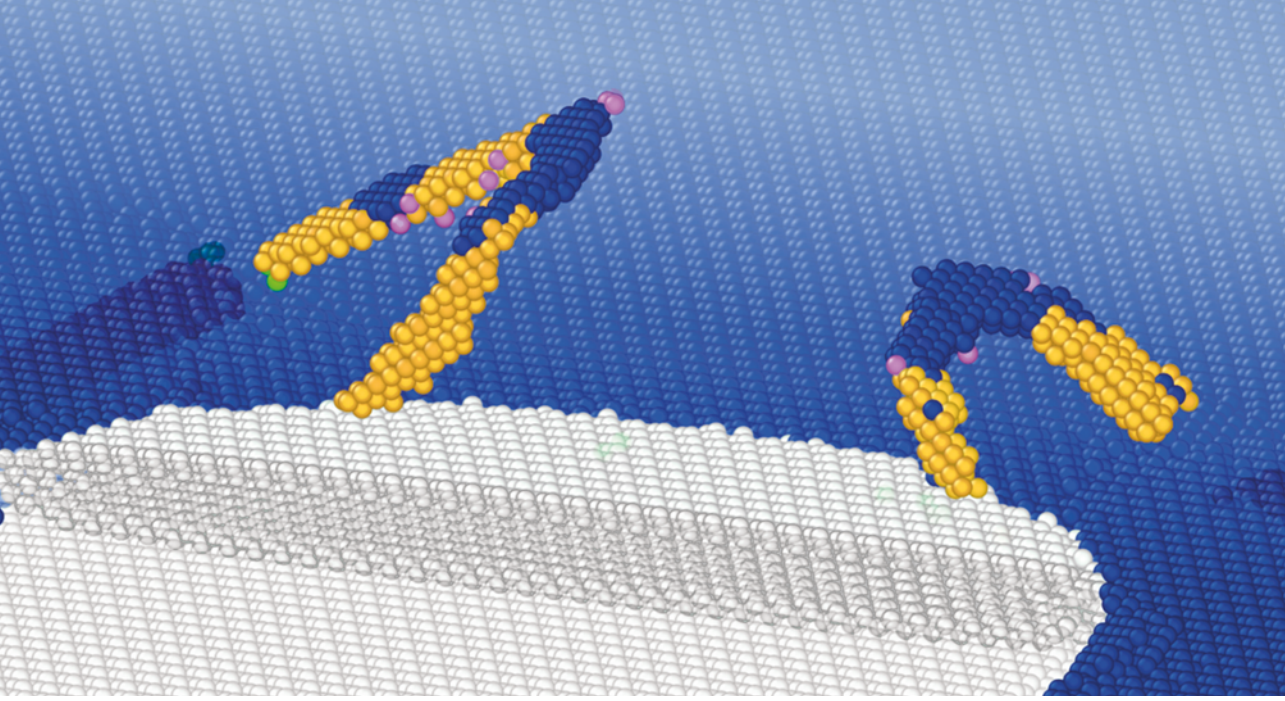

FAU Forschungen, Reihe B, Medizin, Naturwissenschaft, Technik 14

Johannes J. Möller

Atomistic Simulations of Crack Front Curvature Effects and Crack-Microstructure Interactions

FAU UNIVERSITY PRESS

Johannes Joel Möller

Atomistic Simulations of Crack Front Curvature Effects and Crack-Microstructure Interactions

FAU Forschungen, Reihe B
Medizin, Naturwissenschaft, Technik
Band 14

Herausgeber der Reihe:
Wissenschaftlicher Beirat der FAU University Press

Johannes J. Möller

Atomistic Simulations of Crack Front Curvature Effects and Crack-Microstructure Interactions

Erlangen
FAU University Press
2017

Bibliografische Information der Deutschen Nationalbibliothek:
Die Deutsche Nationalbibliothek verzeichnet diese Publikation in der Deutschen Nationalbibliografie; detaillierte bibliografische Daten sind im Internet über http://dnb.d-nb.de abrufbar.

Der vollständige Inhalt des Buchs ist als PDF über den OPUS Server der Friedrich-Alexander-Universität Erlangen-Nürnberg abrufbar:
https://opus4.kobv.de/opus4-fau/home

Verlag und Auslieferung:

FAU University Press, Universitätsstraße 4, 91054 Erlangen

Druck: docupoint GmbH

ISBN: 978-3-96147-007-5 (Druckausgabe)
eISBN: 978-3-96147-008-2 (Online-Ausgabe)
ISSN: 2198-8102

Atomistic Simulations of Crack Front Curvature Effects and Crack-Microstructure Interactions

---

Atomistische Simulationen von Rissfrontkrümmungseffekten und Riss-Mikrostruktur-Wechselwirkungen

---

Der Technischen Fakultät

der Friedrich-Alexander-Universität Erlangen-Nürnberg

zur Erlangung des Doktorgrades

Doktor der Ingenieurwissenschaften (Dr.-Ing.)

vorgelegt von

Johannes Joel Möller

aus Bielefeld

Als Dissertation genehmigt
von der Technischen Fakultät
der Friedrich-Alexander-Universität Erlangen-Nürnberg

Tag der mündlichen Prüfung:	14. Juli 2016
Vorsitzender des Promotionsorgans:	Prof. Dr. Peter Greil
Gutachter:	Prof. Dr.-Ing. Erik Bitzek
	Prof. Dr. Alexander Hartmaier

Acknowledgments

This work was carried out during the years 2011-2016 at the Friedrich-Alexander-Universität Erlangen-Nürnberg, Department of Materials Science and Engineering, Institute I: General Materials Properties.

I owe my deepest gratitude to my supervisor Prof. Dr.-Ing. Erik Bitzek for his helpful comments, stimulating ideas, and endless curiosity. His enthusiasm for my thesis topic always inspired me to delve deeper into the world of atoms, cracks, and dislocations.

I would like to thank the additional members of the review panel, Prof. Dr. Alexander Hartmaier for writing the second review, PD Dr.-Ing. Julia Mergheim for taking over the position as "Fachfremde Prüferin", and Prof. Dr. Mathias Göken for being the chairman.

It is an honor for me to thank Prof. Dr.-Ing. Hans-Jürgen Christ for organizing the DFG priority program SPP 1466 "Life$^{\infty}$" and our local fatigue experts PD Dr.-Ing. habil. Heinz Werner Höppel and Prof. Dr. Haël Mughrabi. The scientific and social discourses with my SPP companions Michael Buck, Philipp Hilgendorff, and Dr.-Ing. Thomas Straub are highly appreciated.

I am grateful to many of my (former) colleagues at WW1, the secretary, and the technical staff for the "WW1 atmosphere"—often copied, never matched. High-Five to Dr.-Ing. Johannes Ast, Dr.-Ing. Dominik Bösch, Markus Kolb, Martin Pröbstle, Dr.-Ing. Mathis Ruppert, and Christopher Schunk! In particular, I wish to thank my SPP comrade Jochen Bach for practical insights into fatigue experiments, Franconian lifestyle, and many 3-for-2-moments; Carolin Zenk for our fruitful discussions, sometimes about science, but mostly about nutrition, sports, and life in general; and the "Pförtner" Martin Kommer and Christopher Zenk: Single Malt Whisky and elbow patches will never be out of style.

I would like to show my gratitude to Sudheer Ganisetti, Frédéric Houllé, and Aviral Vaid, my dear friends in the simulation group. For the smile, the look, and the cook!

I am thankful for the support by Dr. Alexander Stukowski (whenever it came to OVITO), Tobias Klöffel (whenever it came to DFT), Dr.-Ing. Arun Prakash (whenever it came to FE), and Dr.-Ing. Markus Krottenthaler (whenever it came to Linux).

Merci to Dr. Julien Guénolé for helpful comments on the figures. Cheers to Wolfram Nöhring for proof reading of the manuscript and our usually expected friendship.

Thanks to the members of the "WW-Lauftreff"—a Jour fixe that often saved my day.

Märssi, Fabian Haag, for thousands of meters altitude gain—and for the related pain.

I thank Ines Huibens for her interest, encouraging words, and for having lunch with me whenever school was out. I also would like to thank Eva and Wolfgang Ernhofer, as well as Viktoria Trenkle for their individual support, distracting conversations, and for playing cards all night long.

Last, but most important, I am grateful to my family and my girlfriend Katrin. Without their support during the past years, this work would not have been possible.

Parts of this thesis have been already published:

- J.J. Möller, A. Prakash, E. Bitzek, *FE2AT—finite element informed atomistic simulations*, Modelling Simul. Mater. Sci. Eng. **21**, 55001 (2013).
- J.J. Möller, E. Bitzek, *Comparative study of embedded atom potentials for atomistic simulations of fracture in α-iron*, Modelling Simul. Mater. Sci. Eng. **22**, 45002 (2014).
- J.J. Möller, E. Bitzek, *Fracture toughness and bond trapping of grain boundary cracks*, Acta Mater. **73**, 1 (2014).
- J.J. Möller, E. Bitzek, *On the influence of crack front curvature on the fracture behavior of nanoscale cracks*, Eng. Fract. Mech. **150**, 197 (2015).
- J.J. Möller, E. Bitzek, *BDA: A novel method for identifying defects in body-centered cubic crystals*, Methods X **3**, 279 (2016).
- J.Bach, J.J. Möller, M. Göken, E. Bitzek, H.W. Höppel, *On the Transition from Plastic Deformation to Crack Initiation in the High- and Very High-Cycle Fatigue Regimes in Plain Carbon Steels*, Int. J. Fatigue **93**, 281 (2016).

Johannes J. Möller — Atomistic simulations of crack front curvature effects and crack-microstructure interactions

Abstract. The resistance against crack propagation is undoubtedly one of the most important properties of metallic materials. Particularly in the early stage of their existence, the growth of cracks is influenced by interactions with the surrounding microstructure, e.g., grain boundaries and dislocations. In this context, atomistic simulations play an important role in providing valuable information about fundamental crack tip processes, which can be used for the development of larger-scale models to predict crack propagation in realistic microstructures.

The present thesis contributes to this development by systematically determining the influences of crack front curvature and grain boundary (GB) structure on the competition between brittle fracture and crack tip plasticity in body-centered cubic (bcc) metals. For this purpose, multi-million atom molecular statics and dynamics simulations of perfectly straight and penny-shaped cracks were performed in defect-free single crystals and for the first time at GBs. Crack-dislocation interactions were exemplarily investigated for selected crack and slip systems.

At curved crack fronts, many slip planes intersect parts of the crack front and the tendency for crack tip plasticity is consequently higher than for infinitely long and straight crack fronts. Crack tip plasticity was characterized by multiple dislocation-crack interactions as a result of many successive cross slip events along the curved crack front. This information is particularly relevant for meso-scale models of small highly curved crack nuclei or long cracks that are locally curved due to e.g. crack pinning at obstacles.

At GBs, locally varying bonding situations led to the dependence of the fracture resistance on the crack tip position and crack propagation direction. This indicates that the ultimate fracture toughness of a GB is not exclusively determined by its weakest bond and can be higher than predicted by the thermodynamic Griffith theory and even exceed the fracture resistance of single crystals. Including the characteristics of GB fracture could significantly improve meso-scale models of inter- and trans-granular fracture.

Crack-dislocation interactions were dominated by dislocation cross slip and subsequent glide along the crack front leading to local crack tip blunting. The stimulated emission of a dislocation by the direct interaction between a crack and an incoming dislocation was observed here for the first time in a bcc crystal.

Furthermore, two types of dynamic instabilities were frequently observed during the simulations: the arrest of a formerly brittle propagating crack and the emission of dislocations from a growing deformation twin. The underlying reasons for both phenomena and their possible occurrence under experimental conditions are discussed.

In addition, this thesis presents a novel technique for identifying bcc crystal defects, best practices for atomistic fracture simulations, and a survey of existing bcc potentials, which are appropriate for fracture studies. Finally, a contribution to the development of new interatomic potentials is given by providing (i) a semi-empirical equation for the potential-dependent *lattice trapping* range; and (ii) a simple directive to avoid certain nonphysical crack tip transformations.

Johannes J. Möller — Atomistische Simulationen von Rissfrontkrümmungseffekten und Riss-Mikrostruktur-Wechselwirkungen

Kurzzusammenfassung. Der Widerstand gegen Rissausbreitung ist unzweifelhaft eine der wichtigsten Eigenschaften metallischer Werkstoffe. Insbesondere kurz nach ihrer Initiierung wird das Wachstum von Rissen durch Wechselwirkungen mit der umgebenden Mikrostruktur, wie z.B. Korngrenzen und Versetzungen, beeinflusst. In diesem Zusammenhang liefern atomistische Simulationen wichtige Informationen über fundamentale Rissspitzenprozesse, welche anschließend für die Entwicklung höher-skaliger Modelle zur Rissausbreitung in realistischen Mikrostrukturen verwendet werden können.

Die vorliegende Arbeit trägt hierzu bei, indem systematisch die Einflüsse von Rissfrontkrümmung und Korngrenzstruktur auf die beiden konkurrierenden Prozesse Sprödbruch und Rissspitzenplastizität in kubisch-raumzentrierten (krz) Metallen bestimmt werden. Zu diesem Zweck, wurden großskalige Molekulardynamik und -statik Simulationen in defektfreien Einkristallen und erstmalig auch an Korngrenzen durchgeführt. Des Weiteren wurden Riss-Versetzungs-Wechselwirkungen exemplarisch für ausgewählte Riss- und Gleitsysteme untersucht.

An gekrümmten Rissfronten sorgt die höhere Anzahl an zur Verfügung stehenden Gleitsystemen für eine erhöhte Tendenz zur Rissspitzenplastizität im Vergleich zu unendlich langen und geraden Rissfronten. Die Rissspitzenplastizität ist durch eine Vielzahl an Riss-Versetzungs-Wechselwirkungsprozessen gekennzeichnet, welche eine Folge von vielen aufeinanderfolgenden Quergleitprozessen der emittierten Versetzungen entlang der gekrümmten Rissfront sind. Diese Informationen sind besonders relevant für meso-skalige Modelle von kleinen, stark gekrümmten Risskeimen oder langen Rissen, welche lokal gekrümmt sind, z.B. infolge der lokalen Behinderung der Rissausbreitung an Hindernissen.

An Korngrenzen sorgen die lokal unterschiedlichen Bindungssituationen für eine Abhängigkeit des Bruchwiderstandes von der Rissspitzenposition und der Rissausbreitungsrichtung. Dies deutet an, dass die Bruchzähigkeit von Korngrenzen nicht ausschließlich von ihren schwächsten Bindungen bestimmt wird. Sie kann vielmehr höher sein als durch das thermodynamische Griffith-Kriterium vorhergesagt und sogar den Bruchwiderstand von Einkristallen übertreffen. Die Implementierung dieser allgemeinen Eigenschaften des Korngrenzbruchs könnte meso-skalige Modelle zur Vorhersage von zwischen- und innerkristallinem Bruch deutlich verbessern.

Riss-Versetzungs-Wechselwirkungen werden durch Quergleitprozesse der Versetzungen und ihr anschließendes Gleiten entlang der Rissfront dominiert, welches schließlich zum Abstumpfen des Risses führt. Die stimulierte Versetzungsemission durch die direkte Wechselwirkung des Risses mit einer Versetzung wurde hier erstmalig in einem krz Kristall beobachtet.

Des Weiteren wurden während der Bruchsimulationen häufig zwei Typen dynamischer Instabilitäten beobachtet: das Anhalten eines zuvor spröde fortschreitenden Risses und die Versetzungsemission ausgehend von einem wachsenden Verformungszwilling. Die Gründe für diese Phänomene sowie ihr mögliches Auftreten unter experimentellen Bedinungen werden detailiert diskutiert.

Zusätzlich werden eine neuartige Methode für die Identifizierung von Kristalldefekten in krz Strukturen, praktische Empfehlungen für zukünftige atomistische Bruchsimulationen und ein Überblick über existierende Wechselwirkungspotentiale, welche für Bruchsimulationen geeignet sind, präsentiert. Abschließend wird durch (i) das Aufstellen einer semi-empirischen Gleichung für die Potentialabhängigkeit des *lattice trapping* Effektes und (ii) eine einfache Richtlinie zur Vermeidung von nicht-physikalischen Rissspitzen-Transformationen zur Entwicklung neuer Wechselwirkungspotentiale beigetragen.

Contents

List of frequently used symbols

a	Crack length or radius; Fig. 2.1a,b
a_{eff}	Effective crack length after relaxation
a_0	Lattice constant (at 0 K)
$\underline{b}$	Burgers vector
b	Burgers vector length
$\underline{b}_{\mathrm{t}}$	Burgers vector of twinning partial dislocation
C_{ij}	Components of elastic stiffness matrix
c_{l}	Transversal wave speed; Eq. (2.10)
c_{R}	Rayleigh surface wave speed; Eq. (2.11)
c_{t}	Longitudinal wave speed; Eq. (2.9)
$\Delta\varepsilon$	Lattice trapping ratio (strain control); page 57
ΔK	Lattice trapping range (K control); Eq. (2.18)
Δk	Predicted lattice trapping ratio; Eq. (7.9)
ΔL	Distance from crack tip to boundary; page 11
Δx	Crack propagation distance
Δ_{y}	Separation in y direction; section 7.1.3
d	Particle spacing; Eq. (2.17)
d	Spacing of parallel crystallographic planes
$\delta\varepsilon$	Size of strain step in quasi-static simulations
δt	Time step in dynamic simulations
E	Young's modulus
E^*	Orientation-dependent elastic modulus; Eq. (C.3)
E_{y}	Sample-dependent Young's modulus in y direction
E_{pot}	Potential energy
F_{eff}	Effective pair force; Fig. 3.1
$F_{\mathrm{x,y,z}}$	Interatomic force in x, y, or z direction
F_{max}	Maximum of effective pair force
F_{PK}	Peach-Koehler force; Eqs. (7.14-7.15)
ε	Applied strain
$\dot{\varepsilon}$	Strain rate
ε^+	Critical strain for crack propagation
ε^-	Critical strain for crack closure
ε_0	Predicted critical strain; Eq. (3.4)
ε_{c}	Critical fracture (quasi-static) strain; section 3.3.3
ε_{a}	Strain at crack arrest
$\varepsilon_{\mathrm{abs}}$	Absorption strain for GB dislocations; section 6.3
ε_{e}	Strain where dislocation emission takes place

ε_{G}	Predicted critical strain after Griffith; Eq. (3.3)
ε_{i}	Critical strain (dynamic); section 3.3.3
$\varepsilon_{\mathrm{in}}$	Initial strain; section 3.3.3
$\varepsilon_{\mathrm{p,small}}$	Predicted critical strain; Eq. (7.5)
$\varepsilon_{\mathrm{p,large}}$	Predicted critical strain; Eq. (7.6)
$\varepsilon^{\mathrm{pre}}$	Prescribed lateral strain method; section 3.3.4
$\varepsilon^{\mathrm{zero}}$	Zero lateral strain method; section 3.3.4
G	Energy release rate (ERR); Eq. (2.2)
G_0	Sample-dependent critical ERR; Eq. (3.5)
G_{G}	Critical ERR after Griffith; Eq. (2.3)
$G_{\mathrm{G,GB}}$	Critical ERR of GBs; Eq. (2.22)
G_{e}	Critical ERR for dislocation emission; Eq. (2.14)
Γ	Fracture energy; page 6
γ	Surface energy
$\gamma_{1,2}$	Surface energy for grain (crystal orientation) 1 or 2
γ_{GB}	Grain boundary energy; section 2.2
γ_{usf}	Unstable stacking fault energy; Eq. (2.14)
γ_{ut}	Unstable twinning energy; section 2.3.2
K	Stress intensity factor (SIF)
K^{+}	Critical SIF for crack propagation
K^{-}	Critical SIF for crack closure
K_{e}	Predicted SIF for dislocation emission, Eq. (2.15)
$K_{\mathrm{I,II,III}}$	SIF in mode I, II, or III; page 9
K_{Ic}	Determined fracture toughness; section 3.3.3
K_{Ic}^{*}	Calculated fracture toughness from ε_{c}; Eq. (2.6)
K_{in}	Initial SIF for K-controlled simulations; section 3.3.3
K_{G}	Critical SIF after Griffith; Eq. (2.7)
$K_{\mathrm{G,GB}}$	Critical SIF of GBs; Eq. (2.23)
K_{t}	Predicted SIF for twin formation; Eq. (2.31)
$L_{\mathrm{x,y,z}}$	Box length of x, y, or z axis
λ	Length of structural unit; section 5
λ_0	CSL repeat distance along GB; section 5
λ_{crit}	Relative additional load in Eq. (2.30)
μ	Shear modulus; page 11
N	Number of atoms
n	Number of twin layers; section 2.3.2
$\underline{n}$	Plane normal vector
ν_{ij}	Poisson ratio
φ	Orientation of Burgers vector in slip plane; Fig. 3.3a
Ψ	Misorientation angle of CSL grain boundary
ψ	Angle in cylindrical coordinate system; Fig. 2.1
r	Distance from crack tip; Fig. 2.1
r_{B}	Radius of Hydrogen atom

r_{cut}	Cutoff radius of interatomic potential
r_{ij}	Distance of atoms i and j; Eq. (3.2)
Σ	Relative volume of coincidence site lattice; Eq. (2.19)
σ_{ij}	Components of stress tensor
σ^{min}	Minimum stress lateral strain method; section 3.3.4
σ_{y}	Applied remote tensile stress
T	Twinning tendency; Eq. (2.30)
T	Higher-order T-stress; Eq. (7.7)
T_0	Start temperature in dynamic simulations
T_{BDT}	Brittle-ductile transition temperature; section 2.1.2
T_{crack}	Crack line tension; Eq. (2.17)
t_{b}	Propagation time of elastic wave to configuration boundary; Eq. (2.12)
θ	Angle in polar coordinate system; Fig. 2.1a
θ	Inclination angle of slip plane; Eq. (2.14)
$\langle u\, v\, w \rangle$	Misorientation axis of grain boundary; Eq. (2.21)
$u_{\mathrm{x,y,z}}$	Displacement in x, y, or z direction
V_{eff}	Effective pair potential; Fig. 3.1
x, y, z	Simulation box axes
Y	Geometry factor; Eq. (2.6)

List of frequently used abbreviations

a-CNA	Adaptive common neighbor analysis
ADP	Angular-dependent potential
AT	Antitwinning (direction)
ATFS	Ackland-Thetford-Finnis-Sinclair (potential)
ATGB	Asymmetrical tilt grain boundary
bcc	Body-centered cubic
BDA	BCC Defect Analysis
BDT	Brittle-ductile transition
BFGS	Broyden-Fletcher-Goldfarb-Shanno (relaxator)
BOP	Bond-order potential
CN	Coordination number
CNA	Common neighbor analysis
CSL	Coincidence site lattice
CSP	Centrosymmetry parameter
CTT	Crack tip transformation
CZ	Cohesive zone (model)
DD	Dislocation dynamics (simulation)
DD	Differential displacement (map)
DFT	Density functional theory
DFT-R	Relaxed DFT calculation
DFT-NR	Non-relaxed DFT calculation
DOF	Degree(s) of freedom
EAM	Embedded atom method (potential)
EFG	Element-free Galerkin (method)
ERR	Energy release rate
fcc	Face centered cubic
FE	Finite element (calculation/method)
FIB	Focused ion beam
FIRE	Fast inertial relaxation engine
FS	Finnis-Sinclair (potential)
GB	Grain boundary
GGA	Generalized gradient approximation
GNU	GNU's Not Unix
GPL	General Public License
GSFE	Generalized stacking fault energy
HP	Half plane
IMD	ITAP Molecular Dynamics

LCM	Lateral strain method
MD	Molecular dynamics (simulation)
MEAM	Modified embedded atom method
MEMS	Micro electro-mechanical system
MFS	Marchese-Finnis-Sinclair (potential)
MIK	Microconvergence (integrator)
MS	Molecular statics (simulation)
nn	Next-nearest neighbor
nn2	Second-nearest neighbor
NVE	Microcanonical ensemble
OVITO	Open visualization tool
PAW	Projector augmented wave
PBE	Perdew-Burke-Ernzerhof
PBC	Periodic boundary conditions
PK	Peach-Koehler (force)
PN	Peierls-Nabarro (model)
PX	Polycrystal
SIF	Stress intensity factor
SSF	Stable stacking fault
STGB	Symmetrical tilt grain boundary
SX	Single crystal
TD	Twinning dislocation
TEM	Transmission electron microscope
TW	Twinning (direction)
TWE	Twinning energy
US	Ultrasoft (pseudopotential)
usf	Unstable stacking fault (energy)
ut	Unstable twinning (energy)
X-FEM	Extended finite element method

1 Introduction

Let us start with the definition of fracture, being the main theme of this thesis:

> **frac·ture** (frăk′chər) *n.* **1.** The act or process of breaking.
> **2.** The condition of having been broken or ruptured: *"a sudden and irreparable fracture of the established order" (W. Bruce Lincoln).*
>
> American Heritage Dictionary
> Fifth Edition

The fracture of a material is caused by cracks, which propagate through it and separate it into two or more parts. In nearly all metallic materials, small crack nuclei exist as a result of e.g. manufacturing, heat treatment, or loading. Upon further (monotonic or cyclic) deformation, such embryonic cracks can grow and finally cause the macroscopic failure of the component. Careful component design therefore accounts for this scenario and avoids the sudden loss of structural integrity. Furthermore, the costs of damage caused by cracks can be considerable budget items for national economies [1, 2]. As a result, many billions of dollars could be spared if the existing fracture mechanics concepts were considered [3, 4].

Fracture mechanics is a multi-disciplinary and multi-scale field, in which cracks are studied from at least three different points of view: analytical, numerical, and experimental [4]. It is multi-disciplinary since it encompasses effects that are classically located in the fields of e.g. solid-state physics, materials science, or continuum mechanics [5]. Likewise, it is a multi-scale problem since the fracture resistance of a material is determined by a complex interaction of physical processes at scales ranging from below 1 nm to 100 μm or more [6, 7]. Examples for such processes are the interaction of cracks with microstructural defects, such as impurities, voids, dislocations, precipitates, and grain or phase boundaries. Local variations in the microstructure lead inevitably to varying crack propagation distances and to the curvature of the crack front. This is particularly the case for embryonic cracks shortly after crack nucleation; in this stage of their existence, the growth of cracks is strongly influenced by interactions with the surrounding microstructure [8].

The multitude of crack-microstructure interactions makes it *de facto* impossible to predict the fracture resistance of a material by means of theories or numerical calculations. The reliability of such predictions is highly relevant for the safety assessment and construction of technical components as well as for the development of new failure-tolerant materials. Most fracture theories derive from the famous Griffith concept [9] or modifications of it [10]. In his classic 1921 paper, Griffith notionally compared the energies of the same strained body for two different scenarios; one containing a crack and one without a crack. According to his theory, the critical condition for crack propagation is the energy balance of the two configurations. The great success of this idea, however, should not distract us

from situations where it does not apply. Prime examples for such phenomena become especially obvious when it comes down to the atomic length scale. At this scale, cracks in crystalline materials are trapped by the discreteness of the bonds within a crystal lattice [11–13]. The effect of this so-called *lattice trapping* can have macroscopically measurable implications [14]. Likewise, the continuum description used by Griffith does not account for the nucleation of dislocations at the crack tip [15, 16]. The competition between these two processes plays a key role for materials which show a brittle-to-ductile transition, such as most body centered cubic (bcc) metals [10].

While many theoretical models work sufficiently well for (microstructurally) homogeneous materials like glasses, the prediction of the crack propagation behavior in complex, heterogeneous microstructures is an insurmountable obstacle for them. This opens the field for so-called meso-scale models, which operate between the atomic (discrete) and macroscopic (continuum) length scales [7, 17]. Meso-scale models can include microstructural information, e.g., about grain boundaries [18] and dislocations [19], and contain libraries of characteristic defect properties and possible interaction mechanisms, which are active under certain circumstances. They finally help to develop constitutive equations for the material's behavior and can predict the microstructure-dependent fracture criterion. The reliability of meso-scale models obviously depends on the quality of the input parameters and the implemented mechanisms. In other words, they can not predict the effect of a process or a microstructural detail which has not been included in the model. The great challenge therefore is to determine the fundamental interaction mechanisms of cracks with isolated defects in order to include them in new numerical models.

The precise sequence of events as well as meso-scopic and atomic-level details are either not accessible or they are restricted to only the specimen surface even if studied using modern scanning or transmission electron microscopes [7]. An alternative approach is to derive the necessary information from atomic-scale simulation techniques, e.g., using classical semi-empirical potentials [20] or density functional theory (DFT) calculations [21]. The study of crack-microstructure interactions, however, is currently only possible with large-scale molecular dynamics (MD) simulations using classical interatomic potentials as the necessary number of atoms is too large for more accurate methods of material modeling.

The objective of this thesis is to obtain a better understanding of the effect of crack front curvature and crack-microstructure interactions at the atomic scale. Thereby the foundations are laid for the development of new microstructure-sensitive meso-scale models for bcc-based materials. For this purpose, I determine the fracture properties of perfectly straight cracks in differently oriented defect-free single crystals to obtain reference data sets. The dependencies of the fracture behavior and criteria on crack front curvature, locally varying bonding situations at GBs, and pre-existing dislocations are investigated for selected single crystal and bicrystal configurations in the bcc metals iron (Fe) and tungsten (W). The determination of these influences is highly relevant for bcc metals in the context of crack initiation [8, 22–24], brittle intergranular fracture [25, 26], and pre-deformation, which can alter the brittle-ductile transition [27]. Fe and W are chosen as model materials for the semi-brittle bcc metals, where the competition between cleavage and crack tip

plasticity is particularly important; for both materials the determined fracture properties in single crystals can be compared to literature data from both experiments [14, 28] and atomistic simulations [29, 30].

The systematic increase in the level of complexity of the studied interactions allows to finally address the following key questions: (i) what is the general influence of crack front curvature on the competition between brittle fracture and crack-tip plasticity? Especially, how is it related to theoretical fracture criteria and to the fracture properties of perfectly straight cracks? What is the influence of crack front curvature on the lattice trapping effect and on the evolution of crack tip plasticity? (ii) How do locally different bonding situations influence the crack propagation behavior at GBs? In particular, how does it compare to theoretical fracture criteria and to cracks in defect-free single crystals? Which effect has the possibility for local re-arrangements at long 3D crack fronts and which mechanisms are specific to GB cracks with curved crack fronts? (iii) How do cracks interact with pre-existing dislocations? In this context, the role of the dislocation character (edge, screw, mixed), the relative orientation between the crack and possible slip planes, and the effect of absorbed dislocations on the fracture resistance of GBs are of fundamental interest.

The following chapter presents a brief introduction to the relevant theories of fracture mechanics, grain boundaries, and dislocations. It also contains reviews on previous atomistic studies of fracture, grain boundary fracture, and crack-dislocation interactions, as well as meso-scale models for fracture. Chapter 3 introduces the computational methods, setups, and visualization techniques used. In chapters 4-5, the determined fracture properties are presented for cracks in defect-free single crystals and at grain boundaries, respectively. Examples for important crack-dislocation interactions are shown in chapter 6. Thereafter, the presented results are compared to theory, literature, and experiments in chapter 7, where the key questions of this thesis are addressed in detail. Finally, I summarize the most important consequences of this thesis in chapter 8 and give an outlook for future work on this topic in chapter 9.

2 Theoretical background and literature overview

This chapter summarizes the most important theories in the field of fracture mechanics as well as relevant experimental and numerical studies on semi-brittle body-centered cubic (bcc) metals with focus on iron (Fe) and tungsten (W). In addition to many other technological and environmental factors, the fracture behavior and resistance of materials strongly depends on the interaction of cracks with microstructural defects. Among the multitude of defects, the perhaps most interesting ones are grain boundaries since they exist in nearly all metallic materials of industrial importance. The basic theoretical concepts and fundamental literature work on grain boundaries are summarized in section 2.2 with special emphasis on GB fracture. Section 2.3 presents the two main carriers of plastic deformation in metals, namely dislocations and deformation twins. Their relevance for this thesis is twofold: on the one hand, both can nucleate at crack tips as a way to relief stresses; on the other hand, particularly dislocations exist *a priori* in nearly all materials and are possible interaction partners for cracks.

The expected impact of this thesis is to identify fundamental atomic-scale aspects of crack interactions with microstructure, which can be used for the development of new larger-scale models for fracture in polycrystals. For this reason, section 2.4 provides a brief overview of how fracture theory, experiments, and simulations can be combined to model fracture at the meso scale.

Based on the presented theories and literature, I finally identify a number of key questions, which will be addressed in the following course of this thesis. These questions are detailed in section 2.5.

2.1 Fracture

In this section, I introduce the most important theories of fracture, including fracture criteria and the distribution of stresses around crack tips in continuous media. In section 2.1.2, we focus on experimental results of fracture tests in single crystalline bcc metals with emphasis on Fe and W. Finally, atomistic simulations of fracture in single crystals are reviewed in section 2.1.3.

2.1.1 Fundamental aspects of fracture

Like all materials defects, such as dislocations, vacancies, impurities, and grain boundaries, cracks are always present in nearly every technologically important material. Understanding their fundamental properties is therefore crucial for any study of materials deformation

and failure as well as for the safety assessment of technical components. For brevity, this section is limited only to those aspects relevant for this study, i.e., the theoretical criteria for brittle fracture and crack tip plasticity, the stress distribution around crack tips, the plane stress and plane strain states, the different modes of fracture, dynamic effects, 3D aspects and the effects of crack front curvature and crystal structure. For an in-depth introduction to the theory of fracture, the reader is referred to textbooks [10, 31–33].

Griffith criterion for brittle fracture

The fracture of a material or component is always caused by a heterogeneous stress distribution in the body, which occurs at material imperfections, such as inclusions or holes. Here, the cohesion of the material is weakened and the local stresses can be much higher than in the surrounding. This concentration of stresses was first evaluated by Inglis, who solved the boundary value problem of the excess of stress caused by a hole in a thin plate [34]. He introduced the stress concentration factor $2\sqrt{a/\rho}$ to estimate the increase of stresses at an elliptic hole with respect to the applied stress σ. Here, a is the long axis of the ellipse and ρ the radius of curvature at the tip of the ellipse. Alternatively, ρ can be interpreted as the radius at the root of a flaw with a being the overall flaw size.

In 1921, Griffith developed his theory of brittle fracture based on the comparison between a stressed sheet of unit thickness and the same sheet containing a central crack of length $2a$ [9]. Assuming linear elasticity, the difference in the stored elastic energy between the two states is then proportional to σ^2/E^* and a (with E^* describing the elastic response in the loading direction). The main legacy of Griffith's theory is the observation that crack propagation in a brittle material starts when the applied stress reaches the critical stress σ_c, at which the stored elastic energy exceeds the necessary energy for the creation of new surfaces with surface energy γ at both sides of the crack faces. The critical fracture stress σ_c, however, depends on the crack length a; as a consequence, it is insufficient to describe a material's resistance against fracture. Instead, he identified the term $\sigma_c\sqrt{a}$ as the critical material parameter.

According to the Griffith theory, the critical energy to overcome equals 2γ, which is an invalid assumption whenever a material's response deviates from ideally brittle, linear-elastic behavior. Owing to this observation, the Griffith criterion was generalized by replacing 2γ by the more general term fracture energy Γ [35, 36]. In addition to 2γ, it contains non-linear and potential plastic effects and has to be determined by evaluating the elastically stored energy in the body, the so-called energy release rate G, at which the crack starts to propagate. The energy release rate G is defined as the rate of change in potential energy with crack area:

$$G = \frac{\partial E_{\mathrm{pot}}}{\partial A}. \tag{2.1}$$

A general formulation for G in presence of a crack with length a was obtained by Orowan and Irwin [35, 36]:

$$G = \beta\frac{\sigma^2 a}{E^*}. \tag{2.2}$$

where β is a geometric factor that depends on the boundary conditions. With this, the Griffith criterion for purely brittle fracture is expressed in the well-known form:

$$G = G_{\mathrm{G}} = 2\gamma, \tag{2.3}$$

where the subscript 'G' stands for 'Griffith'. As mentioned earlier, most materials are not perfectly brittle, but show non-linear and plastic effects prior to fracture. For this reason, the Griffith criterion is only a lower limit for the critical energy release rate.

Crack tip stress field

Westergaard and Sneddon showed that the first-order solution of the crack tip stress field is proportional to $1/\sqrt{r}$, which leads to a singularity at the tip [37, 38]. Later, Williams and Irwin approximated the stress distribution around the crack tip, as follows [39, 40]:

$$\sigma_{\mathrm{ij}}(r,\theta) \quad = \quad \frac{\sqrt{GE^*}}{\sqrt{2\pi r}} f_{\mathrm{ij}}(\theta) + \text{higher-order terms} \tag{2.4}$$

where r and θ are polar coordinates centered at the crack tip, see Fig. 2.1a. The dimensionless factor $f_{\mathrm{ij}}(\theta)$ can be solved analytically for linear-elastic isotropic materials [39, 40]. Higher-order terms, such as the 'background' stress [41] and the T-stress [42] are r-independent contributions to the σ_{xx} and σ_{yy} components, respectively; both are especially important for finite-size specimen [43]. The precise functional forms and numerical values of the higher-order terms are, however, sample-dependent and available only for a limited number of specimen geometries [43–45]. For this reason, higher-order terms are often neglected. Furthermore, the elastic response of most materials is not isotropic, but anisotropic. In this case, the factors f_{ij} become more complex and must be solved numerically for the given combination of crystal orientation and elastic constants C_{ij} [46, 47].

Independent of the elastic properties of the material, the amplitude of the stress field scales with a single parameter, the so-called stress intensity factor (SIF) K. It is related to both the energy release rate G and the applied stress σ using Eq. (2.2), as follows [39, 40]:

$$K \quad = \quad \sqrt{GE^*} \tag{2.5}$$

$$K \quad = \quad Y\sigma\sqrt{a} \tag{2.6}$$

where Y is a dimensionless number or function that depends on the shape of the crack and the body as well as on the distribution of the load. Much effort has been put into the determination of the geometry functions Y for many different situations [49–51]. In infinite bodies and under uniformly applied loads, $Y = \sqrt{\pi}$ for a central through-thickness crack of length $2a$, i.e., the so-called Griffith crack [9].

The Griffith criterion, Eq. (2.3), can be expressed in terms of the stress intensity factor, as follows:

$$K_{\mathrm{G}} \quad = \quad \sqrt{G_{\mathrm{G}}E^*} = \sqrt{2\gamma E^*} \tag{2.7}$$

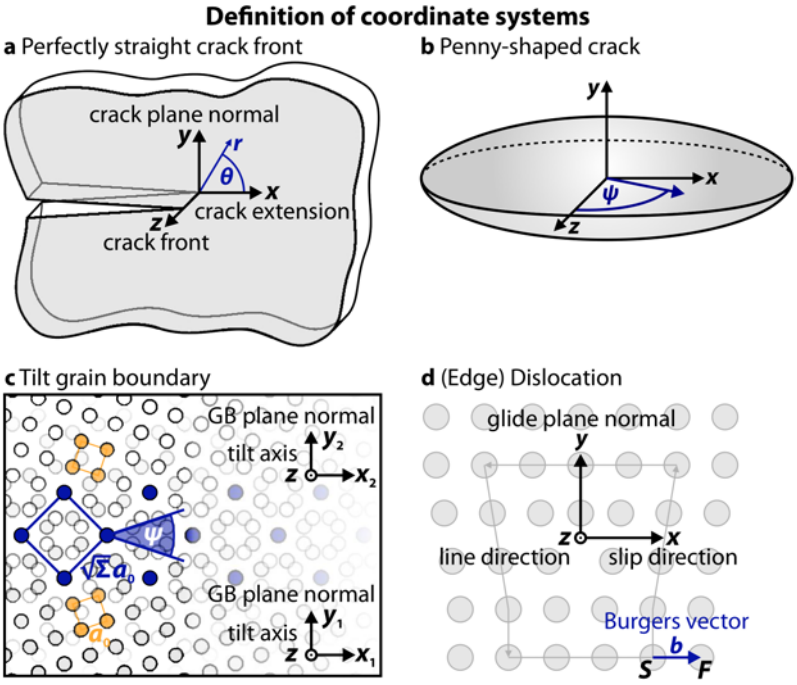

Figure 2.1: Definition of coordinate systems. **a**: crack tip with a perfectly straight crack front; indication of polar coordinates r and θ; **b**: penny-shaped crack with angular component ψ of the cylindrical coordinate system around the y axis; **c**: tilt CSL grain boundary with tilt angle Ψ and axis z; the original unit cells are marked with orange color in the adjacent crystals; the unit cell of the coincidence site lattice (CSL) is marked with blue color; the ratio of the unit cell volumes of the CSL and the original lattice equals Σ; note that the coordinate systems in different grains 1 and 2 are indicated with subscripts 1 and 2, respectively; **d**: edge dislocations with indicated Burgers vector $\underline{b}$ according to the SF/RH definition in Ref. [48].

Plane stress vs. plane strain

For surface cracks, i.e., cracks where parts of the crack front are located at the material's surface, the magnitude of the crack-tip stresses depends not only on the distance from the crack-tip. In this situation, the position along the crack front direction z also influences the stress state. The definition of the coordinate system is shown in Fig. 2.1a: x points along the crack extension direction and y perpendicular to the crack plane. At a free surface perpendicular to the crack front, the stresses in crack front direction can relax, i.e., $\sigma_{zz} = 0$. This situation is referred to as plane stress. In the interior of the material, on the other hand, the crack tip stresses along the crack front cannot relax. Instead, they respond on the crack tip stresses in the xy plane, i.e., $\sigma_{zz} = \nu(\sigma_{xx} + \sigma_{yy})$ for an isotropic linear-elastic material with Poisson ratio ν. In this so-called plane strain state, the strains ε_{zz} are only equal to zero if no external loads are applied. In presence of an external load σ, the lateral contraction,

i.e. $\varepsilon_{zz} = \varepsilon_{xx} = -\nu\sigma/E$ has to be accounted for [32]. The different distributions of the stresses and strains under conditions of plane stress and plane strain are schematically shown in Fig. 2.2a-c for a crack tip in an infinitely large body and for a remote tensile load.

In typical fracture tests, cf. the ASTM standard E 399-90 [52], the plane strain state is a necessary condition for valid test results [32]. For this reason, the simulation setups used in the present work aim to model plane strain conditions whenever this is possible.

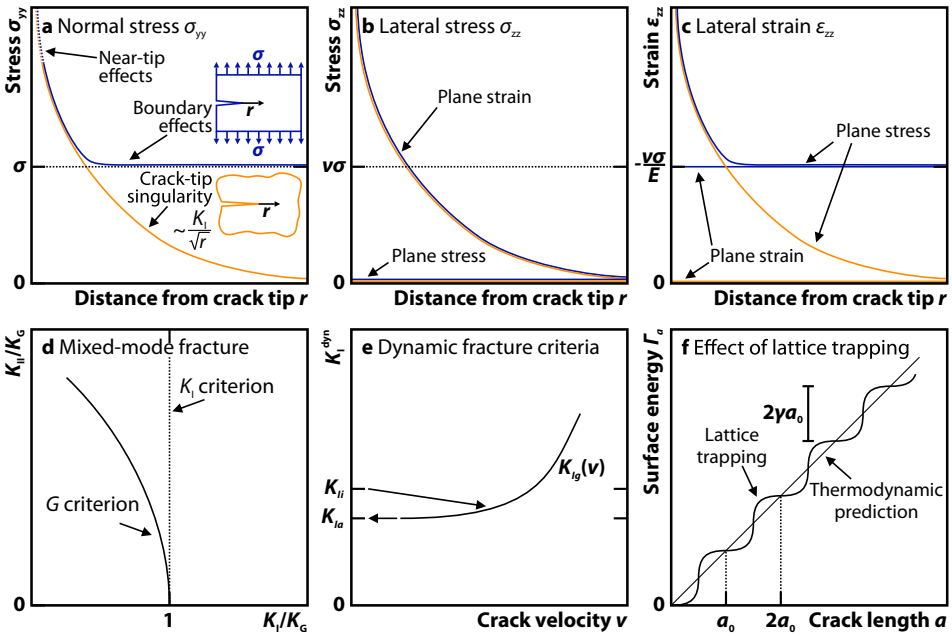

Figure 2.2: Schematic illustrations of various theoretical relationships in the field of fracture. **a**: the distribution of σ_{yy} stresses is mainly determined by the singular crack tip field and boundary effects (higher-order terms); nonlinear-elastic effects play only a role in the close vicinity of the crack tip; **b**: evolution of lateral σ_{zz} stresses under plane strain and plane stress conditions; **c**: evolution of lateral ε_{zz} strains under plane strain and plane stress conditions; **d**: G vs. K_I criteria for mixed-mode fracture (after Ref. [53]) **e**: dynamic fracture criteria for crack initiation, growth, and arrest: K_{Ii}, $K_{Ig}(v)$, and K_{Ia} (after Ref. [54]) **f**: effect of lattice trapping on the surface energy created by an advancing crack (after Ref. [10]). Coordinate systems as introduced in Fig. 2.1a.

Modes of fracture

According to Irwin [55], the relative displacement of the crack faces leads to the distinction of the following three fracture modes:

- **Mode I:** tensile or opening mode
- **Mode II:** in-plane shear or sliding mode
- **Mode III:** anti-plane shear or tearing mode

Each of them is characterized by a corresponding stress intensity factor K_I, K_{II}, or K_{III}. The critical stress intensity factor under pure mode I loading is called the fracture toughness K_{Ic}. This characteristic material parameter can only be determined experimentally and is influenced by e.g., impurity contents, heat treatment, microstructure, testing temperature, and loading rate. It is important to note, that special rules exist for the experimental determination of K_{Ic} [52] and that it cannot be estimated from, e.g., tensile tests.

Under mixed-mode conditions, the energy release rate G characterizes the amplitude of the applied load, but does not differentiate the modes of fracture:

$$G = \frac{1}{E^*}\left(K_I^2 + K_{II}^2 + K_{III}^2\right) \tag{2.8}$$

An energy criterion for crack propagation under mixed-mode conditions can be obtained when this equation is set equal to Eq. (2.3). It is based on the postulate that all elastically stored energy can be used for the creation of new surfaces. The validity of this G-criterion is questionable since it would still be reached for vanishing mode I loading when the mode II and III components are high enough [56]. Without a mode I component, however, no free surface can be created. It might therefore be appropriate to use the so-called K_I-criterion (K_I=K_G) even in case of mixed-mode loading [57]. This criterion states that a certain degree of tensile loading is required to separate the crack faces and to prevent crack closure [56]. Both criteria are schematically visualized for mixed mode I/II loading in Fig. 2.2d.

Dynamic effects during fracture

Until now, the theory of fracture was presented for quasi-static, i.e., time-independent loading. Under dynamic, i.e., time-dependent, conditions both the dynamic stress intensity factor and the crack tip stress field generally depend on loading rate, crack speed, and temperature. This becomes important if, for instance, the loads are not homogeneously distributed over the configuration, but are suddenly applied to the crack faces. Such a situation, in which the stress intensity factor at the crack tip exceeds the quasi-static value by far, is called dynamic overshoot [41].

For time-dependent fracture testing, the quasi-static fracture criterion is replaced by its dynamic equivalents [41, 54]:

- **Crack initiation toughness:** onset of crack growth; depends on temperature and loading rate
- **Crack growth toughness:** characterizes necessary conditions to ensure energy rate balance during crack growth; depends on loading rate, time, and crack position; increases with crack speed
- **Crack arrest toughness:** the smallest value of the dynamic stress intensity factor for which a growing crack cannot be maintained

An interesting consequence of the difference between crack initiation and crack growth toughness is that the crack will generally jump to a large finite speed immediately upon initiation [54]. Nevertheless, crack propagation at arbitrarily low crack speeds is experimentally possible when loading conditions and setup are very carefully controlled [58]. The

crack arrest criterion is necessary since the crack speed is very sensitive to small changes in the stress intensity factor for very low crack speeds. Under such conditions, the dynamic crack growth criterion is unable to treat crack arrest in a reliable manner [54]. The three different fracture criteria under dynamic conditions are schematically displayed as function of the crack velocity in Fig. 2.2e.

Many dynamic effects are closely linked to the velocities of elastic waves that travel in the material's bulk and at its surface. In the context of fracture simulations, these waves are particularly important when an elastic wave is emitted from the crack tip due to bond breaking. The wave will travel away from the crack tip and reach the boundary after a certain time period t_b. At the boundary, it will be reflected and propagate back to the crack tip. As a result, events at the crack tip, which occur after the wave has returned to it, are influenced by the (artificial) boundary conditions. For this reason, the critical assessment of the results requires the knowledge of the relevant wave speeds. The longitudinal and transversal (bulk) wave speeds, c_l and c_t, as well as the Rayleigh (surface) wave speed, c_R, are approximated for an isotropic linear-elastic material, as follows [41, 54]:

$$c_\mathrm{l} = \sqrt{\frac{E(1-\nu)}{\rho(1+\nu)(1-2\nu)}} \tag{2.9}$$

$$c_\mathrm{t} = \sqrt{\frac{\mu}{\rho}} \tag{2.10}$$

$$c_\mathrm{R} = c_\mathrm{t}\frac{0.862+1.14\nu}{1+\nu} \tag{2.11}$$

with $\mu = E/\left[2(1+\nu)\right]$, E, and ν being the shear modulus, Young's modulus, and Poisson's ratio of the material.

For the above described emission of an elastic wave from a brittle breaking bond, the time period $2t_\mathrm{b}$, in which the simulation results are not influenced by the boundary conditions is estimated as:

$$2t_\mathrm{b} = \frac{2\Delta L}{c_\mathrm{l}} \tag{2.12}$$

where ΔL is the minimum distance from the crack tip to any (non-periodic) boundary. For W, the longitudinal wave speed c_l is approximately 5.3 km/s. For Fe, c_l lies in the range of 4.2 km/s (in $\langle 0\,0\,1\rangle$ direction) and 6.2 km/s (in $\langle 1\,1\,1\rangle$ direction).

Dislocation emission from crack tips

In many metallic materials, the stress concentration at the crack tip is reliefed by crack tip plasticity, i.e., the nucleation and motion of dislocations [10]. The region around the crack tip, where the stresses are high enough to initiate plasticity, is called plastic zone. Its radius is commonly estimated as [32]:

$$r_\mathrm{p} = \frac{1}{\pi}\left(\frac{K_\mathrm{I}}{\sigma_\mathrm{y}}\right), \tag{2.13}$$

where σ_y is the yield strength. If crack tip plasticity occurs prior to brittle fracture, it progressively blunts the crack tip thereby reducing the driving force for cleavage [10]. Such cases represent a clear breakdown of the linear-elastic behavior originally assumed by Griffith [9] and the measured fracture toughness K_{Ic} of the material can exceed his prediction K_G by orders of magnitude.

The competition between ideally brittle fracture and crack tip plasticity was analyzed by Rice and Thomson [15]. They classified materials as either intrinsically brittle or ductile by comparing the critical condition for homogeneous dislocation emission to the Griffith criterion, see Eq. (2.3). According to their framework, this competition is entirely determined by the parameters b (Burgers vector length), γ (surface energy), and μ (shear modulus). Their criterion for an intrinsically brittle material was approximated as $\mu b/\gamma > 7.5 \ldots 10$.

The original Rice-Thomson criterion was refined by Rice [16] who used the Peierls-Nabarro approach [59, 60] to model the emitted dislocation. According to this framework, dislocation emission takes place when $G_e < G_G$ with G_G being defined in Eq. (2.3) and G_e being the critical energy release rate for dislocation emission [16]:

$$G_e = 8\frac{1+(1-\nu)\tan^2\varphi}{(1+\cos\theta)\sin^2\theta}\gamma_{usf}\,, \tag{2.14}$$

where ν denotes the Poisson ratio and γ_{usf} the unstable stacking fault energy [61], θ is defined in Fig. 2.1a, and φ is the angle between the Burgers vector of the emitted dislocation and the normal direction to the crack front in the slip plane. An overview of possible slip systems for selected crack systems in bcc metals is given in Table A.1 in the appendix.

The fracture behavior in a given orientation is then determined by the lower of the two critical stress intensity factors for brittle fracture, K_G in Eq. (2.7), and for dislocation emission [15]:

$$K_e = \sqrt{G_e E^*}. \tag{2.15}$$

Three-dimensional aspects and crack front curvature

The crack front z has been reduced to a point in a two-dimensional (2D) space thus far. This might be sufficient to describe fracture and fatigue on the macroscale where the crack front can often be approximated by a quasi-2D infinitely long and straight line. Nevertheless, such simplified 2D or quasi-2D views of fracture neglect fundamental mechanisms in brittle fracture and crack tip plasticity. Fig. 2.3 shows examples, where such effects along the crack front are of crucial importance for the details of the fracture process. In fact, brittle fracture on the original crack plane often proceeds via (thermally-activated) kink formation and propagation [58, 62] or micro-faceting [14, 29]. In addition, out-of-plane deflection of the crack onto an inclined crack plane, so-called crack kinking [28, 63], and the crack growth on oblique crack planes leading to e.g. ridges [28, 64] is possible under fully 3D conditions. It is important to note, that crack kinking is possible even under (quasi-)2D conditions, even though a propagation process by e.g. kink pairs, see Fig. 2.3d, would be suppressed in this case. Fig. 2.3g-j show possible variants of crack tip plasticity

under 3D conditions in comparison to the 2D scenario assumed in the previous paragraph, see subfigure f. Such essentially 3D processes include the dislocation emission by prior loop formation on an inclined [65] or oblique slip plane [66], e.g., by out-of-plane steps (jogs) [67], as well as the local reorientation and curvature of the crack front at an obstacle [68, 69].

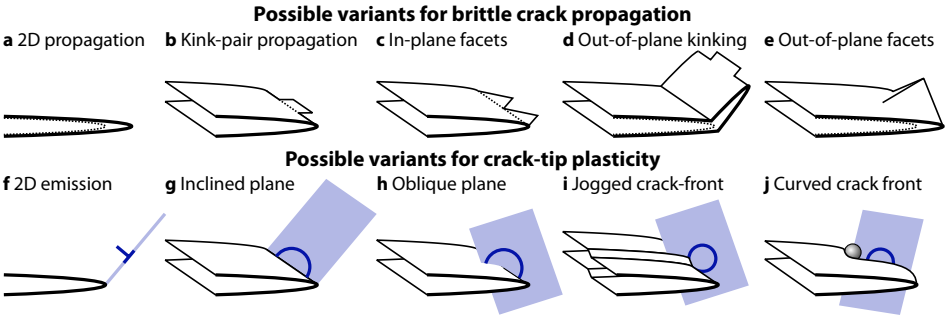

Figure 2.3: Schematic variants of fracture behavior in metals. **a,f**: basic processes of brittle fracture and crack tip plasticity under (quasi-)2D conditions; **b-e**: possibilities of brittle crack propagation under fully 3D conditions; note that brittle out-of-plane kinking on an inclined plane (**d**) is also possible under 2D conditions if the crack front does not propagate by the kink-pair mechanism (**b**); **g-j**: possibilities of dislocation emission from a crack tip under fully 3D conditions.

The influence of crack front curvature is classically studied in fracture mechanics using the penny-shaped crack geometry, where a circular crack is embedded in an infinitely large body. Sack extended Griffith's criterion for brittle fracture to this scenario and determined the dimensionless geometry factor in Eq. (2.6) to be $Y = 2/\sqrt{\pi}$ [70]. Sneddon [38] found that the stress components of penny-shaped cracks differ from those of straight central cracks by the same factor and that crack front curvature leads to the evolution of a hoop stress σ_ψ, which has the linear-elastic isotropic form [38]:

$$\sigma_\psi(r,\theta) \quad = \quad 2\nu\sqrt{\frac{GE^*}{2\pi r}}\cos\left(\frac{\theta}{2}\right), \tag{2.16}$$

where ψ is the angular component of the cylindrical coordinate system with longitudinal axis perpendicular to the crack plane and origin at the center of the crack, see Fig. 2.1b for the coordinate system. Similar to the other normal stress components, this circumferential stress, for which no 2D analog exists, exhibits a singularity at the crack tip. Isotropic linear-elastic solutions were also determined for penny-shaped cracks on an interface [71] and even for interacting penny-shaped cracks [72].

In the context of crack-obstacle interactions, Lange [73] introduced the concept of the 'crack line tension' T_{crack} in analogy to the line tension that describes the energy of a dislocation line per unit length [48, 74]. According to this concept, the fracture energy of an

ideally brittle material ($G_G = 2\gamma$) with average particle spacing d would be:

$$\Gamma = 2\left(\gamma + \frac{T_{\text{crack}}}{d}\right). \tag{2.17}$$

This means that the fracture energy should increase as the distance between the obstacles decreases. Although the analogy is not perfect, it enabled the pinning effect by particles to be visualized [75]. Later, Evans [76] showed that the crack line tension is not a constant value, but strongly depends on the obstacle type.

In the 1980s, much effort [77–81] was put in the determination of first-order elastic solutions for the acting stress intensity factors and energy release rates $G(z)$ of slightly perturbed, wavy crack fronts z. Gao and Rice [80] showed for acting shear loads that $G(z)$ is incompatible with a spring-like model with the 'crack line tension' effect. Their analysis, although it is qualitatively correct in predicting the proper effect of curvature on the crack extension direction, fails quantitatively [80].

Since the first fundamental analyses of 3D problems in fracture mechanics, substantial progress has been made in the treatment of complex 3D crack geometries using continuum-scale numerical methods, such as the finite-element (FE) or the boundary element method (BEM), see Ref. [82] for a brief overview. With the widespread FE method, for instance, the decreased compliance of specimens for fracture tests [83], the effect of material anisotropy on the the mode I [84] and mixed-mode stress intensity factors [85], even for non-planar fracture surfaces [86], were calculated for curved crack fronts. To allow for a higher variability of the crack paths, mesh-free methods, such as extended finite element (FE) method (X-FEM) [87], the element-free Galerkin (EFG) method [82], and the FE method with enriched elements [88] were developed. These techniques were successfully applied to dynamic crack propagation [82], fatigue crack growth [89], and crack healing at elevated temperatures [90] under 3D conditions.

The underlying material models and fracture criteria usually assume homogeneous microstructures and direction-independent fracture behavior. Contrary to this assumption, many crystalline materials show a direction-dependent fracture toughness [28, 91], even for purely brittle fracture [14, 92], and in case of grain boundary fracture [93, 94]. Furthermore, the orientation of slip systems with respect to the crack front is one of the determining factors whether an existing crack will blunt or propagate by brittle cleavage as we have seen before [15, 16]. Here, atomic-scale simulations offer valuable information for the understanding of 3D aspects and the role of crack front curvature for the competition between brittle fracture and crack tip plasticity [95].

Effects of crystal structure on fracture

In the continuum treatment of fracture, surface energy and elastic constants are the main influences on the stability of the crack. For a sufficiently long, ideally brittle, and sharp crack, the configuration according to the Griffith criterion in Eq. (2.3) would be its only stable situation. An infinitesimal reduction or increase of the applied load would thus lead to crack closure or crack propagation, respectively. This view neglects the underlying

atomic nature of every crystalline material. At the atomic scale, the propagation of cleavage cracks is determined by the forces required to break the bonds directly at the crack tip. The breaking of discrete atomic bonds manifests itself in the so-called *lattice trapping effect* [11–13]: an atomically sharp crack tip remains stable at its position until a load K^+ larger than K_G is reached. This load is called the upper trapping limit. Similarly, a lower trapping limit $K^- < K_G$ exist, at which the crack closes [96]. The lattice trapping range is defined as

$$\Delta K = K^+/K^- - 1. \tag{2.18}$$

The effect of lattice trapping on the increase of surface energy by an advancing crack is schematically shown in Fig. 2.2f.

Important implications of lattice trapping even for macroscopically propagating cracks were, for example, the preference of $\{1\,0\,0\}$ cleavage over cleavage on the $\{1\,1\,0\}$ planes in W [14, 56], direction dependence of the preferred propagation direction within the same cleavage plane [97], and direction-dependent crack propagation speeds in Si [64].

2.1.2 Fracture experiments in bcc metals

The bcc transition metals tungsten (W), iron (Fe), molybdenum (Mo), vanadium (V), niobium (Nb), chromium (Cr), and tantalum (Ta), have closely related mechanical properties [98]. Their fracture behavior is characterized by a pronounced transition from brittle glass-like cleavage fracture at low temperatures and high strain rates to ductile response at high temperatures and moderate loading rates [27]. Such a brittle-ductile transition (BDT) was experimentally observed for single crystals (SX) and polycrystals (PX) of all these materials, except for Ta [98]. Fig. 2.4a gives an overview of the BDT for various bcc metals. The characteristic temperature, at which the fracture behavior changes from brittle to ductile, is called BDT temperature T_{BDT}. The value of the T_{BDT} generally depends on a multitude of parameters, such as the loading rate [99], grain diamater [100], grain boundary character distribution [101], dislocation density [102], material composition [103–105], structural ordering [106] as well as content of hydrogen [107–109] and other impurity elements [110]. The BDT temperatures for single- and poly-crystalline technically pure bcc metals are presented in Table 2.1. The table also lists the preferred cleavage planes in the various bcc metals, which are presented in Fig. 2.4b. Here and in the following, crystallographic crack systems are written in the (crack plane)[crack front] notation, i.e., as $(\ldots)[\ldots]$ or more general as as $\{\ldots\}\langle\ldots\rangle$ representing the whole family of crack systems.

The wish to understand and to predict the brittle-ductile transition has led to much research in this field and yielded the development of phenomenological equations [117] as well as mechanism-based models [111, 118, 119]. It is now understood that dislocation nucleation limits the ductility at low temperatures while the BDT itself becomes a thermally-activated process at high temperatures and is controlled by dislocation mobility [27].

The following literature survey is focused on the details on fracture experiments in single crystals of W and Fe as two representatives for semi-brittle bcc metals. Both metals are comparably well-studied in both experiments and atomistic simulations. Likewise, due to their well-defined crystallography, experimental results for single crystals can be compared

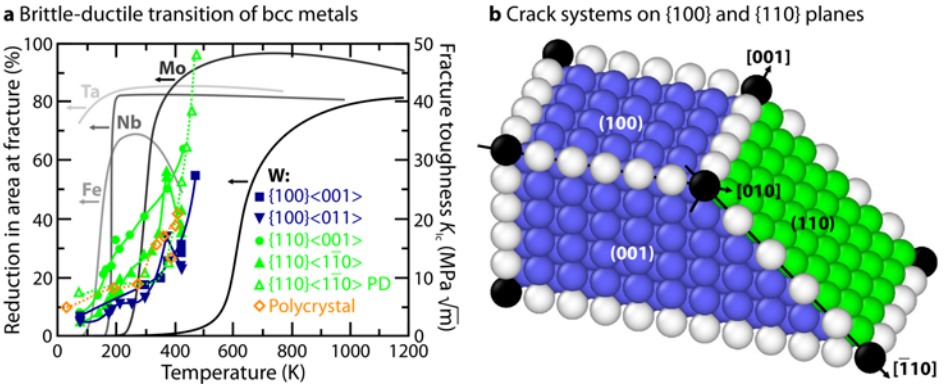

Figure 2.4: Brittle-ductile transitions and typical crack systems of bcc metals. **a**: reduction in area at fracture (left axis) for the bcc metals Ta, Fe, Nb, Mo, and W [110]; fracture toughness (right axis) for W single crystals (PD: pre-deformed) [27] and polycrystals [111]; **b**: {100} and {110} crack planes with indicated $\langle 0\,0\,1\rangle$ and $\langle 1\bar{1}\,0\rangle$ crack front directions.

Table 2.1: Summary of BDT temperatures and preferred cleavage planes of bcc metals. The grain diameters of the polycrystals were 40 μm on average; the preferred cleavage planes are displayed in Fig. 2.4b.

Material	T_{BDT} of single crystals (K)	T_{BDT} of polycrystals (K)	Cleavage plane(s)
W	370[a]–470[b] [27]	413 [98]	{100}, {110} [112]
Mo	230[c] [113, 114]	228 [100]	{100}, {110} [112]
V	164[d] [115]	203 [110]	{100} [10]
Nb	—	77 [98]	{110} [108]
Fe	130[b,e]–154[b,f] [111]	73 [116]	{100} [112]

[a] (100)[011] orientation
[b] (100)[001] orientation
[c] {100} plane
[d] $\dot{\varepsilon} = 4.1\times10^{-4}$ s^{-1}
[e] $\dot{\varepsilon} = 4.46\times10^{-5}$ s^{-1}
[f] $\dot{\varepsilon} = 4.46\times10^{-3}$ s^{-1}

to the outcome atomistic simulations [14]. Although this thesis is mainly focused on Fe, I will start with W, which has been more widely studied because high-purity single crystals can be easier produced. Parts of the following overview were taken from Refs. [120, 121] and have been published in Refs. [94, 122].

Tungsten (W)

Studies on the deformation behavior of W single crystals at temperatures ranging from 20 to 465 K showed that W is not inherently brittle [123–125]. Wolff [123] observed that deformation twins accompanied brittle fracture on $\{1\,0\,0\}$ planes or even at the twin interfaces. Beardmore and Hull [124] showed that the yield strength increased with decreasing temperature and from $\langle 1\,0\,0\rangle$- over $\langle 1\,1\,1\rangle$- to $\langle 1\,1\,0\rangle$-oriented tensile axes. Without exception,

fracture surfaces of broken specimens exhibited $\{1\,0\,0\}$ cleavage facets. In addition to slip markings on the $\{1\,1\,0\}$ and $\{1\,1\,2\}$ planes at high deformations, Argon and Maloof [125] found indication for $\{1\,1\,2\}$ slip on planes that had not the highest Schmid factor. In agreement with Wolff [123], they observed that interactions of non-parallel deformation twins could promote crack nucleation.

Fracture experiments with single crystals revealed that the $\{1\,0\,0\}$ and $\{1\,1\,0\}$ planes are the primary and secondary cleavage planes, respectively [126–130]. Hull and co-workers [126] performed fracture experiments showing that the $\{1\,0\,0\}$ fracture energy increased with increasing temperature. Cordwell and Hull [127–129] studied specimens oriented for fracture on $\{1\,0\,0\}$ and $\{1\,1\,0\}$ planes and estimated the surface energy of $\{1\,1\,0\}$ planes to be lower than that of $\{1\,0\,0\}$ planes [128]. This finding indicated that relative values of surface energy do not alone dictate the preferred cleavage plane of a single crystal, as it is predicted by the Griffith theory. Additionally, Liu and Bilello [130] found that the fracture toughness of $\{1\,0\,0\}$ planes was lower for $\langle 0\,1\,1\rangle$-oriented crack fronts as compared to crack fronts along $\langle 0\,0\,1\rangle$ directions.

The perhaps most systematic experimental study of fracture in W single crystals was carried out by Riedle [14, 63] using four-point bending tests at temperatures between 77 K and 293 K. He determined the fracture toughness in several crack systems on $\{1\,0\,0\}$, $\{1\,1\,0\}$, $\{1\,1\,1\}$ and $\{1\,1\,2\}$ planes. In agreement with the findings of Liu and Bilello [130], K_{Ic} was lower for $\langle 0\,1\,1\rangle$ crack front directions than for $\langle 0\,0\,1\rangle$ directions for both $\{1\,0\,0\}$ and $\{1\,1\,0\}$ planes. On $\{1\,1\,1\}$ and $\{1\,1\,2\}$ planes, the fracture behavior was found to be brittle with fracture surfaces containing both the primary $\{1\,0\,0\}$ and the secondary $\{1\,1\,0\}$ cleavage planes. Riedle's results are shown in Table 2.2 for the experimentally observed cleavage planes, i.e., the $\{1\,0\,0\}$ and $\{1\,1\,0\}$ planes. It can be clearly seen that the crack front direction has a larger influence on K_{Ic} than the crack plane. Based on atomistic simulations by Kohlhoff *et al.* [29], the preference for $\{1\,0\,0\}$ cleavage planes was explained with the possibility of an arbitrarily oriented crack front to split into facets along the $\langle 0\,1\,1\rangle$ and $\langle 0\,\bar{1}\,1\rangle$ directions. On $\{1\,1\,0\}$ planes, on the contrary, such a faceting is not possible as these planes only contain *one* easy $\langle 1\,\bar{1}\,0\rangle$ crack front direction.

Fe and Fe-Si alloys

In the literature, several studies can be found on the deformation behavior of Fe single crystals [131–137]. Instead of high-purity Fe, single crystals with small Si contents up to 3 wt.% were often used since their experimental handling is more practicable [138–144]. Similar to W, it turned out that Fe(-Si) single crystals were not intrinsically brittle and that the yield strength increased with decreasing temperature [131, 137, 139, 142]. The formation of twins was identified as important deformation mechanism, especially at low temperature [132, 134, 135, 138, 139]. Moreover, twinning accompanied brittle fracture [134, 135] or even promoted crack nucleation [138]. Conventional slip was mostly confined to $\{1\,1\,0\}$ planes and was only occasionally found to happen on planes with maximum resolved shear stresses, e.g. $\{1\,1\,2\}$ planes [139, 144]. In the rare cases when the specimens fractured in a brittle manner, cleavage facets were found exclusively on $\{1\,0\,0\}$ planes [133, 141].

Table 2.2: Summary of fracture experiments on W and Fe single crystals at $T = 77$ K. The fracture toughness K_{Ic} of W and Fe was determined using four-point bending experiments [14, 63] and wedge tests [28], respectively.

Crack system		W single crystals (Ref. [14, 63])		Fe single crystals (Ref. [28])	
Plane	**Front**	**Behavior**	**K_{Ic} (MPa$\sqrt{m}$)**	**Behavior**	**K_{Ic} (MPa$\sqrt{m}$)**
{100}	<001>	brittle	3.4±0.6	brittle	8.8±0.4
{100}	<011>	brittle	2.4±0.4	brittle	8.4±0.3
{110}	<001>	brittle	3.8±0.4	kinked onto {100} planes	17.3±0.5
{110}	$<1\bar{1}0>$	brittle	2.8±0.2	kinked onto {100} planes	16.5±0.6

As for the deformation behavior of Fe single crystals, experimental studies on the fracture behavior of pure Fe are relatively scarce [28, 111, 145, 146] and more work exists on Fe-Si alloys [140, 143, 147–150]. Most of these publications identified the $\{1\,0\,0\}$ planes as preferred cleavage planes [28, 140, 147, 148, 150] and the $\langle 0\,1\,1\rangle$ directions as easy propagation directions [28, 148]. In fact, cleavage on $\{1\,1\,0\}$ planes was never observed. Instead, cracks on $\{1\,1\,0\}$ planes were found to initiate dislocation emission [28, 143, 150]. In these cases, the identified slip planes were either of $\{1\,1\,0\}$- or $\{1\,1\,2\}$-type [28, 147, 150].

Ohr *et al.* [145, 146] studied the emission of dislocations from a crack tip via in-situ TEM fracture experiments. Emitted dislocations immediately slipped away from the crack tip and came to rest in a plastic zone of approximately 10 μm size thereby leaving behind a dislocation-free zone, as observed earlier by Kobayashi and Ohr [151]. Tanaka *et al.* [111] investigated the $\{1\,0\,0\}\langle 0\,0\,1\rangle$ crack system by four-point bending experiments at temperatures between 77 and 180 K. The tendency for brittle fracture increased with decreasing temperature and increasing strain rate. The same rate dependency was earlier reported by Landa *et al.* [149] and Spielmannová *et al.* [150].

In a systematic experimental study similar to the work by Riedle [63], Hribernik [28] investigated the fracture toughness on $\{1\,0\,0\}$ and $\{1\,1\,0\}$ planes using the wedge test method. The results of his work are summarized in Table 2.2. Contrary to the data for W, but in agreement with other results for Fe [150], the fracture toughness K_{Ic} was about twice as high for $\{1\,1\,0\}$ planes as for $\{1\,0\,0\}$ planes. The influence of the crack front direction, on the other hand, was within the limits of the experimental error. Cleavage never occurred on $\{1\,1\,0\}$ planes. Instead, cracks inserted on $\{1\,1\,0\}$ planes kinked onto $\{1\,0\,0\}$ planes. In these situations, extensive dislocation activity on $\{1\,1\,0\}$ and $\{1\,1\,2\}$ planes was additionally observed.

In summary, both materials exhibit a pronounced dependence of deformation and fracture behavior on temperature and loading rate. They share this transition from low toughness and brittle behavior at low temperature to high toughness and ductile response at higher temperature with many other technologically important materials, such as the other bcc transition metals and silicon [27, 98, 116, 152, 153]. The BDT is caused by the competition between bond-breaking processes and dislocation nucleation at the crack tip in the

low temperature regime and the thermally activated motion of dislocations at higher temperatures [27]. This view was, however, developed for high-purity single crystals and does not yet allow a predictive microstructure-sensitive modeling of the BDT for polycrstals, which would include effects arising from e.g. GBs, alloying elements, and pre-deformation (pre-existing dislocations). Furthermore, cracks in real microstructures are not perfect, i.e., they contain defects (ledges, kinks, jogs), might be blunted, or exhibit local curvature. How these atomic-scale imperfections influence the competition between bond breaking and crack tip plasticity in the low temperature regime of semi-brittle metals is mainly not addressed in the literature. In this context, atomistic simulations have already considerably improved our understanding of fracture [27, 64, 97, 154–156] and are therefore ideally suited to tackle the aforementioned problems.

2.1.3 Atomistic simulations of fracture

Atomistic simulations are an ideal tool to provide valuable insights into the details of crack-tip processes and thereby improve our understanding of fracture, see the recent review in Ref. [95]. Since the first reported atomic-scale study on crack propagation in 1970 [157], atomistic methods uncovered the fundamental importance of crystal orientation [97, 157], lattice trapping [11–13], material anisotropy [29], and twin or dislocation emission from the crack tip [158]. Cleri *et al.* [159] showed, for instance, the influence of emitted dislocations on the reduction in average tensile crack tip stresses, the so-called *crack-tip shielding*. Buehler and Gao [160] demonstrated that strongly nonlinear, hyperelastic, behavior of the interatomic forces at the crack tip plays an important role for the dynamic instability of fast moving cracks leading to macroscopic roughening of the fracture surface. Similarly, Gumbsch [161, 162] attributed the limitation of crack speeds in Si to about 40 % of the Rayleigh wave speed, cf. Eq. (2.11), to nonlinear effects.

Whereas early atomistic studies were mostly limited to 2D or quasi-2D simulations, the computational power of today's high performance computing clusters allows the investigation of inherent 3D problems. A prominent example for such a 3D process is the crack propagation by the formation and motion of kinks at the crack front [58, 65] and the emission of dislocation half loops on inclined [62, 66] or oblique glide planes [66], see Fig. 2.3b,g, and h for schematic illustrations of these processes. Refs. [58, 62, 65] showed that these kink processes reduce the necessary energy barriers for both brittle propagation and crack tip plasticity as compared to the alternative 2D processes shown in Fig. 2.3a and f. Gordon *et al.* [67] studied the influence of jogs, cf. Fig. 2.3i, and substitutional solute atoms at the crack tip on the energy barriers for dislocation emission. They found that the necessary energy barrier for emission is reduced as compared to the perfect crack front and depends on the heterogeneity density and the activation volume at a given stress intensity factor. Thaulow *et al.* [163] reported on the nucleation of dislocation loops in Si, which were linked to geometrical ledges at the crack tip triggering slip on $\{111\}$ planes. Recently, Ersland *et al.* [164] observed that penny-shaped cracks, i.e., an extreme scenario of a multitude of kinks along a crack front, show a generally more ductile response than quasi-2D infinitely long, straight crack fronts. This tendency was explained with the 'self organiza-

tion' of the crack front by limited bond breaking processes in such a way that certain slip planes become favorably oriented with respect to the local crack front segment.

Besides the investigation of 3D aspects reviewed so far, crack propagation in complex microstructures [165–168] or under complex loading conditions [169, 170] are another important development trend in modern atomistic simulations of fracture. The results of such studies are, however, less fundamental. In nanocrystalline structures, the chosen crack paths strongly depend on, for instance, the precise initial position of the crack and the GB (character) distribution; similarly, plastic responses are highly suppressed by the frequently employed quasi-2D setups. In this context, meso-scale models are clearly more capable to capture the complexity of metallic microstructures, see section 2.4. Such models will benefit from atomic-scale simulations that investigate the properties of individual interfaces in bicrystal setups [171], which can then be extrapolated to larger scales.

Under *cyclic* loading conditions, on the other hand, dynamic effects can not be excluded *per se*; furthermore, what limits the fatigue life of materials is frequently the time spent to *initiate* cracks rather than to *propagate* them [8, 172]. A strong focus on how cracks nucleate in metallic materials [173] would therefore be a promising route to tackle the fatigue problem. Particularly in the context of freshly nucleated (fatigue) cracks, which are still very small in size, curvature effects will inevitably play an important role [95].

After this brief overview of the state-of-the-art in atomistic fracture simulations, I focus on studies of bcc metals with emphasis on W and Fe as the two selected bcc representatives. Thereafter, I summarize important influencing variables for atomistic simulations (of fracture).

Fracture in body-centered cubic (bcc) metals

The vast majority of atomic-scale studies on crack propagation in bcc single crystals is focused on Fe [30, 122, 154, 164, 174–201], which was also the first bcc metal studied by means of atomistic simulations [157]. Whereas the fracture behavior of W is also comparably well studied [14, 29, 56, 202], only few reports can be found on Mo [167, 203], V [204], Nb, or Ta [205, 206]. Most of these studies focus, however, on fracture-*related* topics, e.g., void growth in nanocrystals [167, 203, 205, 207]. Publications on fracture in single crystals of these materials are even more scarce [204, 206]. The comparably high interest in the atomic-scale details of fracture in Fe is most likely due to its industrial importance as the base element of steels.

In the following, I focus on the reported work on Fe and W; for pure single crystals, the zero- or low-temperature fracture behavior should be material specific only to a limited extend. Instead, most observations can be attributed to fundamental fracture mechanical concepts or atomic-scale aspects, such as crystal structure, dynamic effects, or loading conditions. Most of the results presented in the following paragraphs should therefore be transferable to the other bcc metals. Parts of this literature review were taken from Ref. [120] and have been published in Refs. [122, 201].

Under quasi-static loading conditions, both Fe and W prefer to extend by cleavage on both $\{1\,0\,0\}$ and $\{1\,1\,0\}$ planes [29, 30, 56, 122, 198]. Cracks in the $\{1\,0\,0\}\langle 0\,0\,1\rangle$ crack system often kinked onto $\{1\,1\,0\}$ planes under these conditions [29, 122, 198]. In some cases, dislocation emission was observed from crack tips in the $\{1\,1\,0\}\langle 1\bar{1}\,0\rangle$ system instead of brittle fracture [30, 122, 181, 198, 199]. In addition to dislocations on $\{1\,1\,0\}$ planes, both $a_0/2\langle 1\,1\,1\rangle\{1\,1\,2\}$ dislocations [30, 122, 181, 194, 199] and $\{1\,1\,2\}$ deformation twins were emitted [30, 122, 164, 178, 182, 186, 188, 189, 191, 193, 195, 199]. Twin formation occurred favorably under dynamic conditions at cracks on both $\{1\,0\,0\}$ and $\{1\,1\,0\}$ planes [164, 178, 182, 186, 188, 189, 191, 193, 195, 199]. Under quasi-static conditions, in contrast, twins were only observed at $\{1\,1\,1\}$ crack tips [30, 122]. An additional prominent feature of fracture simulations under dynamic loading were structural or phase transformations directly at the crack tip [164, 182, 187, 190, 191, 194, 196–199, 208].

In the few studies where different crack systems were compared [29, 30, 122], cleavage on $\{1\,0\,0\}$ and $\{1\,1\,0\}$ crack planes proceeded easier for crack fronts oriented along $\langle 1\bar{1}\,0\rangle$ directions than for $\langle 1\,0\,0\rangle$ crack fronts. This prevalence was attributed to the higher lattice trapping effect [11–13, 96, 209] at $\langle 1\,0\,0\rangle$-oriented fronts, which leads to an increased stability of the crack [14, 29, 56].

As mentioned in section 2.1.1, the influence of crack front curvature on the competition between brittle fracture and crack-tip plasticity is insufficiently understood thus far. Atomic-scale simulations of cracks with curved crack fronts under fully 3D conditions were only recently reported by Ersland *et al.* [164]. They investigated the fracture behavior of penny-shaped cracks on $\{1\,0\,0\}$, $\{1\,1\,0\}$, and $\{1\,1\,1\}$ planes in Fe and found that these cracks were generally more prone to develop extensive crack tip plasticity than quasi-2D central cracks. All penny-shaped cracks showed extensive crack tip plasticity and only very limited bond breaking. Infinitely long, straight cracks in quasi-2D setups, on the other hand, showed the formation of deformation twins and dislocations only at $\langle 1\,1\,0\rangle$ and $\langle 1\,1\,2\rangle$ crack fronts whereas cracks with $\langle 0\,0\,1\rangle$ crack fronts propagated by cleavage. These observations agree well with other simulations on Fe using quasi-2D setups, see e.g. Refs. [181, 187, 195] for $\langle 1\,1\,0\rangle$ and $\langle 1\,1\,2\rangle$ crack fronts and Refs. [29, 30, 122, 192] for $\langle 0\,0\,1\rangle$ crack fronts. The authors attributed the inhibition of unstable cleavage fracture in case of penny-shaped cracks to limited local crack propagation which changes the circular crack shape in such a way that slip systems become more easily activated [164]. Characteristic features of the interactions between the nucleated defects, i.e., dislocations and twins, and the curved crack front were, however, not yet described and analyzed in detail [201].

Influencing variables in atomistic simulations (of fracture)

Despite their unquestionable importance for the uncovering of hitherto unknown mechanisms of materials behavior, atomistic simulations are limited in size and time scale and their results depend on a number of influencing variables. A comprehensive and systematic variation of these influencing factors is currently lacking in the literature and will be presented in section 4.2 of this thesis. This will finally allow us to give a number of recommendations how to best simulate fracture by means of atomistic simulations, see section 7.6.

Atomic interactions. The first and perhaps most critical influencing variable for atomistic simulations is how and to which level of detail the interactions between atoms are described. Unfortunately, the most accurate description of interatomic forces using density functional theory (DFT) calculations is limited to very small system sizes of up to 1,000 atoms [210]. With less accurate and therefore less costly potentials, such as bond order potentials (BOP) [211], the modified embedded atom method (MEAM) [212], or angular-dependent potentials (ADP) [213], the maximum practical system sizes lies in the range between 10 thousand and 10 million atoms [210]. For fully 3D simulations of crack-microstructure interactions, the numbers of atoms, however, easily reach 25 million and above [155, 214, 215]. For this reason, most studies of fracture still use potentials following the embedded atom method (EAM) scheme [216]. Modern EAM potentials for Fe reproduce numerous important defect properties, e.g., the correct symmetry of screw dislocation cores [217, 218] the energies of point defects [219], or the contribution of magnetism [220, 221]. They were, however, not developed for the study of fracture. It is therefore unclear, how reliable the different EAM potentials are in terms of their fracture properties. For cracks on the experimentally observed preferred $\{1\,0\,0\}$ cleavage planes in Fe [28, 133, 138, 139, 222], some simulations predict kinking onto $\{1\,1\,0\}$ planes, see e.g., Ref. [29]. Similar confusion exists for cracks in the $\{1\,1\,0\}\langle 1\bar{1}\,0\rangle$ system, for which some potentials predict brittle fracture and some dislocation emission even in the same simulation setup, see e.g. Ref. [30]. Furthermore, several studies report on structural transformations at the crack tip, e.g. in Refs. [164, 182, 187, 190, 194, 197–199]. However, these studies did not analyze the structural transformations in detail or compare between different potentials to elucidate the role of the interatomic potential on the structure at the crack tip [122].

In most presented publications, only one interatomic potential and only a limited number of crack systems were tested. The work by Gordon *et al.* [30] displays the only exception as it compares four different potentials [223–226] in five different crack systems. They, however, did not compare to experimental data [28] and it is therefore unclear, which EAM potential is best adapted for modeling the fracture behavior of Fe. Furthermore, a number of new EAM potentials has been developed since then [217–219, 221, 227] and an update of the work by Gordon *et al.* is currently lacking.

Loading rate and method. The restriction to very small lengths and very short time scales available for atomistic simulations is an additional general limitation of this simulation method with particular importance for comparability with experiments. Whereas experimental strain rates $\dot{\varepsilon}$ mostly vary between 10^{-5} to 10^{-3} s^{-1}, see e.g. Ref. [111], the strain rates in atomistic simulations are typically in the order of 10^{6} to 10^{9} s^{-1}. With quasi-static loading with an effective strain rate of zero, however, it is not possible to simulate inherently time-dependent processes, such as crack propagation and crack-dislocation interactions. To determine the influence of different strain rates and the different loading procedures on the occurring crack-tip processes is therefore import for the reliability and comparability of the simulation results.

Setup geometry. With exception of Refs. [164, 193, 194, 200, 201], the presented studies used quasi-2D setups with periodic boundary conditions along the crack front thereby making it infinitely long and straight. Among them, the most common setups are:

- **Quasi-2D *K*-controlled setup.** A circular or quadratic simulation box, in which the crack tip is located at the center; the crack is loaded by quasi-static prescription of the atomic displacements according to the linear-elastic solution of the crack-tip deformation (K-)field, see e.g. Refs. [29, 30, 178, 180, 184, 187, 190, 191, 196, 198].
- **Quasi-2D edge crack setup.** A rectangular box containing an edge crack; in this setup, the box size is often larger in propagation direction than in crack plane normal direction; loads are applied uniformly on the box faces, see e.g. Refs. [156, 162].
- **Quasi-2D central (through thickness) crack setup.** Similar to the previous setup with the exception that both crack tips are located inside the simulation box, see e.g. Refs. [164, 181, 185, 186, 194, 197, 228].
- **3D edge crack setup.** The edge crack setup with a long crack front, see e.g. Refs. [67, 155, 163, 215, 229].

The choice of geometry and loading conditions can dramatically change the observed fracture behavior. Using the same EAM potential for Fe [226], the quasi-static K-controlled setup predict brittle advance of a crack in the $\{1\,1\,0\}\langle 1\,\bar{1}\,0\rangle$ system, e.g. in Ref. [30], whereas dynamic loading of the central crack in Ref. [164] leads to a ductile response. Obviously, the study of dislocation nucleation from crack tip defects like ledges [67, 163] requires to simulate sufficiently long crack fronts and is therefore not covered in quasi-2D setups with short box dimensions along the crack front. These examples highlight how important it is to understand the influences of the simulation details on the outcome of the simulation.

Crack-tip configuration. The atomic arrangement at the crack tip does mainly depend on the interatomic potential, but also on the way how the crack is created. In the vast majority of publications, atomically sharp cracks were inserted using one of the following methods: First, atoms on opposite sides of a given crack plane can be moved away from each other by using e.g. the theoretical crack tip displacement field [30, 191] or the mathematical equation for a semi-ellipse [155, 215]. Second, the atomic interactions of atoms on opposite crack faces can be disabled or 'screened', see e.g. Refs. [200, 230, 231]. The second method is, however, clearly nonphysical and will lead to an artificial atomic arrangement at the crack tip thereby inevitably influencing the crack tip stress distribution. To overcome this issue, cracks are sometimes created by removing one atomic half layer, which leads to the *blunting* of the crack tip, see e.g. Refs. [173, 215, 232]. This models the situation after virtual dislocation emission and has the practical side effect that it stabilizes the crack against closure. If and how, blunting influences the simulation results in comparison to atomically sharp crack tips was studied by Gumbsch [233], who determined the effects of various crack-tip blunting scenarios in fcc Ni. He demonstrated that blunting generally increases

the critical stress intensity factor and that certain combinations of blunting geometry and crystal orientation can even affect the fracture behavior. A comparison of atomically sharp and blunted cracks in bcc crystals for varying setup geometries and loading conditions is not yet reported in the literature.

Lateral strain. In the context of fracture mechanics, the lateral contraction or extension of the cracked body perpendicular to the applied (uni-axial) loads becomes particularly important. In presence of a crack, the stress distribution in the body strongly varies and the *locally* acting stresses cause *local* lateral stresses. Under plane strain conditions, these stresses cannot fully relax and therefore influence the stresses at the crack tip. Unfortunately, most studies do not report on whether and how they accounted for lateral strains. Despite this lack of information, we can think of the following different possibilities: (i) fixing the lateral box lengths, i.e., not taking lateral strains into account; an example for this can be found in e.g. Ref. [186]; (ii) adjusting the lateral box lengths to minimize the average stresses in the simulation box; (iii) adjusting the lateral box lengths according to the corresponding Poisson ratios. As a result of the scarce information situation on this topic in the literature, it is not clear how these different methods influence the qualitative and quantitative simulation results.

Boundary conditions. As with all simulations, the choice of boundary conditions is crucial. In a previous study [120], I have already compared four different combinations of boundary conditions in the outer layers parallel and perpendicular to the crack plane for the quasi-2D edge crack setup. In this setup, a mismatch occurs where the crack faces meet the boundaries if atoms are completely fixed in the boundary layers perpendicular to the crack plane. Apart from this option, the influence of boundary conditions was marginal as long as (i) atoms are fixed perpendicular to the crack plane in the boundaries parallel to it; and (ii) atoms are free to move parallel to the crack plane normal in the boundary layers perpendicular to the crack extension direction.

2.2 Grain boundaries

Density, distribution, character, and orientation of grain boundaries are known to determine important material properties, such as the yield strength [234], fracture toughness [235, 236] as well as creep [237] and fatigue properties [238]. A detailed introduction to GBs can be found in several textbooks [239–241] and basic reference works [242, 243]. The following theoretical concepts are therefore limited to aspects that are relevant for this thesis. Finally, the current state of atomistic simulations of GB fracture is reviewed. Parts of the following overview have been taken from Ref. [121] and have been published in Ref. [94].

A grain boundary is described by eight degrees of freedom (DOF). Five of them are *macroscopic*, the remaining three are *microscopic* [243]. Of the five macroscopic DOF, four define two directions (each two) and one defines an angle. The identity of these DOF depends on the scheme which is used to describe the GB geometry. The microscopic DOF

describe the relative translation of the two grains parallel and perpendicular to the GB plane. This is of particular importance for optimizing the GB structure [243] in order to find its lowest energy configuration.

The GB energy γ_{GB} is defined as the energy difference between a GB configuration and a perfect crystal per unit GB area. It is important to note that the GB energy does not correlate with phenomenological descriptions, such as misorientation angle and axis. Instead, it has a stronger dependence on the surface energies of the GB planes of the two connected grains [241].

Possible methods to optimize the GB structure include the simple minimization of interatomic forces [173], relative displacement of both grains [244–247], heating and quenching [156, 248, 249], and the removal of GB atoms with genetic algorithms, see e.g. Refs. [250, 251]. Here, optimizing means the generation of the GB structure that has the overall lowest GB energy. For a compendium of GB structures of several tilt grain boundaries in fcc and bcc metals, the reader is referred to the work by Vítek and co-workers [242, 244, 252–254].

The relationship between the interpenetrating lattices of the two adjacent grains is mathematically described within the coincidence site lattice (CSL) concept [243]. When a certain number of atoms coincides with lattice points of the other lattice, these coincidence points create the new CSL unit cell. The characteristic value of CSL GBs, Σ, is defined as the ratio between the CSL unit cell and the original unit cell [243]:

$$\Sigma = n^2 + m^2\left(u^2 + v^2 + w^2\right), \tag{2.19}$$

$$\tan \Psi/2 = \left(m/n\sqrt{u^2 + v^2 + w^2}\right), \text{ and} \tag{2.20}$$

$$\langle u\, v\, w\rangle = \frac{\underline{n}_1 \times \underline{n}_2}{\|\underline{n}_1\| \cdot \|\underline{n}_2\|}. \tag{2.21}$$

with n and m being integer numbers, $\langle u\, v\, w\rangle$ and Ψ the misorientation axis and angle, see Fig. 2.1c. The vectors $\underline{n}_1$ and $\underline{n}_2$ are the GB normal directions of the two crystals. The physical significance of CSL GBs is that their atomic arrangement along the GB plane is non-random, but periodic [243].

Whereas the CSL concept describes the misorientation of two grains mathematically, the structural unit model [255–257] is used to describe the relaxed atomic structure of a GB by the stacking of polyhedral units along the grain boundary. The most common structural units are tetrahedra, octahedra, trigonal, prisms and capped trigonal prisms. Extended research on this topic has been performed in fcc metals [242, 252–254, 258] and in the bcc lattice [244, 259, 260].

The characterization and description of GBs is a steady growing and evolving field, see the recent review by Mishin *et al.* [261] and the works by Wolf, Olmsted, and others [247, 262–267]. In what follows, the focus is, however, on the fracture properties of grain boundaries rather than details of characterization or structural and energetic predictability.

Grain boundary fracture

For a GB crack, i.e., a crack with crack plane equal to the GB plane, the theoretical critical energy release rate and fracture toughness following the Griffith principle is [241, 268, 269]

$$G_{\mathrm{G,GB}} = \gamma_1 + \gamma_2 - \gamma_{\mathrm{GB}}, \tag{2.22}$$

$$K_{\mathrm{G,GB}} = \sqrt{G_{\mathrm{G,GB}} E^*}, \tag{2.23}$$

with γ_1 and γ_2 being the surface energies of the two neighboring grains. The reader is referred to the review by Lane [269] for an introduction to interface fracture.

Similar to single crystals, the criterion in Eq. (2.22) gives only a lower limit for the actual GB fracture toughness. For this reason, the study of the fracture behavior of individual GBs is particularly important for the development of realistic continuum models for intergranular fracture. Such models ultimately aim at predicting the macroscopic failure of polycrystals, see e.g. Ref. [18]. A better understanding of the failure of individual bicrystals might be useful for the field of grain boundary engineering [270, 271], where the grain boundary characters and distributions are controlled to obtain superior materials properties. The experimental determination of the fracture toughness, on the other hand, necessitates the preparation of shallow, nearly defect-free GBs with well-defined misorientation. As a result of these problems, only few studies on the fracture behavior and fracture toughness of individual GBs exist [93, 272, 273]. Instead of dedicated fracture tests, most experiments determine the fracture strength by means of uniaxial tensile tests, see e.g. the corresponding publications for W [274], Mo [275–278], Ni_3Al [279, 280], Ni-20Cr [281], and Si [282].

Experimental investigations of the fracture strength of GBs often show that their strength is not directly predictable [279] and that GBs are not *per se* weak [94]: in particular, specimens with GBs normal to the tensile direction can have fracture strength in the same range as single crystals [270, 277, 278, 281] or higher [276, 279, 280, 282] and even show intergranular instead of transgranular fracture [278–281]. In most cases the strong GBs are $\Sigma 3$, $\Sigma 9$, and $\Sigma 17$ CSL GBs [276, 279–281], but there are exceptions, see e.g., Refs. [278, 282]. In addition, the GB fracture strength does not always correlate with the GB energy [280, 281].

It should, however, be noted that uniaxial tensile tests are only of limited suitability to investigate the strength of GBs. Dependent on the orientation of the two adjacent grains, the nearly homogeneous stress state in a tensile test will cause plastic deformation in the grains prior to GB failure. The resulting increase in strength will therefore often mask the effect of the grain boundary itself.

Atomistic simulations of grain boundary fracture

Owing to experimental difficulties in specimen preparation for GB fracture, atomistic simulations play an important role in providing fundamental insights into this topic. The study of intergranular fracture in bicrystal setups dates back to the early 1990s, see the review by Yip and Wolf [283] for a detailed introduction to atomistic concepts in GB fracture. The

published work was mainly focused on ductile fcc metals, see e.g., Refs. [20, 156, 231, 284–286]. Only very few quantitative calculations of the GB fracture toughness of (semi-) brittle materials exist [94, 121, 246, 249, 287–290]. The following overview is partially taken from Ref. [121] and has been partially published in Ref. [94].

Many atomic-scale studies on GB fracture reported on direction-dependent fracture behavior of GBs with respect to two opposite propagation directions [94, 121, 156, 284, 291]. This prominent feature of GB fracture was explained with the Rice-Thomson model [15, 292]. Experimentally, direction-dependent fracture behavior was reported for GBs in Cu [93] and for a Cu/sapphire bimaterial [293]. Contrary to theory and experiments, Cheng *et al.* [156] reported dislocation emission in two opposite propagation directions for the $\Sigma 9\{2\,\bar{2}\,1\}$ GB in Cu. This behavior was explained with the modified stress state at the crack tip in presence of a GB leading to high resolved shear stresses on otherwise unfavorably oriented slip systems. Atomistic simulations of GB fracture additionally showed dynamic initiation of dislocation activity, which was not observed for single crystals [231]. No evidence for superior deformation behavior of low-Σ GBs was found [294]. On the other hand, indications exist for the occurrence of non-Schmid effects even for GBs in fcc materials [294] and a pronounced influence of the fracture mechanisms on the local atomic structure, i.e., the structural GB unit [246, 287]. Many publications treat changes in the GB properties by the addition of other material defects, such as alloying elements [249, 288, 289, 295]. A study on how absorbed dislocations influence structure and fracture behavior of certain GBs is currently lacking.

Particularly for Fe, most studies focused on the interaction of transgranular cracks with grain boundaries [232, 296, 297] rather than on cracks at grain boundaries [295]. Grain boundaries are, however, preferred sites of crack initiation [298, 299], especially under fatigue conditions [8, 22–24]. In this stage of their existence, freshly nucleated GB cracks are of nanoscale dimensions and exhibit a highly curved crack front; their potential growth is thus crucial for the further structural integrity of the component. The fracture behavior of very small GB cracks with highly curved crack fronts has, however, not yet been studied by means of atomistic simulations. In this context, the choice of the GB is also crucial. Under the assumption that massive plastic deformation in the adjacent grains triggers crack nucleation at GBs, the fracture behavior of GBs that bound a grain with maximum Schmid factor $m = 0.5$ [300] becomes particularly interesting.

2.3 Carriers of plastic deformation

Plastic deformation in crystalline materials takes place by the nucleation and motion of defects. These line-like (dislocations) or planar defects (twins) literally carry portions of the material away from the highest stressed regions. In the context of cracks, both carriers of plastic deformation are important as they can nucleate at the crack tip thereby enhancing the fracture resistance of the material [159]. Dislocations are introduced in section 2.3.1 along with brief reviews on dislocations in bcc crystals and atomistic simulations of crack-dislocation interactions. Section 2.3.2 focuses on deformation twins, which play a particular role for bcc metals [138].

2.3.1 Dislocations

The nucleation, motion, and interaction of dislocations is not only important for the plastic deformation behavior of crystalline solids, but also for their fracture behavior. On the one hand, crack tips are preferential sites for dislocation nucleation and emission due to the concentration of very high stresses [15]. Emitted dislocations do not only blunt the crack tip [301], they can act as shielding dislocations and effectively reduce the crack tip stresses [159]. On the other hand, *pre-existing* dislocations can act as obstacles for crack propagation or cause dislocation multiplication [155].

The knowledge of the basic properties of dislocations is therefore highly relevant for this thesis. For an in-depth introduction to the theory of dislocations, the reader is referred to textbooks [48, 74] and especially to the fundamental work by Vítek on dislocations in bcc crystals [61, 259, 302–304]. In the following, only those theoretical aspects are presented that are necessary for the understanding of the subsequent chapters.

The stress field caused by a straight edge dislocation with slip plane y and Burgers vector $\underline{b}$ along the x direction, see Fig. 2.1d for the coordinate system, in an ideally isotropic linear-elastic material is [48]:

$$\sigma_{xx} = -\frac{\mu b}{2\pi(1-\nu)}\frac{y(3x^2+y^2)}{x^2+y^2}, \tag{2.24}$$

$$\sigma_{yy} = \frac{\mu b}{2\pi(1-\nu)}\frac{y(x^2-y^2)}{x^2+y^2}, \text{and} \tag{2.25}$$

$$\sigma_{xy} = \frac{\mu b}{2\pi(1-\nu)}\frac{x(x^2-y^2)}{x^2+y^2}. \tag{2.26}$$

Similarly, for a straight screw dislocation on the y plane with $\underline{b}$ parallel to the dislocation line direction z, the dislocation stress field is [48]:

$$\sigma_{xz} = -\frac{\mu b}{2\pi}\frac{y}{x^2+y^2} \text{ and} \tag{2.27}$$

$$\sigma_{yz} = \frac{\mu b}{2\pi}\frac{x}{x^2+y^2}. \tag{2.28}$$

Note that no normal stresses are present around a screw dislocation whereas no shear stresses in the xz and yz plane can be found around an edge dislocation.

The previous description of dislocations in a continuum framework neglects effects that arise from the discreteness of the crystal lattice. For this reason, the Peierls-Nabarro (PN) model was historically developed to combine continuum theory with a discrete description of the dislocation [59, 60]. In this framework, the Peierls stress τ_P was introduced to describe the stress necessary to move a dislocation from one stable position to the next. It can be estimated by [305]:

$$\tau_P = \frac{2\mu}{1-\nu}\exp\left(-\frac{2\pi d}{(1-\nu)b}\right), \tag{2.29}$$

where $d = a_0/\sqrt{h^2 + k^2 + l^2}$ is the distance between two crystallographic $\{h\,k\,l\}$ planes in cubic crystal lattices. This simple formulation shows that the Peierls stress is minimal for the highest value of d and the lowest value of b. The fundamental consequence of the PN model is therefore that the motion of dislocations is confined to crystallographic planes with large d and in directions with small b. Since the magnitudes of d and b are different for different crystal structures, the details of dislocation slip ultimately depend on the atomic-level structure of a material.

Dislocations in body-centered cubic crystals

As predicted by the indirect criterion presented in Eq. (2.29), slip in bcc crystals occurs exclusively in the closed-packed directions, i.e., in $\langle 111 \rangle$ directions. Unlike in fcc crystals, the bcc lattice does not exhibit a closed-packed plane. For this reason, the following different slip planes are possible (in descending order of likelihood): $\{110\}$, $\{112\}$, $\{123\}$. Exemplary $\{110\}$ and $\{112\}$ slip planes are shown in Fig. 2.5a for screw dislocations with $a_0/2[11\bar{1}]$ Burgers vectors. In the past, considerable effort has been devoted to determining the effective slip planes in various bcc metals. For a comprehensive overview on this issue, the reader is referred to the recent review by Weinberger *et al.* [306].

Unlike in fcc metals, dislocations in bcc metals do not dissociate into partial dislocations and form stable stacking faults [48]. This was explained by Vítek [61] with the nonexistence of a local minimum in the generalized stacking fault energy (GSFE) surface, the so-called γ surface, of $\{110\}$ and $\{112\}$ planes. The contraction of bcc dislocation cores makes cross slip generally much easier for them as for dissociated dislocations in the fcc lattice, which would need to contract in order to undergo cross slip [48].

The structure of the screw dislocation core, see Fig. 2.5, is the perhaps most frequently discussed issue in the context of dislocations in the bcc lattice, see the overview article by

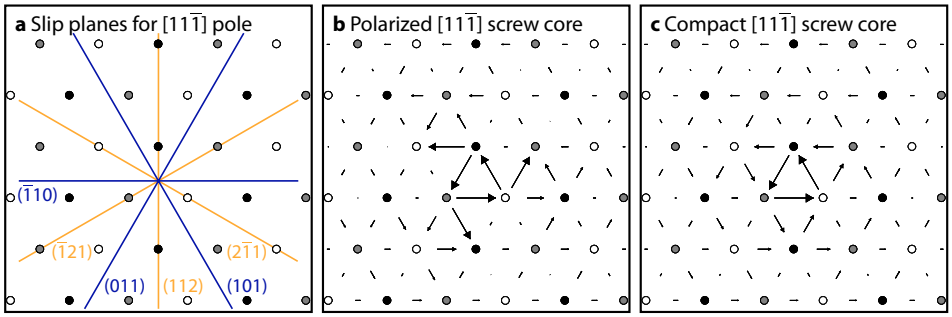

Figure 2.5: Examples for core structures of the $a_0/2[11\bar{1}]$ screw dislocation in Fe. **a**: possible {110} (blue) and {112} (orange) slip planes for screw dislocation; **b**: polarized core structure exhibiting the C3 symmetry (MFS potential [307, 308]); **c**: compact core structure exhibiting the full D3 symmetry (Chiesa potential [221]). In each plot the largest arrow corresponds to the largest magnitudes ($b/3$) of relative displacements parallel to the Burgers vector $\underline{b} = a_0/2[11\bar{1}]$. The shades of the atoms represent different out-of-plane positions in the three stacking planes parallel to the $[11\bar{1}]$ direction.

Duesbery and Vítek [309]. Unlike in fcc metals, the screw dislocation core is not confined to a single slip plane, but dissociates onto several planes. Several macroscopic phenomena, such as the temperature and rate dependence of the flow stress [310, 311] and the occurrence of non-Schmid effects [312] were attributed to the dissociated core structure. Even though this has been known for a long time, there is still uncertainty about the exact structure of the core, i.e., whether it exhibits a C3 or D3 symmetry. The C3 symmetric, or degenerate, or polarized, core dissociates on only three $\{1\,1\,0\}$ planes of the $\langle 1\,1\,1\rangle$ pole, which are separated by 120°. The D3 symmetric, or compact, or non-polarized, or non-degenerate, core splits onto six $\{1\,1\,0\}$ planes separated by 60°. Both core structures are compared in Fig. 2.5b and c. The reader is again referred to Weinberger *et al.* [306] for more details on this topic. Currently, dedicated DFT calculation suggest that the compact core structure is the preferred dislocation configuration of bcc metals [313–315]. These findings motivated developers of interatomic potentials to put much effort in the creation of potentials that lead to the compact core structure [217, 218, 221].

Atomistic simulations of crack-dislocation interactions

Owing to the general 3D nature of the interaction between cracks and dislocations, the very large system sizes for atomistic simulations became affordable only recently. Bitzek and Gumbsch [155] reported on stationary and propagating cracks interacting with dislocations on oblique slip planes in Ni. Here, Ni was chosen as a model material for Si, where dislocation motion is thermally activated and too sluggish to be sensibly treated by current atomistic methods. They showed that pre-existing dislocations can lead to dislocation multiplication and a re-orientation of the crack front. These simulations allowed to explain the differences in the observed dislocation sources in static and dynamic fracture experiments [69, 316, 317]. Apart from these studies, only few in-situ experiments [318–321] exist where the precise interaction mechanisms of crack tips with pre-existing dislocations were studied in detail. This highlights the importance of atomistic simulations for a deeper understanding of the fundamental interaction mechanisms between cracks and dislocations.

To the author's knowledge, the interaction of cracks with pre-existing dislocations in bcc crystals has not yet been investigated by atomistic methods. Particularly in bcc metals, dislocations can glide and cracks can propagate on the same $\{1\,1\,0\}$-type planes. It is therefore interesting how a crack and a dislocation interact on this plane and if this might explain the non-observation of $\{1\,1\,0\}$ cleavage in Fe, see e.g., Ref. [28].

In most industrially important materials, dislocations can freely glide only until they interact with each other or other obstacles, such as grain boundaries [305, 322]. At GBs, dislocations can be absorbed or transmitted; in case they are followed by other dislocations with the same Burgers vector, a so-called dislocation *pile up* forms. In this context, it is of fundamental interest how dislocations, which have been absorbed by a GB, influence the growth behavior of a GB crack. As with crack-dislocation interactions in bcc crystals, an atomistic study on this topic is currently lacking.

2.3.2 Deformation twinning

Unlike in fcc structures, twinning in bcc crystals does not occur on the preferred glide planes for dislocation motion, see section 2.3.1. Instead, deformation twinning takes place by successive shear of adjacent (parallel) $\{112\}$ planes by twinning dislocations (TD) with Burgers vector $\underline{b}_t = a_0/2\langle 111\rangle$ [48, 74]. The orientation of $\{112\}$ planes within the bcc unit cell is shown in Fig. 2.6a. The glide of n TDs results in a n-layer twin, see Fig. 2.6b.

Similar to twinning in the fcc lattice [48, 74], twin formation is preferred only in one of two antiparallel $\langle 111\rangle$ directions. This phenomenon is called *twinning/anti-twinning asymmetry*; the corresponding twinning (TW) and anti-twinning (AT) direction are indicated in Fig. 2.6b. It is obvious from the figure, that shearing in AT direction by the same amount as in TW direction results in a configuration where atoms are located unfavorably close to each other. Or inversely, the successive shear by $n(-2\underline{b}_t)$ would be necessary to reach the same final twin structure as produced by a shear of $n\underline{b}_t$ in the TW direction.

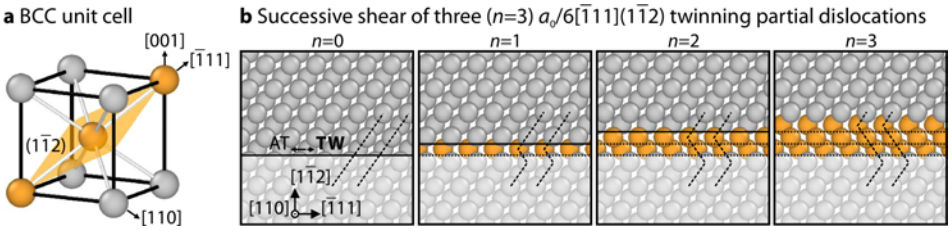

Figure 2.6: Illustration of deformation twinning in bcc metals. **a**: bcc unit cell with indicated $(1\bar{1}2)$ twin plane and $[\bar{1}11]$ direction. **b**: sequential configurations during the formation of a three-layer (n=3) twin by the successive glide of three $\underline{b}_t = a_0/2[\bar{1}11]$ twinning dislocations on adjacent $(1\bar{1}2)$ planes in twinning (TW) direction; subsequent glide planes are indicated by solid lines in each subfigure; two atomic columns along the initial [001] direction are marked with dashed lines to indicate the twinned structure.

Twin formation at crack tips

Using the framework of Rice [16], Tadmor and Hai [323] developed an expression for the tendency of fcc metals to nucleate a two-layer microtwin at a crack tip rather than to form a dissociated dislocation. Their twinning criterion does not depend on the crack orientation and can be written as [323]:

$$T = \lambda_{\text{crit}} \sqrt{\frac{\gamma_{\text{usf}}}{\gamma_{\text{ut}}}}\,, \tag{2.30}$$

where microtwin nucleation is predicted for $T > 1$ and dislocation emission for $T < 1$. In Eq. (2.30), γ_{ut} is the unstable twinning energy, i.e., the energy barrier for successive shift of adjacent atomic layers on the twinning plane in the twinning direction of the corresponding crystal system. The additional load necessary to nucleate the trailing partial relative to the leading partial dislocation is characterized by λ_{crit}. As shown in the appendix B, λ_{crit}

equals unity for bcc metals and T depends only on the ratio γ_{usf}/γ_{ut}. The critical stress intensity factor for twin formation is then written as [323]:

$$K_t = K_e T^{-1} = K_e \sqrt{\frac{\gamma_{ut}}{\gamma_{usf}}}, \tag{2.31}$$

where K_e is calculated using Eqs. (2.14-2.15) for θ and φ of the corresponding $\{1\,1\,2\}$ plane.

2.4 Meso-scale modeling of crack-microstructure interactions

The quantitative, material-specific, and predictive modeling of fracture requires both accurate atomistic models and the inclusion of microstructural complexity within the plastic zone [95], see Ref. [324] for a review on computational modeling of fracture in polycrystals. Here, the fundamental challenge lies in the fact that the plastic zone, cf. Eq. (2.13), in most metallic materials is much too large to be fully treated atomistically. On the other hand, the microstructures of most technical components are too heterogeneous to be simplified by a continuum. For this reason, the problem has to be tackled at the meso-scopic length scale, i.e., between the atomic and the continuum levels [7, 17].

At the meso scale, fracture of polycrystalline microstructures is often studied using finite element (FE) calculations in combination with cohesive zone (CZ) models [18, 325, 326]. These well-established models resort to traction-separation relationships, i.e., mathematical descriptions of the separation of the material in front of the crack tip in dependence of the applied load, see Ref. [327] for a review of common CZ models. In the recent years, CZ models have been frequently used to study crack propagation through polycrystals [328–335]. The vast majority of these studies is limited to 2D microstructures, GB crack propagation, and linear-elastic material behavior; only few of them account for 3D aspects [332], trans- vs. intergranular fracture [334, 335], and plastic deformation behavior [329]. Particularly the inclusion of a more realistic and less phenomenological material behavior within the plastic zone requires the inclusion of cracks in discrete dislocations (DD) simulations [19], which are today still limited to 2D [336, 337] or the study of stationary cracks in single crystal [338] or bicrystal [339] configurations. In this context, the direct atomic-scale representation of fundamental crack interactions with pre-existing dislocation arrangements in single crystals [155, 214] and bicrystals can help to parameterize both future CZ and DD models.

Typical CZ parameters are experimentally measurable quantities, such as stiffness and ultimate tensile strength. They are therefore limited to specific material conditions, including e.g. the alloy composition, existing phases, and grain boundary character distributions. Alternatively, traction-separation relationships can be obtained from atomic-scale simulations to include the fundamental relationships between the aforementioned aspects and mechanical or thermodynamic properties. This can be done, e.g., by determining the tensile stress-strain behavior with MD simulations [340, 341] or even density functional theory (DFT) calculations [21, 342]. Tensile tests, however, neglect both direction-dependent

resistance against fracture [29] and the effect of the stress concentrations at a crack tip. To account for such effects, the CZ law has to be parameterized by atomic-scale simulations of crack configurations, see e.g. Refs. [286, 343–345]. With information derived in this manner, it is in principle possible to include direction-dependent fracture behavior and toughness. To the author's knowledge, a detailed comparison of the two different methods of deriving traction-separation relationships is not yet reported in the literature.

Whereas experimentally-parameterized CZ models have already been used for fracture simulations in 3D [332, 346, 347], studies using atomistically-informed CZ models are still limited to quasi-2D bicrystal setups [21, 286, 340, 342–345], which inherently prohibit crack front curvature. It is thus key for the future development of atomistics-informed 3D CZ models to determine the fracture criteria and atomic-scale crack-tip processes of curved cracks under fully 3D conditions. In particular, the role of curvature for crack propagation in single crystals has not yet been compared to its role for cracks in bicrystals, i.e., at GBs. This comparison can finally help to develop CZ models for studying the competition between inter- and transgranular fracture, see e.g. Refs. [334, 335], in three dimensions.

2.5 Key questions of this thesis

The objective of this thesis is to lay the foundations for developing new microstructure-sensitive meso-scale models for bcc-based materials that include important crack-defect interactions. For this purpose, I start with the determination of the fracture properties of perfectly straight cracks in defect-free single crystals to obtain a reference data set for the bcc metals Fe and W. Thereafter, the dependency of fracture behavior and criteria on crack front curvature, characteristics of grain boundaries, and pre-existing dislocations will be assessed. This systematic procedure allows to finally address the following key questions:

(i) What is the general influence of crack front curvature on the competition between brittle fracture and crack-tip plasticity?
This includes the fundamental questions of
- the relation to theory and fracture properties of perfectly straight cracks,
- the influence of crack front curvature on the lattice trapping effect, and
- the evolution of crack tip plasticity at curved crack fronts.

(ii) How do locally different bonding situations influence the crack propagation behavior at grain boundaries?
In this context, the central aspects are
- the relation to theory and cracks in defect-free single crystals,
- the possibility for local re-arrangements at long 3D crack fronts, and
- the mechanisms that are specific to GB cracks with curved crack fronts.

(iii) How do cracks interact with pre-existing dislocations?
This question particularly involves
- the role of the dislocation character (edge, screw, mixed),
- the influence of the relative orientation between crack and slip plane, and
- the role of absorbed dislocations for the fracture resistance of GBs.

3 Methods

This chapter provides all necessary information about the computational methods that were used in the present study. Section 3.1 and 3.2 present the basics of atomistic simulations and density functional theory calculations, respectively. Detailed information about the simulation setups, boundary and loading conditions are given in section 3.3. Section 3.4 describes how to create atomistic configurations with grain boundaries and dislocations. The chapter closes with techniques for visualization and analysis of the simulation results in section 3.5.

3.1 Atomistic simulations

In atomic-scale molecular dynamics (MD) simulations, the time-dependent movement of all atoms in a system is tracked by treating them as classical, Newtonian, particles and numerically integrating the equations of motion [210]. MD evolved from statistical mechanics [210] and is a well-established method in physics and materials science [348, 349]. Detailed descriptions are available in several textbooks [350–352]. Throughout this study, the massively-parallel MD software package IMD (ITAP molecular dynamics) [353–355] is used, see Ref. [356] for a detailed documentation. All MD simulations are carried out using the microcanonical ensemble (NVE), in which the number of particles, the volume, and the total energy of the system is controlled. Since the scope of this thesis is to identify (temperature-independent) crack-tip mechanisms rather than to make precise quantitative predictions, the starting temperature in all MD simulations is set to $T_0 = 0$ K. The time step was always $\delta t = 1$ fs.

The term molecular statics (MS) describes the search for minima in the so-called potential energy landscape. Finding such energy minima is one of the great challenges in the field of computational mathematics [210]. For most problems in this study, a sequential combination of the following two minimization algorithms is found to work well: atomic positions are optimized locally by using the microconvergence (MIK) integrator [357] for about 100 to 500 steps followed by force minimization with the fast inertial relaxation engine (FIRE) [358]. The FIRE algorithm is based on conventional molecular dynamics with additional velocity modifications and adaptive time steps. Typically, the system's energy is deemed to be sufficiently minimized if the force norm, i.e., the norm of the $3N$-dimensional force vector, falls below a threshold value of 10^{-8} eV/Å. In cases where this is computationally too costly the threshold value is increased to 10^{-6} eV/Å.

In MS simulations, *unrelaxed* and *relaxed* structures are commonly distinguished. The unrelaxed structure is the starting configuration or the initial guess for the energetically minimized structure, which is then referred to as the relaxed configuration. It is important to note that not all unrelaxed configurations will necessarily lead to a relaxed structure. In

other words, if the initial guess is too far away from the equilibrium structure, the minimization algorithm will not be able to successfully relax the configuration. Setting up starting configurations as close to the energy minimum as possible is therefore one of the crucial tasks in the field of atomistic simulations.

3.1.1 Interatomic potentials

The study of crack-microstructure interactions under fully 3D conditions requires atomistic configurations with typically more than 50 million atoms. To treat such a large number of atoms within reasonable amounts of time, interatomic potentials following the embedded atom method (EAM) [216] are used here. According to the EAM formalism, the total energy of a N-atom configuration is given by [216, 359, 360]:

$$E_{\mathrm{tot}} = \frac{1}{2}\sum_{\mathrm{i,j,i\neq j}}^{\mathrm{N}} V(r_{\mathrm{ij}}) + \sum_{\mathrm{i}}^{\mathrm{N}} F(\rho_{\mathrm{i}}) \text{ and} \tag{3.1}$$

$$\rho_{\mathrm{i}} = \sum_{\mathrm{j,i\neq j}} f(r_{\mathrm{ij}})\,, \tag{3.2}$$

where r_{ij} is the distance between two atoms i and j and ρ_{i} is the host electron density at the site of atom i. $V(r_{\mathrm{ij}})$ and $f(r_{\mathrm{ij}})$ are radial-symmetric functions. The non-pairwise part of E_{tot}, the so-called embedding energy term $F(\rho_{\mathrm{i}})$, describes the energy contribution arising from the host electron density. The original physical interpretation of these terms is less important in current EAM potentials, and Eqs. (3.2) and (3.2) are used simply as a reliable semi-empirical expression with adjustable parameters. For single-component systems, the EAM model is identical to the Finnis-Sinclair form [307] with the exception of the embedding function $F(\rho_{\mathrm{i}})$. In Finnis-Sinclair potentials, $F(\rho_{\mathrm{i}})$ is a square-root function whereas its form is arbitrary in the EAM formalism [225]. Many recent potentials use a combination of piecewise defined functions or splines to allow for greater flexibility in the fitting of $V(r_{\mathrm{ij}})$, $f(r_{\mathrm{ij}})$ and $F(\rho_{\mathrm{i}})$. Typically used functions include polynomial, exponential, or square-root functions.

Over the last decades, much effort has been put into developing reliable EAM potentials for Fe [217–221, 223–227, 307, 308]. Parts of the following overview have been published in Ref. [122]. Since they were not specifically developed for the study of fracture, six of the most recent potentials are selected and checked for their capability to model the fracture behavior of Fe: the Chamati [227], Mendelev-II [225], Gordon[217], Marinica07 [219], Marinica11 [218], and Chiesa [220, 221] potentials. Additionally, two older EAM potential for Fe, the classical Finnis-Sinclair (FS) potential [307] in the modified version of Marchese *et al.* [308] and the Simonelli [223] potential, are chosen for comparison.

Table 3.1 summarizes the cutoff-radii, the main focus for development, and the functional forms of $V(r_{\mathrm{ij}})$, $f(r_{\mathrm{ij}})$, and $F(\rho_{\mathrm{i}})$ for each of the aforementioned Fe potentials. For the sake of comparability, the corresponding potential functions are scaled according to the effective pair format [361] and plotted in Fig. 3.1a. Fig. 3.1b shows the effective pair force, i.e., the derivative of the effective pair potential. The Chamati potential, for example, uses a superposition of two Morse functions [362, 363] for $V(r_{\mathrm{ij}})$. The functional forms

Table 3.1: Summary of EAM potentials for Fe. The potential names used in this study are displayed together with the main focus in their development, cutoff radii r_{cut}, and the functional form for $V(r_{ij})$, $f(r_{ij})$, and $F(\rho_i)$: polynomials (P), square roots (R), exponentials (E), logarithmic functions (L) and splines (S); if piecewise definitions are used, the different parts are separated by commas. All potentials were fitted to the experimental values of the lattice parameter [366] and elastic constants [48], shown in Table 3.2. MFS stands for Marchese-Finnis-Sinclair.

Name	r_{cut} (Å)	$V(r_{ij})$	$f(r_{ij})$	$F(\rho_i)$	Focus of development	Ref.
MFS	3.40	P	P	S	Vacancy diffusion	[307, 308]
Simonelli	4.10	S	E, P	E+S	Properties of point defects	[223]
Chamati	5.67	E	E	P	Self-diffusion on {100} surfaces	[227]
Mendelev-II	5.30	E, E(P), S	S	R+P	Crystalline and liquid states	[225]
Gordon	6.00	E, E(P), S	S	R+P	Flow stress, 3D kink nucleation, compact screw dislocation core	[217]
Marinica07	5.20	E, E(P), S	S	R+P	Point defects, defect clusters	[219]
Marinica11	5.20	S	S	R+P	Compact screw dislocation core, single hump Peierls potential	[218]
Chiesa	4.00	S	S	R+L	Third-order elastic constants, compact screw dislocation core	[220, 221]

of the Mendelev-II, Gordon, and Marinica07 potentials are similar. All of them use the piecewise definition of $V(r_{ij})$ described by Ackland *et al.* [224]: very short-range interactions ($r_{ij} < r_1$) are modeled with a universal screened Coloumb function [364] and an exponential function of a third order polynomial ($r_1 < r_{ij} < r_2$); above a certain distance r_2, a cubic spline function is used. The Marinica11 potential differs from the Mendelev-type potentials in that $V(r_{ij})$ is not piecewise defined but consists only of the cubic spline function, cf. Eq. (A1) in Ref. [225] and Eq. (11) in Ref. [218]. Splines are also used for the radial functions of the Chiesa potential. Its functional form of $F(\rho_i)$ was derived using Stoner's theory of band magnetism [365] and therefore differs from the other potentials [220]. The properties of the different EAM potentials for Fe are shown in Table 3.2 in comparison to experimental data and density functional theory (DFT) calculations, see section 3.2. I have documented the determination of potential properties using MS simulations in great detail in chapter 3.2 of Ref. [120].

In addition to EAM potentials for Fe, the Finnis-Sinclair potential for W [307] in the parametrization of Ackland and Thetford [367] is chosen as nearly isotropic reference material, see Table 3.3 for the potential properties. This is particularly the case in the presence of (asymmetrical) grain boundaries. To correlate the determined fracture properties with the (equilibrium) potential properties, various EAM potentials for the other bcc refractory metals V, Nb, Ta, Cr, and Mo were studied additionally. For V, Nb, Ta, and Mo, the corresponding Ackland-Thetford-Finnis-Sincliar (ATFS) potentials [307, 367] were used. Cr was modeled with the original FS potential [307]. In addition, the properties of the Fellinger potential for Nb [368], the Ackland potentials for Mo and W [369, 370], the Smirnova potential for Mo [371], and the Wang potential for W [372] were determined for comparison. Table 3.3 lists the corresponding equilibrium potential properties.

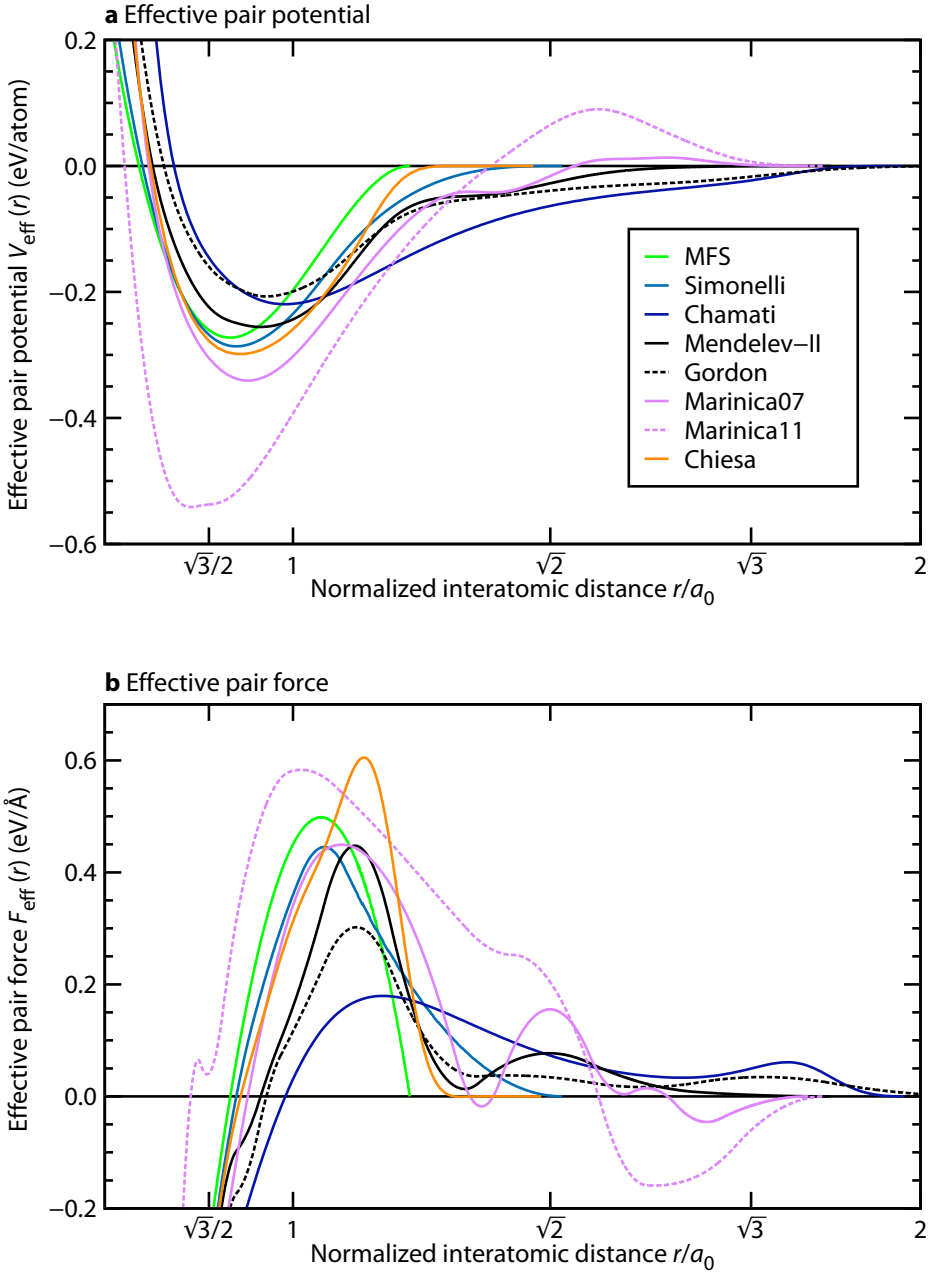

Figure 3.1: Comparison of the potentials for Fe in terms of atomic interactions. **a**: effective pair potentials $V_{\text{eff}}(r)$ according to the effective pair format [361]; **b**: effective pair forces $F_{\text{eff}}(r)$, i.e., the first derivatives of $V_{\text{eff}}(r)$. Note, that both the Marinica07 and Marinical1 potentials exhibit zero crossings of $V_{\text{eff}}(r)$ and $F_{\text{eff}}(r)$.

Table 3.2: Properties of Fe as determined by experiments, DFT calculations, and MS simulations with various EAM potentials. The details of the DFT calculations are provided in section 3.2. a_0: lattice parameter (in Å), E_0: equilibrium energy per atom (in eV/atom), C_{ij}: elastic constants (in 10^{11}Pa), $\gamma(hkl)$: surface energy of *(hkl)* plane, γ_{usf}: unstable stacking fault energy, γ_{ut} unstable twinning energy (all in J/m^2).

Property	Exp.	DFT	MFS	Simonelli	Chamati	Mendelev-II	Gordon	Marinica07	Marinica11	Chiesa
a_0	2.8665[a]	2.8377	2.8665	2.8660	2.8661	2.8553	2.8552	2.8552	2.814	2.8665
E_0	-4.28[b]	—	-4.280	-4.280	-4.280	-4.122	-4.210	-4.122	-4.122	-13.883
C_{11}	2.420[c]	2.236	2.431	2.426	2.416	2.434	2.445	2.434	2.434	2.436
C_{12}	1.465[c]	1.569	1.381	1.470	1.475	1.450	1.443	1.450	1.450	1.384
C_{44}	1.120[c]	0.854	1.218	1.119	1.140	1.159	1.154	1.159	1.157	1.222
γ(100)	2.360[d]	2.451	1.908	1.627	2.480	1.792	2.124	2.311	1.754	1.902
γ(110)	2.360[d]	2.404	1.703	1.436	2.359	1.651	1.980	1.870	1.232	1.672
γ(111)	2.360[d]	2.669	2.137	1.793	2.657	1.999	2.293	2.317	1.865	2.113
γ(112)	2.360[d]	2.50[e]	1.948	1.640	2.558	1.887	2.171	2.180	1.666	1.942
γ_{usf}(110)	—	0.890	0.974	0.737	0.742	0.661	0.780	0.817	0.942	0.886
γ_{usf}(112)	—	1.116[f]	1.139	0.859	0.788	0.766	0.858	0.922	0.869	1.042
γ_{usf}(123)	—	—	1.172	0.843	0.799	0.755	0.857	0.921	0.951	1.023
γ_{ut}(112)	—	—	0.926	0.634	0.752	0.694	0.760	0.862	0.887	0.942

[a] Lattice parameter at T = 300 K taken from Ref. [366]

[b] Cohesive energy at T = 300 K taken from table 3.3 in Ref. [373]

[c] Elastic constants at T = 300 K taken from Ref. [374]

[d] Surface energies for average orientations extrapolated to T = 0 K by Tyson and Miller [375]

[e] According to Ref. [376] (GGA)

[f] According to Ref. [377] (GGA, PAW)

Finally, it should not be forgotten that there are some known shortcomings of EAM potentials. The binding energy of an atom, for example, strongly correlates with the number of its nearest neighbors [210]: in the presence of a vacancy, only the energy contribution of the missing bond is subtracted from the system, but the effect on the other bonds is not (or only weakly) taken into account. This is in clear contrast to DFT calculations where a strong environmental dependence is found, i.e., isolated bonds are stronger than bonds in the presence of other bonds [378]. EAM potentials particularly fail to reproduce the partially covalent bonding character of bcc metals. For this reason, new potential formulations with angular-dependent terms have been proposed, see e.g. Refs. [212, 213]. Such modified EAM (MEAM) or angular-dependent potentials (ADP) are, however, computationally more demanding and not yet usable for the large system sizes used here.

3.1.2 Boundary conditions

As with all simulation techniques, the choice of the boundary conditions critically influences the quantitative—and sometimes also qualitative—simulation results. Boundary conditions literally define how atoms at the boundaries of the simulation box are treated. In this study, the following boundary conditions are used:

- **Periodic boundary conditions (PBC).** The simulation box is virtually embedded in an infinite periodic space built up of the same box. To ensure that atoms are not interacting with their images, the minimum thickness in directions where PBC are used, should be twice the cutoff radius. As the simulation box becomes infinitely long in the direction of the PBC, it is possible to model bulk (3D PBC), thin film (2D PBC), and fibrous (1D PBC) structures.
- **Fixed boundary conditions.** Atoms are not allowed to move. This type of boundary conditions is mainly used to maintain the overall applied strain of an atomistic configuration. The minimum thickness of these boundaries should be twice the cutoff radius to prevent possible influences of the free space at one side on atoms at the other side of the fixed boundary layers.
- **Free boundary conditions.** Atoms are free to move. These boundary conditions are used whenever a free surface should intentionally be present.
- **1D- or 2D-dynamic boundary conditions.** Atoms are free to move in a certain direction (1D) or within a certain plane (2D) whilst being fixed in the other direction(s).
- **Force boundary conditions.** A special case of free, 1D-, or 2D-dynamic boundary conditions where atomic positions are adjusted in such way that an average force vector is acting on the atoms.

Table 3.3: Properties of bcc refractory metals as determined by MS simulations with various EAM potentials. Symbols and units as in Table 3.2. All potentials were fitted to experimental and/or DFT data; please consult the corresponding publications for the precise fitting parameters: FS: Finnis-Sinclair [307]; ATFS: Ackland-Thetford modification of the FS potential [367]; Fellinger: Ref. [368]; Ackland: Ref. [369, 370]; Smirnova: Ref. [371]; Wang: Ref. [372]. Note that the determination of the corresponding property was not possible (non-convergent energy minimization) in case of missing values.

Property	V ATFS	Nb ATFS	Nb Fellinger	Ta ATFS	Cr FS	Mo ATFS	Mo Ackland	Mo Smirnova	W ATFS	W Ackland	W Wang
a_0	3.0399	3.3008	3.3079	3.3058	2.8845	3.1472	3.1470	3.1474	3.1652	3.1652	3.1652
E_0	-5.310	-7.570	-7.091	-8.100	-4.100	-6.820	-6.831	-6.929	-8.900	-8.910	-8.900
C_{11}	2.279	2.466	2.331	2.660	3.871	4.647	4.500	5.701	5.224	5.326	5.225
C_{12}	1.187	1.332	1.239	1.612	1.035	1.615	1.729	2.307	2.044	2.050	2.044
C_{44}	0.426	0.281	0.321	0.824	1.008	1.089	1.251	1.695	1.606	1.632	1.606
$\gamma(100)$	1.742	1.987	—	2.337	1.774	2.103	2.520	3.142	2.930	2.982	2.990
$\gamma(110)$	1.482	1.685	2.046	1.985	1.632	1.831	2.212	2.827	2.578	2.611	2.552
$\gamma_{usf}(110)$	0.718	0.720	0.709	0.949	0.584	0.919	1.655	1.438	1.024	1.960	1.120
$\gamma_{usf}(112)$	0.833	0.832	0.825	1.104	0.679	1.064	1.910	1.566	1.190	2.262	1.319
$\gamma_{ut}(112)$	1.465	—	0.626	1.481	0.969	0.889	1.478	1.567	0.888	2.849	1.050

3.2 Density functional theory (DFT) calculations

In addition to MS simulations using EAM potentials, see section 3.1, selected material properties were additionally determined with DFT calculations, see Table 3.2. DFT was developed by Hohenberg, Kohn, and Sham and is based on the assumption that the ground state energy of an electron gas is a unique and universal functional of the electron density [379]. According to this theory, it is possible to replace the many-electron problem by equivalent one effective particle problems [380]. The reader is referred to textbooks [210, 381, 382] for an introduction to DFT. In the following, I focus on the specifics of the DFT calculations performed for this thesis.

Unless stated otherwise, all DFT calculations were carried out with the plane-wave code *PWscf* of the Quantum ESPRESSO software package [383, 384] using the Perdew-Burke-Ernzerhof (PBE) exchange-correlation functional [385], which is based on the generalized gradient approximation (GGA), and Vanderbilt ultrasoft (US) pseudopotentials [386] provided by B. Meyer [387]. The kinetic energy cutoff was 30 Ry for wave functions and 120 Ry for charge densities and potentials [387]. To calculate the properties of magnetic Fe, spin-polarized calculations are performed with a starting magnetization of 0.5. The convergence threshold for self-consistent calculations is 10^{-8} Ry (approximately $1.3{\times}10^{-7}$ eV) with a mixing factor of 0.7. Shifted k-point meshes for Brillouin zone integrations are generated by the Monkhorst-Pack scheme [388] and the fractional occupation numbers of the electronic states were determined by a Gaussian broadening [389].

To determine the elastic constants, the surface energies, and the (1 1 0) GSFE, atomic positions were relaxed by minimizing the atomic forces using the Broyden-Fletcher-Goldfarb-Shanno (BFGS) relaxation scheme [390] with a convergence threshold for the largest residual force component of 10^{-3} Ry/r_B (approximately $2.6{\times}10^{-2}$ eV/Å). Elastic constants were calculated by finite deformations generated by the ElaStic tool 1.0 [391, 392].

Fig. 3.2a shows the relative stability of the bcc phase in comparison to fcc and hcp for Fe. It can be seen that the preference of the bcc phase is due to ferro-magnetism as non-magnetic Fe is clearly more unstable than fcc and hcp. To determine whether the calculated results are independent of the k-point grid and the magnitude of the Gaussian smearing parameter s_Gauss, the number of k-points was varied between 24×24×24 and 80×80×80 k-points and s_Gauss was varied between 0.0005 and 0.02 Ry. The dependence of the calculated lattice parameter a_0 and the elastic constants C_ij on k and s_Gauss is shown in Fig. 3.2b-e. As it can be seen in the figure, the choice of s_Gauss = 0.005 Ry and $k/a_0 \approx 33$ is a good compromise between computational efficiency (small k and high s_Gauss) and accuracy of the results (high k and small s_Gauss). For this reason, all properties presented in this thesis, see e.g., Table 3.2, were calculated with these values.

The surface energies were calculated in boxes of 1×12×1 unit cells, which are periodically repeated in all three spatial directions. To model the free surfaces, an empty space was added in the direction of the long box axis that corresponded to six unit cell lengths. The independence of the calculated surface energies on the box size was tested by varying the number of unit cells in the long box direction between 4 and 16. The generalized stacking fault energies on the (1 1 0) plane were determined in fully periodic boxes of 1×8×1 unit cells by shifting one half of the box with respect to the other [61].

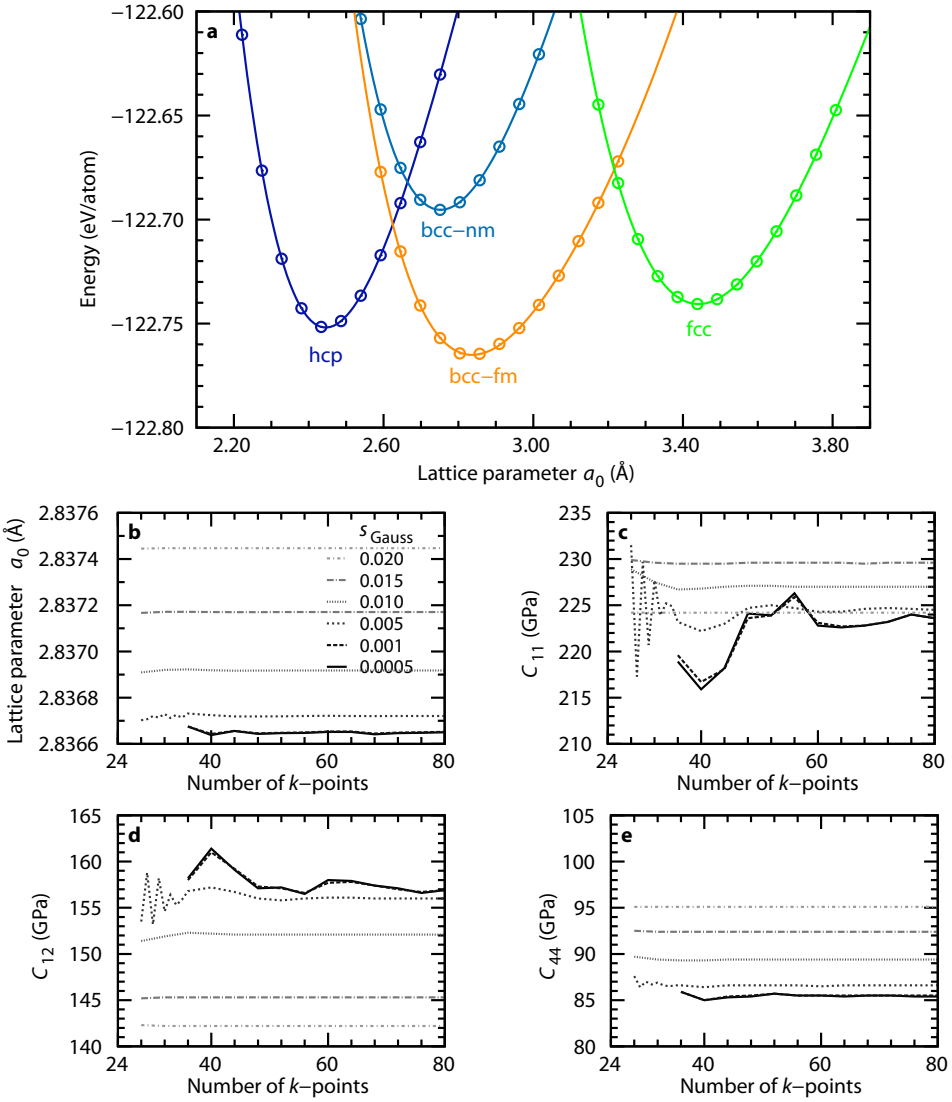

Figure 3.2: Properties of Fe as determined with DFT calculations. **a**: energy of different crystal structures in dependence of the lattice parameter a_0 ($s_{\mathrm{Gauss}} = 0.005$, $k \approx 33$); nm: non-magnetic; fm: ferro-magnetic; fcc and hcp ($c/a_0 = 1.6$) are non-magnetic. Dependence of calculation results on number of k-points and Gaussian smearing parameter s_{Gauss} for magnetic bcc Fe: **b**: lattice parameter a_0; **c-e**: elastic constants C_{11}, C_{12}, and C_{44}.

3.3 Simulation setups

Throughout this thesis, fracture simulations are performed using the following strategy: first, an atomic configuration is deformed to artificially insert a crack. Second, the so-obtained structure is energetically minimized to determine whether the crack is stable or not under the given conditions. During the relaxation, the boundaries of the simulation box are fixed in such a way that the applied deformation field is globally maintained. If the *local* crack tip position does not change significantly (by more than three atomic distances) during relaxation, i.e., it is stable, the created structure is used as initial configuration for subsequent fracture simulations.

The different setup geometries for the crack configurations used in this study are shown in Fig. 3.3. The subsequent section 3.3.1 details the geometries for straight cracks, see Fig. 3.3a-d. Thereafter, the penny-shaped crack setup geometry, see Fig. 3.3e, is described in section 3.3.2.

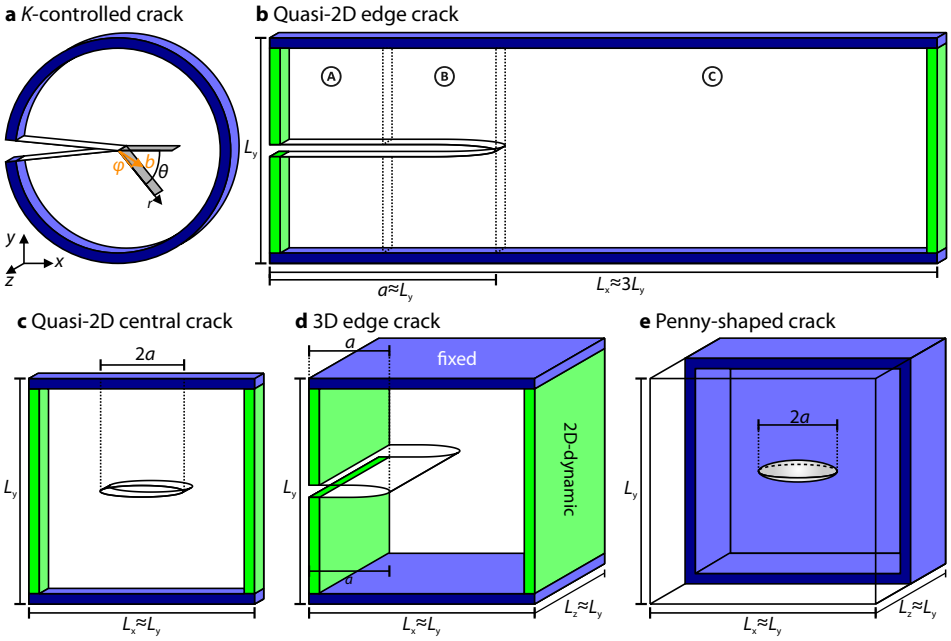

Figure 3.3: Overview of the different setup geometries. **a**: K-controlled setup, where atoms are displaced according to the linear-elastic displacement field around a crack tip; r: distance from the crack tip; θ: angle between r and crack plane; φ: inclination angle of Burgers vector and normal direction to crack front in the slip plane; **b**: strain-controlled quasi-2D edge setup; **c**: strain-controlled quasi-2D central setup; **d**: strain-controlled 3D edge setup; **e**: strain-controlled penny-shaped crack with center at ($L_x/2$,$L_y/2$,$L_z/2$); a: crack length or radius, i.e., the long half axis of the ellipse (**c**) or ellipsoid (**e**). Boundary conditions: fixed (blue); 2D-dynamic (green, fixed in x direction); periodic boundary conditions (PBC) in z direction (**a**-**d**).

3.3.1 Setup geometries for straight cracks

The methods to artificially insert a crack differ in the deformation field that is used to apply the crack-tip displacements. Either the whole configuration is deformed according to the theoretical K-field of the crack-tip strains *or* an overall strain is globally applied to the configuration in addition to the local creation of the crack. The different setups are shown in Fig. 3.3 and described in the following sections. The specifics about the crack-tip displacement fields are given in the appendix C.

In the following, the same convention for the box axes is used as it was introduced in Fig. 2.1. This means, x is the crack propagation direction, y is the direction normal to the crack plane, and z is parallel to the crack front. A crack system (hkl)[uvw] in a single crystal is described by the crack plane (hkl) and the crack front direction [uvw].

K-controlled geometry

The K-controlled setup aims to model a crack tip in a semi-infinite body under pure opening (mode I) loading, see Fig. 3.3a. To this end, atoms in the whole configuration are shifted from their original lattice positions according to the far field solution for the displacements $u_{\mathrm{x,y}}(r, \theta, K_{\mathrm{I}})$ around a crack tip. For orthotropic materials under plane strain conditions, $u_{\mathrm{x,y}}(r, \theta, K_{\mathrm{I}})$ was derived by Sih and Liebowitz [46, 47]. Special attention has to be paid to the determination of the orientation-dependent elastic modulus E^*. The details are given in the appendix C. To prescribe the displacement field, atoms in the boundary layer of minimum thickness $2r_{\mathrm{cut}}$ are kept fixed in the xy-plane during the simulation. Typical configurations have a radius of $R = 150$ Å and contain approximately 100,000 atoms.

The clear advantage of this geometry is the unambiguous connection between the applied displacements and the corresponding stress intensity factor K_{I} [47]. This well-defined relationship allows to determine the fracture toughness K_{Ic}. On the other hand, all atomic displacements are applied under the assumption that the crack tip is located exactly at the center of the simulation box. If this is not the case, the actual crack tip state does not correspond to the situation, which is prescribed by the boundary conditions. As a consequence, the K-controlled setup is unable to properly handle crack propagation.

Strain-controlled geometries

Contrary to the K-controlled geometry, the whole simulation box is set under a constant overall strain and opposite box boundaries remain parallel in strain-controlled setups. Above a certain threshold crack length, the crack experiences a constant energy release rate G and the configurations can be used for the simulation of propagating cracks [41, 53, 161, 162]. Due to the small possible simulation box sizes, the necessary strains for crack stabilization and propagation are comparably high in these geometries. They are, however, not meant as quantitative predictions and will frequently be normalized to the thermodynamic prediction for the critical fracture strain. Furthermore, it is necessary to repeat selected simulations for different box sizes to ensure that the observed mechanisms are size-independent. The different geometries are presented for straight crack fronts in Fig. 3.3b-d and described in the following paragraphs.

- **Quasi-2D edge crack.** The quasi-2D edge crack setup, which is commonly used for the study of long propagating cracks, is shown in Fig. 3.3b. The crack is introduced as a semi ellipse only in region B. The two blocks in region A are rigidly displaced whereas region C is set under the constant strain ε. The detailed displacement fields are presented in the appendix C. Atoms in the boundary layers parallel to the crack plane (blue in Fig. 3.3b) are not allowed to move in the xy plane. In boundary layers normal to the crack propagation direction (green), atoms are not allowed to move in x direction. Typical configurations are $L_x \times L_y \times L_z = 3000$ Å $\times 1000$ Å $\times 2r_{cut}$ in size and contain approximately three million atoms.

  The theoretically predicted strain for the onset of crack advance is in this setup [41]:

$$\varepsilon_G = \sqrt{\frac{2G_G}{E_y L_y}}, \tag{3.3}$$

  with the Griffith criterion $G_G = 2\gamma$, the elastic modulus E_y in y direction, and the box length L_y in y direction. This prediction, however, neglects the strain dependence of E^* and γ as well as the influence of the boundary conditions on the overall stored elastic energy. To take into account these effects, a new threshold strain ε_0 is determined by applying Griffith's principle of energy balance directly on the average potential energy of the simulation box [214]: the dependence of the potential energy on the applied strain is compared for two different situations. The first is a defect-free configuration. The second models the situation after virtual crack propagation and contains two free surfaces. This procedure is performed in a quasi-static manner, i.e., iterative loading of the configuration by homogeneously scaling the atomic positions in y direction according to the strain ε and subsequent structural relaxation by energy minimization. The threshold strain ε_0 is defined as the strain at which both configurations exhibit the same average potential energy:

$$E_{pot}^{uncut}(\varepsilon_0) = E_{pot}^{cut}(\varepsilon_0) \tag{3.4}$$

  At the same time, the sample-dependent elastic modulus E_y, which is needed to determine ε_G in Eq. (3.3), is determined from the energy-strain relationship of the defect-free configuration. It can also be used to calculate the sample-dependent predicted critical energy release rate as:

$$G_0 = G(\varepsilon_0) = \frac{1}{2} L_y E_y \varepsilon_0^2. \tag{3.5}$$

  It is important to note, that the precise value of L_y depends on whether the crack tip is supposed to be atomically sharp or blunted. In the first case, L_y has to be chosen such that the number of crystallographic planes in y-direction is even, which ensures that the crack tip lies *between* two atomic layers. When the number of y planes is odd, an atomic layer is located at $y = L_y/2$. In this case, a blunted crack tip is created by removing the atoms in this layer in front of the desired crack tip position before applying the crack-tip displacement field.

- **Strain-controlled quasi-2D central crack.** The quasi-2D central crack setup consists of an elliptical crack of length $2a$ at the center of a quasi-2D simulation box, i.e. at $(L_x/2, L_y/2)$. This setup is shown in Fig. 3.3c. It may be seen as equivalent to the crack originally considered by Griffith [9], which was, however, assumed to be embedded in an infinite body. The crack tip displacement fields are presented in the appendix C. Boundary and loading conditions are the same as for the quasi-2D edge crack. Typical configurations are $L_x \times L_y \times L_z = 1000 \times 1000 \times 2r_{cut}$ Å^3 in size and contain approximately one million atoms.

- **Strain-controlled 3D edge crack.** With the 3D edge crack it is possible to investigate, for example, local reorientation of the crack front and dislocation nucleation on oblique slip planes [155]. Here, the box length L_z is considerably longer than in the quasi-2D setups, see Fig. 3.3d. Boundary conditions, loading conditions, and crack-tip displacement fields are the same as for the quasi-2D edge crack, which are detailed in the appendix C. It should be noted, that the PBCs in z direction are still in use to allow for direct comparison with the other setups. Typical configurations are $L_x \times L_y \times L_z = 1000 \times 1000 \times 1000$ Å^3 in size and contain approximately 84 million atoms.

3.3.2 Setup geometry for penny-shaped cracks

To investigate the fracture behavior of cracks with curved crack fronts, the setup shown in Fig. 3.3e is used. It contains a penny-shaped crack of radius a at the exact center of the fully 3D configuration, i.e., at $(L_x/2, L_y/2, L_z/2)$. Atoms in the outer layer of minimum thickness $2r_{cut}$ are kept fixed during the simulations, where a tensile strain ε is applied along the y direction. The penny-shaped crack is inserted by displacing the atoms in the configuration according to the linear-elastic solution for the displacement field around a penny-shaped crack [393]. The detailed displacements are presented in the appendix C. Typical configurations are $L_x \times L_y \times L_z = 1000 \times 1000 \times 1000$ Å^3 in size and contain approximately 84 million atoms. The calculation of the theoretical Griffith strain ε_G follows Eq. (3.3). The determination of the threshold strain ε_0 and the critical fracture strains ε_c and ε_i takes place in the same manner as described in the next section.

3.3.3 Loading conditions

To address the questions of interest for this thesis, e.g., about bond trapping, it is of fundamental importance to precisely determine the conditions and modes of crack-tip instabilities. After a crack geometry is successfully set up at an initial stress intensity factor K_{in} or strain ε_{in}, the critical conditions are determined by iteratively loading the configuration until the initial structure becomes unstable. The mode of this instability is either the brittle propagation of the crack by bond breaking or the emission of twins or dislocations from the crack tip. The iterative loading of the given atomic structure is performed either quasi-statically (time-independent) or dynamically (time-dependent):

- **Quasi-static loading of *K*-controlled geometry.** For the quasi-static determination of the critical SIF K_{Ic}, an initial configuration has to be found at first. The characteristic feature of this initial configuration is, that the crack tip is located at the exact center of the configuration. For this purpose, different configurations are generated with displacement fields $u_{\mathrm{x,y}}(r, \theta, K_{\mathrm{I}})$ for different K_{I} values, see appendix C. The K_{I} values are chosen to be somewhat lower than the theoretical fracture toughness K_{G} after Griffith [9], see Eq. (2.7). The configuration for the lowest K_{I}, where the crack tip did not move during energy minimization, is then used as initial configuration. The corresponding SIF is denoted as K_{in}. Thereafter, atoms in this configuration are displaced by an incremental deformation field according to $\Delta K_{\mathrm{I}} = 0.0025\sqrt{\pi}\,\mathrm{eV/\AA^{2.5}}$ ($\approx 0.007\ \mathrm{MPa}\sqrt{\mathrm{m}}$) and the so-created structure is subsequently relaxed. This procedure is iteratively applied on each newly obtained minimized configuration until either bond breaking or plastic deformation takes place at the crack tip. K_{Ic} is the K_{I} value at which one of these events occurs.

- **Quasi-static loading of strain-controlled geometries.** Incremental displacement fields are repeatedly applied to the initial configuration, which is subsequently relaxed. Here, the strain that leads to no or only very limited movement of the crack during energy minimization is denoted as the initial strain $\varepsilon_{\mathrm{in}}$. Its value lies typically around the theoretical value for the fracture strain ε_0, see section 3.3. After the initial configuration is obtained, displacements can be either applied by homogeneously scaling the atomic positions according to a given strain or by using the linearly re-scaled (inhomogeneous) displacement field between the relaxed deformed and undeformed configurations. Since the second method makes direct use of the relaxed deformation field, it should in general lead to configurations that are closer to the energy minimum at increased strains. However, it should not be forgotten that the displacements in the vicinity of certain defects, such as cracks or dislocations, might be highly non-linear already at comparably low overall strains. The linear extrapolation of these displacements could therefore result in highly unfavorable situations leading to premature instability of the scaled configuration. For this reason, the homogeneous scaling method represents a more conservative approach and is used in this study unless noted otherwise. Quasi-static methods can only be used to determine the critical strain ε_{c} and nature (ductile or brittle) of the instability.

- **Dynamic loading of strain-controlled geometries.** Atomic positions are homogeneously scaled according to e.g. $\delta\varepsilon$ in each simulation step leading to a strain rate $\dot{\varepsilon} = \delta\varepsilon/\delta t$. For example, the displacement per time step is $\delta\varepsilon = 10^{-7}$ to achieve a strain rate of $\dot{\varepsilon} = 10^{8}\mathrm{s}^{-1}$ with the typical time step for NVE simulations ($\delta t = 1\,\mathrm{fs}$). Dynamic loading can also be used to determine critical loads. Its main purpose is, however, to investigate dynamic processes, such as crack propagation, crack arrest, nucleation of crack tip plasticity, and dislocation motion. The initial configuration is the same as used for quasi-static loading. The critical load obtained in dynamic simulations is symbolized by the fracture initiation strain ε_{i}. The strains at which an initially advancing crack arrests or initiates plasticity are marked by ε_{a} or ε_{e}, respectively.

3.3.4 Lateral straining methods

In uni-axial loading states, attention must be paid to the strains perpendicular to the loading axis. The concepts of plane stress and plane strain [10, 31, 32], which are important in this context, were introduced in section 2.1.1. Since the tensile crack tip stresses exceed the stresses in the remaining configuration by far, the lateral material response depends on whether it belongs to the vicinity of a crack tip, $\sigma_{\mathrm{lat}}^{\mathrm{tip}}$ and $\varepsilon_{\mathrm{lat}}^{\mathrm{tip}}$, or to the remaining configuration, $\sigma_{\mathrm{lat}}^{\mathrm{rem}}$ and $\varepsilon_{\mathrm{lat}}^{\mathrm{rem}}$. Whereas the remaining configuration will generally tend to reduce the lateral stresses, $\sigma_{\mathrm{lat}}^{\mathrm{rem}} = 0$, and to adopt the lateral strains accordingly, $\varepsilon_{\mathrm{lat}}^{\mathrm{rem}} = \nu\varepsilon$, the behavior of the material at the crack tip depends on the exact position along the crack front. At a free surface, the lateral stresses at both the crack tip and the remaining material are allowed to relax, i.e., $\sigma_{\mathrm{lat}}^{\mathrm{tip}} = \sigma_{\mathrm{lat}}^{\mathrm{rem}} = 0$ (plane stress) and $\varepsilon_{\mathrm{lat}}^{\mathrm{tip}} \neq \varepsilon_{\mathrm{lat}}^{\mathrm{rem}}$. In contrast, the lateral crack tip stresses cannot relax in the material's interior ($\sigma_{\mathrm{lat}}^{\mathrm{tip}} \neq \sigma_{\mathrm{lat}}^{\mathrm{rem}} = 0$), where the lateral strains at the crack tip are defined by the strain state of the remaining configuration, i.e., $\varepsilon_{\mathrm{lat}}^{\mathrm{tip}} = \varepsilon_{\mathrm{lat}}^{\mathrm{rem}}$ (plane strain). The latter condition dominates in a bulk material and is clearly more capable to reflect a material's inherent resistance against fracture. For this reason, the plane strain state is commonly used for fracture mechanical testing, see e.g., Ref. [52]. As stated earlier in section 2.1.3, most atomistic studies of fracture do not report on whether and how they accounted for lateral strains. Despite this lack of information, we can think of the following different possibilities:

- **Zero strain method ($\varepsilon^{\mathbf{zero}}$).** Lateral box dimensions are kept fixed independent of the applied strain.
- **Minimum stress method ($\sigma^{\mathbf{min}}$).** Lateral box dimensions are adjusted and atomic positions accordingly re-scaled in such way that the average stresses in the corresponding directions are minimized. This method works well with both molecular statics and dynamics simulations and also accounts for non-linearity effects. Due to the minimization of *average* stresses, on the other hand, the results become size dependent: the smaller the box size, the higher is the contribution of crack tip stresses to the mean stresses in the whole configuration. As a result, the lateral stresses in the non-tip regions deviate from zero.
- **Prescribed strain method ($\varepsilon^{\mathbf{pre}}$).** The calculated Poisson ratios ν_{xy} and ν_{zy} can be directly used to prescribe the (homogeneous) scaling both box dimensions and atomic positions according to $u_{\mathrm{z}} = \nu_{\mathrm{zy}}\varepsilon z$ and $u_{\mathrm{x}} = \nu_{\mathrm{xy}}\varepsilon x$. The disadvantage of this method is that the Poisson ratio is assumed to be independent of the applied strain.

As a result of the scarce information situation on this topic in the literature, it is not clear how these different methods influence the qualitative and quantitative simulation results. To compare these three different methods for lateral straining and to assess their ability to model the plane strain state is therefore one of the goals of this thesis.

3.4 Creation of dislocations and grain boundaries

This section introduces different methods to generate configurations containing dislocations and/or grain boundaries.

3.4.1 Dislocations

To create configurations containing dislocations, a similar two-step strategy is used as for the previously described insertion of cracks: first, an atomic structure is deformed to artificially insert an edge, screw, or mixed dislocations. Second, this configuration is energetically minimized to obtain the dislocation core structure with the lowest energy. Similar to cracks, the following two main techniques for dislocation insertion are distinguished:

- **Application of far-field solution.** The atomic configuration is deformed according to the anisotropic linear-elastic solution for the displacement field around a dislocation core [48]. This allows to determine the dislocation core structure, see e.g. Ref. [259] or to calculate the Peierls barrier, see e.g. Ref. [394].
- **Dislocation between two parallel boundaries.** Atomic planes in a region on one side of the desired slip plane are moved with respect to the other side. For an edge dislocation, the straining direction is perpendicular to both the desired line direction and slip plane normal. This leads to the *removal* or *insertion* of an atomic half plane (HP), respectively. The accumulated relative displacement of the two blocks below and above the slip plane are equal to the Burgers vector $\underline{b}$. For more details on this method, the reader is referred to Ref. [214].

3.4.2 Grain boundaries

The generation of grain boundary structures follows the method detailed in Ref. [94], which is based on the work by Pond and Vítek [242]. Two crystal grains are rotated with respect to each other according to Eq. (2.20) and joined along the GB plane. All GBs studied in this thesis are CSL GBs, which have a periodically repeated structure within the GB plane. This makes it possible to use periodic boundary conditions along the box directions within the GB plane (x and z directions). Thereby the computational costs are reduced, the studied GB structures become reproducible, and the calculated GB energies can in principle be compared to literature data. Free or 2D-dynamic (in the xz-plane) boundary conditions are applied in the outer layers parallel to the GB plane (y direction). The GB structure is optimized in terms of the microscopic degrees of freedom by rigidly translating the two crystals with respect to each other and subsequent energy minimization. During the minimization, atoms are allowed to move only parallel to the GB normal direction. Repetition of this procedure allows to determine the configuration with the overall lowest potential energy. This configuration serves as input structure for a full relaxation (atomic motion in all spatial directions) while also allowing for box size changes in x and z direction. The resulting structure is then used as input configurations for further studies.

3.5 Visualization and analysis

Throughout this study, the Open Visualization Tool (OVITO) by A. Stukowski [395–397] is used for visualizing atomic configurations.

Sometimes it can be appealing to rationalize the results of atomistic simulations in the language of continuum mechanics, i.e., in terms of (per-atom) stresses. Although such continuum interpretations of atomic force fields do not have any physical relevance for single atoms [56], they can be very useful as they allow the measurement of intensity and nature of interactions in the material's interior [398]. In this work, atomic stresses are calculated following the definition of the virial stress [399] normalized by the Voronoi volume of the respective atom [398, 400]. Note that a direct consequence of the Voronoi procedure is that it cannot be applied to surface atoms.

Information about atomic stress distributions are useful to visualize the field character around certain defects. For *identifying* crystallographic defects, they are less helpful. For this reason, special structure analysis algorithms were developed, of which the most common ones are briefly summarized in the following section. Since most of them can primarily be used for fcc crystals [395, 401], I invented a novel method for defect characterization in bcc structures, which will be presented in section 3.5.2.

3.5.1 Structure analysis

The following paragraphs briefly review the basic ideas of the most common methods for structure analysis in crystalline solids.

- **Energy filter.** Only atoms with increased potential energy (typically $E_{\mathrm{pot}} > 0.98E_0$) are displayed [229]. This filtering method makes use of the fact that atoms in the neighborhood of defects are usually in an higher energy state compared to atoms in a perfect bulk configuration. When applied on-the-fly, i.e., at the run time of the simulation, it can also be used to drastically reduce the simulation output data. This method, however, works well only for simulations at low temperatures.

- **Common neighbor analysis (CNA).** Each bond that connects a central atom and its near neighbors is characterized by a set of four characteristic numbers $ijkl$ [396, 402]. These numbers depend on whether the atoms are nearest (1) or next-nearest (2) neighbors (i), the number of near neighbors that they have in common (j), the number of bonds among these common neighbors (k), and the number of bonds in the longest continuous chain of bonds connecting the common neighbors (l). It is important to note that atoms are treated as near neighbors, which are consequently connected by bonds, if they are within a certain distance of each other. In fcc structures (characterized by a CNA number of 1421) this distance lies between the first and the second nearest neighbors and thus only bonds between nearest neighbors are counted. For bcc structures, however, also second nearest neighbors are taken into account and the cutoff distance should lie between the second and the third neighbor shell. A bcc environment is then characterized by eight nearest neighbor

bonds having a CNA number of 1666 and six next-nearest neighbor bonds with a CNA number of 2444. With the adaptive common neighbor analysis (a-CNA) implemented in OVITO the optimal cutoff radius for each particle is automatically identified [396].

- **Coordination number (CN).** The number of atoms within a given cutoff distance is counted. This distance typically lies between the nearest (nn) and second nearest neighbor (nn2) distance to count only nearest neighbor atoms. Using a cutoff radius between the second and third nearest neighbor distance can increase the sensitivity of this characterization method particularly for bcc metals, where the inclusion of second nearest neighbor interactions is important for the correct description of the material's behavior [403]. Atoms that have the coordination of the corresponding perfect host lattice (CN(nn) = 8 or CN(nn2) = 14 for bcc) are usually not shown in the visualization of defects. This method is, however, unable to identify twinned structures or screw dislocation cores, where the number of neighboring atoms does not change compared to the perfect crystal.

- **Centrosymmetry parameter (CSP).** The difference of the vectors pointing to opposite nearest neighbor pairs are summed [404]. In this manner, the local lattice distortion around an atom can be characterized. For a perfect bulk structure all vectors cancel out and the CSP is zero, but whenever the symmetry around an atom is broken, e.g., in presence of a vacancy or a surface, it takes on values larger than zero. A necessary input parameter for this analysis is the number of nearest neighbors in the host lattice. The CSP is a useful characterization method to detect typical defects in the bcc lattice, e.g., twins, vacancies, and dislocations, but not necessarily to distinguish them uniquely.

3.5.2 BCC Defect Analysis

Fig. 3.4 gives an overview of the aforementioned characterization methods for typical crystallographic defects in bcc metals: a single vacancy, perfect $a_0/2[1\bar{1}1]$ edge and screw dislocation, (112) twin boundary, and four low-index surfaces. Planar faults of $s/2[1\bar{1}0](110)$ type, where $s \approx 1/3$, are included in this overview since various EAM potentials for bcc metals predict deformation by this defect type [122]. It can be clearly seen that none of the presented methods is able to uniquely distinguish between these defects. As stated earlier,most of these algorithms were developed for face-centered cubic (fcc) crystals [395, 401] and only few methods are specifically adapted to the identification of defects in body centered cubic (bcc) crystals. An unambiguous, automatized classification of bcc crystal defects is of particular importance as large-scale atomistic simulations are increasingly used to study specific aspects of bcc plasticity [405], dislocation-defect interactions [406], and fracture [164].

For this reason, I developed a new method for analyzing atomistic configurations of bcc metals, the BCC Defect Analysis (BDA). The following description of the BDA has been published in Ref. [407]. The BDA uses the results of the aforementioned CN, CSP, and CNA

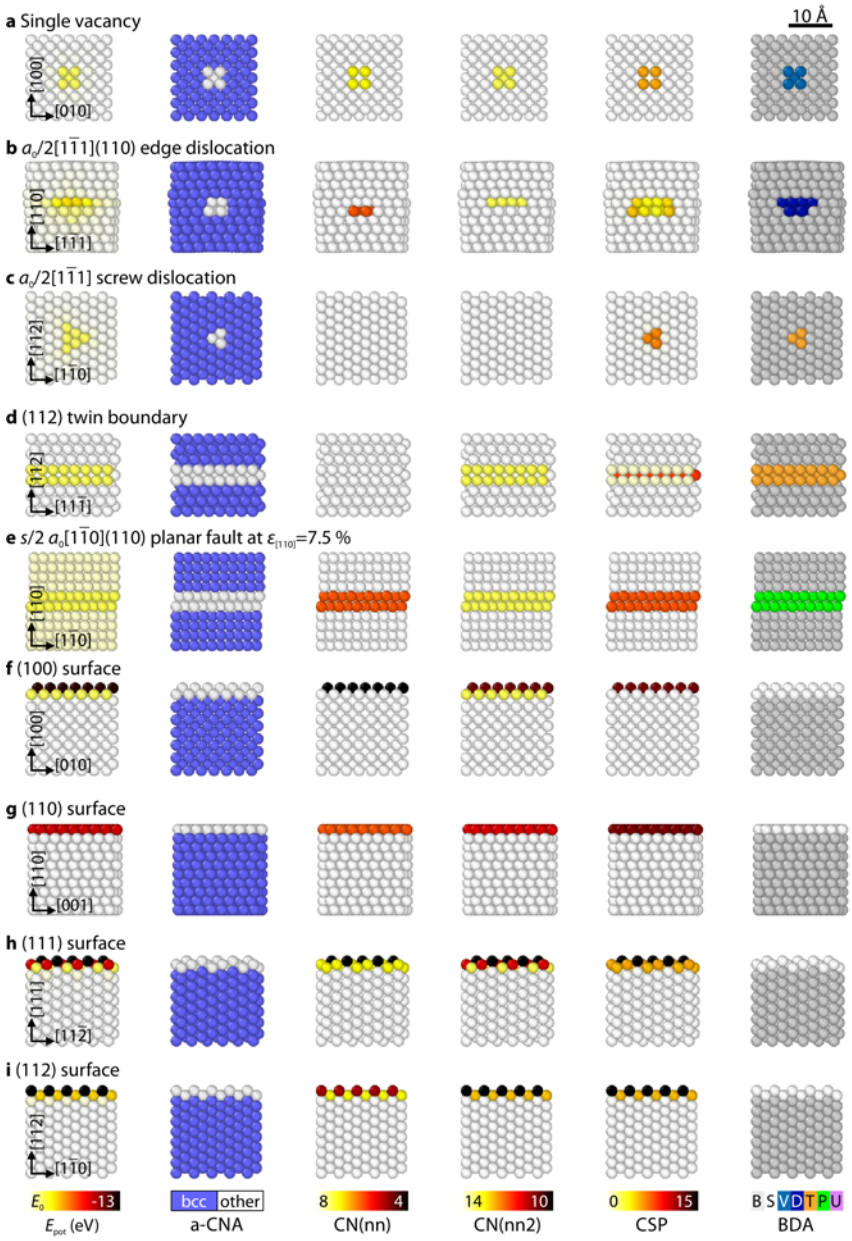

Figure 3.4: Overview of typical crystallographic defects in bcc metals as identified by different characterization methods: E_{pot} filtering, a-CNA [396], CN including first (nn) and second nearest neighbors (nn2), CSP [404], and the newly developed bcc defect analysis (BDA); note the following abbreviations in the color scheme of the BDA: B: bulk, S: surface, V: vacancy; D: (non-screw) dislocation, T: (112) twin and screw dislocation, P: (110) planar fault, U: unidentified; the Chiesa potential for Fe was used here.

techniques to identify defects that are typical for bcc crystals. The first step within the BDA approach is to analyze all atoms in a given configuration with the CN, CSP, and CNA techniques. Here, it is noteworthy that the cutoff radius for the CN is $r_c = (1+\sqrt{2})/2a_0$ with a_0 being the lattice parameter. Since the six next-nearest neighbors of perfect bcc atoms are within this cutoff distance, their CN increases from 8 to 14. Then, the CN and CSP values of each atom, which is not in a bcc environment according to the CNA or has a CN of 14, are compared to empirically determined values for the following typical defects: surfaces, vacancies, twins, screw dislocations, $\{1\,1\,0\}$ planar faults, and edge dislocations. The criteria for this pre-characterization are presented in the first three columns of Table D.1 in the appendix.

The novelty of the BDA method is that not only the atom itself, but also each of its neighbors is evaluated against characteristic defect criteria. To this end, all atoms within the cutoff distance are classified according to their values of CN and CSP. Neighbor atoms in a perfect bcc environment rank among the number of perfect neighbor atoms, N_p. The non-perfect neighbor atoms are compared to a number of different criteria, see the columns no. 5-9 in Table D.1 in the appendix. If a neighbor atom fulfills a criterion, i.e., a certain combination of CN and CSP, the number N_d is increased for the respective criterion. If the occurrences of N_p and N_d match the characteristic occurrences for a defect, this defect is assigned to the atom. If not, the atom and its neighbors are evaluated against the criteria for the next defect in Table D.1 in the appendix. This comparison is performed for all non-bcc atoms in the configuration. To minimize the number of erroneously identified defects, every identified defect is then compared to its neighboring defects and is flagged as 'unidentified' if it is not representing the relative majority among its neighbors. In the final step, all unidentified atoms are assigned to the predominant defect in their neighborhood. As a result, the number of unidentified defects is reduced by repeating this comparison until the number of unidentified defects is smaller than a threshold value or does not change upon further repetition. This step is optional, but recommended, since it homogenizes the resulting output data.

The BDA method is currently implemented as a Python script for OVITO's scripting interface [397] and is available as an open-source tool [408] under the GNU General Public License (GPL) v3. More detailed information, an application example, and comments on the usability of the BDA at high temperatures are provided in the appendix D.

Evaluated defect structures

To identify the typical values of common bcc defects for both coordination number and centrosymmetry, see Table D.1 in the appendix, a number of different ideal (in an energetic minimum) and excited systems (during dynamic simulations starting at $T = 0$ K) were evaluated. The configurations contained the following known defects: $(1\,0\,0)$, $(1\,1\,0)$, $(1\,1\,1)$, and $(1\,1\,2)$ surfaces, mono- and di-vacancies as well as vacancy rows, twin boundaries on $\{1\,1\,2\}$ planes, planar faults on $\{1\,1\,0\}$ planes, screw dislocations, and edge dislocations on $\{1\,1\,0\}$ and $\{1\,1\,2\}$ planes. Fig. 3.4 gives an overview of most of the different defects as identified with the aforementioned characterization methods and the new BDA method.

The figure presents the defects as obtained with the Chiesa potential [220, 221] for Fe. As different potentials can show different defect structures [122], selected simulations were performed and analyzed using the Mendelev-II [225] and Chamati [227] potentials for Fe. The following paragraphs summarize the most important subtleties and issues that occurred during the characterization of the defects.

- **Vacancies.** Atoms in the vicinity of a mono-vacancy, see Fig. 3.4a, are missing one neighbor and thus exhibit a coordination of 13. Such an under-coordinated state, as we will see later, is also common to most other defects. For this reason, the centrosymmetry parameter is used here as additional indicator. Nearest neighbors to a vacancy exhibit a relatively high CSP, for which a value of 4 was found as a good lower limit. Next-nearest neighbors, which are also 13-coordinated, have comparably low CSP values lower than unity. For di-vacancies and vacancy rows, the characterization has to additionally account for 12-coordinated atoms, but the CSP thresholds of mono-vacancies are still valid.

- **Edge dislocations.** Unlike near vacancies, atoms in the vicinity of edge dislocations exhibit less well-defined characteristics. Especially under dynamic and 3D conditions, the dislocation structure is not as simple as the static structure of a pure edge dislocation shown in Fig. 3.4b. When the dislocation moves, for instance, it is spread out over some atomic distances on its glide plane and a variety of CNs are frequently observed ranging from 12 to 15. Further characterization according to the CSP was difficult as the determined values highly depended on the used interatomic potential. It turned out that there is a high possibility for the presence of a (non-screw) dislocation if the number of non-14-coordinated neighbors is higher than the number of 14-coordinated neighbors. Since this criterion is relatively weak, it is important to note, that the (non-screw) dislocation is the *last* defect type, which is tested in the BDA approach, see Table D.1. That means, if all other criteria do not apply, the given defect structure can only be a (non-screw) dislocation or an unknown defect. As a consequence, the tips of twins and planar faults are frequently identified as (non-screw) dislocations. Since these tips generally consist of partial dislocations, the identification as 'dislocation' is of course not wrong per se. It has to be noted in this context, that some tilt grain boundaries in Fe and W exhibit similar characteristics as (non-screw) dislocations. This observation is interesting since the relative tilt rotation of two grains can always be expressed by the accumulation of many dislocations [241]. Both defect types can, however, still be differentiated since grain boundaries are planar and dislocations are linear defects. This double identification does therefore not limit the applicability of the BDA method. This limitation of the BDA method can be overcome by using more advanced and computationally more expensive methods, such as the *Crystal Analysis Tool* [409].

- **Screw dislocations.** Screw dislocations are treated separately from edge dislocations for two reasons: first, screw dislocations can easily cross slip and therefore have a generally different glide behavior as compared to edge dislocations. As a result, it

is appealing to directly find them in a given configuration. Second, their line direction corresponds to the shearing direction to produce a deformation twin. For this reason, it was not possible to distinguish their characteristics from those of twin boundaries. Dislocations are, however, line defects and can thus easily be differentiated from the planar twin structures by comparing the defects' dimensionalities. Unlike around edge dislocations, atoms in the neighborhood of screw dislocations are generally not under-coordinated, see Fig. 3.4c. Instead, they exhibit a coordination of 14 and have a relatively high number of 14-coordinated neighbors, which are not identified as bcc by the CNA.

- **Twin boundaries.** Twin boundaries contain both 13- and 14-coordinated atoms, see Fig. 3.4d. Two main issues significantly complicate their unique identification: first, the precise twin boundary structure determined with different interatomic potentials frequently differs from the ideal one shown in the figure. Second, in dynamically evolving structures, $a_0/6\langle 111\rangle$ twinning dislocations glide on existing twin boundaries. Twinning dislocations are often detected as bcc by the CNA and characterized by a comparably high CSP (>8), but less than 9 perfect bcc neighbors. Atoms within the twin boundary close to such a twinning dislocation, are missing one neighbor atom and have either a low CSP (<1) but four 14-coordinated neighbors with CSP larger than 8 or a relatively high CSP (>4.5) and fixed numbers of perfect, 13-, and 14-coordinated neighbors.

- **{110} Planar faults.** Planar faults of $s/2[1\bar{1}0](110)$ type, where $s \approx 1/3$, are included in the list of known defects since many EAM potentials for bcc metals predict their formation [122]. Their occurrence is, however, limited to highly stressed areas, e.g., in the close vicinity of a crack tip—even under fully three-dimensional conditions [201]. The planar fault presented in Fig. 3.4e is therefore shown for an applied tensile strain of $\varepsilon_{[110]} = 7.5\,\%$. Planar faults are 13-coordinated at the boundary layer between the fault and the perfect lattice and 12-coordinated in the interior of the defected region. Similar to twin boundaries, further complications arise due to the glide of partial dislocations of $s/2[1\bar{1}0]$ type on the existing fault. It should finally be noted, that the existence of planar faults is most probably due to an artificial minimum in the generalized stacking fault energy surface of many EAM potentials under applied tensile strains [122].

- **Surfaces.** The surface structures of (100), (110), (111), and (112) surfaces are shown in Fig. 3.4f-i. Since the bcc lattice is not a dense-packed structure, even these low-index surface planes do not exhibit unique coordination numbers, as e.g., low-index surfaces up to the (111) plane in the fcc structure. Here, the (110) surface is the only exception, see Fig. 3.4g, which exhibits a unique CN value of 10. For a correct identification of an atom sitting at a surface, it is sufficient, if the atom's CN is lower than 12 *or* if it has more than three neighbors, which fulfill this criterion while being under-coordinated itself.

4 Cracks with straight and curved crack fronts in defect-free single crystals

This chapter presents the fracture properties of straight and curved cracks in defect-free bcc single crystals: (i) the fracture behavior, i.e, brittle bond breaking, dislocation emission, or twin formation; (ii) the critical loading condition for the observed fracture event, i.e., the fracture toughness K_{Ic} in the K-controlled geometry, see Fig. 3.3a, or the critical fracture strains ε_{i} (for dynamic loading) and ε_{c} (for quasi-static loading) in the strain-controlled geometries, see Fig. 3.3b-e. The values for K_{Ic} were determined as described in section 3.3.3 and compared to the theoretical critical stress intensity factors for brittle fracture K_{G}, dislocation emission K_{e}, and twin formation K_{t} as calculated with Eqs. (2.7), (2.15), and (2.31), respectively. For purely brittle fracture, the lattice trapping range ΔK [97] was additionally determined, cf. Eq. (2.18). The determination of ε_{i} and ε_{c} is described in section 3.3.3. Similarly to K_{G}, the theoretical fracture strain ε_{G} was calculated according to the Griffith criterion, cf. Eq. (3.3). The determination of the sample-dependent threshold strain ε_0 is described in section 3.3.1 for the quasi-2D edge crack, cf. Eq. (3.4), but generally applies to all strain-controlled cracks. For comparison, an analogous lattice trapping range $\Delta\varepsilon = \varepsilon^{+}/\varepsilon^{-} - 1$ was determined for selected strain-controlled cracks with $\varepsilon^{+} = \varepsilon_{\mathrm{c}}$ and ε^{-} being the necessary strain for crack closure.

To determine the general influence of the interatomic potential and their equilibrium properties on the fracture properties, the fracture behavior and toughness of different EAM potentials for Fe and the bcc refractory metals V, Nb, Ta, Cr, Mo, and W were determined using the K-controlled setup for infinitely long and straight cracks in the common crack systems on the lowest-energy $\{1\,0\,0\}$ and $\{1\,1\,0\}$ planes of all bcc crystals. Crack systems are written in the (crack plane)[crack front] notation, i.e., as $(\ldots)[\ldots]$ or more general as as $\{\ldots\}\langle\ldots\rangle$ representing the whole family of crack systems.

The influence of crack front curvature as well as the dynamic and quasi-static crack propagation behavior on the $(1\,0\,0)$, $(1\,1\,0)$, $(1\,1\,1)$, and $(\bar{1}\,1\,1)$ planes is exemplarily shown for the Chiesa, Mendelev-II, and Chamati potentials for Fe using the different strain-controlled setups presented in section 3.3. The potentials were selected because they best agree with experimental data and usually do not exhibit unexpected deformations in the highest stressed regions at the crack tip. To determine the influence of the different variables introduced in section 2.1.3, the $(1\,1\,0)[1\bar{1}\,0]$ crack system and the Chiesa potential were selected; this combination of crack system and interatomic potential is a good model system as it showed ideally brittle crack propagation in the K-controlled setup under quasi-static loading conditions.

Under dynamic loading conditions, elastic waves are emitted by the rupture of crack-tip bonds and subsequently reflected by the fixed boundary layers. Upon their returning,

the reflected waves can cause nonphysical effects at the crack tip. For this reason, only events before the reflected wave reached the crack tip are described, cf. Eq. (2.12). Similarly, processes of crack-tip plasticity are only described until the emitted dislocations or twins have reached the fixed boundaries.

In the following, the results for cracks in defect-free bcc single crystals are described separately for the different crack planes. In each section, the results for K-controlled cracks are presented first, followed by the results for straight and curved strain-controlled cracks. The described crack-tip events are additionally visualized for selected Fe potentials, which represent the behavior of the remaining potentials. Most results for K-controlled and strain-controlled penny-shaped cracks in Fe have been published in Ref. [122] and [201], respectively. An overview of available slip systems for straight and curved cracks is given in the appendix A.

4.1 Cracks on {100} planes

Independent of element and potential, cracks on the $\{1\,0\,0\}$ planes showed brittle fracture in the quasi-static K-controlled setup. However, with the vast majority of the studied potentials, planar faults formed on the 45°-inclined $(1\,1\,0)$ and $(\bar{1}\,1\,0)$ planes at crack tips in the $(1\,0\,0)[0\,0\,1]$ crack system prior to the brittle kinking of the crack onto one of these planes. For straight cracks under strain control, the overall fracture behavior is similar among the different potentials; the only exception was the occurrence of crack tip plasticity under dynamic conditions for $\langle 1\,1\,0\rangle$ crack front directions. Plastic deformation behavior was even more pronounced for penny-shaped cracks, which initiated planar faults and deformation twins thereby sometimes even changing their geometrical crack shape. The detailed descriptions of the observed fracture processes and effects are given in the following subsections.

4.1.1 K-controlled setup: Cleavage and crack kinking

The results for K-controlled cracks on the $(1\,0\,0)$ plane are given in Table 4.1 for Fe and in Table 4.2 for the remaining bcc metals. Independent of crack front direction and interatomic potential, cracks on the $(1\,0\,0)$ plane showed brittle fracture behavior, see Fig. 4.1 for the Mendelev-II, Chamati, Gordon, and Marinica11 potentials. The crack paths, however, varied markedly. For the $[0\,1\,1]$ crack front direction, all potentials showed crack propagation along the initial $(1\,0\,0)$ plane. For the $[0\,0\,1]$ crack front direction, on the other hand, the observed crack path strongly depended on the used potential. The vast majority of the potentials showed the departure of the crack from the original $(1\,0\,0)$ plane onto an inclined $\{1\,1\,0\}$ plane. This is shown in Fig. 4.1e for the Gordon potential as a representative example for the MFS and Simonelli potentials. From the other bcc potentials, all ATFS potentials and the Smirnova potential showed the same behavior. In case of the Mendelev-II potential (which showed the same behavior as the Chiesa potential), the crack initially stayed on the $(1\,0\,0)$ plane, but kinked out onto the inclined $(1\,1\,0)$ plane when K_I

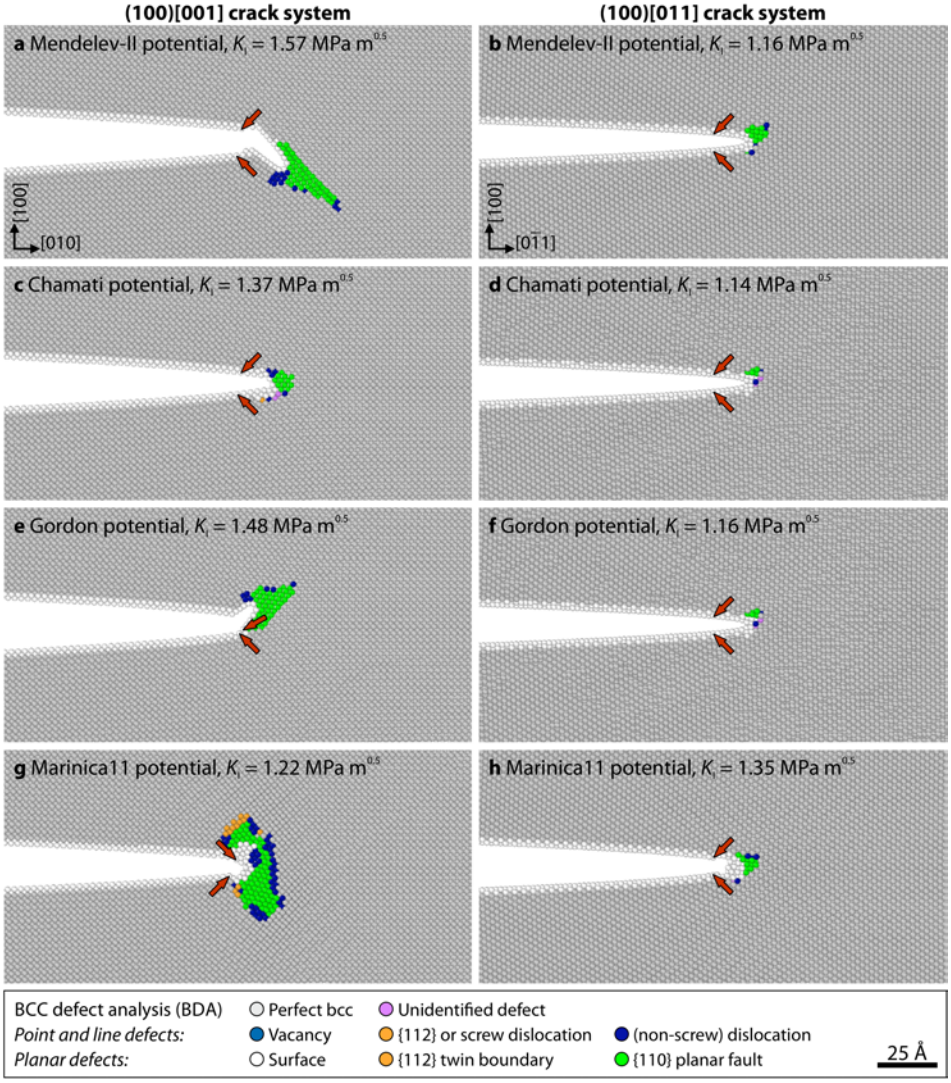

Figure 4.1: Fracture behavior of cracks on the (100) plane under quasi-static K-controlled loading for selected Fe potentials. **a,b**: Mendelev-II potential; **c,d**: Chamati potential; **e,f**: Gordon potential; **g,h**: Marinica11 potential; right subfigures: [011] crack front direction, brittle fracture behavior on the original (100) plane; left subfigures: [001] crack front direction, potential-dependent crack path either on the original (100) plane (**c**), on an inclined {110} plane (**a**,**e**), or on no clear crystallographic plane (**g**); note that the departure of the crack onto {110} planes was preceded by the formation of {110} planar faults; the Marinica11 showed structural transformations at the crack tip for both crack front directions (**g**,**h**). Red arrows mark the position of the original crack tip atoms.

was further increased, see Fig. 4.1a. Only the crack modeled with the Chamati potential propagated on the initial (1 0 0) plane, see Fig. 4.1c. Similar behavior was observed for the FS potential for Cr and the Wang potential for W. In this context, it is interesting to note that the crack kinking onto {1 1 0} planes was preceded by planar defect structures on adjacent {1 1 0} planes. This is indicated by the BDA, as shown in Fig. 4.1a,e. The Marinical1 potential (which showed a similar behavior to the Marinica07 potential) exhibited structural transformations ahead of the crack tip for both (1 0 0) crack systems, see Fig. 4.1g-h: here, the crack created a fracture surface which could not be assigned to a distinct crystallographic plane. Extensive structural transformations with brittle fracture on no clear crystallographic plane were also found for both Ackland potentials for Mo and W.

For all potentials, K_{Ic} was higher for the [0 0 1] crack front direction than for the [0 1 1] direction. For Fe, cracks with [0 0 1] crack front direction showed K_{Ic}-values around 1.34 MPa$\sqrt{\text{m}}$. Only the values of the Simonelli and Marinica11 potentials were more than 10 % lower. The average value for the [0 1 1] crack front direction was 1.08 MPa$\sqrt{\text{m}}$. Here, only

Table 4.1: Summary of simulation results for cracks on {100} planes in Fe. K-controlled cracks: K_{Ic}: critical stress intensity factors; ΔK: lattice trapping ranges for brittle fracture; K_G, K_e, K_t: theoretical fracture criteria; all values for stress intensity factors are in MPa$\sqrt{\text{m}}$. Strain-controlled cracks: ε_i: critical strain for dynamic loading; ε_c: critical strain for quasi-static loading; ε_0: sample-dependent critical strain; ε_G: theoretical Griffith strain, see Eq. (3.3); strain rate in dynamic simulations: $\dot{\varepsilon} = 10^8$ s^{-1}; incremental straining step size in quasi-static simulations: $\delta\varepsilon = 0.025$ %; lateral straining method: $\sigma^{\min}$.

***K*-controlled cracks (quasi-statically loaded)**						
Potential	K_{Ic}	ΔK	K_G	K_e	K_t	Fracture behavior
(100)[001] crack system						
MFS	1.37	0.92	0.92	1.63	—	(1$\bar{1}$0) planar faults (PFs) precede (1$\bar{1}$0) cleavage
Simonelli	0.98	0.16	0.82	1.38	—	(1$\bar{1}$0) PFs precede (1$\bar{1}$0) cleavage
Chamati	1.24	0.28	1.02	1.38	—	Brittle on (100) plane
Mendelev-II	1.39	0.81	0.87	1.31	—	(110) PFs, then (100) cleavage (kinked onto (110) plane)
Gordon	1.35	0.59	0.95	1.44	—	(1$\bar{1}$0) PFs, then (1$\bar{1}$0) cleavage
Marinica07	1.27	0.77	0.99	1.47	—	Crack tip transformations, brittle on no specific plane
Marinica11	1.09	0.67	0.86	1.57	—	Crack tip transformations, brittle on no specific plane
Chiesa	1.39	0.88	0.92	1.55	—	(110) PFs, then (100) cleavage (kinked onto (110) plane)
(100)[011] crack system						
MFS	1.11	0.29	0.95	2.00	1.81	Brittle on (100) plane
Simonelli	0.92	0.09	0.85	1.70	1.46	Brittle on (100) plane
Chamati	1.07	0.04	1.06	1.63	1.60	Brittle on (100) plane
Mendelev-II	1.05	0.28	0.91	1.62	1.54	Brittle on (100) plane
Gordon	1.07	0.15	0.99	1.71	1.62	Brittle on (100) plane
Marinica07	1.02	0.23	1.03	1.78	1.71	Crack tip transformations, brittle on (100) plane
Marinica11	1.17	0.60	0.90	1.73	1.75	Crack tip transformations, brittle on (100) plane
Chiesa	1.21	0.44	0.95	1.92	1.83	Brittle on (100) plane

Continued on next page

Continued from previous page

Quasi-2D edge cracks on the (010) plane with $a \approx 1000$ Å								
Potential	L_x (Å)	L_y (Å)	Crack tip	Loading	$\varepsilon_{i,c}$ (%)	ε_0 (%)	ε_G (%)	Behavior
(010)[001] crack system								
Chamati	3018.0	1004.6	sharp	dynamic	3.65	2.81	2.76	Brittle
Chamati	3018.0	1003.1	blunted	dynamic	3.19	2.81	2.76	Brittle
Mendelev-II	3006.7	1000.8	sharp	dynamic	3.94	2.31	2.25	Brittle[a]
Mendelev-II	3006.7	1000.8	sharp	quasi-static	4.14	2.31	2.25	Brittle[a]
Mendelev-II	3006.7	999.4	blunted	dynamic	3.06	2.31	2.25	Brittle[a]
(010)[101] crack system								
Chamati	3003.5	1004.6	blunted	dynamic	3.21	2.80	2.70	Dislocation[b]
Mendelev-II	3000.3	1003.1	sharp	dynamic	2.98	2.32	2.25	Brittle[c]
Mendelev-II	3000.3	1000.8	sharp	quasi-static	2.96	2.32	2.25	Brittle[d]
Mendelev-II	3000.3	999.4	blunted	dynamic	3.32	2.32	2.25	Brittle[c]
Penny-shaped cracks on the (010) plane with $a = 100$ Å and $L_z \approx L_x$								
Potential	L_x (Å)	L_y (Å)	Crack tip	Loading	ε_i (%)	ε_0 (%)	ε_G (%)	Behavior
Chamati	816.8	1011.7	blunted	dynamic	5.32	4.46	2.58	Twins
Mendelev-II	813.8	1006.5	sharp	dynamic	4.89	4.15	2.19	Twins[a]
Mendelev-II	813.8	1007.9	blunted	dynamic	4.88	4.15	2.19	Twins[e]
Mendelev-II	813.8	2003.0	sharp	dynamic	4.88	4.08	1.56	Twins[a]

[a] Preceded by formation of {110} planar faults
[b] Emission of dislocations on {112} planes
[c] Followed by twin formation
[d] Followed by formation of {110} planar faults
[e] Preceded by limited formation of {110} planar faults

the Simonelli and the Chiesa potential exhibited values which were more than 10 % lower and higher, respectively. From the other bcc potentials, Nb showed the lowest K_{Ic} values for each crack front direction, followed by V, Ta, and Cr. On average, the potentials for Mo exhibited the highest values (1.91 MPa$\sqrt{\text{m}}$), followed by the W potentials (1.86 MPa$\sqrt{\text{m}}$). The only exception in the ordering occurred for the $[0\,1\,1]$ crack front direction, where K_{Ic} was higher for Cr than for the ATFS potential for Mo. For both directions, the average values for Fe were higher than for Ta and lower than for Cr and Mo. To calculate the average K_{Ic} values, both Ackland potentials were excluded as they showed extensive structural transformations at the crack tip leading to abnormal high critical stress intensity factors.

4.1.2 Strain-controlled straight cracks: Crack-tip plasticity under dynamic conditions

The results for strain-controlled quasi-2D edge cracks, see Fig. 3.3b for the setup geometry, are given in Table 4.1. The simulation box contained approximately 4.2 million atoms with a cross section of $L_x \times L_y \approx 3000 \times 1000$ Å^2 and a crack length of $a \approx 1000$ Å. Selected simulation parameters were varied to exclude spurious effects and for comparison with future simulations of penny-shaped cracks on the same plane. These parameters were the

Table 4.2: Summary of simulation results for K-controlled cracks on {100} planes for various bcc potentials. Symbols and units as in Table 4.1.

Element	Potential	K_{Ic}	ΔK	K_G	K_e	K_t	Fracture behavior
			(100)[001] crack system				
V	ATFS	0.97	0.77	0.72	1.15	—	Brittle, kinking on {110} plane
Nb	ATFS	0.94	0.71	0.72	1.07	—	Brittle, kinking on {110} plane
Ta	ATFS	1.24	0.61	0.97	1.52	—	Brittle, kinking on {110} plane
Cr	FS	1.57	0.47	1.07	1.57	—	Brittle on (100) plane
Mo	ATFS	1.74	0.64	1.24	2.07	—	Brittle, kinking on {110} plane
Mo	Ackland	3.45	8.53	1.37	2.79	—	Brittle, crack tip transformations
Mo	Smirnova	2.36	0.47	1.73	2.98	—	Brittle, kinking on {110} plane
W	ATFS	2.09	0.38	1.61	2.40	—	Brittle, kinking on {110} plane
W	Ackland	3.37	0.98	1.64	3.36	—	Brittle, crack tip transformations
W	Wang	1.95	0.38	1.63	2.52	—	Brittle on (100) plane
			(100)[011] crack system				
V	ATFS	0.75	0.18	0.72	1.27	1.68	Brittle
Nb	ATFS	0.71	0.12	0.71	1.14	1.06	Brittle
Ta	ATFS	1.02	0.12	0.98	1.78	2.07	Brittle
Cr	FS	1.41	0.08	1.06	1.63	1.95	Brittle
Mo	ATFS	1.37	0.28	1.23	2.19	2.00	Brittle
Mo	Ackland	2.25	1.03	1.36	3.03	2.66	Brittle
Mo	Smirnova	2.17	0.32	1.73	3.17	3.17	Brittle
W	ATFS	1.71	0.19	1.61	2.64	2.29	Brittle
W	Ackland	2.95	0.70	1.64	3.68	4.13	Brittle, crack tip transformations
W	Wang	1.68	0.05	1.63	2.79	2.48	Brittle

loading conditions, crack tip sharpness, and interatomic potential. The Mendelev-II and Chamati potentials were chosen since they showed significantly different crack paths in the K-controlled setup, cf. Fig. 4.1a and c.

Fig. 4.2 compares the crack tip configurations for the $(0\,1\,0)[0\,0\,1]$ and $(0\,1\,0)[1\,0\,1]$ crack systems. In case of the Mendelev-II potential, planar faults emerged from $[0\,0\,1]$-oriented crack fronts on both 45°-inclined $(1\,1\,0)$ and $(1\bar{1}\,0)$ planes in $\langle 1\bar{1}\,0\rangle$ directions. This behavior was independent of the loading conditions, cf. Fig. 4.2a and c. Planar faults were also formed at the blunted crack tip, see Fig. 4.2e, but only on the $(1\,1\,0)$ plane. When the Chamati potential was used, similar defect structures formed, but very limited to the vicinity of the crack tip and not on clear $\{1\,1\,0\}$ planes, see Fig. 4.2g.

At the $[1\,0\,1]$ crack front, the crack propagated in a brittle manner in case of the Mendelev-II potential. This behavior was independent of loading conditions, cf. Fig. 4.2b and d, and crack tip blunting, cf. subfigures d and f. Under dynamic conditions, a deformation twin formed after initial brittle propagation, see subfigures d and f. Under quasi-static conditions, planar defect structures were created that were similar to the $\{1\,1\,0\}$ planar faults observed for $[0\,0\,1]$ crack fronts. In case of the Chamati potential, neither propagation nor twin formation was observed. Instead, the crack tip emitted mixed dislocations on the $(1\,2\,\bar{1})$ and $(1\bar{2}\,\bar{1})$ planes, see Fig. 4.2h.

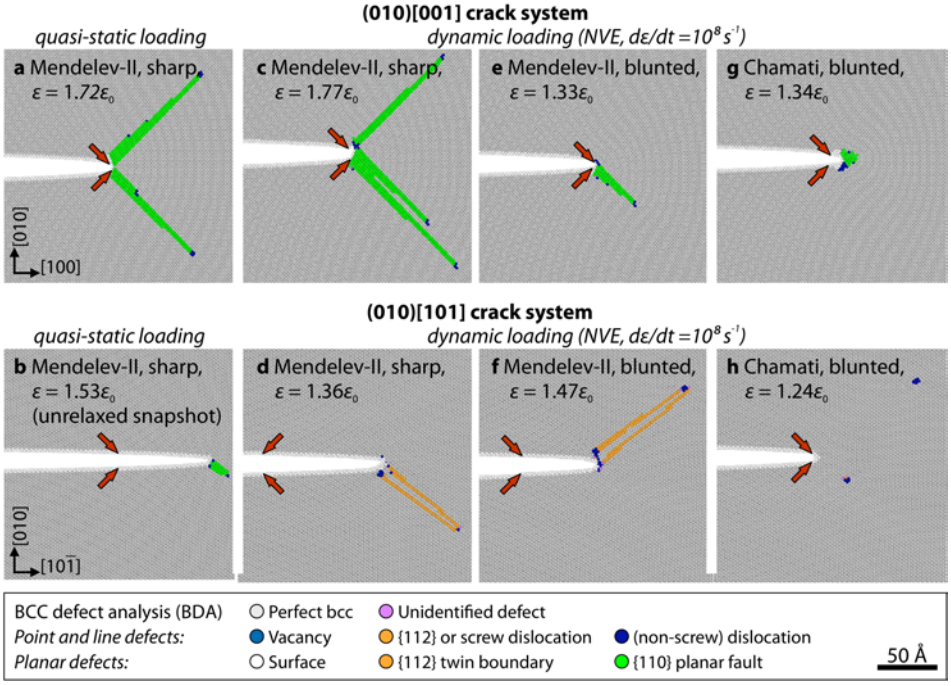

Figure 4.2: Fracture behavior of cracks on the (010) plane in Fe in the strain-controlled quasi-2D edge crack setup ($a \approx 1000$ Å). **a**,**b**: Mendelev-II potential, quasi-static loading, atomically sharp crack tip; **c**,**d**: Mendelev-II potential, dynamic ($\dot{\varepsilon} = 10^8$ s^{-1}), sharp crack tip; **e**,**f**: Mendelev-II potential, dynamic ($\dot{\varepsilon} = 10^8$ s^{-1}), blunted crack tip; **g**,**h**: Chamati potential, dynamic ($\dot{\varepsilon} = 10^8$ s^{-1}), blunted crack tip. [001] crack front direction: planar fault formation and brittle crack-tip events; [101] crack front direction: brittle propagation (Mendelev-II potential, quasi-static loading), twin formation (Mendelev-II, dynamic), or dislocation emission (Chamati, dynamic). Note that an unrelaxed snapshot is shown in **b**, where the visible crack tip transformation was erroneously detected as $\{110\}$ planar fault instead of a small $(12\bar{1})$ twin; red arrows: original crack tip atoms.

4.1.3 Strain-controlled penny-shaped cracks: Crack tip plasticity

Penny-shaped cracks on the (010) plane were studied using the Mendelev-II and Chamati potentials for Fe since both showed significantly different crack-tip responses in case of cracks with straight crack fronts on this plane as shown in the preceding subsections. The results are shown in Table 4.1. The simulation box contained approximately 57 million atoms with a box size of $L_x \times L_y \times L_z \approx 800 \times 1000 \times 800$ Å^3 and a crack radius of $a = 100$ Å. The evolution of the crack tip plasticity in case of the Mendelev-II potential is shown in Fig. 4.3a and b for an atomically sharp and blunted crack, respectively. Fig. 4.3c shows the characteristic configuration for the Chamati potential.

Independent of crack tip sharpness and potential, the initial plastic event was always the formation of half-lenticular shaped deformation twins by emission of $a_0/6\langle 111\rangle$ twinning

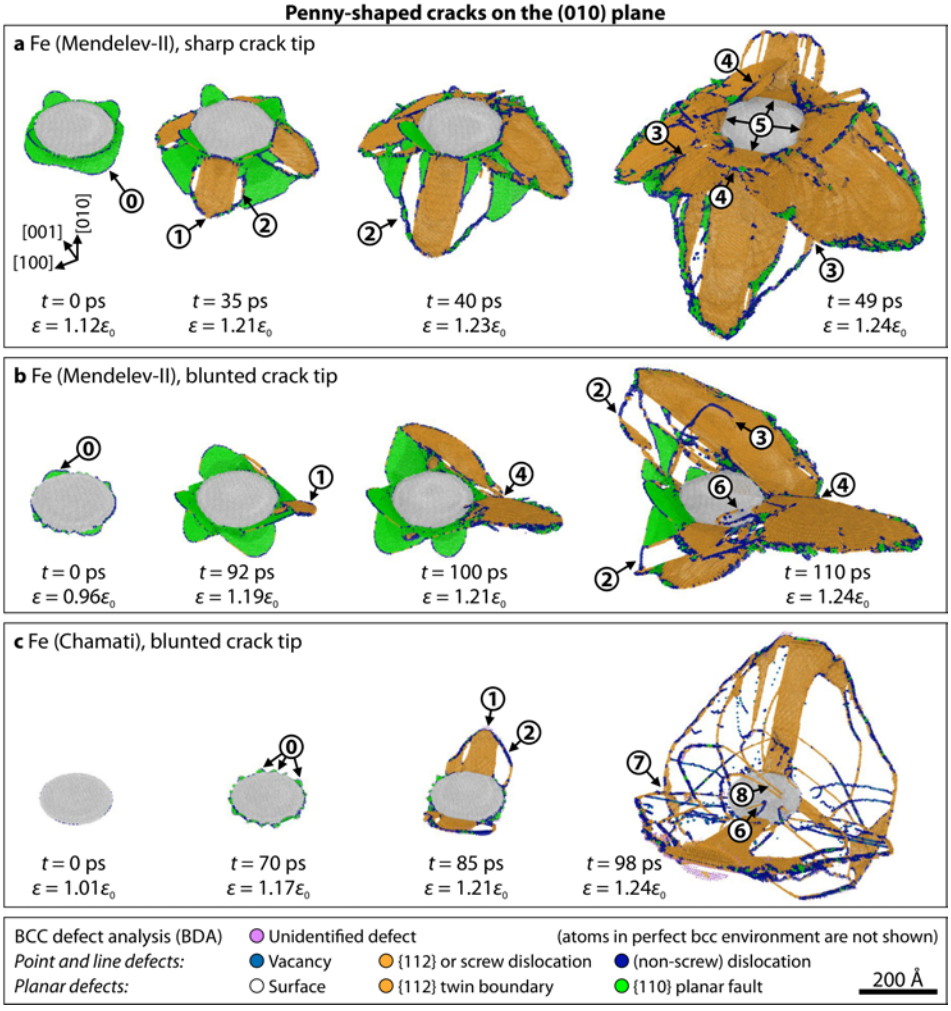

Figure 4.3: Crack tip plasticity of penny-shaped cracks on the (010) plane in Fe (L_y = 1000 Å; a = 100 Å; $\dot{\varepsilon} = 10^8$ s^{-1}). **a**: Mendelev-II potential, atomically sharp crack tip; initial presence of {110} planar faults (⓪); twin formation on {112} planes at ⟨1 1 0⟩ crack front segments (①); where the nucleated twins and planar faults met, screw dislocations (②) formed and slipped along the faulted {110} planes; the nucleated defects grew and led to multiple dislocation-twin (③) and twin-twin (④) interactions; the initially circular crack changed to a square-like shape (⑤). **b**: Mendelev-II potential, blunted crack tip; planar faults (⓪) were initially less dominant; twin formation (①) started on oblique twin planes that lied between two {110} planes; dislocations glided along the crack face (⑥). **c**: Chamati potential, blunted crack tip; only very limited planar fault formation (⓪); twin formation (①) and subsequent dislocation emission (②) started on two opposite {112} planes at ⟨1 1 0⟩ crack fronts; compared to the interactions observed before, dislocation-dislocation interactions (⑦) were more dominant; a peculiar case of such interactions was the annihilation of two screw segments of same Burgers vector that glided along the crack face (⑧).

dislocations on adjacent $\{1\,1\,2\}$ planes (marked with 1 in Fig. 4.3). Crack front segments that are locally parallel to $\langle 1\,0\,1\rangle$ directions were found to be the preferred nucleation sites, cf. Fig. A.1a in the appendix. Whereas the edge components of the twinning dislocations glided away from the crack front, the screw segments remained connected to the crack front. Three screw segments of the twinning dislocations, which were initially on adjacent $\{1\,1\,2\}$ planes, combined to one perfect $a_0/2\langle 1\,1\,1\rangle$ lattice dislocation by cross slipping on a common plane (marked with 2 in Fig. 4.3). This process will be discussed in detail in section 7.5.2. In the following, the released dislocations interacted with other twins (marked with 3), the crack face (marked with 6), or other dislocations (marked with 7), which sometimes led to dislocation annihilation (marked with 8). In cases where dislocation emission from twins was less pronounced, twins were also found to directly interact with each other (marked with 4).

There were, however, also fundamental differences in the plastic response of the cracks: first, $\langle 1\,0\,1\rangle$ crack fronts became more and more pronounced leading to a square-like crack shape (marked with 5) in case of the sharp crack, see Fig. 4.3a. This behavior is not observed for the blunted cracks, which remained circular, cf. Fig. 4.3b and c. Second, the incipient formation of $\{1\,1\,0\}$ planar faults at $\pm[1\,0\,0]$ and $\pm[0\,0\,1]$ oriented crack fronts was only observed for the Mendelev-II potential, see Fig. 4.3a and b, but not for the Chamati potential. This observation is similar to what was found for the corresponding straight $(0\,1\,0)$ crack tips, see Fig. 4.2. Finally, the number and kind of activated twin systems was different in all three situations: in case of the sharp crack using the Mendelev-II potential, simultaneous twin formation and growth is observed on four equally inclined $\{1\,2\,1\}$ twin systems, namely the $[1\bar{1}\bar{1}](1\,2\,\bar{1})$, $[1\bar{1}1](1\,2\,1)$, $[\bar{1}\bar{1}1](1\,\bar{2}\,\bar{1})$, and $[\bar{1}\bar{1}\bar{1}](1\,\bar{2}\,1)$ systems. From these four twin systems, only the $[\bar{1}\bar{1}1](\bar{1}\,2\,1)$ and $[\bar{1}\bar{1}\bar{1}](1\,\bar{2}\,1)$ systems are initially active in case of the blunted crack tip. These two twin systems were not inclined but oblique with respect to the part of crack front where they were emitted from, cf. Fig. 4.3a and b. With the Chamati potential, twins formed only in the two $[1\,1\,\bar{1}](\bar{1}\,2\,1)$ and $[\bar{1}\,1\,1](1\,2\,\bar{1})$ twin systems at opposite $\pm[1\,0\,1]$ crack front segments.

The critical initiation strains were 5.32 % for the Chamati potential and 4.89±0.01 % for the Mendelev-II potential when $L_y = 1000$ Å. When these values are normalized to the corresponding ε_0 values (4.46 % and 4.15 %, respectively) the initiation strains are $(1.18\pm0.01)\varepsilon_0$ independent of the potential.

4.2 Cracks on {110} planes

Unlike for the $\{1\,0\,0\}$ planes, the fracture behavior of cracks on the $\{1\,1\,0\}$ planes strongly depended on the crack front direction and the interaction potential. In the quasi-static K-controlled setup, all potentials predicted brittle crack propagation for $\langle 0\,0\,1\rangle$ crack fronts; for the $\langle 1\bar{1}\,0\rangle$ crack fronts, only a limited number of potentials predicted brittle fracture whereas the majority of the potentials showed crack-tip plasticity. For the Chiesa potential, the $(1\,1\,0)[1\bar{1}\,0]$ crack system was extensively studied in strain-controlled setups with varying simulation parameters. Under dynamic conditions, for very short crack lengths,

and very long crack fronts, the brittle propagation behavior observed in the quasi-static K-controlled setup changed to crack tip plasticity. As for the $\{1\,0\,0\}$ plane, crack tip plasticity became even more pronounced at curved crack fronts. Penny-shaped cracks on the $(1\,1\,0)$ plane emitted dislocations, which then cross slipped along the curved crack front thereby blunting formerly atomically sharp crack tips and preventing brittle fracture on this plane. The detailed descriptions of the observed fracture processes and effects are given in the following subsections.

4.2.1 K-controlled cracks: Brittle vs. ductile behavior

The results for K-controlled cracks on the $(1\,1\,0)$ plane are given in Table 4.3 for Fe and Table 4.4 for the remaining bcc metals. The fracture behavior of cracks on the $(1\,1\,0)$ plane was both direction and potential dependent, see Fig. 4.4 for representative examples for Fe. For the $[0\,0\,1]$ crack front direction, all potentials predicted crack propagation on the original $(1\,1\,0)$ plane. For the $[1\bar{1}\,0]$ crack front direction, the observed fracture behavior depended strongly on the potential. For the Chiesa, Marinica07, and Mendelev-II potentials, the fracture behavior was brittle on the $(1\,1\,0)$ plane, see Fig. 4.4d. The same behavior was observed for all ATFS potentials for the other bcc metals except for Mo as well as the FS potential for Cr and the Fellinger potential for Nb. For the Simonelli, Chamati, and Gordon potentials, the crack tip emitted an $a_0/2[1\,1\,\bar{1}](1\,1\,2)$ edge dislocation, see e.g., Fig. 4.4f for the Chamati potential. Dislocation emission was also observed for the ATFS potential for Mo and for the Smirnova potential for Mo. The MFS potential showed a combination of both cleavage and ductile crack tip deformation: the crack first propagated in a brittle manner under deviation of about 45° from the initial $(1\,1\,0)$ crack plane. Then, two $a_0/2[\bar{1}\,\bar{1}\,\bar{1}](1\,1\,\bar{2})$ edge dislocations were successively emitted from the new crack tip. In case of the Marinica11 potential, the crack tip emitted an $a_0/2[\bar{1}\,\bar{1}\,1]\{1\,1\,2\}$ edge dislocation, see Fig. 4.4h. Similar to the $(1\,0\,0)[0\,0\,1]$ crack system, structural transformations occurred in front of some crack tips, i.e., for the MFS, see Fig. 4.4a, Marinica07 and Marinica11 potentials, see Fig. 4.4g,h. Similar crack tip transformations were observed for the Ackland, Smirnova, and Wang potentials for Mo and W. This resulted in very high K_{Ic} values up to 3.93 MPa$\sqrt{\mathrm{m}}$ for the Ackland potential for Mo. For the $[1\bar{1}\,1]$ and $[1\,1\,\bar{2}]$ crack front directions, which were studied using the MFS, Mendelev-II, and Chiesa potentials, brittle fracture on the $(1\,1\,0)$ plane was observed without exception.

Similar to cracks on the $(1\,0\,0)$ plane, all potentials except the Marinica11 potential for Fe and the Fellinger potential for Nb showed higher K_{Ic} values for the $[0\,0\,1]$ crack front direction than for the $[0\,1\,1]$ direction. For Fe, the values were around two different average values for the $[0\,0\,1]$ crack front direction. The Simonelli, Chamati, and Mendelev-II potentials have comparably low K_{Ic}-values around 1.13 MPa$\sqrt{\mathrm{m}}$ whereas the values for the remaining potentials lied around 1.43 MPa$\sqrt{\mathrm{m}}$. For the $[1\bar{1}\,0]$ crack front direction, the average K_{Ic}-value was 1.21 MPa$\sqrt{\mathrm{m}}$.

The Simonelli potential as well as the MFS and Marinica11 potentials were exceptions showing values which were 10 % lower or higher, respectively. The observed fracture behavior was not directly correlated with a certain range of K_{Ic}-values. The K_{Ic} values for

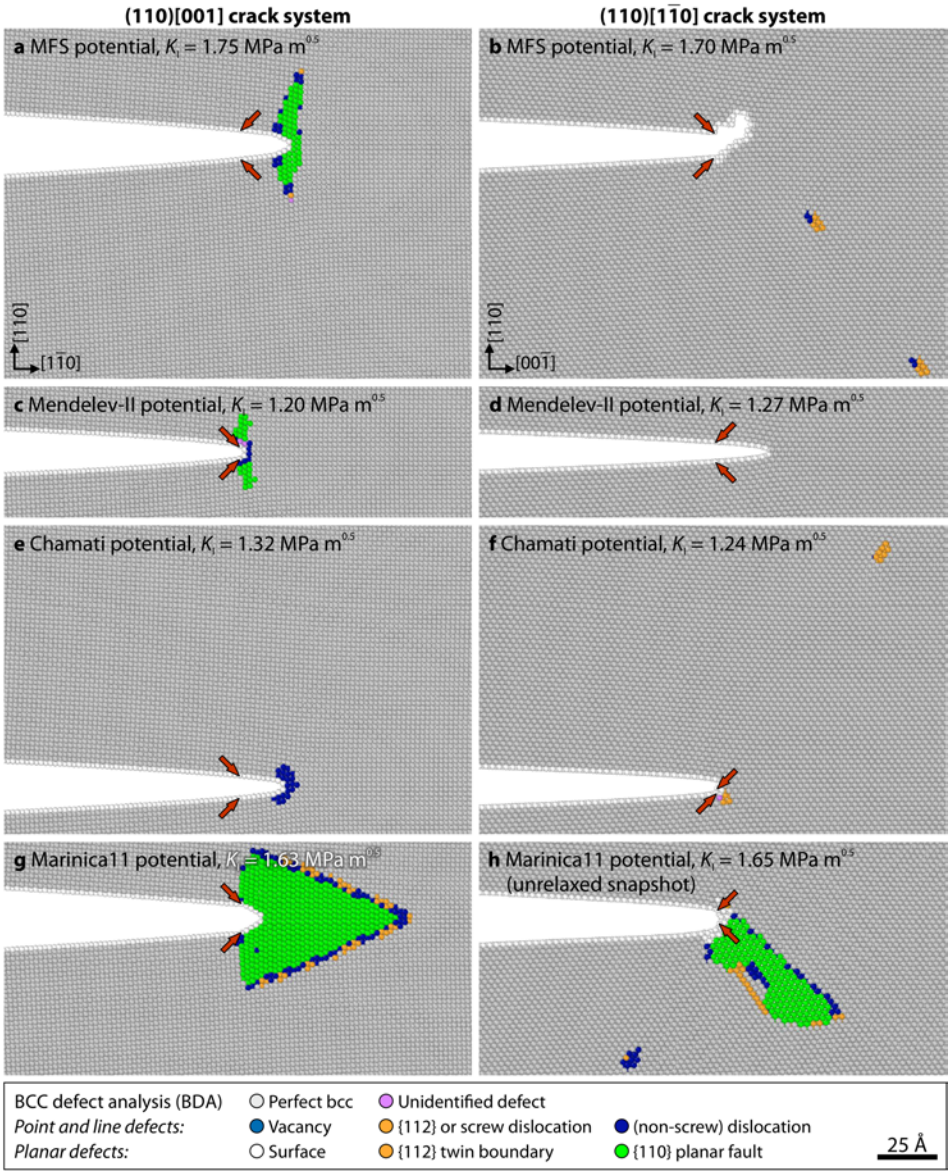

Figure 4.4: Fracture behavior of cracks on the (110) plane under quasi-static K-controlled loading for selected Fe potentials. **a,b**: MFS potential; **c,d**: Mendelev-II potential; **e,f**: Chamati potential; **g,h**: Marinica11 potential; left subfigures: [001] crack front direction, brittle fracture behavior on the original (110) plane; right subfigures: $[1\bar{1}0]$ crack front direction, strongly potential-dependent fracture behavior, i.e., either emission of {112}-type dislocations (**b**,**f**,**h**) or brittle fracture (**d**). Subfigure **h** shows an unrelaxed snapshot after 100,000 steps (the relaxation did not converge properly below the threshold value); red arrows: original crack tip atoms.

dislocation emission scattered between 0.94 and 1.48 MPa$\sqrt{\text{m}}$ whereas the K_{Ic}-values for brittle fracture were between 1.09 and 1.43 MPa$\sqrt{\text{m}}$. From the remaining bcc metals, Nb showed the lowest K_{Ic} values followed by V and Ta. Only for the $[1\bar{1}0]$ crack front direction, the Fellinger potential for Nb deviated from this behavior showing a higher fracture toughness than V. Contrary to their ranking for the $(1\,0\,0)$ plane, Cr exhibited higher values than Mo for the $[0\,0\,1]$ crack front direction whereas the ordering was vice versa for the $[1\bar{1}0]$ direction. The average K_{Ic} values were higher for W (2.03 MPa$\sqrt{\text{m}}$) than for Mo (1.65 MPa$\sqrt{\text{m}}$) whereas the ordering of both materials was inverse for the $(1\,0\,0)$ plane. The large scatter in the critical stress intensity factors of the Fe potentials does not allow to place them unambiguously into the ordering of the other bcc potentials. The bcc potentials that showed extensive structural transformations at the crack tip and thereby affected the determined K_{Ic} values were excluded from this comparison, i.e., the Ackland, Smirnova, and Wang potentials.

4.2.2 Strain-controlled straight cracks: Parameter-dependent behavior

The results for strain-controlled cracks on $\{1\,1\,0\}$ planes in Fe (Chiesa potential) are given in Table 4.3. In general, the brittle fracture behavior and the ordering of the critical strains ε_{i} for the different crack front directions agreed well with the results obtained in the K-controlled setup; the ordering of ε_{i} was for the different front directions (from high to low): $\langle 0\,0\,1\rangle$, $\langle 1\,1\,0\rangle$, $\langle 1\,1\,2\rangle$, $\langle 1\,1\,1\rangle$. The corresponding fracture behavior under dynamic conditions is visualized in Fig. 4.5a-d. The lattice trapping ratio, which was $\Delta K = 0.67$ for the K-controlled setup, was calculated by determining the critical strain ε^{-} for closure in the quasi-2D central crack setup. The corresponding ratios $\Delta\varepsilon$ increased with increasing crack length from 0.63 (a_{eff} = 63 Å) to 0.65 (a_{eff} = 202 Å). Here and in the following, a_{eff} denotes the crack length after relaxation, which sometimes differs from the original crack length a due to limited crack propagation or closure upon energy minimization.

To determine the effect of the simulation parameters, see section 2.1.3, the $(1\,1\,0)[1\bar{1}0]$ crack system was selected, which is a good model system as it showed ideally brittle crack propagation in the K-controlled setup under quasi-static loading conditions. The varied simulation parameters were the setup geometry (including aspect ratio and box size), loading conditions, strain rate, lateral strain method, crack length, and crack-tip configuration (sharp or blunted). The detailed results for the fracture behavior and critical strains determined with the different parameters are given in Table 4.3. The simulation boxes contained approximately one, two, or three million atoms for box sizes of $L_{\text{x}} \times L_{\text{y}} \approx 1000 \times 1000$, 3000×850, or 3000×1000 Å^2; the crack length varied between $a_{\text{eff}} = 24$ and 1480 Å. For very small crack lengths, the fracture behavior changed from brittle to ductile, see Fig. 4.6 for an example of dislocation emission from sharp crack tips with crack length $a \approx 350$ Å in the quasi-2D and 3D edge crack setups. In both cases, the crack tip did not initially emit the dislocation, but started to propagate and arrested thereafter; the arrested crack tip structure is shown for the 3D edge crack in the inset panel in Fig. 4.6d. The glide plane of the emitted dislocation was the (112) plane with Burgers vector $\underline{b} = a_0/2[11\bar{1}]$. Only when the crack length was very small, as for the central crack with a_{eff} = 24 Å in Fig. 4.7a and

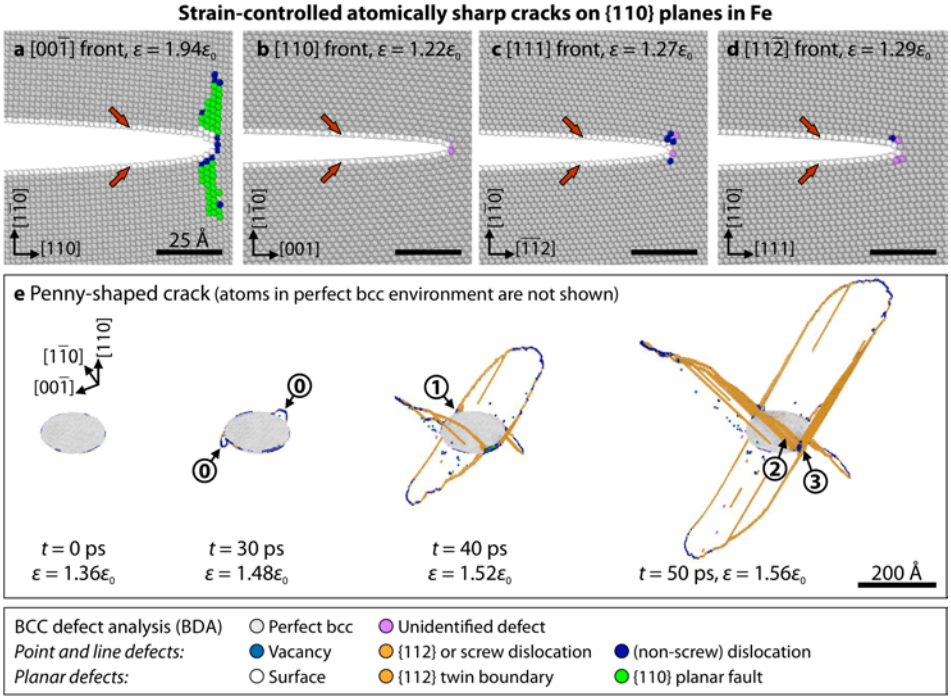

Figure 4.5: Dynamically-loaded atomically sharp cracks on {110} planes in Fe (Chiesa potential, $\dot{\varepsilon} = 10^8$ s^{-1}). **a**-**d**: different orientations for straight cracks with initial brittle propagation independent of crack front direction; $L_y \approx 850$ Å, $a_{\text{eff}} \approx 1000$ Å; red arrows: original crack tip atoms. **e**: penny-shaped crack with $a = 100$ Å ($L_y \approx 1000$ Å); nucleation of {112}-type dislocations at $\langle 1\bar{1}1 \rangle$ crack fronts (⓪); the screw segments of the nucleated dislocations cross slipped along the curved crack front (①); as they cross slipped, thin and elongated twins formed (②); at $\langle 0\,0\,1 \rangle$-oriented crack front segments, twins met twins that have been initiated at the opposite side of the crack (③).

b, dislocations were emitted from the initial crack-tip position and even under quasi-static loading conditions. In this case, the dislocation glide plane was again a $\{112\}$ plane. For the same setup and loading conditions, the crack with $a_{\text{eff}} = 443$ Å propagated in a brittle manner, see Fig. 4.7d. The remaining simulation parameters, i.e., the lateral strain method and the crack-tip configuration, did not alter the fracture behavior. As an example, the brittle re-initiation of atomically sharp cracks from formerly blunted crack tips is shown in the right subfigures of Fig. 4.8 for quasi-static loading in the different setups.

The determined critical strains ε_i mainly depended on crack length a, box length L_y, dynamic strain rate $\dot{\varepsilon}$, lateral strain method but only to minor degree on the setup geometry, aspect ratio, loading conditions, and crack-tip configuration. It can be seen in Fig. 4.9 that ε_i increased with decreasing a and L_y, and with increasing $\dot{\varepsilon}$. For $a < 250$ Å, the influence of the crack length on ε_i was remarkable and showed an asymptotic behavior towards $a \to 0$. Above $a \approx 250$ Å, the crack length dependency vanished and ε_i was ap-

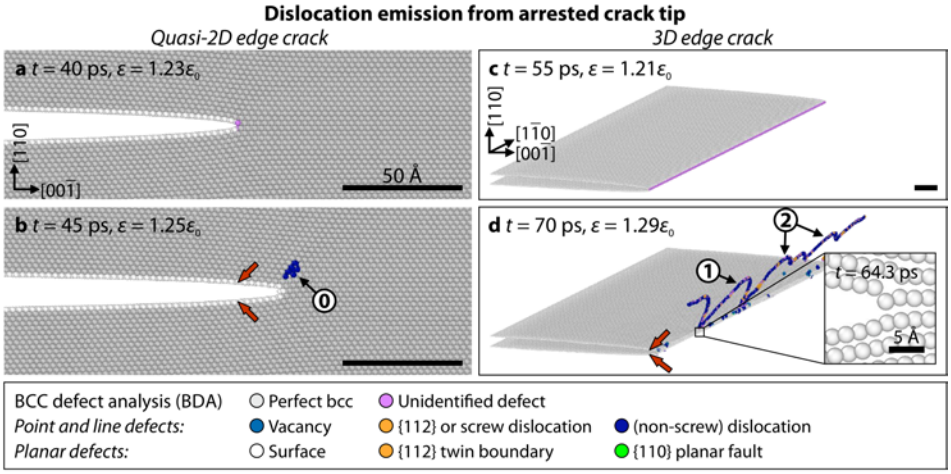

Figure 4.6: Incipient crack propagation and subsequent dislocation emission for sharp edge cracks with straight crack fronts ($\dot{\varepsilon} = 10^8$ s^{-1}; $L_x \approx L_y = 1000$ Å; $a \approx 350$ Å). **a**,**b**: quasi-2D edge crack setup; initial brittle propagation, crack arrest, emission of $a_0[1\bar{1}1](112)$ mixed dislocation (⓪) with line direction parallel to the $[1\bar{1}0]$ crack front; **c**,**d**: 3D edge crack setup; initial brittle propagation, crack arrest, emission of several dislocation half loops (①) that form an edge dislocation (②). Red arrows: original crack tip atoms; atoms in perfect bcc environment are not shown in **c** and **d**.

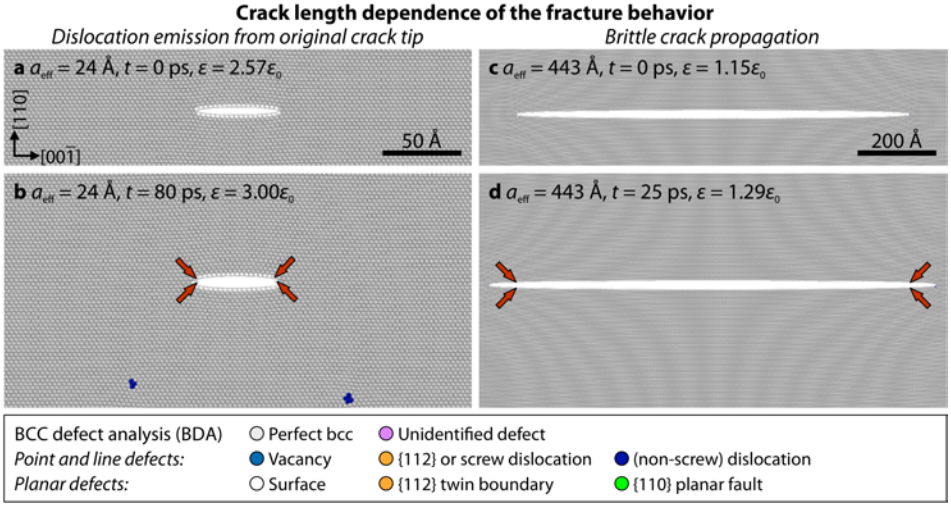

Figure 4.7: Qualitatively different fracture behavior for different crack lengths in the quasi-2D central crack setup ($\dot{\varepsilon} = 10^8$ s^{-1}, $L_x = 3000$ Å, $L_y = 1000$ Å). **a**,**b**: $a_{\text{eff}} = 24$ Å; dislocation emission; **c**,**d**: $a_{\text{eff}} = 443$ Å; brittle crack propagation. Red arrows: original crack tip atoms.

proximately 2.44 % (for the $\varepsilon^{\mathrm{pre}}$ method). The strain rate effect was negligible for strain rates below or equal 10^8 s^{-1}. For this reason, all subsequent dynamic simulations were performed with $\dot{\varepsilon} = 10^8$ s^{-1} or below. The dependency on the box length L_y is expected as L_y influences the necessary strain to reach the energy release rate necessary for crack propagation, cf. Eq. (3.3). This can be easily seen by normalizing the different ε_i values for different L_y with the sample-dependent predictions ε_0, see Eq. (3.4): all ε_i values fall into a range of $(1.25\pm0.02)\varepsilon_0$. The critical strain was lowest for the $\varepsilon^{\mathrm{zero}}$ method and highest for the $\varepsilon^{\mathrm{pre}}$ method for lateral straining with the value for the σ^{min} method lying in between. Similar to the box length effect, the influence of the different methods was partially included in the predicted values ε_0. When comparing ε_c and ε_0, ε_c was approximately $1.26\varepsilon_0$ for the $\varepsilon^{\mathrm{zero}}$ and $\varepsilon^{\mathrm{pre}}$ methods and $1.32\varepsilon_0$ for the σ^{min} method. It is finally noted that relative critical strains around $1.26\varepsilon_0$ agreed very well with the relative critical stress intensity factors ($K_\mathrm{Ic} = 1.27K_\mathrm{G}$) as determined in the K-controlled setup.

4.2.3 Strain-controlled penny-shaped cracks: Dislocation emission and cross slip

The results for strain-controlled penny-shaped cracks on the $(1\,1\,0)$ plane in Fe are given in Table 4.3. Similar as for straight cracks, box size, crack tip sharpness, crack radius, and loading conditions were varied. The simulation boxes contained between 19 and 85 million atoms for box sizes of $L_\mathrm{x} \times L_\mathrm{y} \times L_\mathrm{z} \approx 600 \times 600 \times 600$ and $1000 \times 1000 \times 1000$ Å^3; the crack radius varied between $a = 60$ and 200 Å. Fig. 4.5e shows characteristic snapshots of the evolution of crack tip plasticity in case of a dynamically loaded sharp crack tip with crack radius $a = 100$ Å. The crack tips always initiated extensive crack tip plasticity. The same qualitative behavior was observed when the crack radius was varied and for quasi-static loading, see Table 4.3. Limited bond breaking processes prior to brittle fracture were only observed for $a = 200$ Å and quasi-static loading.

Plastic deformation always initiated on $\{1\,1\,2\}$ planes from $\pm[1\bar{1}\,0]$-oriented parts of the crack front (marked with 0 in Fig. 4.5e). The screw components of $a_0/2[1\,1\,1]$ and $a_0/2[1\,1\bar{1}]$ dislocations, which have been nucleated at opposite regions of the crack, cross slipped along the curved crack front and thereby left behind their respective nucleation sites and moved closer towards each other (marked with 1). The $a_0/2[1\,1\,1]$ screw components, for instance, cross slipped from their initial $(\bar{1}\,\bar{1}\,2)$ plane to $(0\,1\,\bar{1})$ and $(1\,0\,\bar{1})$ planes and further to $(\bar{1}\,2\,\bar{1})$ and $(2\,\bar{1}\,\bar{1})$ planes, cf. Fig. A.1b in the appendix. On these planes, long and elongated twins re-initiated (marked with 2) by distributing the perfect $\{0\,1\,1\}$ screw dislocations onto three adjacent $\{1\,2\,1\}$ twin planes. These twins met twins in the $[1\,1\bar{1}](\bar{1}\,2\,1)$ and $[1\,1\bar{1}](2\,\bar{1}\,1)$ systems that have been formed in a similar process but by dislocations nucleated at the opposite part of the crack. These interactions led to the formation of $[1\,2\,0]$ and $[2\,1\,0]$ junctions (marked with 3) at $\pm[0\,0\,1]$ crack front segments.

On the $(1\,1\,0)$ plane, the initiation strains were $\varepsilon_\mathrm{i} = (1.50\pm0.03)\varepsilon_0$ for $a/L_\mathrm{x} = 0.1$ independent of loading conditions, crack tip sharpness, and box size. An increase of a/L_x to 0.2 led to a decrease of ε_i by approximately 25 % ($\varepsilon_\mathrm{i} = 1.10\varepsilon_0$). Likewise, a a/L_x decrease to 0.06 resulted in an ε_i increase by 35 % ($\varepsilon_\mathrm{i} = 1.99\varepsilon_0$). For the same crack radius $a = 60$ Å, but

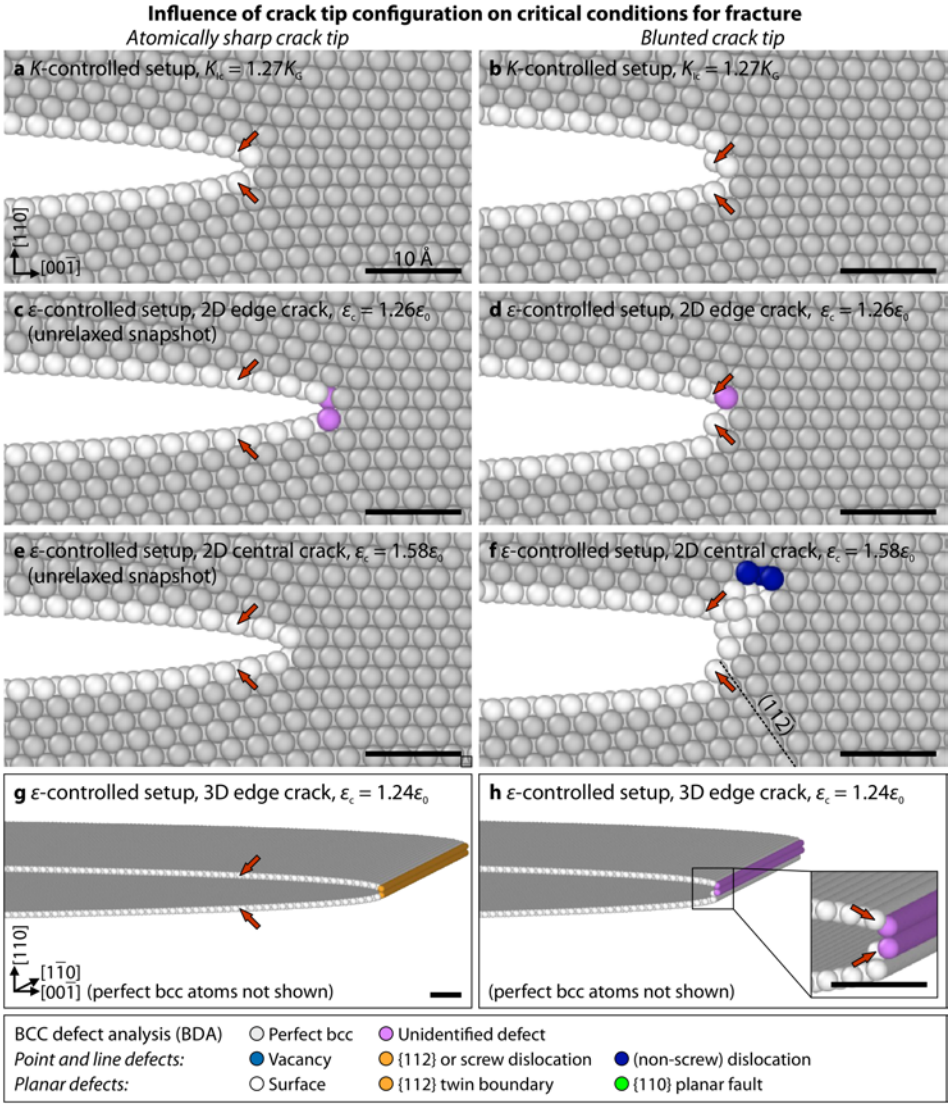

Figure 4.8: Influence of crack tip sharpness on fracture behavior and fracture criteria (K_{Ic} and ε_c) of straight cracks in different setups under quasi-static loading conditions. **a**,**b**: K-controlled setup at K_{Ic}. The configurations in strain-controlled setups are shown at ε_c: **c**,**d**: quasi-2D edge crack, $a \approx 1000$ Å; **e**,**f**: quasi-2D central crack, $a \approx 100$ Å; **g**,**h**: 3D edge crack, $a \approx 350$ Å. Independent of crack tip sharpness, all cracks initiated brittle fracture behavior at the same critical values; after the first bond was broken, all strain-controlled sharp cracks propagated for a significant distance or even unstable (unrelaxed snapshots in **c** and **e**); all blunted cracks arrested after rupture of the original crack tip bond; the quasi-2D central crack immediately arrested and emitted an $a_0/2[\bar{1}\bar{1}1](11\bar{2})$ dislocation (indicated slip plane in **f**). Red arrows: original crack tip atoms.

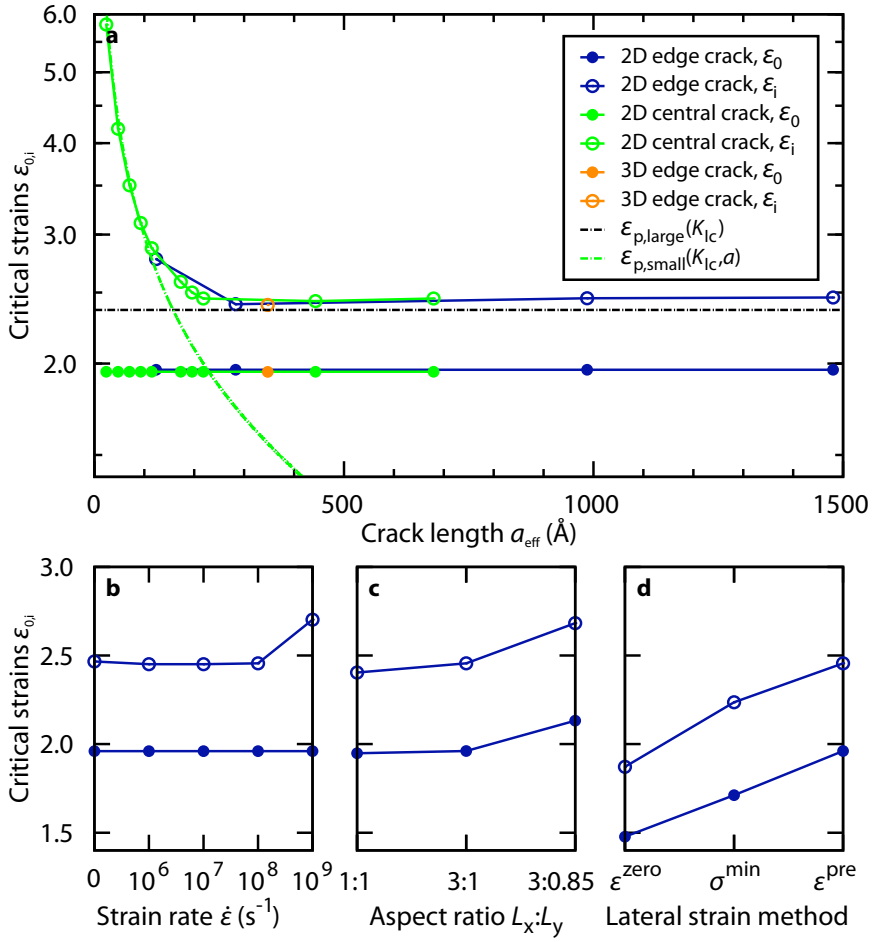

Figure 4.9: Influence of selected simulation parameters on the predicted (ε_0, closed symbols) and determined fracture strains (ε_i, open symbols). The precise values are given in Table 4.3. **a**: influence of crack length for different strain-controlled simulation setups. For the quasi-2D edge crack setup: **b**: influence of strain rate $\dot{\varepsilon}$; **c**: influence of aspect ratio L_x:L_y, where the unit box length equals to L_y = 1000 Å; **d**: influence of method of lateral straining. The following observations were made: ε_i was independent of both simulation setup and crack length for a > 250 Å and strain rates $\dot{\varepsilon} \leq 10^8\,s^{-1}$; changing the aspect ratio from 3:1 to 1:1 did not significantly influence ε_0 and ε_i; decreasing the box size L_y from 1000 to 850 Å led to higher values of ε_i; the ε^{zero} and σ^{min} lateral straining methods decreased ε_i as compared to the ε^{pre} method. The dash-dot lines in subfigure **a** are the predicted critical strains ε_p calculated with Eqs. (7.5-7.6), see section 7.1.4 for details.

different box sizes and thus a different a/L_x ratio, the initiation strains were 5.10±0.02 %.

To study the influence of the crack crack front curvature on the lattice trapping effect, the necessary strains ε^- for closure were determined for three different crack radii (a = 60, 100, and 200 Å) by decreasing the applied strain. The corresponding lattice trapping ranges were on average at $\Delta\varepsilon = 0.24$. Unlike for the straight central cracks, no clear trend in the crack length dependence of the lattice trapping range was observed.

Table 4.3: Summary of simulation results for cracks on {110} planes in Fe. $\delta\varepsilon = 0.025$ %: incremental straining step size in quasi-static simulations; a_{eff}: crack length/radius after relaxation; $\Delta\varepsilon$: lattice trapping range (analogous to ΔK), given in parentheses; LCM: lateral straining method; CTT: Crack tip transformation(s). See caption of Table 4.1 for description of other variables.

***K*-controlled cracks (quasi-statically loaded)**						
Potential	K_{Ic}	ΔK	K_{G}	K_{e}	K_{t}	Fracture behavior
(110)[001] crack system						
MFS	1.52	1.43	0.87	1.62	—	Brittle on (110) plane
Simonelli	1.10	0.72	0.77	1.36	—	Brittle on (110) plane
Chamati	1.14	0.27	0.99	1.36	—	Brittle on (110) plane
Mendelev-II	1.14	0.61	0.84	1.31	—	Brittle on (110) plane
Gordon	1.33	0.66	0.92	1.43	—	Brittle on (110) plane
Marinica07	1.34	1.01	0.89	1.46	—	Brittle on (110) plane preceded by CTT
Marinica11	1.41	2.00	0.73	1.55	—	Brittle on (110) plane preceded by CTT
Chiesa	1.57	1.57	0.86	1.54	—	Brittle on (110) plane
(110)[1$\bar{1}$0] crack system						
MFS	1.43	0.82	0.95	1.43	1.28	Brittle on no specific plane, then dislocation emission
Simonelli	0.94	—	0.85	1.22	1.04	Emission of $a_0/2[11\bar{1}](112)$ edge dislocation
Chamati	1.22	—	1.10	1.15	1.12	Emission of $a_0/2[11\bar{1}](112)$ edge dislocation
Mendelev-II	1.09	0.35	0.92	1.15	1.11	Brittle on (110) plane
Gordon	1.14	—	1.01	1.23	1.15	Emission of $a_0/2[11\bar{1}](112)$ edge dislocation
Marinica07	1.19	0.45	0.98	1.27	1.22	Brittle on (110) plane preceded by CTT
Marinica11	1.48	—	0.80	1.23	1.25	$a_0/2[111](11\bar{2})$ dislocation preceded by CTT
Chiesa	1.21	0.67	0.95	1.36	1.30	Brittle on (110) plane
Potential	K_{Ic}	ΔK	K_{G}	K_{e}	K_{t}	Fracture behavior
(110)[1$\bar{1}$1] crack system						
MFS	0.99	0.18	0.89	1.35	—	Brittle on (110) plane
Mendelev-II	1.07	0.28	0.88	1.09	—	Brittle on (110) plane
Chiesa	0.99	0.18	0.90	1.28	—	Brittle on (110) plane
(1$\bar{1}$0)[11$\bar{2}$] crack system						
MFS	0.91	0.08	0.91	1.41	—	Brittle on (110) plane
Mendelev-II	0.94	0.13	0.86	1.14	—	Brittle on (110) plane
Chiesa	1.11	0.30	0.88	1.35	—	Brittle on (110) plane

Continued on next page

Continued from previous page

Quasi-2D edge cracks (Chiesa potential) with $L_x \approx 3L_y$ if not mentioned otherwise

L_y (Å)	a_{eff} (Å)	Crack tip	Loading, $\dot{\varepsilon}$ (s^{-1})	LCM	$\varepsilon_{i,c}$ (%)	ε_0 (%)	ε_G (%)	Fracture behavior
(1$\bar{1}$0)[001] crack system								
848.4[a]	999	sharp	dynamic, 10^8	ε^{pre}	2.56	2.05	1.84	Brittle, ε_a = 2.64%
(1$\bar{1}$0)[110] crack system								
848.4[a]	987	sharp	dynamic, 10^8	ε^{pre}	2.68	2.13	1.85	Brittle, ε_a = 2.69%
848.4[a]	987	sharp	dynamic, 10^9	ε^{pre}	2.88	2.13	1.85	Brittle[c]
848.4[a]	987	sharp	quasi-static	ε^{pre}	2.70	2.13	1.85	Brittle
848.4[a]	—	—	—	σ^{min}	—	—	1.84	—
999.3	124	sharp	dynamic, 10^8	ε^{pre}	2.78	1.96	1.71	Brittle[c]
999.3	283	sharp	dynamic, 10^8	ε^{pre}	2.41	1.96	1.71	Brittle[c]
999.3	283	sharp	dynamic, 10^9	ε^{pre}	2.66	1.96	1.71	Brittle[c]
999.3[b]	357	sharp	dynamic, 10^8	ε^{pre}	2.43	1.95	1.71	Brittle[c,d]
999.3[b]	357	sharp	quasi-static	ε^{pre}	2.40	1.95	1.71	Brittle
999.3	987	sharp	quasi-static	ε^{pre}	2.47	1.96	1.71	Brittle[c]
L_y (Å)	a_{eff} (Å)	Crack tip	Loading, $\dot{\varepsilon}$ (s^{-1})	LCM	$\varepsilon_{i,c}$ (%)	ε_0 (%)	ε_G (%)	Fracture behavior
999.3	987	sharp	dynamic, 10^6	ε^{pre}	2.45	1.96	1.71	Brittle[c]
999.3	987	sharp	dynamic, 10^7	ε^{pre}	2.45	1.96	1.71	Brittle[c]
999.3	987	sharp	dynamic, 10^8	ε^{pre}	2.46	1.96	1.71	Brittle[c]
999.3	987	sharp	dynamic, 10^9	ε^{pre}	2.70	1.96	1.71	Brittle[c]
999.3	990	sharp	dynamic, 10^8	σ^{min}	2.24	1.71	1.70	Brittle[c]
999.3	990	sharp	dynamic, 10^9	σ^{min}	2.44	1.71	1.70	Brittle[c]
999.3	990	sharp	quasi-static	σ^{min}	2.26	1.71	1.70	Brittle
999.3	999	sharp	quasi-static	ε^{zero}	1.86	1.48	1.53	Brittle
999.3	999	sharp	dynamic, 10^8	ε^{zero}	1.87	1.48	1.53	Brittle[c]
997.3	1000	blunted	quasi-static	ε^{zero}	1.85	1.48	1.53	Brittle
997.3	1000	blunted	quasi-static	σ^{min}	2.26	1.71	1.70	Brittle
997.3	1000	blunted	dynamic, 10^8	σ^{min}	2.25	1.71	1.70	Brittle[c]
997.3	1000	blunted	quasi-static	ε^{pre}	2.46	1.96	1.71	Brittle[c]
999.3	1480	sharp	dynamic, 10^8	ε^{pre}	2.46	1.96	1.71	Brittle[c]
999.3	1480	sharp	dynamic, 10^9	ε^{pre}	2.71	1.96	1.71	Brittle[c]
(1$\bar{1}$0)[111] crack system								
848.4[a]	992	sharp	dynamic, 10^8	ε^{pre}	2.33	1.89	1.78	Brittle
(1$\bar{1}$0)[11$\bar{2}$] crack system								
848.4[a]	995	sharp	dynamic, 10^8	ε^{pre}	2.39	1.91	1.78	Brittle

Quasi-2D central cracks (Chiesa potential) with $L_x \approx 3L_y$ if not mentioned otherwise

L_y (Å)	a_{eff} (Å)	Crack tip	Loading, $\dot{\varepsilon}$ (s^{-1})	LCM	$\varepsilon_{i,c}$ (%)	ε_0 (%)	ε_G (%)	Behavior ($\Delta\varepsilon$)
(110)[1$\bar{1}$0] crack system								
999.3	24	sharp	dynamic, 10^8	ε^{pre}	5.81	1.96	1.71	{112} dislocation
999.3	24	sharp	quasi-static	ε^{pre}	5.81	1.96	1.71	{112} dislocation
999.3	47	sharp	dynamic, 10^8	ε^{pre}	4.91	1.96	1.71	Brittle[c]

Continued on next page

Continued from previous page

L_y (Å)	a_{eff} (Å)	Crack tip	Loading, $\dot{\varepsilon}$ (s^{-1})	LCM	$\varepsilon_{i,c}$ (%)	ε_0 (%)	ε_G (%)	Behavior ($\Delta\varepsilon$)
999.3[b]	63	sharp	quasi-static	ε^{pre}	3.67	1.96	1.71	Brittle (0.63)
999.3	70	sharp	dynamic, 10^8	ε^{pre}	3.50	1.96	1.71	Brittle[c]
999.3	93	sharp	dynamic, 10^8	ε^{pre}	3.11	1.96	1.71	Brittle[c]
999.3[b]	95	sharp	dynamic, 10^8	ε^{pre}	3.11	1.96	1.71	Brittle[c]
999.3[b]	95	sharp	quasi-static	ε^{pre}	3.09	1.96	1.71	Brittle
997.3[b]	100	blunted	dynamic, 10^8	ε^{pre}	3.11	1.96	1.71	Brittle[c]
997.3[b]	100	blunted	quasi-static	ε^{pre}	3.08	1.96	1.71	Brittle
999.3[b]	102	sharp	quasi-static	ε^{pre}	3.01	1.96	1.71	Brittle (0.64)
999.3	115	sharp	dynamic, 10^8	ε^{pre}	2.88	1.96	1.71	Brittle[c]
999.3	173	sharp	dynamic, 10^8	ε^{pre}	2.59	1.96	1.71	Brittle[c]
999.3	196	sharp	dynamic, 10^8	ε^{pre}	2.50	1.96	1.71	Brittle[c]
999.3[b]	202	sharp	quasi-static	ε^{pre}	2.52	1.96	1.71	Brittle (0.65)
999.3	218	sharp	dynamic, 10^8	ε^{pre}	2.45	1.96	1.71	Brittle[c]
999.3	443	sharp	dynamic, 10^8	ε^{pre}	2.43	1.96	1.71	Brittle[c]
999.3	443	sharp	quasi-static	ε^{pre}	2.44	1.96	1.71	Brittle
999.3	679	sharp	dynamic, 10^8	ε^{pre}	2.45	1.96	1.71	Brittle[c]

3D edge cracks (Chiesa potential) with $L_x \approx L_y \approx L_z$

(110)[1$\bar{1}$0] crack system

L_y (Å)	a_{eff} (Å)	Crack tip	Loading, $\dot{\varepsilon}$ (s^{-1})	LCM	$\varepsilon_{i,c}$ (%)	ε_0 (%)	ε_G (%)	Fracture behavior
997.3	333	blunted	dynamic, 10^8	ε^{pre}	2.43	1.95	1.71	Brittle[c,d]
997.3	333	blunted	quasi-static	ε^{pre}	2.41	1.95	1.71	Brittle
999.3	347	sharp	dynamic, 10^8	ε^{pre}	2.40	1.95	1.71	Brittle[c,d]
999.3	347	sharp	quasi-static	ε^{pre}	2.41	1.95	1.71	Brittle

Penny-shaped cracks (Chiesa potential) with $L_x \approx L_y \approx L_z$

L_y (Å)	a_{eff} (Å)	Crack tip	Loading, $\dot{\varepsilon}$ (s^{-1})	LCM	$\varepsilon_{i,c}$ (%)	ε_0 (%)	ε_G (%)	Behavior ($\Delta\varepsilon$)
595.9	60	blunted	dynamic, 10^8	ε^{pre}	5.06	3.36	2.17	Dislocation[e]
597.9	60	sharp	dynamic, 10^8	ε^{pre}	5.09	3.36	2.17	Dislocation[e]
597.9	60	sharp	quasi-static	ε^{pre}	5.09	3.36	2.17	Dislocation[e]
999.3	60	sharp	dynamic, 10^8	ε^{pre}	5.12	2.57	1.71	Dislocation[e]
999.3	60	sharp	quasi-static	ε^{pre}	5.12	2.57	1.71	Dislocation[e] (0.24)
999.3	100	sharp	dynamic, 10^8	ε^{pre}	3.79	2.57	1.71	Dislocation[e]
999.3	100	sharp	quasi-static	ε^{pre}	3.85	2.57	1.71	Dislocation[e] (0.22)
997.3	100	blunted	dynamic, 10^8	ε^{pre}	3.82	2.57	1.71	Dislocation[e]
997.3	100	blunted	dynamic, 10^8	ε^{pre}	3.86	2.57	1.71	Dislocation[e]
999.3	200	sharp	dynamic, 10^8	ε^{pre}	2.82	2.57	1.71	Dislocation[e]
999.3	200	sharp	quasi-static	ε^{pre}	2.84	2.57	1.71	Dislocation[e,f] (0.26)

[a] $L_x \approx 3.53 L_y$
[b] $L_x \approx L_y$
[c] Crack arrest observed after a period of brittle propagation
[d] Dislocation emission observed after crack arrest
[e] {112} dislocation
[f] Limited bond breaking processes prior to dislocation emission

Table 4.4: Summary of simulation results for K-controlled cracks on {110} planes for various bcc potentials. Symbols and units as in Table 4.1.

Element	Potential	K_{Ic}	ΔK	K_G	K_e	K_t	Fracture behavior
				(110)[001] crack system			
V	ATFS	1.24	1.64	0.67	1.06	—	Brittle
Nb	ATFS	1.06	1.22	0.66	0.95	—	Brittle
Nb	Fellinger	0.91	1.00	0.74	0.96	—	Brittle
Ta	ATFS	1.43	1.14	0.89	1.47	—	Brittle
Cr	FS	1.76	0.95	1.02	1.41	—	Brittle
Mo	ATFS	1.73	0.80	1.15	1.86	—	Brittle
Mo	Ackland	2.98	1.56	1.28	2.56	—	Brittle, crack tip transformations
Mo	Smirnova	2.31	0.53	1.64	2.76	—	Brittle, crack tip transformations
W	ATFS	2.34	0.89	1.51	2.23	—	Brittle
W	Ackland	3.93	—	1.54	3.11	—	Brittle, crack tip transformations
W	Wang	2.43	1.18	1.51	2.32	—	Brittle, crack tip transformations
				(110)[1$\bar{1}$0] crack system			
V	ATFS	0.77	0.64	0.66	0.98	1.30	Brittle
Nb	ATFS	0.70	0.52	0.63	0.90	0.83	Brittle
Nb	Fellinger	0.98	1.60	0.72	0.91	0.80	Brittle
Ta	ATFS	1.08	0.46	0.93	1.31	1.52	Brittle
Cr	FS	1.24	0.46	0.99	1.28	1.54	Brittle
Mo	ATFS	1.57	—	1.12	1.70	1.55	{112} dislocation
Mo	Ackland	1.90	0.38	1.27	2.31	2.03	Brittle, crack tip transformations
Mo	Smirnova	2.09	—	1.64	2.40	2.40	{112} dislocation, crack tip transformations
W	ATFS	1.72	0.22	1.51	2.00	1.73	Brittle
W	Ackland	2.97	4.81	1.54	2.79	3.12	Brittle, crack tip transformations
W	Wang	1.73	0.21	1.51	2.11	1.89	Brittle

4.3 Cracks on the {111} plane

Independent of element and potential, cracks on the $\{111\}$ planes initiated crack tip plasticity in the quasi-static K-controlled setup. Most potentials showed twin formation at $[1\bar{1}0]$ oriented crack fronts and dislocation emission at $[11\bar{2}]$ crack front directions. Similarly, the penny-shaped crack on the (111) plane emitted dislocations with Burgers vectors perpendicular to the crack plane and finally formed a prismatic dislocation loop. The detailed descriptions of the observed fracture processes and effects are given in the following subsections.

4.3.1 K-controlled cracks: Pronounced crack tip plasticity

The results for K-controlled cracks on the (111) plane in Fe are given in Table 4.5. The fracture behavior was predominantly ductile, see Fig. 4.10. At crack fronts parallel to the $[1\bar{1}0]$ direction, nuclei of deformation twins initiated on the $(11\bar{2})$ plane independent of the used potential. In most cases, these nuclei were found at crack tips even for very low K_I values in the range of $0.9K_G$. Twins formed by the glide of $a_0/6[111](11\bar{2})$ dislocations

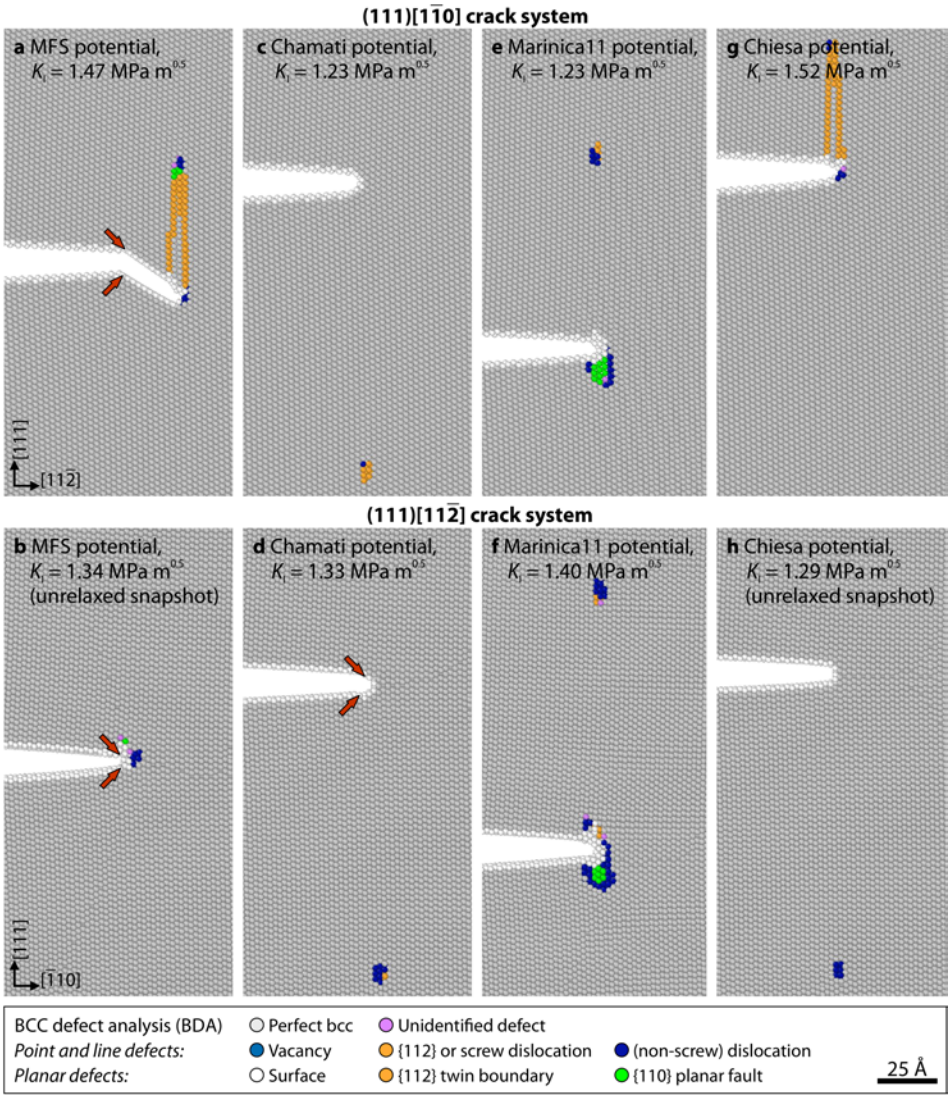

Figure 4.10: Fracture behavior of cracks on the (111) plane under quasi-static K-controlled loading for selected Fe potentials. **a,b**: MFS potential; **c,d**, Chamati potential; **e,f**: Marinica11 potential; **g,h**: Chiesa potential; top subfigures: [1$\bar{1}$0] crack front direction, formation of deformation twins in case of most potentials (**a**,**g**); only the cracks modeled with the Chamati and Marinica11 potentials emitted {112}-type dislocations (**c**,**e**); bottom figures: [11$\bar{2}$] crack front direction, strongly potential-dependent fracture behavior, either brittle fracture on the (111) plane (**b**) or emission of a {110}-type dislocation (**d**,**f**,**h**); in both crack front orientations, the Marinica11 potential showed structural crack tip transformations in front of the crack tip (**e**,**f**). Subfigures **b** and **h** show unrelaxed snapshots after 100,000 steps (relaxations did not converge properly); red arrows: original crack tip atoms.

on adjacent twin planes. The subsequent growth of the twinned region happened continuously with the applied stress intensity factor rather than at a unique critical value. For this reason, K_{Ic} values for twin formation are not presented in Table 4.5. Only the Chamati and Marinica11 potentials emitted $a_0/2\langle 111\rangle\{11\bar{2}\}$ dislocations, see Fig. 4.10c,e.

For the $[11\bar{2}]$ crack front direction, the fracture behaviors ranged from brittle to ductile or a combination of both. In case of the Simonelli, Mendelev-II, Gordon, Marinica11, and Chiesa potentials, $a_0/2\langle 111\rangle\{\bar{1}10\}$ edge dislocations were emitted from the crack tip, see Fig. 4.10f,h. The crack tip modeled with the Simonelli potential additionally emitted a mixed $a_0/2[1\bar{1}\bar{1}](312)$ dislocation. The Chamati and Gordon cracks exhibited a somewhat different fracture behavior, which is shown in Fig. 4.10d for the Chamati potential. In both cases, the crack first propagated by cleavage before it emitted an $a_0/2[\bar{1}\bar{1}\bar{1}](\bar{1}10)$ edge dislocation. The crack propagated on the (111) plane without any plastic deformation only for the MFS and Marinica07 potentials.

The majority of the potentials showed K_{Ic} values around 1.21 MPa$\sqrt{\text{m}}$ for the $[11\bar{2}]$ crack front direction. The Simonelli and Gordon potentials, however, had more than 10 % lower and higher values, respectively. It is important to note, that the plane perpendicular to

Table 4.5: Summary of simulation results for cracks on the (111) plane in Fe. Lateral straining method: ε^{pre}; CTT: Crack tip transformations; see caption of Table 4.1 for further description.

***K*-controlled cracks (quasi-statically loaded)**						
Potential	K_{Ic}	ΔK	K_G	K_e	K_t	Fracture behavior
(111)[1$\bar{1}$0] crack system						
MFS	—	—	1.05	1.49	1.35	Twin formation on (11$\bar{2}$) plane
Simonelli	—	—	0.93	1.25	1.07	Twin formation on (11$\bar{2}$) plane
Chamati	1.23	—	1.13	1.20	1.17	Emission of $a_0/2[\bar{1}\bar{1}\bar{1}](11\bar{2})$ edge dislocation
Mendelev-II	—	—	0.99	1.19	1.12	Twin formation on (11$\bar{2}$) plane
Gordon	—	—	1.06	1.27	1.19	Twin formation on (11$\bar{2}$) plane
Marinica07	—	—	1.07	1.31	1.27	Twin formation on (11$\bar{2}$) plane
Marinica11	—	—	0.96	1.27	1.28	CTT and $a_0/2[111](11\bar{2})$ edge dislocation
Chiesa	—	—	1.04	1.43	1.36	Twin formation on (11$\bar{2}$) plane
(111)[11$\bar{2}$] crack system						
MFS	1.34	0.50	1.02	1.35	—	Brittle on (111) plane and structural CTT
Simonelli	1.06	—	0.91	1.14	—	$a_0/2[111](\bar{1}10)$ edge, then $a_0/2[\bar{1}\bar{1}\bar{1}](312)$ mixed dislocation
Chamati	1.17	0.07	1.11	1.14	—	First brittle on (111), then $a_0/2[\bar{1}\bar{1}\bar{1}](\bar{1}10)$ dislocation
Mendelev-II	1.27	—	0.97	1.09	—	Emission of $a_0/2[111](\bar{1}10)$ edge dislocation
Gordon	1.08	0.10	1.04	1.19	—	First brittle on (111) plane, then $a_0/2[111](\bar{1}10)$ dislocation
Marinica07	1.25	0.41	1.04	1.22	—	Brittle on (111) plane and CTT
Marinica11	1.22	—	0.94	1.30	—	$a_0/2[111](\bar{1}10)$ dislocation emission and CTT
Chiesa	1.29	—	1.02	1.28	—	Emission of $a_0/2[111](\bar{1}10)$ edge dislocation

Penny-shaped cracks with a = 100 Å and $L_z \approx L_x$								
Potential	L_x (Å)	L_y (Å)	Crack tip	Loading	ε_i (%)	ε_0 (%)	ε_G (%)	Fracture behavior
Mendelev-II	804.3	1008.9	blunted	dynamic	3.85	2.59	1.89	{110} dislocation

the $[11\bar{2}]$ crack front direction is not a mirror plane of the bcc structure. The solution of the crack-tip displacement field according to Ref. [47], however, requires orthotropic elasticity. Its application to the $(111)[11\bar{2}]$ crack system is therefore questionable and the corresponding results for this crack system are only provided for completeness and will not be discussed further.

4.3.2 Strain-controlled penny-shaped cracks: Formation of prismatic dislocation loops

The results for strain-controlled penny-shaped crack on the (111) plane in Fe are given in Table 4.5. The simulation box contained approximately 56 million atoms with a box size of $L_x \times L_y \times L_z \approx 800 \times 1000 \times 800$ Å^3 and a crack length of $a = 100$ Å. Similar to the fracture behavior of straight cracks, the penny-shaped crack initiated crack tip plasticity, see Fig. 4.11. At $\varepsilon_i = 3.85$ %, the crack tip emitted a $a_0/2[111](\bar{1}01)$ dislocation (marked with 0 in the figure), which cross slipped along the curved crack front (marked with 1) and thereby initiated a small deformation twin (marked with 2). The repetition of this process at different parts of the crack front finally led to the annihilation of the cross slipping screw segments and the formation of a full prismatic loop with $a_0/2[111]$ Burgers vector.

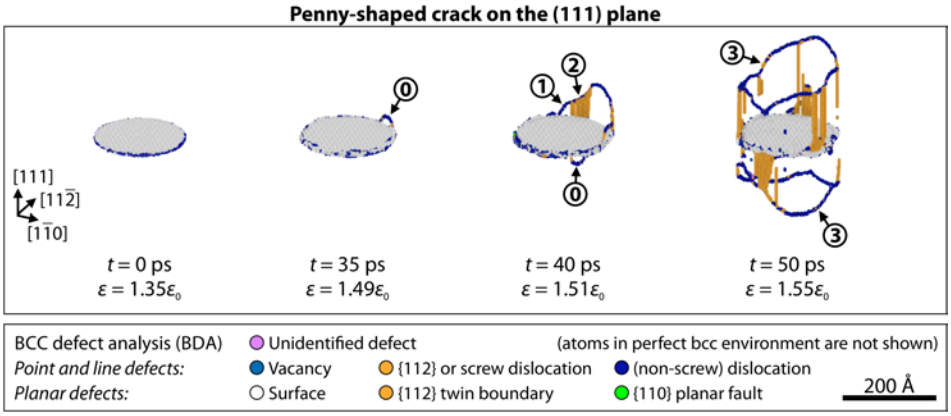

Figure 4.11: Evolution of crack tip plasticity at the atomically sharp penny-shaped crack front on the (111) plane in Fe ($\dot{\varepsilon} = 10^8$ s^{-1}; $a = 100$ Å). Dislocation emission from ⟨112⟩-oriented crack front segments (⓪); cross slipping screw dislocations (①) initiated deformation twins (②); prismatic dislocation loops formed where multiple cross-slipped dislocations accumulate (③).

4.4 Cracks on higher-index planes

Independent of interatomic potential, cracks on $\{112\}$ planes in Fe showed twin formation for $[1\bar{1}0]$ oriented crack fronts and brittle fracture for $[11\bar{1}]$ crack fronts in the quasi-static K-controlled setup. This behavior did not change for dynamically loaded straight and penny-shaped strain-controlled cracks. Similarly, cracks on the (112), (114), and (710) planes in W, which were studied for comparison with the corresponding symmetric grain boundaries (section 5) showed twin formation for $[1\bar{1}0]$ crack fronts and brittle fracture for other crack front directions. The detailed descriptions of the observed fracture processes and effects are given in the following subsections.

Cracks on {112} planes in Fe: Brittle fracture vs. twin formation

The results for cracks on the $(11\bar{2})$ plane in Fe are given in Table 4.6. The simulation boxes contained approximately two million atoms for a box size of $L_x \times L_y \approx 3000 \times 850$ Å^2; the crack length was $a = 1000$ Å. At the $[\bar{1}10]$ crack front orientation, a deformation twin formed by successive emission of $a_0/6[11\bar{1}](112)$ twinning dislocations, see Fig. 4.12a for the strain-controlled quasi-2D edge crack setup. The crack with [111] crack front direction, see Fig. 4.12b, propagated first on the inclined $(\bar{1}01)$ plane until $\varepsilon_a = 2.87\%$. Thereafter, the crack kinked onto the $(10\bar{1})$ plane and finally continued to grow on a plane parallel to the initial $(11\bar{2})$ crack plane. The same initial crack kinking on an inclined $\{110\}$ plane was observed for the K-controlled setup.

The penny-shaped crack initiated deformation twins in the $[11\bar{1}](\bar{1}\bar{1}\bar{2})$ system (marked with 0) at $\pm[1\bar{1}0]$-oriented crack front segments, shown in Fig. 4.12c. The growing twins emitted screw dislocations from their $[11\bar{1}]$-oriented (incoherent) twin boundary (marked with 1). This emission of dislocations from the formed twins took place repeatedly (marked with 3). Emitted dislocations cross slipped from their initial $(\bar{1}\bar{1}\bar{2})$ plane to $(\bar{1}0\bar{1})$ and $(0\bar{1}\bar{1})$ planes while still being attached to the curved crack front (marked with 3). Unlike the (110) crack, however, the screw components did not continue to slip on the next $(\bar{2}1\bar{1})$ and $(1\bar{2}\bar{1})$ planes thereafter. Instead, they cross slipped back on a plane parallel to the initial $(\bar{1}\bar{1}\bar{2})$ plane. In the following, the screw components slipped away from the crack front into the remaining material whilst bowing out on the $(\bar{1}\bar{1}\bar{2})$ twin plane. The same processes took place at the opposite part of the crack, but with opposite sign of the Burgers vector. Where two bowed-out dislocation lines of opposite Burgers vector remained attached to the crack front (marked with 4), the crack propagated in a brittle manner. The propagation was restricted to the region between the two glide planes of the dislocations, which were about 40 Å away from each other. This growing crack did neither show a clear crystallographic crack front direction nor a clear propagation direction, but its macroscopic growth direction was parallel to the $\pm[1\bar{1}0]$ directions. Likewise, the fracture surface exhibited some $\{110\}$ facets, but was in general not on a well-defined crystallographic plane. The initiation strain was $\varepsilon_i = 4.55 \pm 0.02\ \% \approx 1.37\varepsilon_0$ for $a = 60$ Å independent of crack tip sharpness and loading conditions.

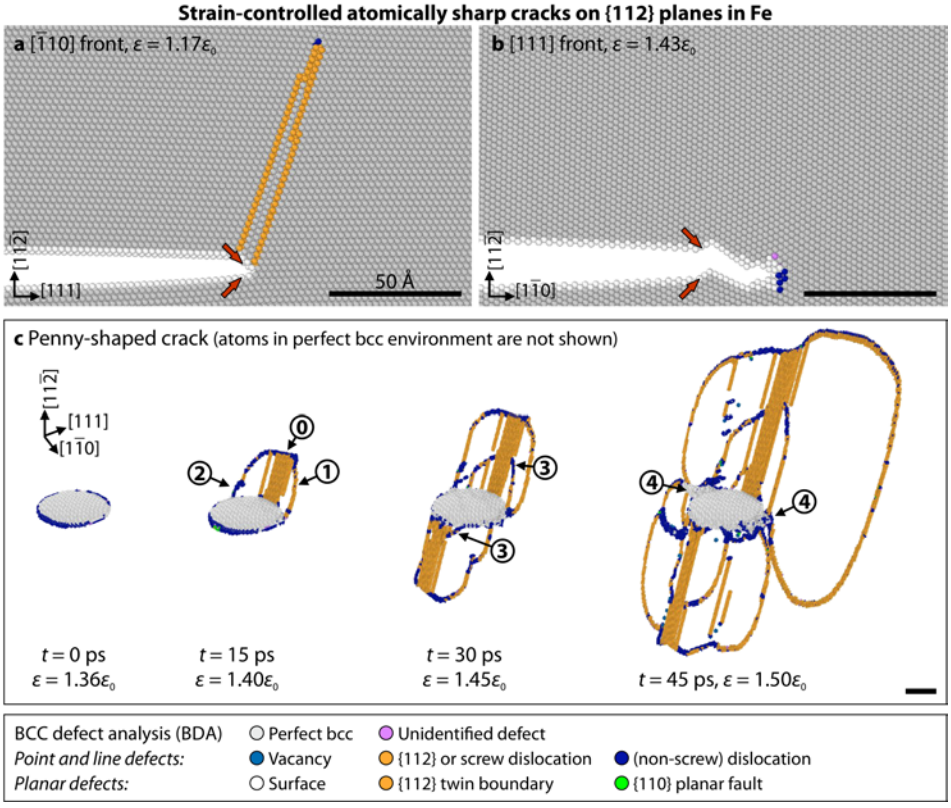

Figure 4.12: Dynamically-loaded atomically sharp cracks on {112} planes in Fe ($\dot{\varepsilon} = 10^8$ s^{-1}). For straight cracks with $a \approx 1000$ Å, different crack front orientations are shown: **a**: $(11\bar{2})[\bar{1}10]$ crack system, deformation twinning in the $[11\bar{1}](112)$ system; **b**: $(11\bar{2})[111]$ crack system, initial brittle crack propagation on inclined {110} planes. **c**: penny-shaped crack with $a = 60$ Å; formation of a twin (⓪), which emitted dislocations (①) from its incoherent twin boundary (along a $[11\bar{1}]$ direction); the emitted dislocations cross slipped along the curved crack front (②) similar to the behavior observed for the (110) crack; the emission of dislocations from $[11\bar{1}]$-oriented twin boundaries took place repeatedly (③); dislocations emitted from twins at opposite sides of the crack met at ±[111]-oriented crack front segments (④). Red arrows: original crack tip atoms.

Table 4.6: Summary of simulation results for cracks on {112} planes in Fe. Lateral straining method of strain-controlled cracks: $\varepsilon^{\mathrm{pre}}$. See caption of Table 4.1 for further description.

***K*-controlled cracks (quasi-statically loaded)**							
Potential	K_{Ic}	ΔK	K_{G}	K_{e}	K_{t}	Fracture behavior	
(112)[1$\bar{1}$0] crack system							
MFS	—	—	0.97	1.41	1.27	Twin	
Mendelev-II	—	—	0.94	1.14	1.09	Twin	
Chiesa	—	—	0.97	1.35	1.28	Twin	
(112)[11$\bar{1}$] crack system							
MFS	1.21	0.50	0.97	1.43	—	Brittle on {110} plane	
Mendelev-II	1.24	0.55	0.94	1.15	—	Brittle on {110} plane	
Chiesa	1.40	0.88	0.97	1.36	—	Brittle on {110} plane	

Quasi-2D edge cracks with $a \approx 1000$ Å								
Potential	L_{x} (Å)	L_{y} (Å)	Crack tip	Loading	$\varepsilon_{\mathrm{i,c}}$ (%)	ε_0 (%)	ε_{G} (%)	Fracture behavior
(11$\bar{2}$)[$\bar{1}$10] crack system								
Chiesa	3003.8	848.4	sharp	dynamic	2.41	2.12	2.01	(112) Twin
(11$\bar{2}$)[111] crack system								
Chiesa	3003.9	848.4	sharp	dynamic	2.85	2.10	2.01	Brittle on ($\bar{1}$01) plane, arrest ($\varepsilon_{\mathrm{a}} = 2.87\%$), brittle on (10$\bar{1}$) plane

Penny-shaped cracks with $a = 60$ Å and $L_{\mathrm{z}} \approx L_{\mathrm{x}}$								
Potential	L_{x} (Å)	L_{y} (Å)	Crack tip	Loading	$\varepsilon_{\mathrm{i,c}}$ (%)	ε_0 (%)	ε_{G} (%)	Fracture behavior
Chiesa	600.8	602.7	sharp	dynamic	4.54	3.31	2.30	Twin
Chiesa	600.8	602.7	sharp	quasi-static	4.55	3.31	2.30	Twin
Chiesa	600.8	603.8	blunted	dynamic	4.54	3.31	2.30	Twin
Chiesa	600.8	603.8	blunted	quasi-static	4.57	3.31	2.30	Twin

Cracks on higher-index planes in W: Twinning, cleavage, crack kinking

For comparison with cracks on the corresponding grain boundary planes, the fracture properties of cracks on additional high-index planes were determined using the ATFS potential for W in the *K*-controlled setup. The results are given in Table 4.7. While the crack tips in the $(114)[1\bar{1}0]$ and $(\bar{1}\bar{1}5)[\bar{1}10]$ systems formed deformation twins, the fracture behavior was brittle in the $(112)[11\bar{1}]$, $(112)[11\bar{1}]$, and $(710)[001]$ crack system. In the latter case, the crack kinked onto an inclined $\{110\}$ plane; in the $(111)[11\bar{2}]$ crack system, a perfect $a_0/2[111](1\bar{1}0)$ edge dislocation was emitted.

The penny-shaped cracks on the (111), (114), and (710) planes initiated deformation twins at $\langle 110\rangle$ oriented crack front segments. For the (114) plane, the influence of the crack radius a was additionally tested. Similar as for the cracks on the (110) plane in Fe, an increase in a resulted in decreasing ε_i values. The detailed mechanisms are visualized and described in direct comparison with the corresponding GB cracks in the following chapter.

Table 4.7: Summary of simulation results for *K*-controlled straight and strain-controlled penny-shaped cracks on high-index planes in W single crystals (ATFS potential). See caption of Table 4.1 for further description.

***K*-controlled cracks (quasi-statically loaded)**						
Crack system	K_{Ic}	ΔK	K_G	K_e	K_t	Fracture behavior
$(111)[1\bar{1}0]$	1.70	—	1.71	2.06	1.77	Twin
$(111)[11\bar{2}]$	1.77	—	1.71	1.91	—	$\{1\bar{1}0\}$ dislocation emission
$(112)[11\bar{1}]$	1.86	0.24	1.65	1.99	—	Brittle
$(114)[\bar{1}10]$	1.57	—	1.68	2.01	1.72	Twin
(710)[001]	2.08	0.45	1.63		—	Brittle on inclined {110} plane
$(\bar{1}\bar{1}5)[\bar{1}10]$	1.58	—	1.67	2.07	1.78	Twin

Penny-shaped cracks with $L_x \approx L_z \approx 0.8L_y$								
Plane	L_y (Å)	Crack tip	a (Å)	Loading, $\dot{\varepsilon}$ (s^{-1})	ε_i (%)	ε_0 (%)	ε_G (%)	Fracture behavior
(111)	1118.4	blunted	100	dynamic, 10^8	4.67	2.90	1.95	Twin
(114)	1002.0	blunted	75	dynamic, 10^8	2.28	2.52	1.62	Twin
(114)	1002.0	blunted	100	dynamic, 10^8	2.12	2.52	1.62	Twin
(114)	1002.0	blunted	200	dynamic, 10^8	1.88	2.52	1.62	Twin
(710)	1002.0	blunted	100	dynamic, 10^8	2.19	2.57	1.53	Twin

5 Cracks with straight and curved crack fronts at grain boundaries

To determine the dependence of the fracture resistance on the microstructure, and in particular on locally varying bonding situations, five symmetric (STGB) and two asymmetric (ATGB) tilt grain boundaries were investigated. The investigated grain boundaries are summarized in Table 5.1. For better readability, GBs are often referred to their Σ-values in the following. The Σ3, Σ9, and Σ25 GBs in W were chosen, because their minimum GB structure is known from literature [244, 288]. The Fe grain boundaries were selected because they are interesting model systems for GBs in polycrystals: either one (Σ7) or both (Σ49) of their adjacent grains have a maximum Schmid factor [300] of $m = 0.5$ with respect to the GB plane normal direction. This makes them preferred barriers to dislocations that were nucleated in one of the grains. When these dislocations pile up and increase the local stresses at the GB, crack nucleation becomes more and more likely [410]. For this reason, the crack propagation at these GBs is studied here in detail. For the interaction of a GB crack with absorbed GB dislocations, the reader is referred to chapter 6.

Fig. 5.1 shows the relaxed atomistic configurations and distribution of hydrostatic atomic stresses σ_h at the GB structures. The structural units [255–257] are marked along with their periodicity lengths λ. Periodically assembled triangles and pentagons construct the Σ3 and Σ9 GBs, respectively. The Σ25 STGB contains one triangle followed by two tetragons along the GB. In this case, five different possible crack tip positions are marked in Fig. 5.1f. Fig. 5.1e and g compare the relaxed atomistic configurations of the Σ49 and Σ7 GB structures, respectively. Ship-like structures construct the Σ7 ATGB and distorted rhombuses the Σ49 STGB. Note that the definition of these structural units is somewhat arbitrary as these GB structures have not yet been reported in the literature. Possible positions of crack tips and absorbed dislocations are also marked for the Σ7 ATGB in Fig. 5.1g.

Table 5.1: Overview of grain boundaries in W and Fe, their abbreviations used in the text, surface and GB energies, γ_s and γ_{GB}, shape and characteristic length λ of their periodically repeated structural units, see Fig. 5.1; the subscripts 1 and 2 refer to the corresponding coordinate systems of the two crystals; λ_0 is the repeat distance of the rotated crystal structure in x direction: $\lambda_0 = \max(\|\underline{n}_1\|, \|\underline{n}_2\|)a_0$ ($\underline{n}_{1,2}$: GB plane normal vectors).

Element, grain boundary	Abbrev.	γ_s (J/m^2)	γ_{GB} (J/m^2)	λ (Å)	λ (λ_0)	Structural unit
W, $\Sigma3(111)_1/(11\bar{1})_2$ 70.5°/[1$\bar{1}$0]	Σ3	3.301	2.354	3.88	1/2	triangle
W, $\Sigma3(112)_1/(\bar{1}\bar{1}2)_2$ 60°/[11$\bar{1}$]	Σ3T	3.045	0.391	4.48	1	rhombus
W, $\Sigma3(111)_1/(\bar{1}\bar{1}5)_2$ 70.5°/[1$\bar{1}$0]	Σ3A	3.301/3.139	0.956	11.63	1/2	bow tie
W, $\Sigma9(114)/(\bar{1}\bar{1}4)_2$ 38.9°/[1$\bar{1}$0]	Σ9	3.159	2.011	4.75	1/2	pentagon
W, $\Sigma25(710)_1/(7\bar{1}0)_2$ 16.3°/[001]	Σ25	3.002	1.681	11.19	1/2	triangle, 2 tetragons
Fe, $\Sigma7(\bar{1}\bar{1}1)_1/(11\,\bar{1}\,\bar{5})_2$ 135.6°/[112]	Σ7	2.113/1.948	1.957	14.19	1/2	ship-like
Fe, $\Sigma49(9\bar{1}4)_1/(1\bar{9}4)_2$ 88.8°/[112]	Σ49	1.957	1.792	5.79	1/6	distorted rhombus

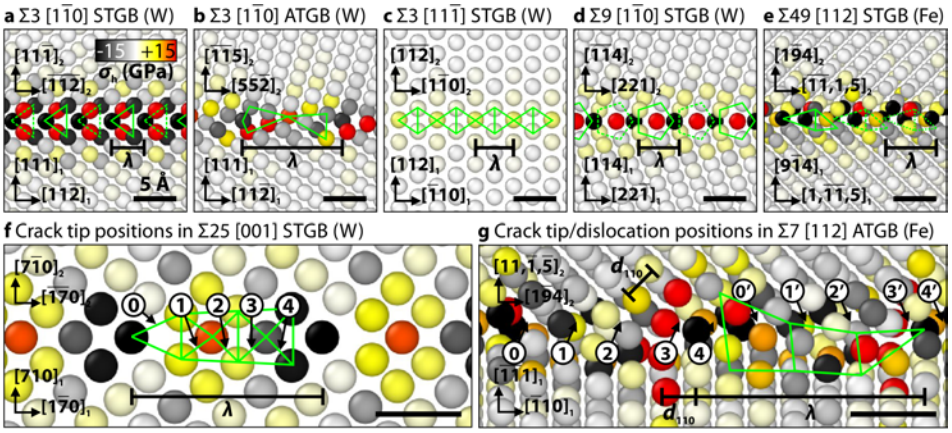

Figure 5.1: Relaxed configurations and distribution of atomic stresses at the studied grain boundaries in W and Fe. **a**-**e**: Σ3, Σ9, and Σ49 GBs; **f**,**g**: Σ25 STGB and Σ7 ATGB; indicated possible crack tip and dislocation positions. See Table 5.1 for the description of the periodically repeated structural units (marked with green lines) and the definition of their periodicity length λ; solid and dashed lines connect atoms lying in different planes; atomic colors: hydrostatic atomic stress $\sigma_h=(\sigma_{xx}+\sigma_{yy}+\sigma_{zz})/3$, see section 3.5 for details.

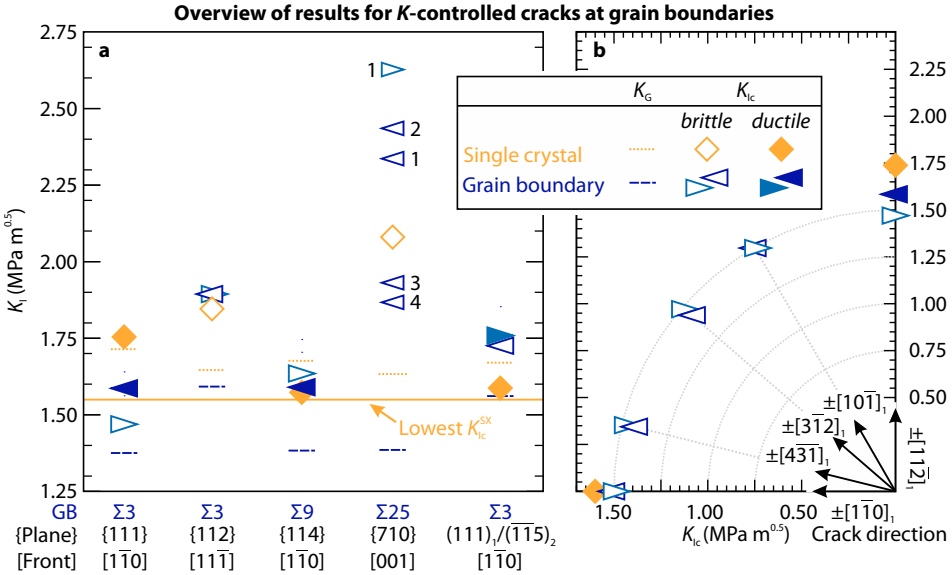

Figure 5.2: Overview of results for quasi-static K-controlled cracks at GBs in W. **a**: Comparison of determined values for the fracture toughness K_{Ic} at different GBs with the theoretical predictions K_G and results for cracks in equally oriented single crystals. **b**: Variation of crack propagation directions within the Σ3(111)$_1$/(11$\bar{1}$)$_2$ 70.5°/[1$\bar{1}$0] STGB. Results are taken from my diploma thesis [121] and have been published in Ref. [94].

Grain boundary cracks were inserted using the same methodologies as described in section 3.3 for K-controlled as well as for strain-controlled straight and penny-shaped cracks. For each GB, at least the two anti-parallel propagation directions $\pm x_1 = \pm[h\,k\,l]$ are investigated, which are perpendicular to both the tilt axis $[uvw]$ and the normal of the GB plane in grain 1 ($\underline{n}_1$): $\underline{x}_1 = [uvw] \times \underline{n}_1$. Here and in the following, the subscript 1 refers to the corresponding coordinate system of crystal 1; likewise, a subscript 2 indicates crystallographic planes and directions in grain 2. The superscripts $+[h\,k\,l]$ and $-[h\,k\,l]$ are used to distinguish the corresponding critical values, i.e., $\varepsilon_\mathrm{i}^{-[h\,k\,l]}$, $K_\mathrm{Ic}^{-[h\,k\,l]}$ and $\varepsilon_\mathrm{i}^{+[h\,k\,l]}$, $K_\mathrm{Ic}^{+[h\,k\,l]}$. If not mentioned otherwise, these directions are always referring to the coordinate system of crystal 1 for the sake of readability. The results for the K-controlled GB cracks are summarized in Fig. 5.2. Since these results were determined during my diploma thesis [121] and have been already published [94], they are only presented here for completeness but not described, analyzed, or discussed in greater detail.

All dynamic simulations were performed at a strain rate of $\dot{\varepsilon} = 10^8$ s^{-1} if not stated otherwise. The remaining simulation details are given in the corresponding Tables 5.2-5.6. Characteristic snapshots of the GB cracks and the corresponding cracks in single crystals are shown in Figs. 5.3-5.9.

5.1 Cracks at Σ3 GBs: Dominance of brittle fracture

The cracks at the $\Sigma3(111)_1/(11\bar{1})_2$ 70.5°/$[1\bar{1}0]$ STGB and the $\Sigma3(111)_1/(\bar{1}\bar{1}5)_2$ 70.5°/$[1\bar{1}0]$ ATGB showed direction-dependent fracture behavior, where the crack propagated brittle in $+[11\bar{2}]_1$ direction and twins formed in $-[11\bar{2}]_1$ direction. Cracks at the $\Sigma3(112)_1/(\bar{1}\bar{1}\bar{2})_2$ 60°/$[11\bar{1}]$ STGB initiated brittle fracture independent of propagation direction. The results in the K-controlled setup are shown in Fig. 5.2 in comparison with the corresponding values for cracks in the equally-oriented single crystal, cf. Table 4.7. In all cases, the observed crack tip events occurred at higher K_Ic values than predicted by the corresponding theoretical fracture toughness according to Griffith for GB cracks, cf. Eqs. (2.22-2.23). For the $\Sigma3(112)_1/(\bar{1}\bar{1}\bar{2})_2$ 60°/$[11\bar{1}]$ STGB, the fracture toughness of the GB (1.90 MPa$\sqrt{\mathrm{m}}$) was even higher than the critical stress intensity factor of the equally-oriented single crystal (1.86 MPa$\sqrt{\mathrm{m}}$). The following paragraphs focus on the $\Sigma3(111)_1/(11\bar{1})_2$ 70.5°/$[1\bar{1}0]$ STGB, which was extensively studied to determine the role of crack line tension and the influence of crack front curvature on the bond trapping effect.

The results for straight cracks at the Σ3 GBs are given in Table 5.2 and exemplarily shown in Fig. 5.3a,b for the strain-controlled quasi-2D edge cracks. For this GB, ten different anti-parallel propagation directions were tested. All cracks initiated brittle fracture with the $-[11\bar{2}]$ crack propagation direction being the only exception. In this direction, a deformation twin formed, see Fig. 5.3a. The twin formation took place in a similar manner as in the corresponding single crystal, see e.g. Fig. 4.10 for examples in Fe. Twin formation was also observed in the corresponding W single crystal, cf. Table 4.7.

In both K- and strain-controlled setups, the critical strains for twin formation ($\varepsilon_\mathrm{i}^{-[11\bar{2}]} = 1.26\varepsilon_0$ and $K_\mathrm{Ic}^{-[11\bar{2}]} = 1.15K_\mathrm{G}$) are higher than for brittle propagation in the opposite direction

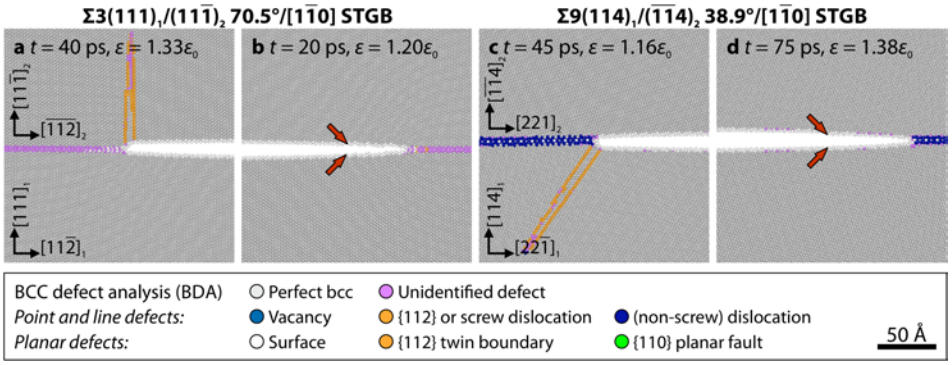

Figure 5.3: Dynamically loaded cracks at the Σ3 and Σ9 STGBs in W (quasi-2D edge crack setup; $\dot{\varepsilon} = 10^8$ s^{-1}). The $[1\bar{1}0]$ tilt axis is orthogonal to the plane of paper; consult Table 5.2 for the simulation details. **a**: Σ3 GB, twin formation; **b**: Σ3 GB, brittle crack propagation; **c**: Σ9 GB, twin formation **d**: Σ9 GB, brittle crack propagation. Red arrows: original crack tip atoms; note that the Σ3 GB was classified as "unidentified defect" whereas the Σ9 GB was detected as "(non-screw) dislocation".

($\varepsilon_i^{+[11\bar{2}]} = 1.22\varepsilon_0$ and $K_{Ic}^{+[11\bar{2}]} = 1.07K_G$). In case of the K-controlled setups, none of the other studied propagation directions exhibited a higher critical value, see Fig. 5.2b. All values for cracks at the Σ3 STGB were lower than the critical stress intensity factor in the equally-oriented $(111)[1\bar{1}0]$ crack system (1.70 MPa$\sqrt{\text{m}}$).

The influence of the crack length on the lattice trapping ratio $\Delta\varepsilon$ was tested using atomically sharp cracks in the quasi-2D central crack setup, cf. Table 5.2. With increasing the crack length from a = 100 Å to 200 Å, the lattice trapping range $\Delta\varepsilon$ increased from 0.06 to 0.11. Both values were lower than the lattice trapping range for the corresponding K-controlled crack ($\Delta K = 0.13$).

The results for penny-shaped cracks on the Σ3 GBs are detailed in Table 5.2. The characteristic crack tip processes of the penny-shaped $\Sigma3(111)_1/(11\bar{1})_2$ 70.5°/$[1\bar{1}0]$ STGB crack are shown in Fig. 5.4 along with the corresponding SX crack on the (111) plane. All cracks showed plastic deformation on planes perpendicular to the local crack propagation direction. The points in time, at which crack tip plasticity was observed, however, were different. Whereas twin formation was an accompanying process to the otherwise purely brittle propagation of the GB crack, the crack tips in the SX deformed in a plastic manner at ε_i.

In case of the W single crystal, see Fig. 5.4a, the initial plastic event was the formation of a deformation twin on the $(11\bar{2})$ plane (marked with 0) at the $[1\bar{1}0]$ crack front segment. The growing twin emitted two dislocations from its ⟨111⟩-oriented incoherent twin boundary (marked with 1). The screw components cross slipped along the curved crack front (marked with 2), annihilated, and formed a prismatic loop (marked with 3).

The GB crack, on the other hand, showed predominantly brittle crack propagation, see Fig. 5.4b. The growth rate was higher in $[11\bar{2}]_1$, $[\bar{2}11]_1$, and $[1\bar{2}1]_1$ direction than in the other directions. As a result, the crack took on a threefold symmetric shape (marked with 4) and those crack front segments became more pronounced, which were perpendicular to

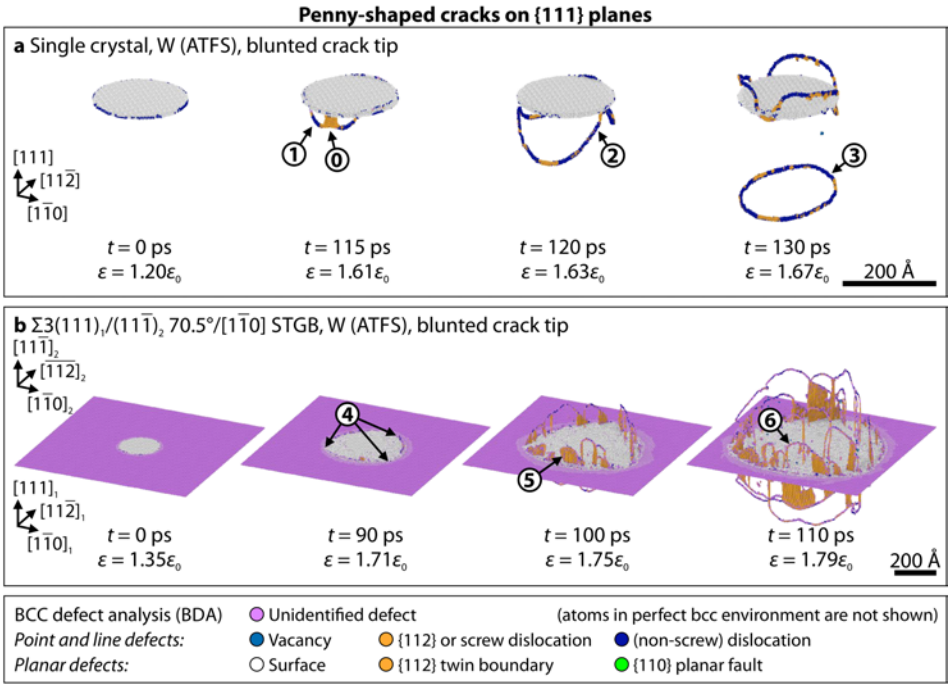

Figure 5.4: Fracture behavior of penny-shaped cracks on the (111) (grain boundary) plane in W ($\dot{\varepsilon} = 5{\times}10^7$ s^{-1}); **a**: single crystal; deformation twins at ⟨110⟩-oriented crack fronts (⓪); dislocation emission from twins (①); cross slip along the curved crack front (②); formation of a complete prismatic dislocation loop (③); **b**: $\Sigma3(111)_1/(11\bar{1})_2$ 70.5°/[1$\bar{1}$0] GB; initial brittle propagation; faster propagation in certain ⟨112⟩ directions than in other directions led to a three-fold rotation symmetry of the propagated crack (④); deformation twins nucleated at ⟨110⟩-oriented crack fronts (⑤) during crack growth; dislocation emission from growing twins (⑥). The Σ3 GB was classified as "unidentified defect".

the fast-growing directions. At these [1$\bar{1}$0], [01$\bar{1}$], and [$\bar{1}$01] crack front segments, twins formed (marked with 5) and dislocations were subsequently emitted from the growing twins (marked with 6).

The critical strains of the GB depended on the crack radius and varied between $\varepsilon_c = 3.81\,\% = 1.47\varepsilon_0$ ($a = 100$ Å) and $\varepsilon_c = 2.64\,\% = 1.02\varepsilon_0$ ($a = 200$ Å). The value for $a = 100$ Å was approximately 9 % lower than the corresponding ratio for the single crystal case ($\varepsilon_i = 1.61\varepsilon_0$). Note that in cases of initially brittle fracture of penny-shaped cracks, the values for the initiation strains were those values that led to an unstable crack growth. The presented values of ε_i thus neglect minor atomic rearrangements at the crack tip and a possible stable crack growth that was limited to a few Å.

Similar to the determination of the lattice trapping ratios $\Delta\varepsilon$ for the quasi-2D central cracks, $\Delta\varepsilon$ was determined for atomically sharp penny-shaped cracks with radii a = 100, 150, and 200 Å, cf. Table 5.2. The determined lattice trapping ratios increased from 0.17

(a = 100 Å) to 0.24 (a = 200 Å), which are all higher than the corresponding values for the straight GB cracks ($\Delta\varepsilon$ = 0.06. . .0.11; ΔK = 0.13).

Table 5.2: Summary of simulation results for cracks at Σ3 GBs in W (ATFS potential); values for $\Delta\varepsilon$ in parentheses; see Table 4.1 for further description.

***K*-controlled cracks (quasi-statically loaded)**						
Propagation direction	K_{Ic}	ΔK	K_G	K_e	K_t	Fracture behavior
$\Sigma3(111)_1/(11\bar{1})_2$ 70.5°/[1$\bar{1}$0] STGB						
+[11$\bar{2}$]$_1$	1.47	0.13	1.38	2.06	1.77	Brittle
−[11$\bar{2}$]$_1$	1.58	—	1.38	2.06	1.77	Twin
+[10$\bar{1}$]$_1$	1.50	—	1.38	1.91	—	Brittle
−[10$\bar{1}$]$_1$	1.50	—	1.38	1.91	—	Brittle
+[3$\bar{1}\bar{2}$]$_1$	1.48	—	1.38	—	—	Brittle
−[3$\bar{1}\bar{2}$]$_1$	1.43	—	1.38	—	—	Brittle
+[4$\bar{3}\bar{1}$]$_1$	1.47	—	1.38	—	—	Brittle
−[4$\bar{3}\bar{1}$]$_1$	1.43	—	1.38	—	—	Brittle
+[1$\bar{1}$0]$_1$	1.50	—	1.38	1.91	—	Brittle
−[1$\bar{1}$0]$_1$	1.50	—	1.38	1.91	—	Brittle
$\Sigma3(111)_1/(\bar{1}\bar{1}5)_2$ 70.5°/[1$\bar{1}$0] ATGB						
+[11$\bar{2}$]$_1$	1.85	—	1.56	2.06	1.77	Brittle
−[11$\bar{2}$]$_1$	1.76	—	1.56	2.06	1.77	Twin
$\Sigma3(112)_1/(\bar{1}\bar{1}2)_2$ 60°/[11$\bar{1}$] STGB						
+[$\bar{1}$10]$_1$	1.90	—	1.59	1.99	—	Brittle
−[$\bar{1}$10]$_1$	1.90	0.30	1.59	1.99	—	Brittle

Quasi-2D edge cracks at $\Sigma3(111)_1/(11\bar{1})_2$ 70.5°/[1$\bar{1}$0] STGB with $L_x \approx 3L_y$									
Dir.	L_y (Å)	a_{eff} (Å)	Crack tip	Loading, $\dot{\varepsilon}$ (s^{-1})	LCM	ε_i (%)	ε_0 (%)	ε_G (%)	Behavior
+[11$\bar{2}$]$_1$	997.8	926	blunted	dynamic, 10^8	σ^{min}	1.71	1.56	1.64	Brittle
−[11$\bar{2}$]$_1$	997.8	926	blunted	dynamic, 10^8	σ^{min}	1.96	1.56	1.64	Twin

Quasi-2D central cracks at $\Sigma3(111)_1/(11\bar{1})_2$ 70.5°/[1$\bar{1}$0] STGB with $L_x \approx L_y$									
Dir.	L_y (Å)	a_{eff} (Å)	Crack tip	Loading, $\dot{\varepsilon}$ (s^{-1})	LCM	ε_c (%)	ε_0 (%)	ε_G (%)	Behavior ($\Delta\varepsilon$)
±[11$\bar{2}$]$_1$	903.7	100	sharp	quasi-static	ε^{pre}	2.38	1.56	1.64	Brittle (0.06)
±[11$\bar{2}$]$_1$	903.7	150	sharp	quasi-static	ε^{pre}	2.14	1.56	1.64	Brittle (0.10)
±[11$\bar{2}$]$_1$	903.7	200	sharp	quasi-static	ε^{pre}	2.06	1.56	1.64	Brittle (0.11)

Penny-shaped cracks at $\Sigma3(111)_1/(11\bar{1})_2$ 70.5°/[1$\bar{1}$0] STGB with $L_z \approx L_x \approx L_y$								
L_y (Å)	a_{eff} (Å)	Crack tip	Loading, $\dot{\varepsilon}$ (s^{-1})	LCM	$\varepsilon_{i,c}$ (%)	ε_0 (%)	ε_G (%)	Behavior ($\Delta\varepsilon$)
903.7	100	sharp	dynamic, 5×10^7	ε^{pre}	3.84	2.59	1.64	Brittle
903.7	100	sharp	quasi-static	ε^{pre}	3.81	2.59	1.64	Brittle (0.17)
902.9	100	blunted	dynamic, 5×10^7	ε^{pre}	3.87	2.59	1.64	Brittle
902.9	100	blunted	dynamic, 10^8	ε^{pre}	3.91	2.59	1.64	Brittle
903.7	150	sharp	quasi-static	ε^{pre}	3.10	2.59	1.64	Brittle (0.19
903.7	200	sharp	quasi-static	ε^{pre}	2.64	2.59	1.64	Brittle (0.24)

5.2 Cracks at the Σ9 GB: Direction-dependent behavior

The results for straight cracks at the $\Sigma9(1\,1\,4)_1/(\bar{1}\,\bar{1}\,4)_2$ 38.9°/$[1\bar{1}0]$ GB are given in Table 5.3 and exemplarily shown in Fig. 5.3c,d for the strain-controlled quasi-2D edge cracks. Similar to the straight cracks at the Σ3 STGB, cracks at the Σ9 STGB showed direction-dependent fracture behavior. A deformation twin formed at the crack tip in $-[2\,2\,\bar{1}]_1$ propagation direction, see Fig. 5.3c. In the opposite propagation direction, the fracture behavior was completely brittle, see Fig. 5.3d. The critical strain for brittle propagation ($\varepsilon_i^{+[2\,2\,\bar{1}]} = 1.23\varepsilon_0$) was higher than for twin formation ($\varepsilon_i^{-[2\,2\,\bar{1}]} = 1.13\varepsilon_0$).

In both $\pm[2\,2\,\bar{1}]$ propagation directions, the fracture toughness of the GB was higher ($K_{Ic}^{-[2\,2\,\bar{1}]} = 1.58\ \mathrm{MPa}\sqrt{\mathrm{m}}$; $K_{Ic}^{+[2\,2\,\bar{1}]} = 1.63\ \mathrm{MPa}\sqrt{\mathrm{m}}$) than in the equally-oriented single crystal ($K_{Ic} = 1.57\ \mathrm{MPa}\sqrt{\mathrm{m}}$), cf. Table 4.7, where twin formation was observed.

The fracture behavior of penny-shaped cracks was predominantly ductile, both for cracks at the GB and in the corresponding single crystal. Characteristic configurations of both cracks are shown in Fig. 5.5.

Table 5.3: Summary of simulation results for cracks on $\Sigma9(1\,1\,4)_1/(\bar{1}\,\bar{1}\,4)_2$ 38.9°/$[1\bar{1}0]$ STGB in W (ATFS potential). See caption of Table 4.1 for further description.

***K*-controlled cracks (quasi-statically loaded)**									
Propagation direction		K_{Ic}	ΔK	K_G	K_e	K_t	Fracture behavior		
$+[22\bar{1}]_1$		1.63	—	1.38	2.74	4.64	Brittle		
$-[22\bar{1}]_1$		1.58	—	1.38	2.01	1.72	Twin		
Quasi-2D edge cracks with $L_x \approx 2L_y$									
Direction	L_y (Å)	a_{eff} (Å)	Crack tip	Loading, $\dot{\varepsilon}$ (s^{-1})	LCM	$\varepsilon_{i,c}$ (%)	ε_0 (%)	ε_G (%)	Behavior
$+[22\bar{1}]_1$	1002.0	667	blunted	dynamic, 10^8	ε^{pre}	1.75	1.42	1.36	Brittle
$-[22\bar{1}]_1$	1002.0	667	blunted	dynamic, 10^8	ε^{pre}	1.60	1.42	1.36	Twin
Penny-shaped cracks with $L_z \approx L_x$									
L_x (Å)	L_y (Å)	a_{eff} (Å)	Crack tip	Loading, $\dot{\varepsilon}$ (s^{-1})	LCM	$\varepsilon_{i,c}$ (%)	ε_0 (%)	ε_G (%)	Behavior
797.6	1002.0	75	blunted	dynamic, 10^8	ε^{pre}	2.40	2.14	1.35	Twin
797.6	1002.0	100	blunted	dynamic, 10^8	ε^{pre}	2.21	2.14	1.35	Twin
797.6	1002.0	150	blunted	dynamic, 10^8	ε^{pre}	2.00	2.14	1.35	Twin
797.6	1002.0	200	blunted	dynamic, 10^8	ε^{pre}	1.86	2.14	1.35	Twin
1586.8	1002.0	100	blunted	dynamic, 10^8	ε^{pre}	2.21	2.14	1.35	Twin
1586.8	1002.0	200	blunted	dynamic, 10^8	ε^{pre}	1.87	2.14	1.35	Twin
1586.8	1002.0	300	blunted	dynamic, 10^8	ε^{pre}	1.73	2.14	1.35	Twin
1586.8	2000.0	75	blunted	dynamic, 10^8	ε^{pre}	2.33	1.56	0.96	Twin
1586.8	2000.0	100	blunted	dynamic, 10^8	ε^{pre}	2.11	1.56	0.96	Twin
1586.8	2000.0	200	blunted	dynamic, 10^8	ε^{pre}	1.73	1.56	0.96	Twin
1586.8	2000.0	300	blunted	dynamic, 10^8	ε^{pre}	1.56	1.56	0.96	Twin
1586.8	2000.0	400	blunted	dynamic, 10^8	ε^{pre}	1.40	1.56	0.96	Twin

In the single crystal, see Fig. 5.5a, crack tip plasticity started with twin formation in the $[111](11\bar{2})$ twin system at both $\pm[1\bar{1}0]$ crack front segments (marked with 0). At their $\langle 111\rangle$-oriented incoherent twin boundaries, the twins emitted dislocations that remained attached to the crack front (marked with 1). This led to the bowing out of the nucleated dislocation (marked with 2) and the cutting of the screw components along the crack face (marked with 3).

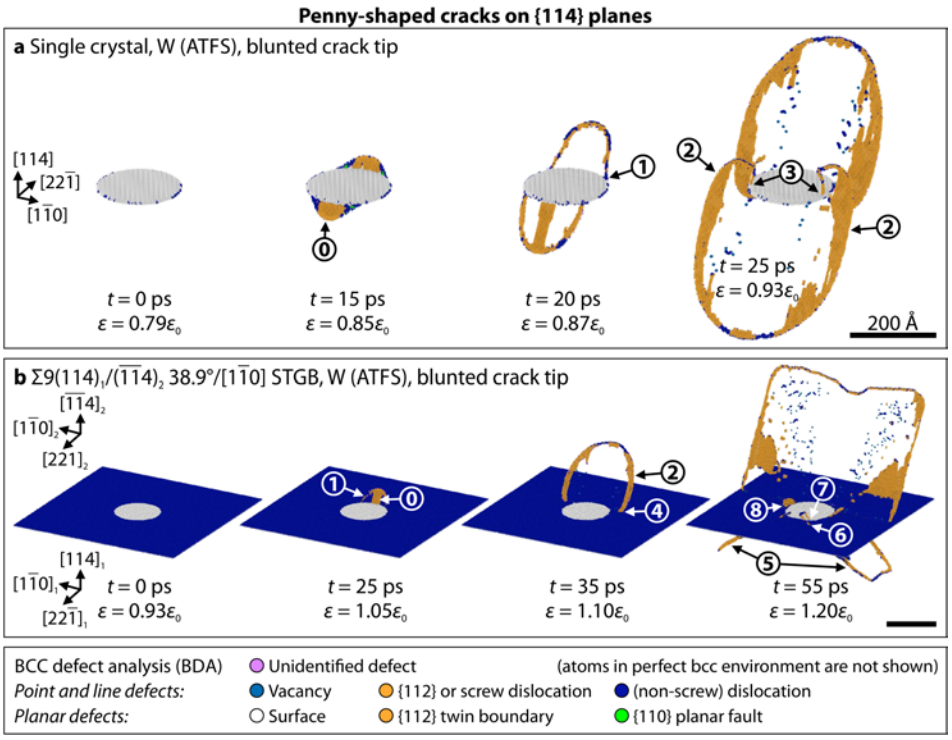

Figure 5.5: Crack tip plasticity at penny-shaped cracks on the (114) (grain boundary) plane in W ($\dot{\varepsilon} = 10^8$ s^{-1}). **a**: the crack in the single crystal emitted two deformation twins (⓪) from the $\langle 110\rangle$-oriented crack fronts at opposite sides of the crack; the twins vanished and emitted screw-oriented dislocations (①); the dislocations glided away from the crack front leading to a bow out of the dislocation half loop (②); dislocations cut the crack front on the opposite crack face where they were emitted from (③). **b**: the crack at the Σ9{114} GB first emitted a $(112)_2$ deformation twin (⓪) in grain 2; then, the twin collapsed into a dislocation half loop (②), which cut along the GB (④); deformation in grain 1 started afterwards and on other {112} planes (⑤) than in grain 2; dislocations nucleated on these planes glided first along the GB (⑥) and then entered grain 2 by penetrating through the GB (⑦); thereafter, a twin also formed on the $(1\bar{1}\bar{2})_2$ plane (⑧). The GB was classified as "(non-)screw dislocation".

At the GB, see Fig. 5.5b, twin formation (marked with 0) and subsequent dislocation emission (marked with 1) happened in a similar way as described before for the single crystal, but in the $[\bar{1}\bar{1}1]_2(112)_2$ twin system. In this case, the emitted dislocation (marked with 2) did not bow out, but cut along the grain boundary towards the boundary of the simulation box (marked with 4). At the location where the $a_0/2[\bar{1}\bar{1}1]_2(112)_2$ dislocation started to cut along the GB, plastic deformation also started in grain 1: dislocations were emitted from two nucleated twins in the $[1\bar{1}\bar{1}]_1(1\bar{1}2)_1$ and $[1\bar{1}1]_1(\bar{1}12)_1$ systems (marked with 5). They first slipped along the GB (marked with 6) in a similar manner as the $a_0/2[\bar{1}\bar{1}1]_2(112)_2$ dislocation and were then transmitted through the GB onto $\{110\}$ planes in grain 2 (marked with 7):

$$[1\bar{1}\bar{1}]_1(1\bar{1}2)_1 \rightarrow [1\bar{1}\bar{1}]_2(01\bar{1})_2 \quad (5.1)$$

$$[1\bar{1}1]_1(\bar{1}12)_1 \rightarrow [1\bar{1}1]_2(10\bar{1})_2 \quad (5.2)$$

It is interesting to note that such a slip transmission did not occur for the $[\bar{1}\bar{1}1]_2(112)_2$ system, which was activated first. Finally, two twins in the $[1\bar{1}1]_2(1\bar{1}\bar{2})_2$ and $[1\bar{1}\bar{1}]_2(1\bar{1}2)_2$ systems were emitted from the crack tip in grain 2 (marked with 8).

In addition, different box sizes, aspect ratios, and crack radii were tested. In all cases, the observed fracture mechanisms were equal to the processes described above. Whereas variations in the aspect ratio did not influence the critical strain, see Table 5.3, crack radius and box size affected ε_i markedly. Similar to the observations for single crystal cracks, the critical strain decreased with increasing crack radii. In contrast to single crystal cracks, the initiation strains were not independent of the box length L_y. Instead, the values were always higher for smaller L_y than for the larger system. The difference between these values, $\Delta\varepsilon_i$, increased from 0.07 % for $a = 75$ Å to 0.17 % for $a = 300$ Å. It is interesting to note that the critical strains ε_i became smaller than the predicted value ε_0 for $a > 100$ Å and $a > 300$ Å for the small and large systems, respectively. When compared to the simulation results for the single crystal cracks of the same orientation, see Table 4.7, two important observations can be made: first, it is striking that all GB cracks showed critical strains that are approximately 0.1 % higher than in the corresponding single crystals. Second, the critical strains in single crystals were smaller than ε_0 already for $a = 75$ Å.

5.3 Cracks at the Σ25 GB: Position- and direction-dependent fracture properties

The results for straight cracks on the $\Sigma25(710)_1/(7\bar{1}0)_2$ 16.3°/[001] GB are given in Table 5.4 and exemplarily shown in Fig. 5.6 for the strain-controlled quasi-2D edge cracks. In $+[\bar{1}70]_1$ propagation direction, both fracture behavior and critical strains were strongly dependent on the initial crack tip position: when the crack was initially placed at position 4, cf. Fig. 5.1f, this bond broke at $\varepsilon_{i,(4,4)}^{+[\bar{1}70]} = 1.18\varepsilon_0$ (the subscript indicates the initial and current crack tip positions), see Fig. 5.6b. The bond at position 3 broke at $\varepsilon_{i,(4,3)}^{+[\bar{1}70]} = 1.32\varepsilon_0$, see

subfigure c, and the crack arrested at position 2. At this position, the crack no longer propagated in a brittle manner, but initiated plastic deformation on inclined $\{1\,1\,0\}$ planes, see subfigure d. Neither this behavior nor the fracture strain changed when the crack tip was initially placed at position 2, cf. Fig. 5.6d and e, i.e. at $\varepsilon_{\mathrm{i},(4,2)}^{+[\bar{1}\,7\,0]} = \varepsilon_{\mathrm{i},(4,4)}^{+[\bar{1}\,7\,0]} = 1.72\varepsilon_0$. It should be noted, that for this situation a decreased crack length a = 400 Å, quasi-static loading, and the 3D edge crack setup were tested additionally. In all cases, the observed behavior and determined critical strains were similar to the behavior described here. Furthermore, this ordering of the fracture resistances at different crack tip position was the same as in the quasi-static K–controlled setup, cf. Table 5.4.

In the opposite $-[\bar{1}\,7\,0]_1$ propagation direction, position 1 was the only location where the crack tip was stable during energy minimization, see Fig. 5.6f. At all other positions the crack either propagated or closed to another equivalent position 1. As it can be seen in Fig. 5.6f, the crack tip initiated deformation structures that are similar to those observed for the $+[\bar{1}\,7\,0]_1$ propagation direction, but at a lower critical strain $\varepsilon_{\mathrm{i},(1,1)}^{-[\bar{1}\,7\,0]} = 1.68\varepsilon_0$. Dependent

Table 5.4: Summary of simulation results for cracks on $\Sigma25(7\,1\,0)_1/(7\bar{1}\,0)_2$ 16.3°/[0 0 1] STGB in W (ATFS potential). See caption of Table 4.1 for further description. See Fig. 5.1f for the crack tip positions. Lateral straining method for strain-controlled cracks: $\varepsilon^{\mathrm{pre}}$.

***K*-controlled cracks (quasi-statically loaded)**								
Propagation direction			Crack tip position	K_{Ic}	ΔK	K_{G}	K_{e}	K_{t}	Fracture behavior
$+[\bar{1}70]_1$			1	2.34	—	1.39		—	Brittle
$+[\bar{1}70]_1$			2	2.44	—	1.39		—	Brittle
$+[\bar{1}70]_1$			3	1.93	—	1.39		—	Brittle
$+[\bar{1}70]_1$			4	1.87	0.41	1.39		—	Brittle
$-[\bar{1}70]_1$			1	2.63	1.37	1.39		—	Brittle
Quasi-2D sharp edge cracks with $L_x \approx 3L_y$								
Direction	L_y (Å)	a_{eff} (Å)	Position	Loading, $\dot{\varepsilon}$ (s^{-1})	$\varepsilon_{\mathrm{i,c}}$ (%)	ε_0 (%)	ε_{G} (%)	Fracture behavior
$+[\bar{1}70]_1$	982.3	996.5	4	dynamic, 10^8	1.82	1.55	1.34	Brittle, arrest at 3
$+[\bar{1}70]_1$	982.3	996.5	4	quasi-static	1.80	1.55	1.34	Brittle, arrest at 3
$+[\bar{1}70]_1$	982.3	997.7	3	quasi-static	2.06	1.55	1.34	Brittle, arrest at 2
$+[\bar{1}70]_1$	982.3	999.8	2	dynamic, 10^8	2.66	1.55	1.34	Brittle & ductile
$+[\bar{1}70]_1$	982.3	999.8	2	quasi-static	2.57	1.55	1.34	Brittle & ductile
$-[\bar{1}70]_1$	982.3	992.7	1	dynamic, 10^8	2.60	1.55	1.34	Ductile
3D edge crack with $L_x \approx L_y \approx L_z$								
Direction	L_y (Å)	a_{eff} (Å)	Position	Loading, $\dot{\varepsilon}$ (s^{-1})	ε_{i} (%)	ε_0 (%)	ε_{G} (%)	Fracture behavior
$+[\bar{1}70]_1$	982.3	385.7	3	dynamic, 10^8	2.06	2.01	1.33	Brittle, arrest at 2
Penny-shaped cracks with $L_z \approx L_x$								
L_x (Å)	L_y (Å)	a_{eff} (Å)	Crack tip	Loading, $\dot{\varepsilon}$ (s^{-1})	ε_{i} (%)	ε_0 (%)	ε_{G} (%)	Fracture behavior
1000	982.3	100	blunted	dynamic, 10^8	2.32	2.01	1.33	Twin

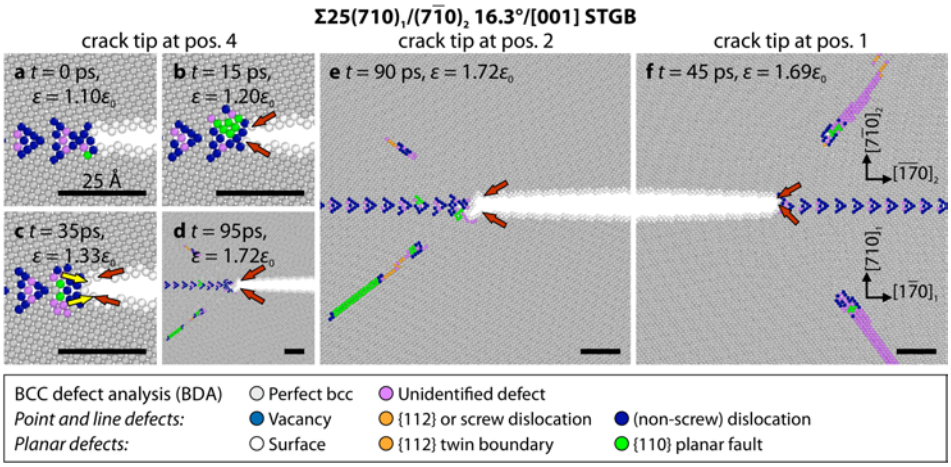

Figure 5.6: Position and direction dependence of the critical strain for the Σ25 STGB in W (quasi-2D edge crack setup; $\dot{\varepsilon} = 10^8$ s^{-1}). The [001] tilt axis is orthogonal to the plane of paper; see Fig. 5.1f for the precise initial crack tip positions; consult Table 5.4 for the simulation details. **a**: $+[\bar{1}70]_1$ propagation direction, initial crack tip position 4; **b**: at pos. 3, after rupture of the bond at pos. 4 (red arrows); **c**: at pos. 2, after rupture of the bond at pos. 3 (yellow arrows); **d**: at pos. 2, after emission of $\{110\}\langle 110\rangle$ deformation structures; **e**: initial crack tip position 2; similar deformation patterns as in **d**; **f**: $-[\bar{1}70]_1$ propagation direction, initial crack tip position 1. The GB was classified as "(non-screw) dislocation".

on the precise position of the crack within the structural unit and the crack propagation direction, the fracture toughness of the Σ25 GB was higher ($K_{\mathrm{Ic}}^{[\bar{1}70]} = 2.63$ MPa$\sqrt{\mathrm{m}}$) or lower (e.g. $K_{\mathrm{Ic},(4,4)}^{+[\bar{1}70]} = 1.87$ MPa$\sqrt{\mathrm{m}}$) than in the equally oriented single crystal ($K_{\mathrm{Ic}} = 2.08$ MPa$\sqrt{\mathrm{m}}$), cf. Table 4.7.

The penny-shaped cracks at the GB crack and in the corresponding single crystal showed predominantly ductile crack tip deformation. Characteristic snapshots of both cracks are shown in Fig. 5.7.

In the single crystal, see Fig. 5.7a, twin formation on the $[111](2\bar{1}\bar{1})$ and $[11\bar{1}](2\bar{1}1)$ systems (marked with 0) was observed at crack front segments that were very close to each other. I.e., the twins were only separated by a small crack front segment parallel to the $\pm[001]$ direction. Due to this immediate vicinity, the $\langle 111\rangle$-oriented incoherent twin boundaries directly interacted to create $[120]$ junctions (marked with 2) and finally penetrated each other (marked with 5). The non-interacting boundaries emitted screw dislocations that cross slipped along the crack front (marked with 1). The emitted screw segments remained pinned to the crack front, bowed out (marked with 3) and interacted with the twins and dislocations nucleated at the other side of the crack (marked with 4).

At the GB, see Fig. 5.7b, the crack tip initiated deformation twins in the $[\bar{1}\bar{1}\bar{1}]_1(2\bar{1}\bar{1})_1$ (not visible in the figure) and $[1\bar{1}1]_2(2\bar{1}\bar{1})_2$ systems (marked with 0). As the twins grew, they emitted dislocations on the same planes (marked with 1). These dislocations slipped along the grain boundary (marked with 6) and were finally transmitted into the other grain

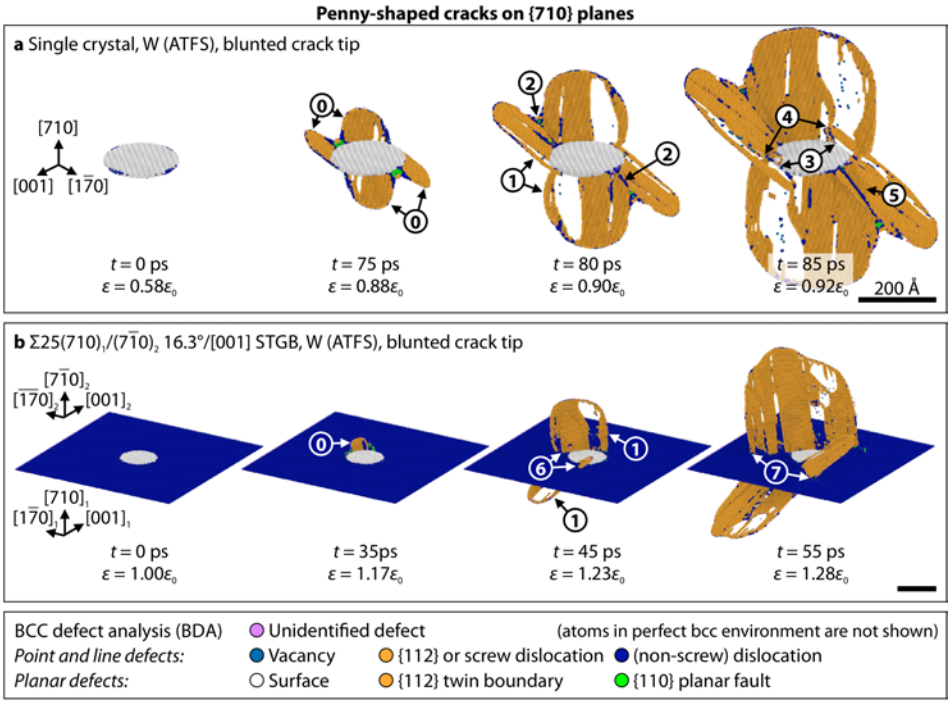

Figure 5.7: Evolution of crack tip plasticity initiated by penny-shaped cracks on the (710) (grain boundary) plane in W ($\dot{\varepsilon} = 10^8$ s^{-1}). **a**: single crystal; crack tip plasticity started by twin formation (⓪) on two different {112} planes; subsequent dislocation emission from growing twins (①) and interaction with other dislocations/twins (②); the emitted dislocations were pinned to the crack front and bowed out (③) leading to an interaction with the twins and dislocations nucleated at the other side of the crack (④); adjacent twins on two different {112} planes penetrated each other (⑤). **b**: Σ25{710} GB; deformation twin (⓪) in grain 2; subsequent dislocation emission from the twin and twin formation in grain 1 (①); dislocations cut along the GB (⑥) and finally penetrated it (⑦). The GB was classified as "(non-)screw dislocation".

(marked with 7). Unlike the transmission process described for the Σ9 GB, the dislocations had the same Burgers vector and slip plane after transmission as before, but in the coordinate system of the neighboring grain.

The penny-shaped GB crack showed an initiation strain of $\varepsilon_i = 2.32\,\% = 1.16\varepsilon_0$. This value is 0.13 % higher than the value determined in the corresponding single crystal ($\varepsilon_i = 2.19\,\%$). This critical strain was smaller than the theoretical threshold strain $\varepsilon_0 = 2.57\,\%$ for the crack in the single crystal.

5.4 Cracks at the Σ7 ATGB: Position- and direction-dependent fracture properties

The results for straight cracks on the $\Sigma7(\bar{1}\bar{1}1)_1/(11\bar{1}\bar{5})_2$ 135.6°/[112] ATGB are given in Table 5.5 and shown in Fig. 5.8 for the strain-controlled quasi-2D edge crack setup. In both propagation directions, cracks propagated in a brittle manner. In $-[\bar{1}10]_1$ direction, the crack at the initial crack tip position 3, cf. Fig. 5.1g, started to propagate at $\varepsilon_i^{-[\bar{1}10]} = 1.80$ %, see Fig. 5.8b. The crack was, however, directly arrested at the next crack tip position 2. Upon further quasi-static loading, the crack propagated and arrested at positions 1, 0, and 4, before it finally fractured through the whole GB at $\varepsilon_i^{-[\bar{1}10]} = 2.67$ %. In the opposite $+[\bar{1}10]_1$ propagation direction, brittle propagation started at a higher initiation strain, $\varepsilon_i^{+[\bar{1}10]} = 2.69$ %, see Fig. 5.8e. After breaking the initial crack tip bond, the crack directly stopped at the next bond at position 4. From here, it propagated until the next position 1 was reached ($\varepsilon_i^{+[\bar{1}10]} = 2.79$ %). Final fracture through the GB started at $\varepsilon_i^{+[\bar{1}10]} = 3.23$ %.

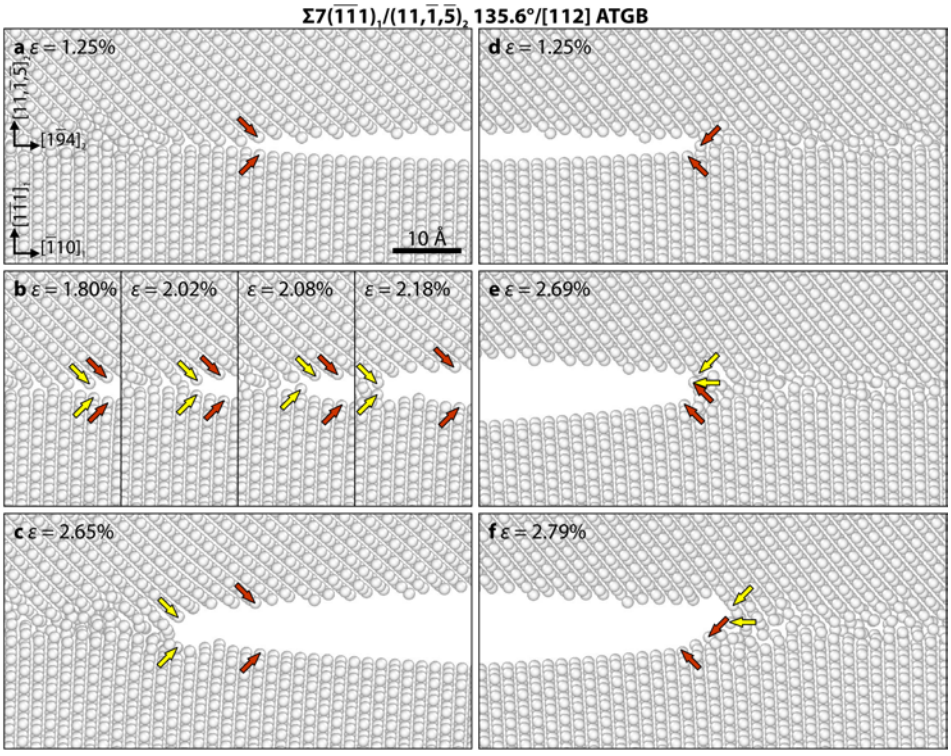

Figure 5.8: Position-dependent fracture resistance of the Σ7 ATGB under quasi-static loading. **a-c**: $-[\bar{1}10]_1$ crack propagation direction, final fracture at $\varepsilon_c = 2.67$ %; **d-f**: $+[\bar{1}10]_1$ crack propagation direction, final fracture at $\varepsilon_c = 3.23$ %. Red/yellow arrows: original/current crack tip atoms.

The penny-shaped crack showed pronounced direction-dependent fracture behavior, see Fig. 5.9a: the crack started to propagate in a brittle manner (marked with 0 in the figure) at ε_i = 3.84 % (1.88ε_0). Thereafter, a deformation twin was initiated in the $[1\bar{1}\bar{1}]_2(211)_2$ system (marked with 1) at a strain that was 0.14 % higher than the initiation strain for brittle fracture. Upon further loading, the crack and the formed twin grew in a way that their tips (marked with 3) kept pinned to each other and a straight crack front was created that lied approximately 8.5° inclined to the $[1\bar{9}4]_2$ axis.

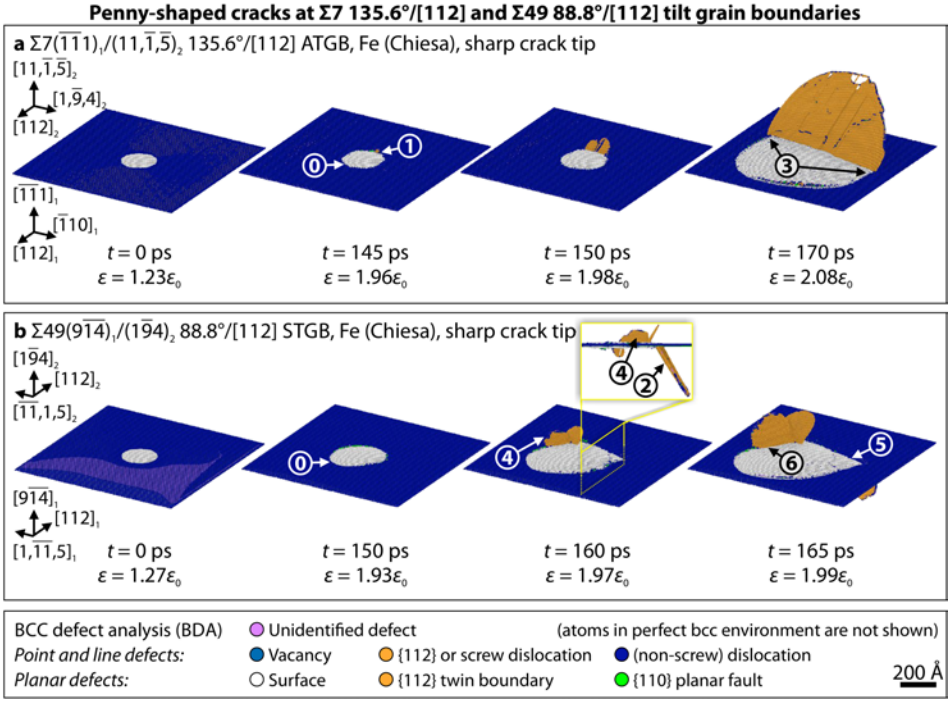

Figure 5.9: Direction-dependent fracture behavior of penny-shaped cracks at the $\Sigma7(\bar{1}\bar{1}1)_1/(11\bar{1}\bar{5})_2$ 135.6°/[112] and $\Sigma49(9\bar{1}\bar{4})_1/(1\bar{9}4)_2$ 88.8°/[112] GBs in Fe ($\dot{\varepsilon} = 10^8$ s^{-1}). **a**: the crack at the Σ7 ATGB simultaneously started to propagate in a brittle manner (⓪) and to nucleate a deformation twin on the $(211)_2$ plane (①); crack and twin grow in a way that their tips (③) kept pinned to each other, and a straight crack front was created that lied approximately 8.5° inclined to the $[1\bar{9}4]_2$ axis. **b**: the crack at the Σ49 STGB first propagated in a brittle manner (⓪); thereafter, twins formed on the $(211)_1$ (②) and the $(\bar{1}21)_2$ planes (④); similar to the behavior at the ATGB, the crack and the twins grew in a coordinated fashion leading to straight crack fronts that lied approximately 9° (⑤) and 50° (⑥) inclined to the $[1\bar{1}\bar{1}5]_1$ and $[\bar{1}\bar{1}15]_2$ axes, respectively. Both GBs were classified as "(non-)screw dislocation".

Table 5.5: Summary of simulation results for cracks on the $\Sigma7(\bar{1}\bar{1}1)_1/(11\bar{1}\bar{5})_2$ 135.6°/[112] STGB in Fe (Chiesa potential). See caption of Table 4.1 for further description; see Fig. 5.1g for the crack tip positions; $a_{\mathrm{eff}} = a/L_{\mathrm{x}}(\varepsilon)L_{\mathrm{x}}(\varepsilon{=}0)$: effective crack length normalized to $\varepsilon = 0$ %; lateral straining method for strain-controlled cracks: $\varepsilon^{\mathrm{pre}}$.

Quasi-2D sharp edge cracks with $L_x \approx L_y$

Dir.	L_y (Å)	a_{eff} (Å)	Pos.	Loading, $\dot{\varepsilon}$ (s^{-1})	$\varepsilon_{i,c}$ (%)	ε_0 (%)	ε_G (%)	Fracture behavior
$+[\bar{1}10]_1$	1000.6	297.7	3	quasi-static	1.05	1.58	1.44	Closure
$+[\bar{1}10]_1$	1000.6	298.6	3	quasi-static	2.69	1.58	1.44	Bond breaking
$+[\bar{1}10]_1$	1000.6	298.6	3	dynamic, 10^8	2.43	1.58	1.44	Bond breaking, arrest at 4
$+[\bar{1}10]_1$	1000.6	300.7	4	quasi-static	2.79	1.58	1.44	Bond breaking
$+[\bar{1}10]_1$	1000.6	305.2	1	quasi-static	3.23	1.58	1.44	Final GB fracture
$-[\bar{1}10]_1$	1000.6	278.2	3	quasi-static	1.20	1.58	1.44	Closure
$-[\bar{1}10]_1$	1000.6	279.8	3	quasi-static	1.80	1.58	1.44	Bond breaking
$-[\bar{1}10]_1$	1000.6	279.8	3	dynamic, 10^8	1.78	1.58	1.44	Bond breaking, arrest at 2
$-[\bar{1}10]_1$	1000.6	282.5	2	quasi-static	2.02	1.58	1.44	Bond breaking
$-[\bar{1}10]_1$	1000.6	285.8	1	quasi-static	2.08	1.58	1.44	Bond breaking
$-[\bar{1}10]_1$	1000.6	287.7	0	quasi-static	2.18	1.58	1.44	Bond breaking
$-[\bar{1}10]_1$	1000.6	293.8	4	quasi-static	2.65	1.58	1.44	Bond breaking
$-[\bar{1}10]_1$	1000.6	264.9	3	quasi-static	2.67	1.58	1.44	Final GB fracture

3D edge crack with $L_x \approx L_y \approx L_z$

Dir.	L_y (Å)	a_{eff} (Å)	Pos.	Loading, $\dot{\varepsilon}$ (s^{-1})	$\varepsilon_{i,c}$ (%)	ε_0 (%)	ε_G (%)	Fracture behavior
$+[\bar{1}10]_1$	1000.6	290.1	0	dynamic, 10^8	1.82	1.58	1.44	Brittle, arrest at 3
$+[\bar{1}10]_1$	1000.6	290.1	0	quasi-static	1.82	1.58	1.44	Brittle, arrest at 3
$+[\bar{1}10]_1$	1000.6	300.7	4	static	2.79	1.58	1.44	Stable
$+[\bar{1}10]_1$	1000.6[a]	300.7	4	dynamic[b]	2.79	1.58	1.44	Propagation
$+[\bar{1}10]_1$	1000.6	305.2	1	static	3.21	1.58	1.44	Stable
$+[\bar{1}10]_1$	1000.6[a]	305.2	1	dynamic[b]	3.21	1.58	1.44	Propagation
$-[\bar{1}10]_1$	1000.6	279.2	2	dynamic, 10^8	1.78	1.58	1.44	Brittle, arrest at 1
$+[112]_1$	1000.6	292.3	—	dynamic, 10^8	1.86	1.58	1.44	Brittle
$-[112]_1$	1000.6	294.9	—	dynamic, 10^8	2.00	1.58	1.44	Brittle

Penny-shaped cracks with $L_z \approx L_x$

L_x (Å)	L_y (Å)	a (Å)	Crack tip	Loading, $\dot{\varepsilon}$ (s^{-1})	ε_i (%)	ε_0 (%)	ε_G (%)	Fracture behavior
1000	1000.6	100	sharp	dynamic, 10^8	3.84	2.04	1.33	Brittle, twinning at ε_t = 3.98 %

[a] $L_z \approx 500$ Å

[b] Dynamic NVE simulation with starting temperature $T_0 = 10$ K to slightly excite the system

5.5 Cracks at the Σ49 STGB: Dominance of brittle fracture

The results for straight cracks on the $\Sigma49(9\bar{1}\bar{4})_1/(1\bar{9}4)_2$ 88.8°/[112] STGB are given in Table 5.6 and shown in Fig. 5.8 for the strain-controlled quasi-2D edge cracks. As it can be seen in the figure, the crack propagation direction had only a minor influence on the critical strains. In $-[1\bar{1}\bar{1}5]_1$ direction, brittle propagation started at $\varepsilon_i^{-[1\bar{1}\bar{1}5]} = 2.52$ %, see Fig. 5.10b. In the opposite $+[1\bar{1}\bar{1}5]_1$ direction, fracture initiated at $\varepsilon_i^{+[1\bar{1}\bar{1}5]} = 2.46$ %, see Fig. 5.10f. In both cases, the crack arrested shortly after incipient propagation, see subfigures c,d and g,h. Unstable fracture finally started at $\varepsilon_i^{-[1\bar{1}\bar{1}5]} = 2.82$ % and $\varepsilon_i^{+[1\bar{1}\bar{1}5]} = 3.38$ %.

At the penny-shaped crack with $a = 100$ Å, brittle fracture initiated at $\varepsilon_i = 4.36$ %, see Fig. 5.9b. During crack propagation, twins formed in the $[\bar{1}11]_1(211)_1$ (marked with 2) and $[\bar{1}\bar{1}1]_2(\bar{1}21)_2$ systems (marked with 4). The crack and the twins grew in a coordinated fashion leading to straight crack fronts that were approximately 9° (marked with 5) and 50° (marked with 6) misaligned to the $[1\bar{1}\bar{1}5]_1$ and $[\bar{1}\bar{1}15]_2$ axes, respectively.

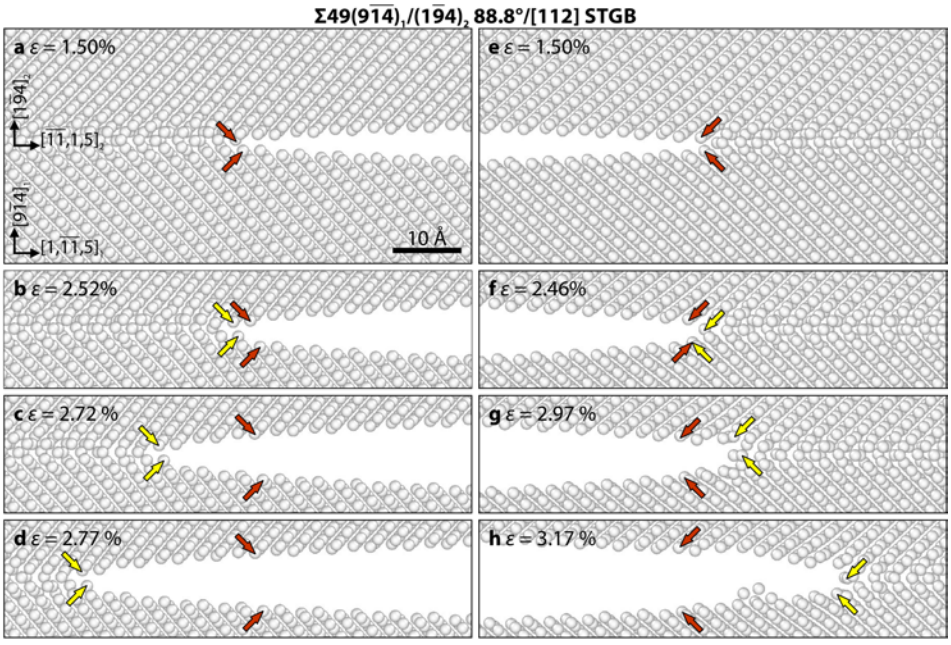

Figure 5.10: Position-dependent fracture resistance of the Σ49 STGB under quasi-static loading. The [112] tilt axis is orthogonal to the plane of paper; details are given in Table 5.6. **a-d**: $-[1\bar{1}\bar{1}5]_1$ crack propagation direction, final fracture at $\varepsilon_c = 2.82$ %; **e-g**: $+[1\bar{1}\bar{1}5]_1$ crack propagation direction, final fracture at $\varepsilon_c = 3.38$ %. Red/yellow arrows: original/current crack tip atoms.

Table 5.6: Summary of simulation results for cracks on $\Sigma49(9\bar{1}\bar{4})_1/(1\bar{9}4)_2$ 88.8°/[112] STGB in Fe (Chiesa potential). See caption of Table 4.1 for further description; lateral straining method for strain-controlled cracks: $\varepsilon^{\mathrm{pre}}$.

Quasi-2D sharp edge cracks with $L_x \approx L_y$							
Direction	L_y (Å)	a_{eff} (Å)	Loading, $\dot{\varepsilon}$ (s^{-1})	$\varepsilon_{i,c}$ (%)	ε_0 (%)	ε_G (%)	Behavior
$+[1\bar{1}\bar{1}5]_1$	1000.0	395.6	quasi-static	2.46	1.85	1.54	Bond breaking
$+[1\bar{1}\bar{1}5]_1$	1000.0	397.2	quasi-static	2.97	1.85	1.54	Bond breaking
$+[1\bar{1}\bar{1}5]_1$	1000.0	402.4	quasi-static	3.17	1.85	1.54	Bond breaking
$+[1\bar{1}\bar{1}5]_1$	1000.0	419.9	quasi-static	3.38	1.85	1.54	Final GB fracture
$-[1\bar{1}\bar{1}5]_1$	1000.0	396.2	quasi-static	2.52	1.85	1.54	Bond breaking
$-[1\bar{1}\bar{1}5]_1$	1000.0	398.9	quasi-static	2.72	1.85	1.54	Bond breaking
$-[1\bar{1}\bar{1}5]_1$	1000.0	410.4	quasi-static	2.77	1.85	1.54	Bond breaking
$-[1\bar{1}\bar{1}5]_1$	1000.0	421.8	quasi-static	2.82	1.85	1.54	Final GB fracture
Sharp penny-shaped crack with $L_z \approx L_x$							
L_x (Å)	L_y (Å)	a_{eff} (Å)	Loading, $\dot{\varepsilon}$ (s^{-1})	$\varepsilon_{i,c}$ (%)	ε_0 (%)	ε_G (%)	Behavior
1007.7	1000.6	100	dynamic, 10^8	4.36	2.36	1.46	Brittle, twinning at ε_t = 4.51 %

6 Cracks interacting with pre-existing dislocations

In this chapter, exemplary scenarios of crack-dislocation interactions are presented. Their influence on the fracture resistance and fundamental crack-tip processes, such as crack-tip blunting, crack plane cutting, and dislocation multiplication, is studied by placing pre-existing dislocations in front of long crack fronts on the (110) plane in Fe. The following subsections present the results for cracks interacting with dislocations that were located at the same plane, see section 6.1, on inclined and oblique planes, see section 6.2, and absorbed at grain boundaries, see section 6.3.

6.1 Dislocations on the crack plane

The interaction of cracks on the (110) plane was studied in a simulation box with approximate box dimensions $L_x \times L_y \times L_z \approx 1000 \times 1000 \times 500$ Å^3, containing around 43 million atoms for different dislocation characters and correspondingly varying crack front directions. The Chiesa potential was used to model the atomic interactions in Fe. Unlike the simulations shown so far, the boundary conditions were slightly changed to reduce possible boundary influences on the long-range strain field of the dislocation: atoms in boundary layers of $2r_{cut}$ thickness in x and y direction were free to move in the yz and xz plane, respectively; atoms in the intersecting regions of both boundaries were thus only allowed to move in z direction. The initial crack length was a = 400 Å and the dislocations were placed at about 100 Å in front of the crack tip. Each inserted dislocation had a Burgers vector $\underline{b}$ parallel or antiparallel to the $[1\bar{1}1]$ direction and was placed on the same (110) plane on which the crack was located. For reasons of symmetry, only one Burgers vector direction was studied for each type of dislocation. The line direction $\underline{l}$ always coincided with the z axis. See Fig. 2.1c for the definition of the coordinate system and for the relationship between line direction, Burgers vector, and the inserted half plane (in case of non-screw dislocations). The complete list of crack orientations and dislocation types can be found in Table 6.1. After energy minimization at ε_{in} = 2.00 %, the resulting configurations were loaded at a constant strain rate $\dot{\varepsilon} = 10^8$ s^{-1} using the ε^{pre} method for lateral straining. In case of edge and screw dislocations, the displacement fields of the relaxed configurations were additionally scaled to ε = 2.40 % in order to carry out simulations under conditions of constant strain, see Fig. 6.1. The detailed processes of crack-dislocation interactions are described in the following paragraphs for the different dislocation characters. All described effects took place before the first reflected elastic waves returned to the crack front.

Table 6.1: Influence of dislocation character on fracture behavior and propagation distance of cracks on the same (110) plane. The dislocation line direction $\underline{l}$ points always in the same direction as the crack front ($\dot{\varepsilon} = 10^8$ s^{-1}; lateral strain method: $\varepsilon^{\mathrm{pre}}$); see text for further details on the simulation setup.

Front	ε_0 (%)	Dislocation (type)	$\varepsilon_{\mathrm{in}}$ (%)	$\dot{\varepsilon}$ (s^{-1})	ε_{i} (%)	Propagation behavior
$[\bar{1}12]$	1.88	no	2.00	10^8	2.33	Brittle (arrest and dislocation nucleation at $\varepsilon = 2.53$ %)
$[\bar{1}12]$	1.88	no	2.40	—	—	Brittle
$[\bar{1}12]$	1.88	yes (edge)	2.00	10^8	2.09	Brittle ($a_0/2[\overline{111}](\bar{1}3\bar{2})$ dislocation emission at $\varepsilon = 2.25$ %)
$[\bar{1}12]$	1.88	yes (edge)	2.40	—	—	Brittle, dislocation emission after $t = 5.8$ ps
$[\bar{1}1\bar{1}]$	1.89	no	2.00	10^8	2.27	Brittle, arrest at $\varepsilon = 2.33$ % after $\Delta x = 4d_{1\bar{1}2}$ ($a_0/2[11\bar{1}](011)$ and $a_0/2[\overline{111}](101)$ dislocation nucleation at $\varepsilon = 2.61$ %)
$[\bar{1}1\bar{1}]$	1.89	no	2.40	—	—	Brittle, $a_0/2[\overline{111}](101)$ dislocation nucleation after $t = 13.2$ ps
$[\bar{1}1\bar{1}]$	1.89	yes (screw)	2.00	10^8	2.19	Brittle, arrest at $\varepsilon = 2.21$ % after $\Delta x = 0.5d_{1\bar{1}2}$ ($a_0/2[11\bar{1}](011)$ dislocation nucleation at $\varepsilon = 2.41$ %)
$[\bar{1}1\bar{1}]$	1.89	yes (screw)	2.40	—	—	Brittle, $a_0/2[11\bar{1}](011)$ dislocation emission after $t = 6.5$ ps
$[1\bar{1}0]$	1.95	no	2.00	10^8	2.29	Brittle, arrest at $\varepsilon = 2.32$ % after $\Delta x = 13d_{001}$
$[1\bar{1}0]$	1.95	yes (35° mixed)	2.00	10^8	2.20	Brittle, arrest at $\varepsilon = 2.21$ % after $\Delta x = 2d_{001}$
[001]	1.97	no	2.00	10^8	2.28	Brittle
[001]	1.97	yes (55° mixed)	2.00	10^8	2.08	Brittle, dislocation absorption at $\varepsilon = 2.20$ %

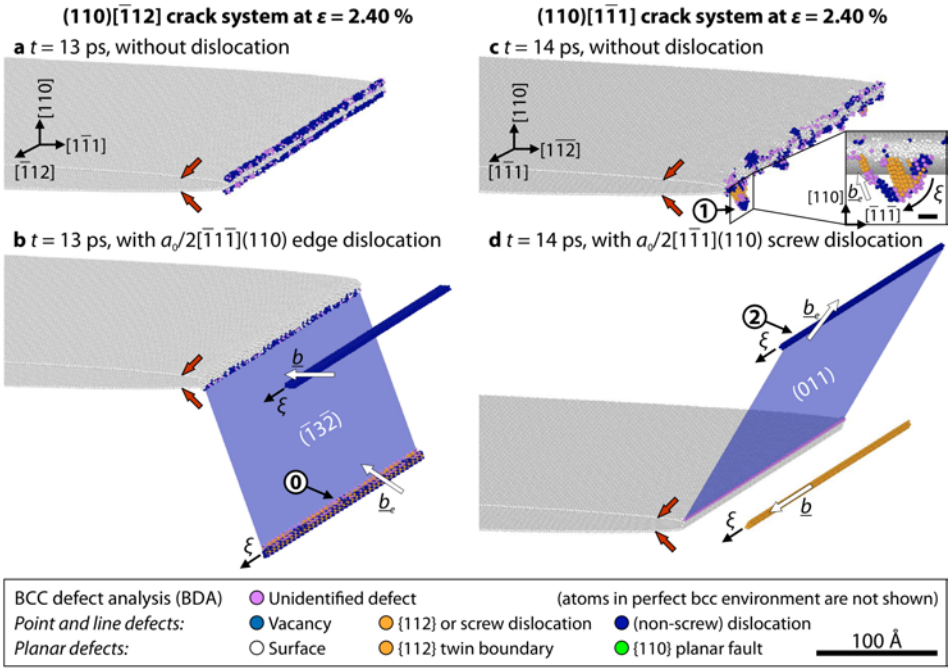

Figure 6.1: Comparison of cracks in defect-free single crystals and interacting with edge and screw dislocations. **a**,**b**: (110)[1̄12] crack system; initial brittle crack propagation; emission of mixed dislocation with $\underline{b}_e = a_0/2[111](\bar{1}3\bar{2})$ (marked with ⓪) in presence of a pre-existing edge dislocation with $\underline{b} = a_0/2[\bar{1}1\bar{1}]$; **c**: (110)[1̄1̄1] crack system; initial brittle propagation; emission of a mixed dislocation with $\underline{b}_e = a_0/2[111]$ on the $(0\bar{1}1)$ and $(\bar{2}11)$ planes (①) from the disturbed [1̄1̄1] crack front (scale bar in inset figure: 10 Å); **d**: (110)[1̄1̄1] crack and screw dislocation; initial brittle propagation; emission of a mixed dislocation on the (011) plane with $\underline{b}_e = a_0/2[1\bar{1}\bar{1}]$ (②). Red arrows: original crack tip atoms.

Edge dislocation

The results for a straight crack in the $(110)[\bar{1}12]$ crack system interacting with a pre-existing edge dislocation with Burgers vector $\underline{b} = a_0/2[\bar{1}1\bar{1}]$ and line direction $\underline{l} = [\bar{1}12]$ are given in Table 6.1. Fig. 6.1a and b compare the propagation behavior of the cracks with and without pre-existing dislocations at a constant strain $\varepsilon = 2.40$ %. In both cases, the crack first propagated in a brittle manner, cf. current and original crack-tip positions in subfigures a and b. In presence of an edge dislocation, the crack arrested and emitted a mixed-type $a_0/2[111](\bar{1}3\bar{2})$ dislocation after 5.8 ps of crack propagation, marked with 0 in subfigure b. In the defect-free scenario, crack arrest was not observed within the first 13 ps of propagation. The critical strains ε_i in presence of a pre-existing edge dislocation was around 11 % lower than in the dislocation-free configurations.

Screw dislocation

The results for a straight crack on the $(1\,1\,0)$ plane interacting with a pre-existing screw dislocation with Burgers vector $\underline{b} = a_0/2[1\bar{1}1]$ and line direction $\underline{l} = [1\bar{1}\bar{1}]$ are given in Table 6.1 and visualized in Fig. 6.1c and d at a constant strain $\varepsilon = 2.40$ %. Similar to the crack in the $(1\,1\,0)[\bar{1}\,1\,2]$ crack system, the initial fracture behavior was brittle. In the dislocation-free scenario, an $a_0/2[111]$-type dislocation was nucleated on the oblique $(0\,\bar{1}\,1)$ and $(\bar{2}\,1\,1)$ glide planes at a local crack front perturbation after 13.2 ps of propagation, marked with 1 in subfigure c. In presence of pre-existing screw dislocations, the crack emitted a mixed-type $a_0/2[11\bar{1}](0\,1\,1)$ dislocation after 6.5 ps of propagation, marked with 2 in subfigure d. The critical strain ε_i in presence of a pre-existing screw dislocation was around 4 % lower than in the dislocation-free configuration.

Mixed dislocations

The results for straight cracks on the $(1\,1\,0)$ plane interacting with pre-existing mixed-type 35° and 55° dislocations with Burgers vector $\underline{b} = a_0/2[1\bar{1}1]$ and line direction $\underline{l} = [1\bar{1}0]$ and $\underline{l} = [0\,0\,1]$ are given in Table 6.1, but not visualized here. In both cases, the initial fracture behavior was brittle and crack propagation started at lower critical strains in the presence of dislocations as compared to the corresponding dislocation-free scenarios. In case of the mixed 35° dislocation, the crack arrested after a short time of propagation. In the corresponding defect-free single crystal with $[1\bar{1}0]$ crack front, the crack also arrested, but after a significantly longer period of propagation. In the defect-free single crystal, the crack with $[0\,0\,1]$ crack front started to propagate at $\varepsilon_i = 2.28$ % in a completely brittle manner. In presence of the mixed 55° dislocation, the crack absorbed the dislocation at $\varepsilon = 2.20$ %.

6.2 Dislocations on inclined and oblique planes

The interaction of an atomically sharp crack with dislocations on inclined and oblique planes was exemplarily studied in the $(1\,1\,0)[0\,0\,1]$ crack system in Fe modeled with the Chamati potential [227]. Approximate box dimensions were $L_x \times L_y \times L_z \approx 500 \times 500 \times 500$ Å^3 corresponding to approximately 10 million atoms. Crack plane normal and front direction were parallel to the y and z axes, respectively. The boundary conditions in the outer layers of minimum thickness $2r_{cut}$ were fixed in x and y direction and 2D-dynamic in the xy plane in z direction. Both the 3D edge crack with crack length $a = 200$ Å and the dislocations were inserted separately in the atomistic configuration, as detailed in sections 3.3.1 and 3.4.1, respectively. The dislocations were created in such a way that their dislocation line ran through the center of the configuration, i.e., at a distance of 50 Å from the later crack-tip position. The four different scenarios of crack-dislocation interactions are schematically illustrated in Fig. 6.2. Dislocations were placed on one inclined (subfigure a) and three oblique glide planes (subfigure b-d). Initially, the dislocations had edge character in three out of four cases (a-c). Since the stabilization of an isolated screw dislocation

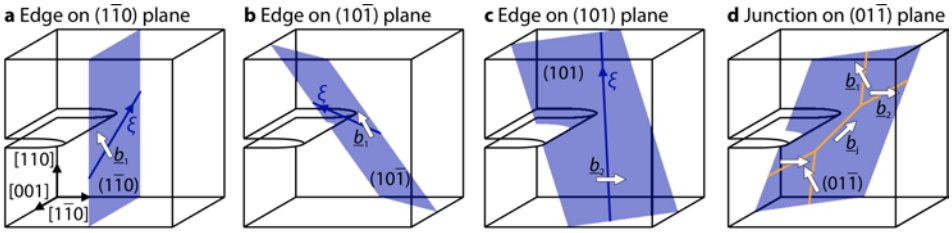

Figure 6.2: Different scenarios for crack-dislocation interactions. **a**: $\underline{b}_1 = a_0/2[111](1\bar{1}0)$ edge dislocation with $\underline{l} = [11\bar{2}]$ line direction; **b**: $\underline{b}_1 = a_0/2[111](10\bar{1})$, $\underline{l} = [\bar{1}2\bar{1}]$; **c**: $\underline{b}_2 = a_0/2[1\bar{1}\bar{1}](101)$, $\underline{l} = [\bar{1}\bar{2}1]$; **d**: $\underline{b}_j = a_0[100](01\bar{1})$ dislocation junction formed by $\underline{b}_1$ and $\underline{b}_2$ screw segments.

in the simulation box was not successful by means of energy minimization, a $\langle 1\,0\,0\rangle$ dislocation junction with screw character was studied instead (d). For slip planes intersecting the crack front, the sign of the dislocations was chosen such that the dislocation is attracted by the crack-tip stress field. After energy minimization of the configurations, the relaxed positions of the systems containing the dislocations were scaled with the deformation field of the relaxed crack configuration similar to the method used e.g. in Refs. [155, 215]. To observe the interaction of the crack with a pre-existing dislocation, NVE simulations were performed with starting temperature $T_0 = 0$ K. The processes of crack-dislocation interactions observed for the different scenarios are described in the following subsections.

6.2.1 Slip plane not intersecting the crack front

The crack in the $(1\,1\,0)[0\,0\,1]$ crack system interacting with a pre-existing dislocation with Burgers vector $\underline{b}_1 = a_0/2[111]$ on the $(1\bar{1}0)$ plane (perpendicular to the crack extension direction) is shown in Fig. 6.3. It can be seen that the initially straight dislocation line ($\underline{l} = [11\bar{2}]$) re-oriented during the dynamic simulation and became locally parallel to the crack front (b). Since the dislocation was pinned at the 2D-dynamic boundaries, a complete re-alignment parallel to the crack front was, however, not possible. During the local reorientation of the dislocation, the crack tip did not move from its original position.

6.2.2 Slip planes intersecting the crack front

The crack in the $(1\,1\,0)[0\,0\,1]$ crack system interacting with a pre-existing dislocation with Burgers vector $\underline{b}_1 = a_0/2[111]$ on the oblique $(1\,0\,\bar{1})$ plane is shown in Fig. 6.4. In this case, the crack-tip stress field attracted the dislocation and it moved towards the crack tip (subfigure a). After the direct interaction of the dislocation with the crack tip, the part of the dislocation, which was originally located above the crack, cuts along the crack face producing a surface step in $\langle\bar{1}\,1\,\bar{1}\rangle$ direction (subfigure c). The part of the dislocation, which was further away from the crack tip, started to move towards the boundaries thereby creating a screw-oriented dislocation segment at the intersection of the original slip plane with the crack plane. This screw segment cross slipped on the $(\bar{1}\,2\,\bar{1})$ plane, which was 90° inclined

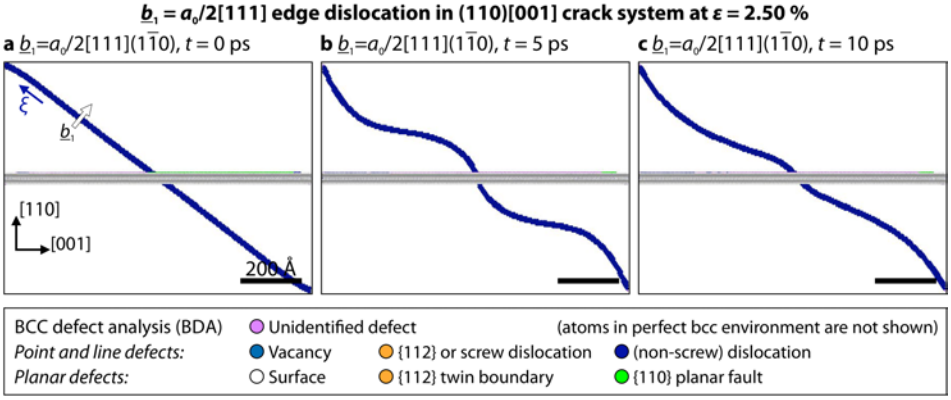

Figure 6.3: Crack in the (110)[001] system interacting with a pre-existing $\underline{b}_1 = a_0/2[111](1\bar{1}0)$ edge dislocation. **a**-**c**: re-orientation of the dislocation caused by stress field interactions.

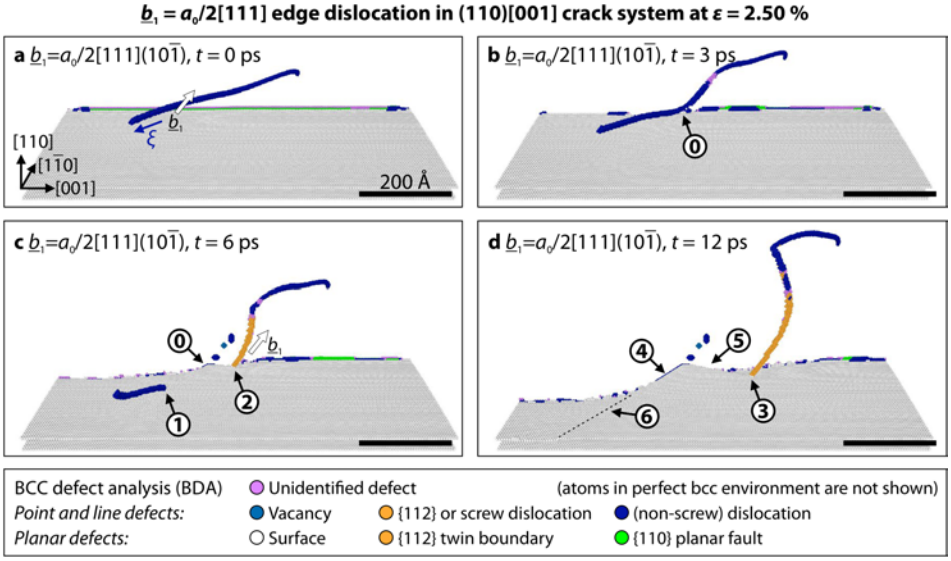

Figure 6.4: Crack in the (110)[001] system interacting with a pre-existing $\underline{b}_1 = a_0/2[111](10\bar{1})$ edge dislocation. **a**-**d**: re-orientation of the crack front by direct interaction (⓪) between dislocation and crack; the original edge component cuts along the crack front (①) whereby a step at the crack face was produced (⑥); at the intersection of crack and slip plane (⓪), a screw segment formed and cross slipped onto the $(\bar{1}2\bar{1})$ plane (②), which lied 90° inclined with the original $(10\bar{1})$ slip plane; as it continued to glide, a surface step was produced on the crack face (③); after the passing of the dislocations, the crack partially closed until it reached the created surface steps leading to a 90° locally blunted crack front, which consisted of $\langle\bar{1}1\bar{1}\rangle$ (④) and $\langle\bar{1}13\rangle$ facets (⑤).

with respect to the original slip plane. Upon motion of the screw segment along the crack face, a surface step was created along the intersection of slip and crack plane, i.e., in $\langle\bar{1}\,1\,3\rangle$ direction. While both dislocation segments moved away from the point of initial interaction with the crack, the crack closed until it reached the created surface steps leading to a locally blunted crack front, which consisted of $\langle\bar{1}\,1\,\bar{1}\rangle$ and $\langle\bar{1}\,1\,3\rangle$ facets (subfigure d).

The interaction of a crack with a dislocation on an oblique slip plane was additionally studied for an edge dislocation with Burgers vector $\underline{b}_2 = a_0/2[1\,\bar{1}\,\bar{1}]$ on the $(1\,0\,1)$ plane, see Fig. 6.5. Again, the dislocation was attracted by the crack tip stress field. This led to the motion of the dislocation towards the crack tip (subfigure b). Upon the direct interaction of the original dislocation with the crack tip, the two parts of the original $\underline{b}_2$ dislocation above and below the crack plane each splitted into a new screw-oriented dislocation segment and a $\langle 1\,0\,0\rangle$-type dislocation junction: Below the crack, a screw dislocation with Burgers vector $\underline{b}_{e1} = a_0/2[\bar{1}\,\bar{1}\,1]$ and a dislocation junction with Burgers vector $\underline{b}_{j1} = a_0[0\,\bar{1}\,0]$ were formed on the $(1\,0\,1)$ glide plane (subfigure c):

$$\underline{b}_{j1} = a_0[0\,\bar{1}\,0] \quad = \quad {}^{a_0}/_2[1\,\bar{1}\,\bar{1}] + {}^{a_0}/_2[\bar{1}\,\bar{1}\,1] = \underline{b}_2 + \underline{b}_{e1}$$

The $\underline{b}_{e1}$ dislocation bowed out around its nucleation site, cross slipped on the $(\bar{1}\,1\,0)$ plane where it moved along the crack front in $[0\,0\,\bar{1}]$ direction thereby blunting it (subfigure d). The $\underline{b}_{j1}$ dislocation junction cut along the crack face on the $(1\,0\,1)$ plane. Similarly, the for-

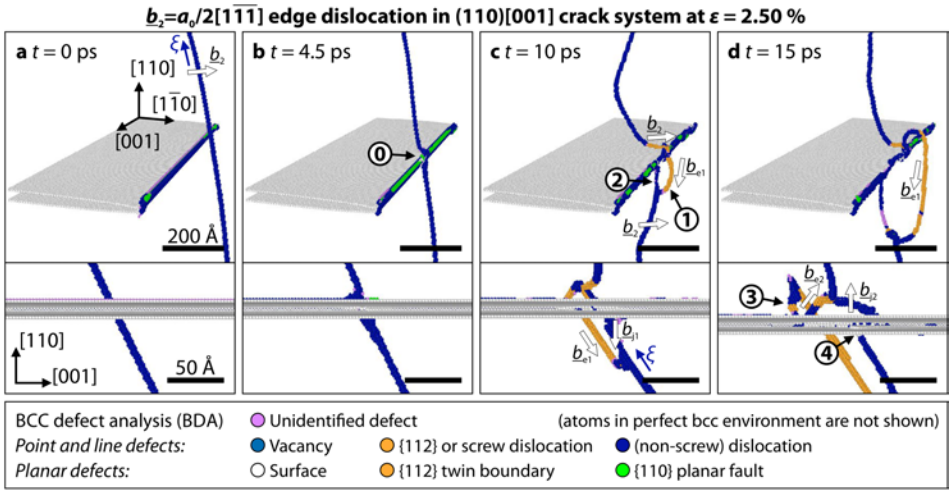

Figure 6.5: Crack in the (110)[001] system interacting with a pre-existing $\underline{b}_2 = a_0/2[1\bar{1}\bar{1}](101)$ edge dislocation. **a**: initial configuration; **b**: attraction of the dislocation by the crack tip (⓪); **c**: emission of $\underline{b}_{e1} = a_0/2[\bar{1}\bar{1}1]$ (①) and $\underline{b}_{e2} = a_0/2[111]$ dislocations from the crack tip whereby $\underline{b}_{j1} = a_0[0\bar{1}0]$ (②) and $\underline{b}_{j2} = a_0[100]$ dislocation junctions were formed, respectively; **d**: bowing out of the $\underline{b}_{e1}$ dislocation on the (101) plane and cross slip on the $(1\bar{1}0)$ plane where it moved along the crack front (③) and further blunted the crack front; the $\underline{b}_{j1}$ junction moved on the initial (101) plane thereby producing a step at the crack face (④).

mer $\underline{b}_2$ dislocation splitted into a screw dislocation with $\underline{b}_{e2} = a_0/2[111]$ and a dislocation junction with $\underline{b}_{j2} = a_0[100]$ at the nucleation site of the $\underline{b}_{e1}$ dislocation:

$$\underline{b}_{j2} = a_0[100] \quad = \quad {}^{a_0}/_2[1\bar{1}\bar{1}] + {}^{a_0}/_2[111] = \underline{b}_2 + \underline{b}_{e2}$$

6.2.3 Dislocation junction

The crack in the $(110)[001]$ crack system interacting with a pre-existing dislocation junction with Burgers vector $\underline{b}_j = a_0[100]$ is shown in Fig. 6.6. To create the junction, two screw dislocations with Burgers vectors $\underline{b}_1 = a_0/2[111]$ and $\underline{b}_2 = a_0/2[1\bar{1}\bar{1}]$ were placed in the configuration such that they intersected each other. The $\underline{b}_j$ junction formed upon energy minimization, as shown in Fig. 6.6a. During the dynamic simulation, the lower $\underline{b}_1$ segment was attracted by the crack tip field, bowed out on the $(\bar{1}\bar{1}2)$ plane (subfigure b), and finally directly interacted with the crack tip (subfigure c). At the crack front, the $\underline{b}_1$ segment first slipped back on the $(01\bar{1})$ plane before it cross slipped on the $(\bar{1}10)$ plane, which lies perpendicular to the crack extension direction. On this plane, the dislocation glided along the crack font in $[001]$ direction and thereby blunted it. Finally, the dislocation cross slipped again onto the $(\bar{1}2\bar{1})$ plane, cut along the crack face where it left behind

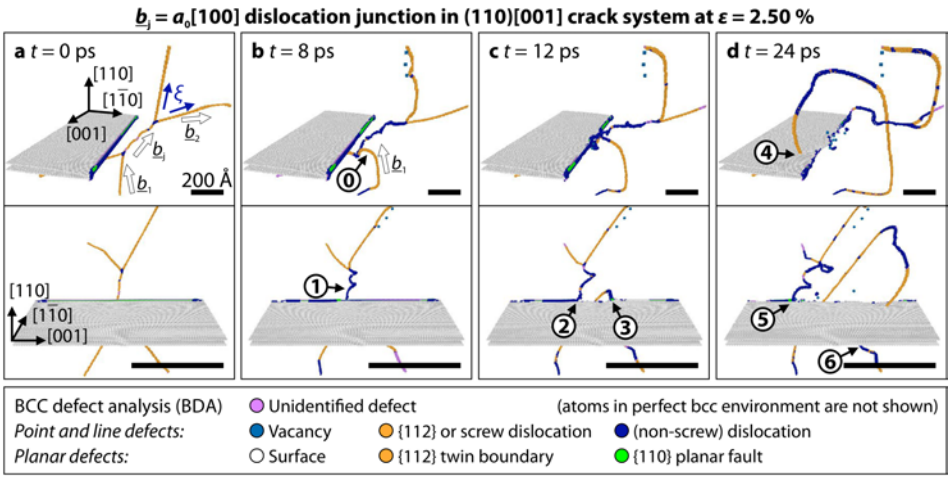

Figure 6.6: Crack in the (110)[001] system interacting with a pre-existing $\underline{b}_j = a_0[100]$ dislocation junction. **a**: initial configuration with the original $\underline{b}_1 = a_0/2[111]$ and $\underline{b}_2 = a_0/2[1\bar{1}\bar{1}]$ segments forming the $\underline{b}_j$ junction on the $(01\bar{1})$ plane; **b**: bowing out of the $\underline{b}_1$ segment on the $(\bar{1}\bar{1}2)$ plane (⓪) and motion of the junction on the (011) plane towards the crack tip (①); **c**: contact of the junction (②) and the $\underline{b}_1$ segment (③) with the crack front; in the following, the $\underline{b}_1$ dislocation first slipped back onto the $(01\bar{1})$ plane followed by cross slip on the $(\bar{1}10)$ plane, where it glided parallel to the crack front thereby blunting it; **d**: cross slip of the $\underline{b}_1$ dislocation onto the $(\bar{1}2\bar{1})$ plane whereby a step at the crack face was produced (④); the $\underline{b}_j$ segment slipped parallel to the crack front on an effective (010) plane in $[00\bar{1}]$ direction (⑤) leading to crack tip blunting; the $\underline{b}_2$ segment cut along the lower crack face (⑥) on the $(01\bar{1})$ slip plane.

a surface step. At the same time, the $\underline{b}_j$ junction moved closer to the crack tip on the $(0\,1\,1)$ plane. After direct interaction, the $\underline{b}_j$ junction glided on an effective $(0\,1\,0)$ plane in $[0\,0\,\bar{1}]$ direction, which also resulted in crack tip blunting. As the junction came in contact with the crack front, the $\underline{b}_2$ segment, which—together with the $\underline{b}_1$ segment—originally formed the junction, glided on the $(0\,1\,\bar{1})$ plane. Here, no surface step was created as the $a_0/2[1\,\bar{1}\,\bar{1}]$ Burgers vector lied within the $(1\,1\,0)$ crack plane.

6.3 Dislocations absorbed in grain boundaries

The interaction of grain boundary cracks with dislocations that have been absorbed by the GB is studied for the $\Sigma 7(\bar{1}\,\bar{1}\,1)_1/(1\,1\,\bar{1}\,\bar{5})_2$ 135.6°/$[1\,1\,2]$ ATGB and the $[\bar{1}\,1\,0]_1$ crack propagation direction. For this GB, the highest Schmid factor [300] in one of the neighboring grains is $m = 0.5$; it is therefore an ideal model for GBs in polycrystalline materials, where dislocations pile up and are eventually absorbed. The dimensions of the simulation box were approximately $1000 \times 600 \times 10$ Å^3. The configuration contained about 730,000 atoms. The same boundary conditions as in the previous section were used to reduce possible boundary influences on the long-range strain field of the dislocation. Under these conditions, the predicted threshold strain was $\varepsilon_0 = 1.95$ %.

Each inserted dislocations had a Burgers vector $\underline{b}$ either parallel or anti-parallel to the $[1\,1\,\bar{1}]_2$ direction on the $(\bar{1}\,1\,0)_2$ plane. The different Burgers vectors are referred to as $\underline{b}^+ = +a_0/2[1\,1\,\bar{1}]_2$ and $\underline{b}^- = -a_0/2[1\,1\,\bar{1}]_2$ in the following. They were chosen such that the angle between them and the crack plane is $\lambda_m = 44.4°$; at the same time, the angle between slip and crack plane is $\phi_m = 45.6°$ and the corresponding Schmid factor is $m_{[1\,1\,\bar{1}](\bar{1}\,1\,0)} = \cos\phi_m \cos\lambda_m = 0.5$, which is the highest possible value for m. The line direction was always parallel to the tilt axis, i.e., $\underline{l} = [1\,1\,2]$. To obtain the correct structure of an absorbed dislocation, the dislocation was first inserted at a distance of about 20 Å from the GB. Dislocations were inserted either by removing or adding atomic half planes, as depicted in Fig. 6.7c,e,g, and i. The dislocation insertion therefore inevitably changes the distribution of the overall applied strains in the configuration. Qualitatively, the effect of half plane removal or addition on the local stress is, as follows: if an atomic half plane is removed or added in the region of the configuration, where the crack tip is located, the applied strain and thereby the driving force for crack propagation is increased or decreased, respectively.

Whether a dislocation was attracted and absorbed by the GB during the following energy minimization, depended on the Burgers vector direction and the exact position of the dislocation with respect to the structural unit of the GB, cf. Fig. 5.1g. If the dislocation was not absorbed initially, the configuration was quasi-statically strained perpendicular to the GB plane in steps of $\delta\varepsilon = 0.25$ % until the GB absorbed the dislocation. The so-determined absorption strains ε_{abs} are summarized in Table 6.2 for the tested combinations of Burgers vector $\underline{b}$ and dislocation position. All possible dislocation positions along the periodicity distance λ_0 were tested, cf. Table 5.1. The table shows that equivalent positions in adjacent structural units lead to the same absorption behavior. E.g., the $\underline{b}^-$ dislocation was absorbed at $\varepsilon = 0$ % only at positions 4 and 4'. In all other cases, additional strains were necessary.

For the Burgers vector $\underline{b}^+$, absorbed dislocations were obtained at pos. 0 and 1 (and their equivalences in adjacent structural units). Upon application of additional tensile strains, the remaining non-absorbed dislocations left the GB region towards the boundaries.

Table 6.2: Overview of necessary strains ε_{abs} to absorb edge dislocations at the Σ7 STGB in Fe. Different positions were tested for dislocations with opposite $\underline{b}^{\pm} = \pm a_0/2[11\bar{1}]$ Burgers vectors, see Fig. 5.1g for the definition of the positions; bold values indicate combinations where ε_{abs} = 0.00 %, i.e., no additional strain was necessary to absorb the dislocation; values of ε_{abs} in %.

Burgers vector	Pos. 0	Pos. 1	Pos. 2	Pos. 3	Pos. 4	Pos. 0′	Pos. 1′	Pos. 2′	Pos. 3′	Pos. 4′
$\underline{b}^- = -a_0/2[11\bar{1}]_2$	1.50	1.00	0.75	0.25	**0.00**	1.50	1.00	0.75	0.25	**0.00**
$\underline{b}^+ = a_0/2[11\bar{1}]_2$	**0.00**	**0.00**	—	—	—	**0.00**	**0.00**	—	—	—

The results for straight quasi-2D GB cracks interacting with absorbed dislocations with line directions parallel to the crack front are given in Table 6.3 and visualized in Fig. 6.7 for ε = 3.55 %. A GB crack of length a = 400 Å was inserted in configurations that contained initially absorbed dislocations. The chosen positions for $\underline{b}^-$ and $\underline{b}^+$ dislocations were the adjacent positions 4 and 0 in the central structural unit of the simulation box, respectively. The resulting distance between crack tip and absorbed dislocation was approximately 100 Å. After energy minimization at ε_{in}, the relaxed configurations were loaded at a constant strain rate $\dot{\varepsilon} = 10^7$ s^{-1} to determine ε_i. Table 6.3 summarizes the observed critical strains and propagation behaviors. All configurations showed purely brittle crack propagation. The initiation strains depended strongly on the precise position of the crack tip and the distance to the dislocation core, which were not exactly the same for the different situations. Additionally, cracks often stopped to propagate directly after initiation. In these cases, they arrested at another GB bond, but were still located within the first structural unit in front of the original crack tip position. For these reasons, a second critical strain ε_i^λ is used to characterize the critical conditions independent of the initial crack tip position. It is defined as the strain at which the crack has propagated through the first structural unit. Using this definition, the following observations can be made: ε_i^λ was always higher for $\underline{b}^+$ than for the $\underline{b}^-$ Burgers vector and the dislocation-free case. Similarly, configurations with dislocations that have been inserted by adding an atomic half plane showed higher critical strains than their counterparts created by half plane removal. In the majority of the studied cases, the insertion of a dislocation yielded higher critical strains ε_i^λ than in the dislocation-free configuration. Only for $\underline{b}^-$ and half plane removal, ε_i^λ was 0.09 % smaller than without dislocation. In this case, the critical strain ε_i^λ was more than 1 % smaller than the highest determined value 3.94 % ($\underline{b}^+$, added half plane).

Simulations at constant strain were then performed with those configurations, which had nearly identical effective crack lengths after relaxation, a_{eff}. The relaxed displacement fields at ε_{in} = 1.75 or 2.00 % were used to scale the configurations to ε = 3.55 %. The crack propagation distance Δx was measured after 15 ps of crack growth. This time period was chosen to ensure that the first emitted elastic wave has not yet returned to the crack tip. The propagation distance Δx was highest in the dislocation-free scenario. Furthermore, it

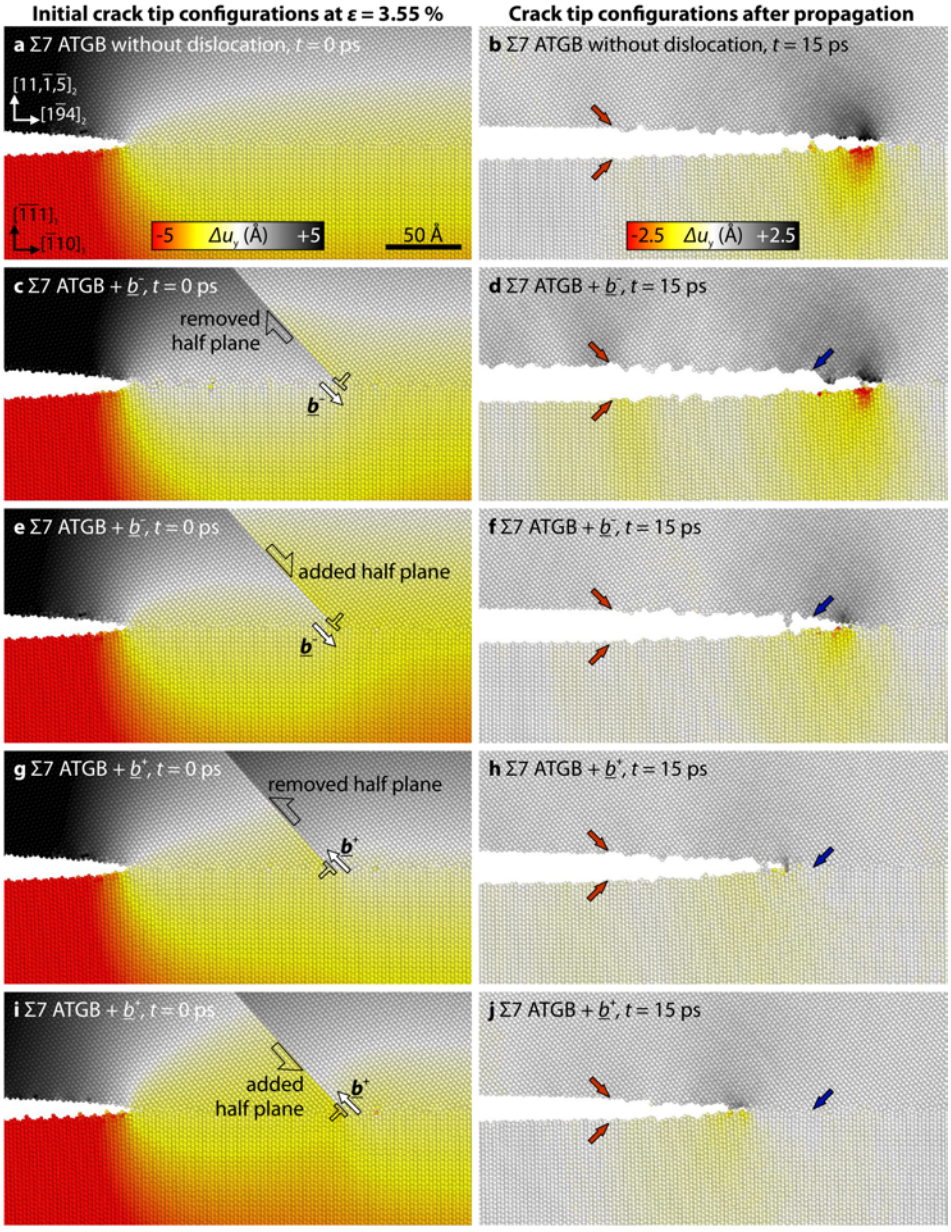

Figure 6.7: Crack propagation through the Σ7 ATGB in Fe (Chiesa potential). **a**-**b**: without absorbed dislocations; **c**-**f**: absorbed $\underline{b}^-$ dislocation; crack propagation by nearly the same distance as without an absorbed dislocation; **g**-**j**: absorbed $\underline{b}^+$ dislocation; decelerated crack growth. Left subfigures: initial configurations at ε = 3.55 %; right subfigures: configurations after 15 ps of crack propagation. Red arrows: original crack tip atoms; blue arrows: dislocation position; atomic colors: displacements normal to the GB plane between the shown structure and the relaxed GB structure (left) or the configuration at t = 14 ps (right).

Table 6.3: Overview of critical strains for cracks at the Σ7 ATGB with and without absorbed edge dislocations. Dislocations were inserted either by removing or adding an atomic half plane (HP); the crack tip position within the structural unit and the effective crack length a_{eff} were determined at the initial strain $\varepsilon_{\mathrm{in}}$; consult Fig. 5.1g for the definition of the different crack tip positions; ε_{i}: strain, where the first bond at the crack tip broke; $\varepsilon_{\mathrm{i}}^{\lambda}$: strain at which the crack has propagated through the first structural unit; the simulations were also carried out at constant strain by scaling the relaxed displacement fields to $\varepsilon = 3.55$ %; Δx: crack propagation distance after $t = 15$ ps under conditions of constant strain.

Burgers vector	Method of insertion	$\varepsilon_{\mathrm{in}}$ (%)	Pos.	a_{eff} (Å)	$\dot{\varepsilon}$ (s^{-1})	ε_{i} (%)	$\varepsilon_{\mathrm{i}}^{\lambda}$ (%)	$\Delta x(t$=15 ps)	Behavior
—	—	1.75	0	390	10^7	2.20	3.02	—	Brittle
		3.55	0	390	—	—	—	148	Brittle
$\underline{b}^- = -a_0/2[11\bar{1}]$	Removed HP	1.75	3	395	10^7	2.55	2.93	—	Brittle
	Removed HP	3.55	3	395	—	—	—	144	Brittle
	Added HP	1.75	0	390	10^7	2.31	3.32	—	Brittle
	Added HP	3.55	0	390	—	—	—	136	Brittle
$\underline{b}^+ = +a_0/2[11\bar{1}]$	Removed HP	1.75	0	391	10^7	1.92	3.46	—	Brittle
	Removed HP	3.55	0	391	—	—	—	96	Brittle
	Added HP	1.75	1	379	10^7	2.39	3.57	—	Brittle
	Added HP	2.00	1	393	10^7	2.48	3.94	—	Brittle
	Added HP	3.55	1	393	—	—	—	67	Brittle

was larger for $\underline{b}^-$ than for $\underline{b}^+$ and larger for removing than for adding a half plane to insert a dislocation. This trend was nearly inverse proportional to the determined values for $\varepsilon_\mathrm{i}^\lambda$: the higher $\varepsilon_\mathrm{i}^\lambda$, the smaller the propagation distance Δx. The only exception was observed when $\underline{b}^-$ and a half plane was removed. In this case, both $\varepsilon_\mathrm{i}^\lambda$ and Δx were smaller than in the dislocation-free configuration.

Fig. 6.7 shows the crack tip configurations at $\varepsilon = 3.55$ % for the different scenarios. In the right subfigures, atomic colors indicate the displacements perpendicular to the GB between the configurations after $t = 14$ and 15 ps. In the dislocation-free case, these displacements were very high at the crack tip indicating that the crack had significantly propagated in this period, see subfigure b. This was also observed for the absorbed $\underline{b}^-$ dislocation inserted by removing an atomic half plane, see subfigure d. In this case, the crack propagated into the region behind the dislocation core. This is shown in subfigure f where an atomic half plane was added to insert the dislocation. Here, the concentration of displacements is less pronounced compared to subfigures b and d. This indicates that the crack has either stopped to propagate or decelerated markedly. Similar behavior is observed for $\underline{b}^+$, see subfigures h and j. Unlike the $\underline{b}^-$ scenarios, the crack has not propagated behind the dislocation core in these cases. During all performed simulations, dislocation emission or desorption was not observed.

7 Discussion

With the aim to lay the foundations for the development of new microstructure-sensitive meso-scale models for fracture in bcc-based materials, the following discussion is mainly focused on the general influences of crack front curvature, general characteristics of grain boundary fracture, and exemplary crack-dislocation interactions leading to crack tip blunting and thereby increasing the fracture resistance.

At first, I shall, however, start with discussing the fracture properties of straight cracks in defect-free bcc single crystals. These properties, i.e., the fracture behavior and critical strains or critical stress intensity factors, were mainly determined for reference; in addition, they are compared with the available literature, existing theories, and experimental data in section 7.1. The effect of the crack length on the critical strain will be discussed as well as the influence of the interatomic potential on the determined fracture toughness, the lattice trapping effect, and the occurrence of $\{1\,1\,0\}$ planar faults.

Section 7.2 focuses on the general influence of crack front curvature on the competition between brittle fracture and crack-tip plasticity. For this purpose, the determined fracture properties of penny-shaped cracks, which were used as model system for curved cracks, are compared to theories and the fracture properties of perfectly straight cracks. Furthermore, the influence of crack front curvature on lattice trapping is discussed and the characteristics of crack tip plasticity at curved crack fronts are analyzed.

Section 7.3 introduces the concept of bond trapping of GB cracks, including the relation of the determined fracture properties of GB cracks to theory and equally-oriented cracks in single crystals. In addition, three-dimensional effects on bond trapping, direction-dependent fracture behavior, mechanisms of crack tip plasticity at curved GB cracks, and effects of absorbed dislocations are discussed.

Section 7.4 presents the identified mechanisms of crack tip blunting at curved and formerly straight crack fronts by their interactions with emitted or pre-existing dislocations.

Thereafter, the last two sections 7.5 and 7.6 focus on dynamic instabilities, i.e., crack arrest and the emission of dislocations from propagating twins, and the influencing variables on the simulation results, i.e., the setup geometry, strain rate effects, and the method of lateral straining. In the end, best practices are presented for future atomistic simulations of fracture.

As with all atomistic simulations, the results of the presented MD and MS studies cannot be directly compared to experiments and need to be critically discussed. The typical atomistic time scales lead to strain rates which are many orders of magnitude higher than in experiments. The usual size limitations of simulation boxes furthermore require very large strains to fulfill the Griffith criterion. Due to the small box size, however, already few dislocations can lead to a significant decrease in the load of the crack. The unloading of the crack caused by locally initiated crack tip plasticity might therefore be overemphasized.

Moreover, the used EAM potentials might not exactly represent the interatomic bonding in the highly strained crack tip region. However, the observed processes are all rooted in the specific geometry and crystallography of cracks in bcc crystals.

7.1 Fracture properties of straight cracks in defect-free single crystals

As expected, the 19 different EAM-type potentials for the bcc metals V, Nb, Ta, Cr, Mo, W, and Fe exhibit relatively similar fracture behavior on the low-index $\{1\,0\,0\}$ and $\{1\,1\,0\}$ planes. The main focus of the following discussion is, however, on Fe as a bcc model material, for which eight different potentials were tested. Parts of this discussion have been published in Ref. [122].

In subsection 7.1.1, fracture behavior and fracture toughness as determined in the K-controlled setup are compared to theory and literature data. The determined properties are then compared to fracture experiments in the common crack systems for Fe in subsection 7.1.2. To assess the possible effect of stress concentrations on tension-separation laws for CZ models, see section 2.4, the forces at an exemplary crack tip are compared to the forces across the cleavage plane during rigid-body separations, and the effective force function of the potential in subsection 7.1.3. Thereafter, the influence of the crack length on both critical strain and fracture behavior is discussed in terms of higher-order terms in the elastic crack tip stress field in subsection 7.1.4. Finally, the influence of the interatomic potential on the lattice trapping ratio ΔK and the formation of $\{1\,1\,0\}$ planar faults is detailed in subsection 7.1.5.

7.1.1 Comparison with theory and literature

The determined fracture behavior and critical values are in good qualitative and quantitative agreement with previous results for the same potentials, e.g. in Refs. [30, 181, 187]. The only exception occurred for the $(1\,1\,0)[1\bar{1}\,0]$ crack system modeled with the Mendelev-II potential, for which Gordon *et al.* [30] found ductile failure. The results of the present study show, however, brittle cleavage, see Fig. 4.4d. Gordon *et al.* used a rectangular simulation setup with dimensions of 250×250×20 Å^3 instead of the more problem-adapted and slightly larger cylindrical setup (R =150 Å) used here. An additional explanation for the different results is the comparably weak convergence criterion used by Gordon *et al.* They used the force norm $\|F\| = 10^{-4}$ eV/Å, which is four orders of magnitude higher than the relaxation criterion used in this study. Studies on minimization algorithms have shown that significant structural changes can still occur at force norms below 10^{-4} eV/Å [358]. Such a high relaxation criterion might lead to an insufficiently relaxed configuration and could finally have caused a different fracture behavior during further loading. This shows how important it is to understand the effect of certain input parameters on the simulation outcome [122].

Furthermore, the Marinica, Ackland, Wang, and Smirnova potentials showed severe crack tip transformations, which were often neither classically brittle nor ductile. This made it highly problematic to determine trustworthy K_{Ic} values; the results for the corresponding potentials are therefore excluded from the following discussions.

Theoretically, the question whether a stressed crystal fractures by brittle cleavage or by ductile rupture is determined by the material's ability to convert elastic strain energy to plastic deformation. Crack tip plasticity usually occurs in the form of nucleation and motion of dislocations or deformation twinning. In the following, the theoretical criteria for brittle cleavage, dislocation emission, and deformation twinning are determined using the material parameters of the potentials and compared to the observed fracture behavior. Parts of the following discussion have been published in Ref. [122].

Dislocation emission vs. brittle fracture

The competition between brittle fracture and dislocation emission is classically treated within the Rice-Thomson framework [15]. According to their model, dislocation emission is expected if the necessary stress intensity factor K_e, see Eq. (2.15), is smaller than the corresponding prediction for brittle fracture according to Griffith K_G, see Eq. (2.7). The corresponding values can be found in the Tables 4.1-4.7. For all potentials and crack system studied here, brittle fracture is expected. Although this prediction is correct for the majority of the studied crack systems, ductile fracture is observed for multiple potentials in the $(1\,1\,0)[1\bar{1}\,0]$ crack system as well as for cracks on the $(1\,1\,1)$ plane. In particular for the $(1\,1\,1)[1\bar{1}\,0]$ orientation, almost all potentials show the formation of twins. The deviations from the Rice theory can be significant: in cases where dislocations were emitted from the crack tips, e.g., for the Simonelli, Chamati, and Gordon potentials for Fe, the K_e-values were on average 23% higher than the corresponding K_G values.

These incorrect predictions of the fracture behavior are caused by the limitations of the two criteria. The Rice criterion neglects that an emitted dislocation leaves behind a surface step at the crack tip [230]. Furthermore, the precise value of the unstable stacking fault energy depends on the applied strain, which is called tension-shear coupling [411]. At the same time, the Griffith criterion neglects the discrete nature of the crystal, i.e. the effect of lattice trapping [11–13]. Including the energy to form a surface step in the process of dislocation emission would increase K_e [230]. This could explain why some of our determined K_{Ic}-values for dislocation emission are higher than the corresponding K_e-values. It does, however, not explain the emission of dislocation in cases where the Rice-Thomson criterion predicts brittle fracture.

The overprediction of K_e by the Rice criterion can be understood in terms of the influence of tensile strains on the γ surface. Fig. 7.1 compares the decrease of the unstable stacking fault and twinning energies for different EAM potentials and DFT calculations for Fe. In the simulations, atoms were only allowed to move perpendicular to the fault plane during energy minimization. The strains were applied by homogeneous straining of the simulation boxes. In case of molecular statics simulations, periodic boundary conditions were used only in the directions of the fault plane and the non-periodic boundary

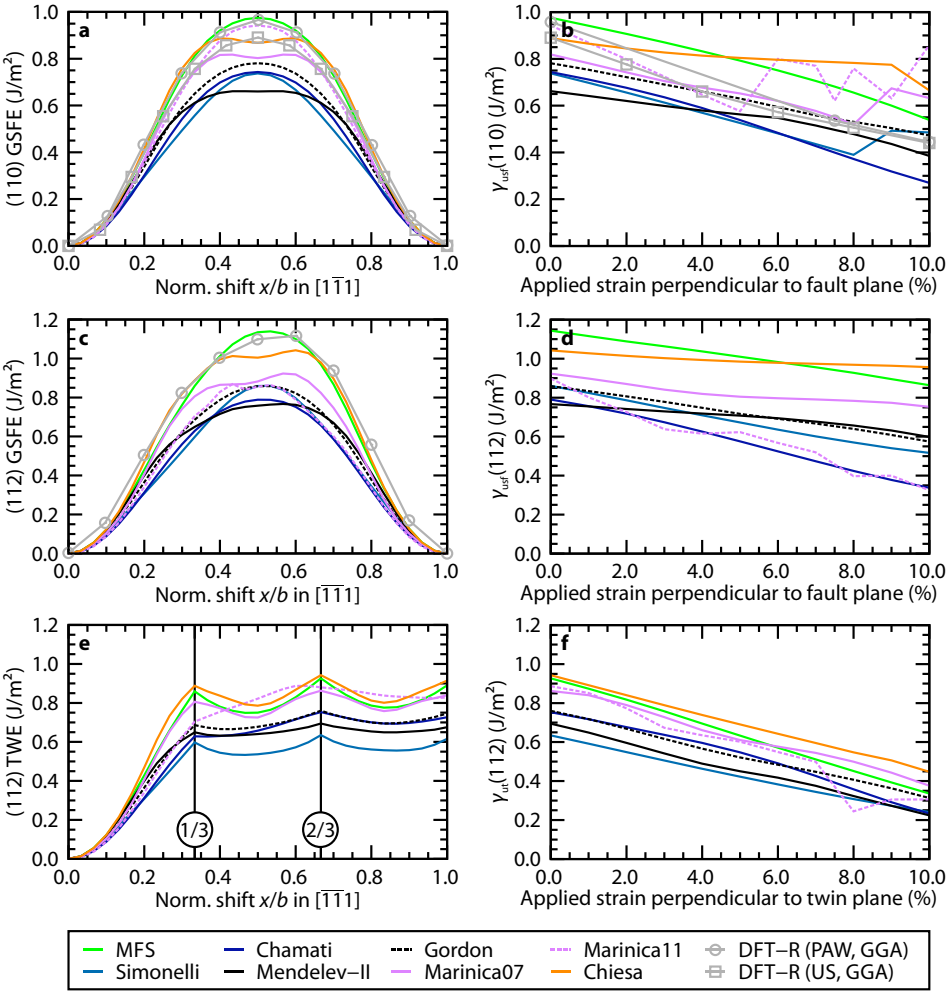

Figure 7.1: Plots of generalized stacking fault energies (GSFE) and twinning energies (TWE) in Fe. Left figures show cross-sectional views of the γ surface and the TWE curves along the [1$\bar{1}$1] direction; right figures show the dependence of the unstable stacking fault (usf) and unstable twinning (ut) energies on the strain applied perpendicular to the corresponding fault or twin plane; **a**,**b**: GSFE and γ_{usf} of the (110) plane; **c**,**d**: GSFE and γ_{usf} of the (112) plane; **e**,**f**: TWE and γ_{ut} of the (112) plane; the data obtained using eight different EAM potentials is compared to relaxed density functional theory (DFT-R) calculations in **a**-**c**; DFT data (PAW, GGA) in **a** and **c** taken from Ref. [377]; strain-dependent DFT data (PAW, GGA) in **b** was calculated by I. Bleskov [412]. The EAM data in the right subfigures was calculated for strain increments $\Delta\varepsilon$ = 1 %, but is plotted with lines for the sake of clarity. The Marinica11 potential shows an unsteady evolution of the unstable energies on all planes, which is mostly caused by the occurrence of phase transformations; this is particularly observed in **b** for the Simonelli, Marinica07 and Marinica11 potentials.

layers of minimum thickness $2r_{cut}$ were fixed. In case of DFT calculations, PBCs were used in all three dimensions and the simulation box was distorted in such a way that only one fault plane existed per simulation box. In both cases, the lateral box dimension were kept fixed (no Poisson contraction/extension). The dependence of $\gamma_{usf}(110)$ and $\gamma_{usf}(112)$ on normal strains up to 10 % is shown for the different potentials in Fig. 7.1b and d. Typical values of the strain in the vicinity of the crack tip vary between 7 and 10 %. As it can be seen, tensile strains reduce the unstable stacking fault energies γ_{usf}. The decrease of $\gamma_{usf}(110)$ due to an applied strain of 8 % ranges from 12 % (Chiesa potential) to 50 % (Chamati potential). On the (112) plane, a similar decrease is observed. For the same potentials as above, it varies between 7 and 46 % at $\varepsilon = 8$ %. According to Eqs. (2.14) and (2.15), this would decrease K_e by 19, 27, and 14 % for the Simonelli, Chamati, and Gordon potentials, respectively. When comparing this estimation to the corresponding K_G values, it becomes clear that the tension-shear coupling alone could only explain the ductile fracture behavior in case of the Chamati potential.

In addition to the decrease of K_e by on average around 20 % due to the tension-shear coupling effect, lattice trapping increases the necessary load for brittle crack advance. From the simulations showing brittle fracture, the average increase of K_{Ic} with respect to to the Griffith value K_G is estimated to be around 30 %.

In summary, the occurrence of crack tip plasticity instead of predicted brittle fracture is explained with the lattice trapping effect, which increases the sustainable stress intensity factor, whereas tension-shear coupling decreases the necessary energy barrier for dislocation nucleation.

An additional reason for the observation of crack tip plasticity in the $(110)[1\bar{1}0]$ crack system will be given in section 7.5.1 where the crack tip configurations are compared for different potentials. All ductile behaving crack tips showed the formation of an 'immobile' structure whereas the brittle propagating cracks, i.e., using the Mendelev-II and Chiesa potentials, exhibited the 'mobile' structure.

Twin formation vs. dislocation emission

As introduced in section 2.3.2, Tadmor and Hai [323] developed a criterion for twin formation at crack tips. Analogous to the Rice-Thomson model, twin formation is expected if the necessary stress intensity factor K_t, see Eq. (2.31), is smaller than the corresponding predictions for brittle fracture, K_G, and dislocation emission, K_e, see Eq. (2.15). The corresponding values can be found in the Tables 4.1-4.7 and have been published along with parts of the following discussion in Ref. [122]. The twinning tendency T, see Eq. (2.30), which is the general tendency for twin formation instead of dislocation emission, predicts preferred twinning for all Fe potentials except for the Marinica11 potential, cf. Table 3.2. T ranges from 1.02 for the Chamati potential to 1.16 for the Simonelli potential. From the remaining bcc potentials, twinning is favored over $\{112\}$ dislocation emission for the Nb potential of Fellinger and the ATFS potentials for Mo and W as well as the Wang potentials.

At crack tips, however, twinning can only occur if the crack front direction lies in a (112) plane, which is the case for all crack systems with $[1\bar{1}0]$ crack fronts. Indeed, twin-

ning takes place with all potentials in the $(111)[1\bar{1}0]$ crack system except for the Chamati potential, which has the overall lowest twinning tendency. On the other hand, twinning is not observed in the $(100)[1\bar{1}0]$ orientation where all potentials show brittle fracture in the K-controlled setup. This changes, however, when the strain-controlled setup is used under dynamic conditions, see Fig. 4.2c-h. In this case, the deformation behavior is equivalent to the observations in the $(111)[1\bar{1}0]$ crack system: twin formation occurs for the Mendelev-II potential and dislocation emission for the Chamati potential. This observation gives rise to the assumption that the twinning tendency for dynamic loading is higher than under quasi-static conditions.

However, deformation twinning does not occur in the $(110)[1\bar{1}0]$ crack system, where ductile crack tip deformation took place by the emission of perfect lattice dislocations on the (112) plane, see e.g. Fig. 4.6. In this case, the prediction following the twinning tendency T fails since the crack tip is oriented in such a way that both $\pm 54.7°$-inclined $\{112\}$ twin systems are loaded in the antitwinning direction of the bcc structure [74], see section 2.3.2. For this orientation dislocation nucleation was shown to be preferred over the formation of twins [182, 413]. The reasoning behind the derivation of the twinning tendency in fcc metals can thus not be transferred one-to-one to bcc metals.

In summary, the twinning tendency provides a reliable trend for the competition between deformation twinning and dislocation emission, but the twinning/antitwinning asymmetry has to be taken into account additionally to predict twin formation at crack tips in bcc metals.

7.1.2 Comparison with experimental data

Fig. 7.2 compares the determined K_{Ic} values for Fe with the theoretical Griffith values, K_{G}, and experimental data at 77 K for 99.94 % purity Fe single crystals [28]. Figs. 4.1, 4.4, and 4.10 show the fracture behavior in the different crack systems for selected Fe potentials. All numerical values for the determined critical stress intensity factors K_{Ic} and the corresponding theoretical criteria are given in Tables 4.1-4.5 along with the detailed descriptions of the fracture events for each potential.

The main parts of the following comparison between the simulation results and the experimental data have been published in Ref. [122]. Such a comparison can only be of qualitative and—in the best case—*semi*-quantitative nature. A direct comparison of the presented simulation results with fracture experiments is not possible for the following reasons: in the simulations, cracks were modeled as perfectly straight and atomically sharp. Such a setup cannot be realized in experiments since micro-faceting can always lead to local deviations from the average crack front direction. Furthermore, experimentally investigated materials are never defect-free, which is in contrast to perfect crystals used in the simulations. Furthermore, pre-existing dislocations will automatically lead to a deviation of the measured K_{Ic} value from the intrinsic fracture toughness. In addition, the presented simulations were all performed at 0 K and therefore cannot account for thermally activated processes or changes of the elastic constants with temperature. Finally, experimental

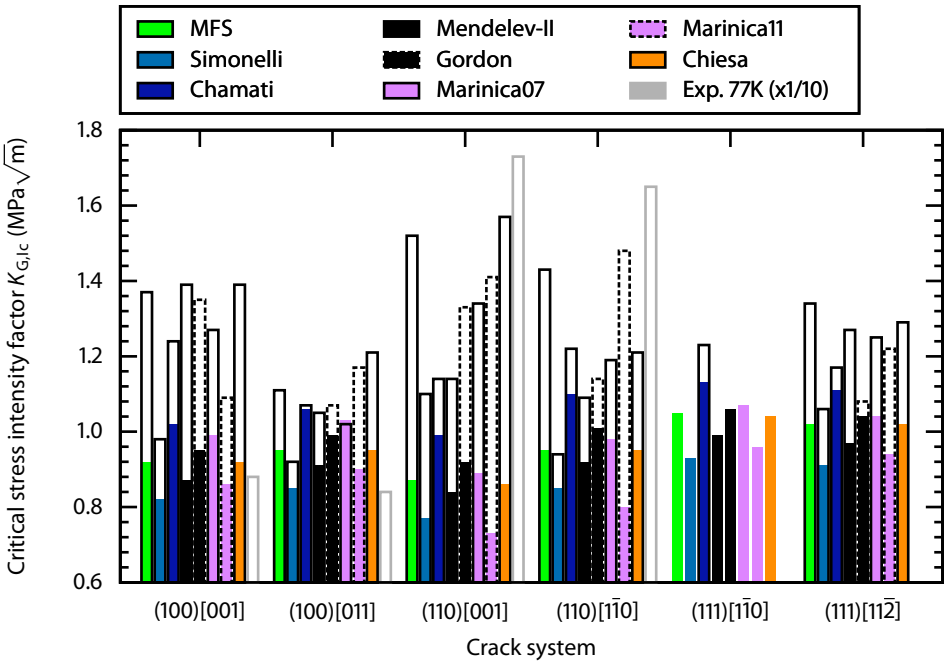

Figure 7.2: Summary of simulation results for K-controlled cracks in defect-free Fe single crystals. Filled bars: fracture toughness K_G as predicted by the Griffith criterion; open bars: fracture toughness K_{Ic} as determined by atomistic simulations and experiments at 77 K [28]; note that the experimental values are multiplied with 1/10 for better visualization.

samples always contain trace amounts of impurities. In the reference work by Hribernik [28], these were mainly Mn and Cr, which might influence the fracture behavior, see e.g. Ref. [131].

In the K-controlled setups, all potentials predict brittle cleavage on the $(1\,0\,0)$ plane, which is consistent with the experimental findings. In the $(1\,0\,0)[0\,0\,1]$ crack system, however, the crack directly kinked out onto the inclined $(1\bar{1}\,0)$ plane at K_{Ic} for the majority of the potentials. This kinking out of the crack is *not* observed in experiments although the surface energy of the $(1\,1\,0)$ plane is lower than for the $(1\,0\,0)$ plane as calculated with EAM potentials and DFT [414]. This makes $\{1\,1\,0\}$ planes the theoretically preferred cleavage plane for $\langle 0\,0\,1\rangle$ oriented crack fronts. Only for the Chamati, Mendelev-II, and Chiesa potentials the crack initially remained on the $(1\,0\,0)$ plane. When the load was further increased, the crack finally kinked out onto the $(1\bar{1}\,0)$ plane for the Mendelev-II and Chiesa potentials whereas it remained on the $(1\,0\,0)$ plane in case of the Chamati potential.

The present simulations show that the kinking out of the crack onto the inclined $(1\bar{1}\,0)$ plane is clearly related to the occurrence of $\{1\,1\,0\}$ planar faults: all potentials (including also the other bcc potentials) in which planar faults form at the tip of the $(1\,0\,0)[0\,0\,1]$ crack,

finally kinked out on the $\{1\,1\,0\}$ plane, see Fig. 4.1. The existence of a small displacement component normal to $\{1\,1\,0\}$ planes has been suggested by Cohen [415] in the context of planar faults created by partial dislocations on $\{1\,1\,0\}$ planes. When measuring the interplanar spacing d_{110} of $\{1\,1\,0\}$ planes of a $\{1\,1\,0\}$ planar fault, an increase of 8 % (in case of the Mendelev-II potential) is indeed found compared to the distance d_{110} in comparable strain states where no PF was created. This additional separation of $\{1\,1\,0\}$ planes will act as a precursor for the later separation of these planes. It should, however, be noted that the occurrence of $\{1\,1\,0\}$ PFs is most likely an artifact of the potentials for two main reasons: first, the observed consequence of the planar fault formation, i.e., the kinking out of $(1\,0\,0)[0\,0\,1]$ on $(1\bar{1}\,0)$ planes, has not been reported in experiments; second, in contrast to most EAM potentials, DFT calculations do not predict the occurrence of local minima in the γ surface of $(1\,1\,0)$ planes and thus no preferable formation of $\{1\,1\,0\}$ planar faults. The influence of the interatomic potential on the formation of $\{1\,1\,0\}$ planar faults is discussed in section 7.1.5 in more detail.

The experimentally observed departure of cracks from $\{1\,1\,0\}$ planes onto $\{1\,0\,0\}$ planes did not occur for the tested Fe potentials. Fracture on $\{1\,0\,0\}$ planes is thermodynamically unfavorable since $\gamma(1\,0\,0)$ is higher than $\gamma(1\,1\,0)$ for all potentials, see Table 3.2. Furthermore, kinking out of the $(1\,1\,0)[1\bar{1}\,0]$ crack system onto $(1\,0\,0)$ planes as reported in Ref. [28] is not possible in the used quasi-2D simulation setup. To include such effects, a sufficiently large simulation setup should be used, which allows for local crack front reorientations [155].

For almost all Fe potentials, the crack front direction has a stronger influence on the fracture toughness K_{Ic} than the crack plane. On average, the atomistically determined K_{Ic} values for the $\{1\,0\,0\}$ and $\{1\,1\,0\}$ planes are 11 % lower for crack fronts along $\langle 1\,1\,0\rangle$ than for $\langle 1\,0\,0\rangle$ directions. This trend has been reported earlier for W [29] and is attributed to the more pronounced lattice trapping effect for $\langle 1\,0\,0\rangle$ crack front directions. In the experiments [28], on the other hand, the choice of the crack plane is the determining factor for the fracture toughness. Among all potentials, only the MFS potential shows the correct order of the crack systems in terms of their K_{Ic} value, see Fig. 7.2 and Tables 4.1 and 4.3. The Simonelli and Chiesa potentials are reproducing the overall highest K_{Ic}-value of the $(1\,1\,0)[0\,0\,1]$ crack system. In addition they predict the correct order of K_{Ic} values for each of the two planes separately, i.e., the fracture toughness for crack fronts along $\langle 1\,1\,0\rangle$ directions have the lowest values on both the $(1\,0\,0)$ and the $(1\,1\,0)$ plane.

For W, the ATFS potential shows a good semi-quantitative agreement with the experimental data measured by Riedle [63], see Table 2.2, as it was reported earlier by Riedle *et al.* [14] and Gumbsch *et al.* [27].

In summary, the predictions of most Fe potentials agree with the experimentally observed preference of $\langle 110\rangle$ over $\langle 001\rangle$ crack front directions; but they fail to predict the preference of cleavage on {100} planes with exception of the MFS potential. The experimental observations can therefore not be rationalized by thermodynamics or with the presented simulation results; it can only be speculated, that they are possibly caused by chemical or magnetic effects, or by imperfections of the material or at the crack front.

7.1.3 Comparison to rigid-body separations

As introduced in section 2.4, the perhaps most critical variables in CZ models for fracture are the parameters that describe the traction and separations in the regions around the crack tip. Due to the large system sizes needed, it is currently not practicable to derive the necessary information from DFT calculations of crack propagation as it is possible e.g. with MD simulations [416]. For this reason, traction-separation laws are often derived from atomistic rigid-body separations, see e.g. Refs. [21, 340] for corresponding MD and DFT studies. Such approaches are, however, not able to include the effect of the stress concentrations at the crack tip. For this reason, it can be questioned whether rigid-body separations reliably predict the critical conditions at a crack tip.

To address this question, I exemplarily compare the interaction forces at a crack tip with the corresponding traction-separation law derived by rigidly displacing two atomic blocks, see Fig. 7.3a. For this comparison, the simple $(1\,0\,0)[0\,0\,1]$ crack system in (nearly isotropic linear-elastic) W is chosen. During the quasi-static displacement of the two blocks, Δ_y, all atomic positions are fixed and the interaction forces between first and second nearest neighbors are determined. The traction acting between the cleaved crystals is then calculated as follows:

$$T(\Delta_y) = \frac{N_{\text{atoms}}}{2A_{xz}} \frac{dE_{\text{pot}}}{d\Delta_y}, \tag{7.1}$$

where N_{atoms} is the number of atoms in the configuration, A_{xz} is the area of the xz plane (see Fig. 7.3a for the coordinate system), and E_{pot} is the average potential energy in the system. With this, the work of separation and theoretical strength σ_{th} as defined by Janisch *et al.* [21] can be calculated as $W_{\text{sep}} = 5.85\ \text{J/m}^2$ and $\sigma_{\text{th}} = 51.53$ GPa.

Since traction, or stress, is a continuum measure, it cannot be directly compared to the information available at a crack tip, i.e., the interaction forces. For this reason, we determine the first derivative of the traction-separation law, i.e., the sum of the forces in y direction between N_{int} interacting atoms across the $(1\,0\,0)$ plane, see Fig. 7.3a, as follows:

$$F_y(\Delta_y) = \frac{dE_{\text{pot}}}{d\Delta_y} = \frac{N_{\text{atoms}}}{2N_{\text{int}}} \frac{dE_{\text{pot}}}{d\Delta_y} \tag{7.2}$$

As a result of the equilibrium of forces, N_{int} first neighbor pairs and $N_{\text{int}}/2$ second nearest neighbor pairs are interacting across the cleavage plane. The total force F_y is thus related to the per-atom forces on opposite surfaces of the crystal halves, as follows:

$$F_y(\Delta_y) = \frac{N_{\text{int}} F_{y,1}(\Delta_y) + {}^{N_{\text{int}}}\!/_{2} F_{y,2}(\Delta_y)}{N_{\text{int}}} = F_{y,1}(\Delta_y) + {}^{1}\!/_{2} F_{y,2}(\Delta_y). \tag{7.3}$$

with $F_{y,1}$ and $F_{y,2}$ being the interaction forces between first and second nearest neighbors in y direction across the cleaved $(1\,0\,0)$ plane, see Fig. 7.3a.

For comparison with the forces between crack tip atoms, the interatomic distance r_{ij} between the crack tip atoms has to be converted to a corresponding Δ_y since the crack

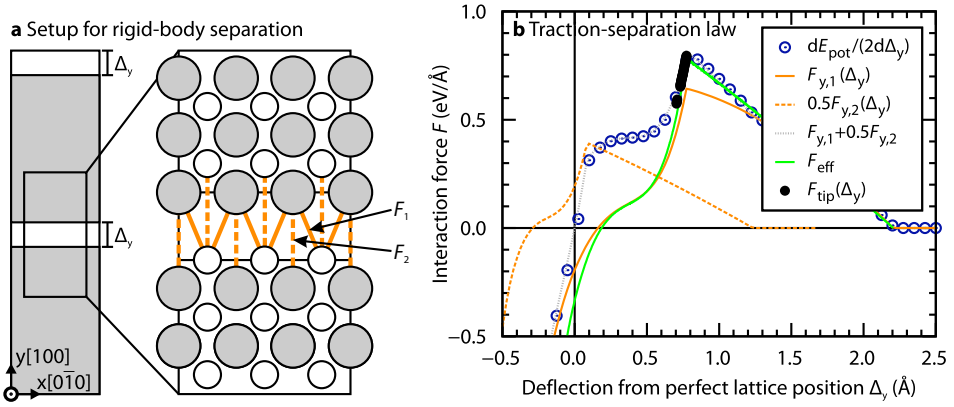

Figure 7.3: Traction-separation law derived from rigid-body separation for (100)[001] crack system. **a**: setup for rigid-body separation; two atomic blocks are rigidly displaced by a distance Δ_y; different atomic shading and size indicates atoms in different planes parallel to the plane of paper; **b**: comparison of the derived global forces $dE_{pot}/(2d\Delta_y)$ per interacting atom pair to the local interatomic forces between first and second nearest neighbors $F_{y,1}$ and $F_{y,2}$ (depicted in **a**), the effective pair force (first derivative of effective pair format [361]), and the interaction force between the atoms at the crack tip in the same orientation.

tip atoms can freely move in all directions; during the rigid-body separation, on the other hand, this is not allowed. The corresponding distances are converted as follows:

$$\Delta_y = -a_0/2 + \sqrt{r_{ij}^2 - a_0^2/2} \tag{7.4}$$

with a_0 being the bulk lattice parameter.

With this correction, all force data points can be plotted with respect to a the same separation distance, Δ_y, see Fig. 7.3b. The effective pair force, i.e., the derivative of the effective pair potential [361], is additionally plotted as function of Δ_y for comparison. By comparing the forces derived for these completely different situations, the following statements can be made: (i) the interatomic forces determined with rigid-body separations agree well with the forces acting at the crack tip immediately before bond rupture; and (ii) the evolution of both forces is equal to the evolution of the effective pair force.

These findings clearly indicate that traction-separation laws derived from atomistic rigid-body separations do not lack of information arising from the stress concentration at crack tips. To properly predict direction-dependent fracture resistance, meso-scale models should, however, also include terms taking into account the lattice trapping effect.

7.1.4 Influence of the crack length

The determined critical strains in strain-controlled setups showed a strong dependence on the crack length a, see Fig. 4.9a. Below a certain threshold crack length, the critical strains dramatically increased whereas being nearly constant otherwise. Furthermore, for very small crack lengths, the fracture behavior was found to alter from brittle to ductile. These influences of the crack length can be understood by considering all contributors to the crack-tip stress field, cf. Eq. (2.4), which generally consists of the singular $K_\mathrm{I}/\sqrt{r}$ term and a number of higher-order terms, such as the constant contributions to the σ_{yy} component by the globally applied 'background' stress or to the σ_{xx} component known as T-stress [31].

It is further important to recall that two necessary conditions have to be fulfilled in order to initiate crack propagation: (i) the stresses σ_{ij} at the crack tip have to be high enough to break the crack tip bonds; and (ii), the elastically stored energy G in the system has to be larger than a critical value, see e.g., Eq. (2.3). In general, the crack tip stresses follow a linear relationship with the applied strain ε, cf. Eq. (2.4) and Eq. (2.6): $\sigma_{ij} \propto E_y \varepsilon \sqrt{a}$. The energy release rate, on the other hand, is related to the applied loads by $G \propto L_y \varepsilon^2$, cf. Eq. (3.5). To initiate brittle fracture it is necessary to fulfill both requirements; as a result, the fracture initiation strain is controlled by the higher strain value for which either the critical crack tip stress or the critical energy release rate is reached. In summary, the following three regimes can be distinguished, cf. Fig. 4.9a:

- **Small cracks:** crack length dependence of the critical strain; controlled by crack tip stresses;
- **Large cracks:** crack length independence of critical strain; controlled by ERR;
- **Transition region:** transition from length dependence to length independence.

In the following, we first derive predictions for the fracture strains in the crack length dependent (crack tip stress controlled) and independent (energy release rate controlled) regimes based on the critical stress intensity factor K_Ic as determined in K-controlled simulations; thereafter, an approximate expression for the transition crack length between both regions is given. Although the focus is on central and edge cracks, the basic derivation of the predictions should be in principle also applicable to other crack geometries. Finally, the change of fracture behavior from brittle to ductile is explained with the increasing effect of the T-stress for very small cracks.

Critical strains for small crack lengths

For small crack lengths, the crack tip stresses are dominated by the singularity term and the critical strains for crack propagation can be predicted by solving Eq. (2.6) for $\varepsilon = \sigma/E$ and $Y = \sqrt{\pi}$ (central crack) as

$$\varepsilon_{\mathrm{p,small}}(K_\mathrm{Ic}, a) \quad = \quad \frac{K_\mathrm{Ic}}{\sqrt{\pi a} E_y}, \tag{7.5}$$

where the subscript 'p' stands for 'predicted' and E_y is the sample-dependent elastic modulus in loading direction. This prediction is compared to the determined critical strains ε_i

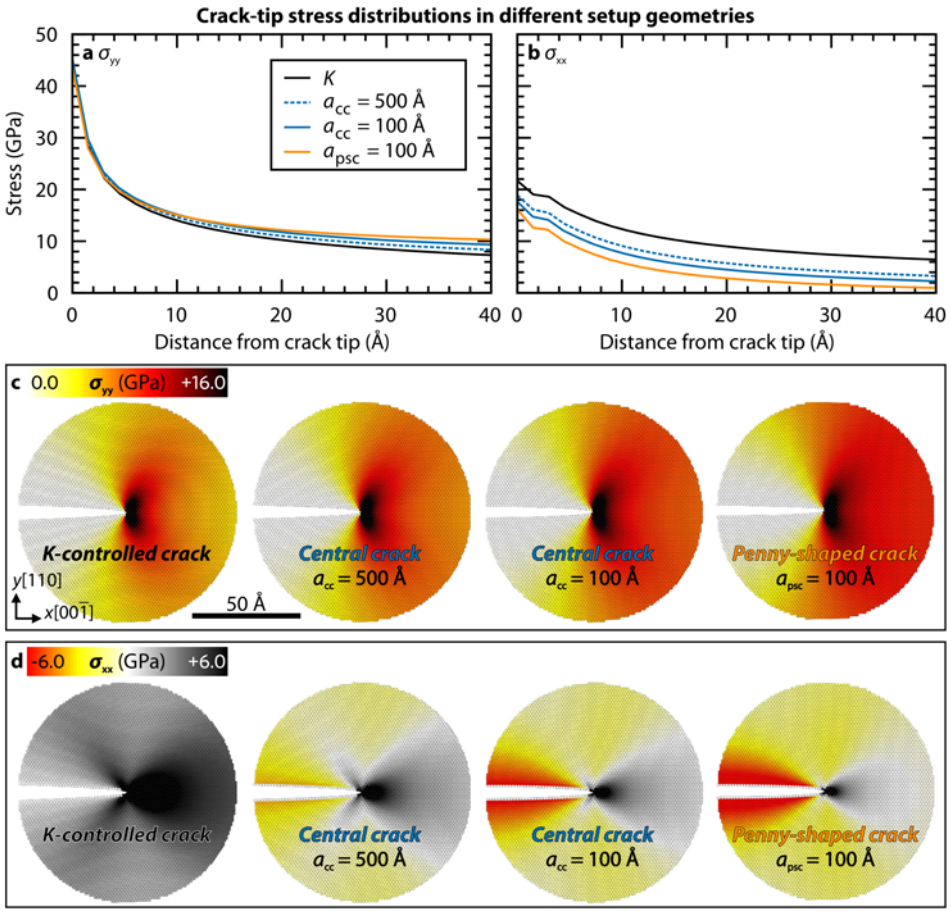

Figure 7.4: Stress distributions around relaxed crack tip configurations in different setup geometries in the (110)[110] crack system. **a**: σ_{yy} distribution in crack plane for K-controlled, central cracks (subscript 'cc') and penny-shaped cracks (subscript 'psc'); **b**: σ_{xx} distribution in crack plane; **c**: $\sigma_{yy}(x,y)$ stresses around the crack tip within a radius of 100 Å. **d**: $\sigma_{xx}(x,y)$ stresses around the crack tip within a radius of 100 Å. $L_y \approx 1000$ Å for the central and penny-shaped cracks; $L_x \approx 1000$ Å for $a_{cc} = a_{psc} = 100$ Å and $L_x \approx 3000$ Å for $a_{cc} = 500$ Å. The applied strains were $\varepsilon = 3.82$ (psc), 3.00 (cc, small), and 2.43% (cc, large); i.e., directly before the corresponding fracture event.

(dynamic loading) and ε_c (quasi-static loading) for the $(11\,0)[1\bar{1}\,0]$ crack system in Fig. 4.9a with $K_{Ic} = 1.21\ \mathrm{MPa}\sqrt{\mathrm{m}}$ being the fracture toughness as determined in the K-controlled setup and $E_y = 228$ GPa. As it can be seen in the figure, the prediction matches the determined ε_i values for very small crack length up to $a \approx 150$ Å.

Critical strains for large crack lengths

For large crack lengths, the fracture strain is controlled by the energy release rate, which can be estimated by Freund's formula for a long crack [41], see Eq. (3.3). If, in this equation, the Griffith criterion $G_c = 2\gamma$ is substituted by the relationship between K and G from Eq. (2.5), the predicted critical is obtained as:

$$\varepsilon_{p,large}(K_{Ic}) = \sqrt{\frac{2}{L_y}}\frac{K_{Ic}}{E_y} \tag{7.6}$$

Using the same values for K_{Ic} and E_y as before and the box length $L_y = 1000$ Å, the predicted critical value is $\varepsilon_{p,large} = 2.37$ %, see Fig. 4.9a. This value is slightly lower than the average value for the ε^{pre} lateral straining method (around 2.44 %), but larger than for the other lateral strain methods, see Fig. 4.9d.

The slight underestimation of the critical strains by $\varepsilon_{p,large}$ can be qualitatively understood by taking into account the other important higher-order term, i.e., the T-stress [31]:

$$T = \frac{\sigma}{B} \tag{7.7}$$

where σ is the global load perpendicular to the crack plane and B is the biaxiality parameter. Since $B = -1$ for the central crack [31], the contribution of the T-stress is negative and the σ_{xx} component of the crack-tip field decreases as the applied stress σ increases. As a result, the necessary applied strains (or stresses) to achieve the critical loading state for crack-tip bond breaking can be higher than predicted by $\varepsilon_{p,large}$, cf. Eq. (7.6), which disregards the T-stress effect.

The T-stress effect is visualized in Fig. 7.4 where the σ_{xx} and σ_{yy} stress distributions are plotted for different crack lengths $a = 100$ and 500 Å for the central crack in comparison to the stresses in the K-controlled setup; the additionally plotted stress distribution for the penny-shaped crack will be discussed in section 7.2.2. In all cases, the stresses are shown for the energetically minimized configurations directly before initiation of brittle fracture (K-controlled and central cracks) or crack tip plasticity (penny-shaped crack). As it can be seen in Fig. 7.4a, the near-tip σ_{yy} stresses are nearly equal in the different scenarios. This means, that the stress intensity factor acting at the crack tip is nearly the same in all configurations even if the applied strains were different, see Fig. 4.9a. As a result of the T-stress, the σ_{xx} component, on the other hand, is constantly reduced with increasing applied strains.

To determine the precise form of $\varepsilon_{p,large}$ as well as the transition crack length between the validity of $\varepsilon_{p,small}$ and $\varepsilon_{p,large}$, the full higher-order stress field function should be determined. As mentioned earlier in section 2.1.1, this can not be done analytically and a numerical solution for the problem of interest here is also lacking. Despite of this uncertainty, the current predictive power of $\varepsilon_{p,small}$ and $\varepsilon_{p,large}$ is very helpful to allow a straightforward prediction of the initial strain ε_{in} for the strain-controlled simulation setup, see section 3.3.3, which must otherwise often be determined by a costly 'trial and error' approach.

Finally, it should be noted that the critical strains, when compared to the thermodynamic prediction ε_0, yield nearly the same ratio for $\varepsilon_c/\varepsilon_0 = 1.25 \pm 0.01$ as compared to the

equivalent values determined in the K-controlled setup $K_{Ic}/K_G = 1.27$. This indicates that the lattice trapping effect does not or only marginally depend on whether a K- or strain-controlled setup is used.

Transition region

In general, the transition between small and large crack length should occur at around

$$a_t = \frac{L_y}{2\pi}, \tag{7.8}$$

which is derived by setting the functions $\varepsilon_{p,small}$ and $\varepsilon_{p,large}$ equal; for the data plotted in Fig. 4.9a, the transition is predicted to occur around $a_t \approx 160$ Å, which fits well with the determined threshold region between 150 and 250 Å. Since the transition has a smooth character, it will, however, generally start at smaller crack lengths than a_t and end at larger values.

Influence on fracture behavior

Besides its contribution to the critical fracture strain, the T-stress has a second implication in that it can also alter the fracture behavior. In Fig. 7.5a-f, the stress distributions are compared for a small and a large crack. The small crack with $a = 24$ Å emitted a dislocation, see Fig. 4.7b, whereas the large crack with $a = 443$ Å propagated in a brittle manner, see Fig. 4.7d. A similar effect was also observed by Machová and Beltz for the ductile-brittle behavior of cracks in the $(0\,0\,1)[1\,1\,0]$ crack system in Fe [186]; they concluded that small cracks have a higher susceptibility to twin formation because of the higher magnitude of the T-stress as compared to large cracks.

As it can be seen in Fig. 7.5g, the σ_{xx} stress component is constantly reduced by the T-stress for the smaller crack length. This can be understood as the T-stress depends on the applied stress, cf. Eq. (7.7); its contribution is thus especially pronounced for very small cracks, which have higher critical strains than large cracks , see Fig. 4.9a. As a consequence, the σ_{xx} stresses are significantly smaller than for the long crack. This reduces the hydrostatic stress state, which also decreases the driving force for crack propagation. At the same time, the resolved shear stress τ_{rss} increases in the dislocation system. This leads to 2-4 GPa higher τ_{rss} values as compared to the long crack, see subfigure g, and thus a higher tendency for dislocation emission. At the same time, the overall applied strains are higher for small cracks, which leads to an increased effect of tension-shear coupling. This was discussed in section 7.1.1. Both explanations indicate that small cracks should generally promote crack tip plasticity rather than brittle fracture.

In this context, it is important to note that the effects of both T-stress and tension-shear coupling are *not* exclusively caused by the small box size in the atomistic configurations and the correspondingly large applied strains. On the one hand, tension shear-coupling obeys a nearly linear relation with the applied strain and will therefore be present also for small strains, see cf. Fig. 7.1. Furthermore, it was observed to have an strong influence on the

onset of plastic deformation in other materials and setups, see e.g. Ref. [417] for nanowire bending in fcc Cu. The T-stress effect, on the other hand, is particularly important when the crack size or specimen dimensions are very small [31] and the crack tip stresses are close to the theoretical strength, as e.g. in micro electro-mechanical systems (MEMS).

In summary, the existence of a crack length dependent and a crack length independent regime of the determined critical strains is explained with (i) the singular term in the crack tip stress field, which leads to a pronounced length dependency for small crack lengths; and (ii) the constant 'background' stress in the configuration, which leads to constant critical strains for large cracks. The transition between both regions is estimated to occur at around $L_y/(2\pi)$ for quasi-2D edge and central cracks.

The change in fracture behavior from brittle to ductile for very small cracks is explained with the increasing contribution of the T-stress to the crack-tip stress field with increasing loads, i.e., decreasing crack length. As this effect should also be present at real crack tips, it can be speculated that small cracks should generally promote crack tip plasticity rather than brittle fracture.

7.1.5 Influence of the interatomic potential

The results of this thesis as well as the work by Sinclair [418], Kohlhoff *et al.* [29], and Gordon *et al.* [30] indicate that the interatomic potential has a pronounced influence on the fracture properties. Fig. 7.6a gives an overview of the interatomic force functions as determined from the potential parameters using the effective pair format scheme [361] for selected bcc potentials. These potentials are selected as they did not show non-physical extensive crack tip transformations or abnormally high fracture toughness values. Fig. 7.6b and c compare the influence of the different potentials on the measured values for K_{Ic} as function of K_G in the $(1\,1\,0)[0\,0\,1]$ and $(1\,1\,0)[\bar{0}\,0\,1]$ crack system. It can be seen that K_G both predicts the values and the correct ranking of the K_{Ic} among the different metals quite accurately for the $[1\bar{1}\,0]$ crack front direction: K_{Ic}/K_G is on average 1.19 ± 0.03. Similarly, the average values of K_{Ic} are 1.11 ± 0.04 times higher than K_G for the $(1\,0\,0)[0\,1\,1]$ crack system. For $[0\,0\,1]$ crack front directions, on the other hand, the predictions are less accurate: $K_{Ic}/K_G \approx$ 1.53 ± 0.07 for the $(1\,1\,0)[0\,0\,1]$ crack system. The quantitative results for the $(1\,0\,0)[0\,0\,1]$ crack system are not discussed here in more detail as nearly all potentials showed crack-tip transformations leading to unreliable values for K_{Ic}.

The reason for the discrepancy between the different crack fronts is rooted in the lattice trapping effect, which is more pronounced for $[0\,0\,1]$ crack fronts, as discussed in section 7.1.1. For the potentials shown in Fig. 7.6b, the lattice trapping range ΔK varies between 0.27 (Fe-Chamati) and 1.64 (V-ATFS) for the $[0\,0\,1]$ crack front, which highly complicates the prediction of a precise K_{Ic} value. Lattice trapping does, however, not only increase the actual stress intensity factor for brittle crack propagation to values higher than the corresponding thermodynamic prediction; it can in principle also *change* the fracture behavior when the crack is trapped until the necessary energy barrier for dislocation emission is reached as it was discussed in section 7.1.1.

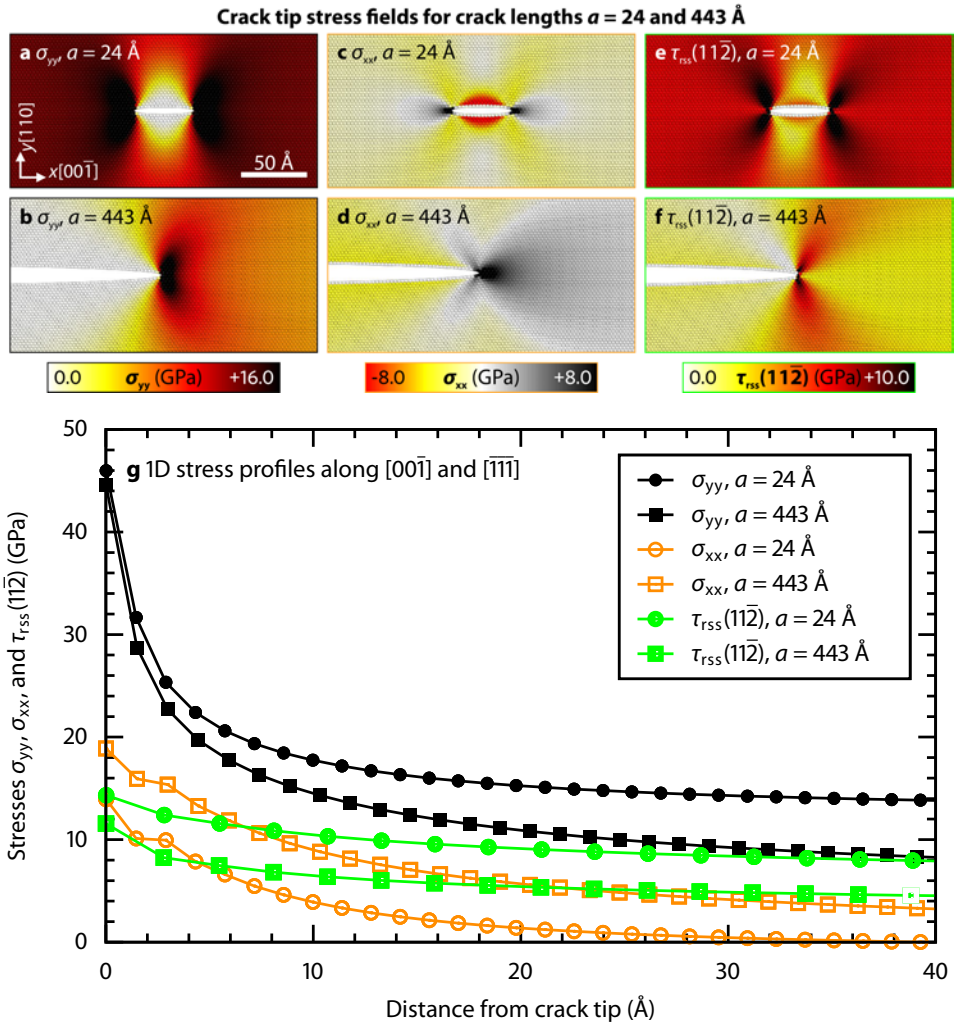

Figure 7.5: Atomic crack-tip stress distributions around small and long dynamically loaded quasi-2D central cracks (L_x = 3000 Å, L_y = 1000 Å; $\dot{\varepsilon} = 10^8$ s^{-1}). Stresses are plotted for applied strains that are slightly lower ($\varepsilon = \varepsilon_i - \delta\varepsilon$, $\delta\varepsilon$ = 0.01 %) than the critical strains, i.e., ε_i = 5.81 % for the small and ε_i = 2.43 % for the long crack; at ε_i, the small crack emits a (11$\bar{2}$) dislocation whereas the long crack starts to propagate, cf. Fig. 4.7; **a**, **b**: normal stresses in crack plane normal direction, σ_{yy}; **c**, **d**: normal stresses in crack propagation direction, σ_{xx}; **e**, **f**: shear stresses resolved in the (11$\bar{2}$) plane, τ_{rss}; **g**: 1D stress profiles of σ_{yy} and σ_{xx} in the prolonged (110) crack plane along the [00$\bar{1}$] direction and the resolved shear stresses τ_{rss} in the (11$\bar{2}$) plane in [$\bar{1}\bar{1}\bar{1}$] direction.

On the other hand, the actual crack path after fracture initiation is strongly influenced by the potential-dependent formation of planar faults on $\{1\,1\,0\}$ planes. In the $(1\,0\,0)[0\,0\,1]$ crack system, for instance, they often cause the kinking of cracks on inclined $\{1\,1\,0\}$ planes, cf. Tables 4.1-4.2 and Fig. 4.1a and e. Planar faults are, however, not only important at straight crack fronts, but also under fully 3D conditions, as it can be seen in case of the penny-shaped crack on the $(0\,1\,0)$ plane in Fig. 4.3a and b.

In the following, the influence of the interatomic potential on both the lattice trapping effect and the formation of $\{1\,1\,0\}$ planar faults is determined; thereafter, all studied potentials are critically assessed in terms of their usability for future atomistic fracture simulations.

Lattice trapping

The current understanding of the dependence of the lattice trapping range $\Delta K = K^+/K^- - 1$ on the interatomic potential is that ΔK is small for soft and long-range potentials and large for spring-like and short-range potentials [12, 418]. While Sinclair [418] resorted to four model potentials for Si to find this qualitative relationship, with the different potentials used in the present thesis it is now possible to relate the determined fracture data to characteristic properties of the studied potentials. A correlation of the form of the atomic interaction potential with ΔK could help to develop future potentials that exhibit typical lattice trapping ranges without the need for performing costly fracture simulations during the optimization of the potential parameters.

As we have seen in Fig. 7.6c, the fracture toughness K_{Ic} can be sufficiently well predicted for the $(1\,1\,0)[1\bar{1}\,0]$ crack system by simply calculating K_{G}. For the $[0\,0\,1]$ crack fronts, the scatter is much larger as a direct consequence of the potential dependence of the lattice trapping. This dependence is shown Fig. 7.7a, where no simple relationship between the fracture toughness and the lattice trapping range can be derived. For instance, ΔK varies between 0.27 and 1.64 for the Fe-Chamati and V-ATFS potentials while they differ by only 0.1 MPa$\sqrt{\mathrm{m}}$ in K_{Ic}. It is, however, interesting to note that for most potentials the lattice trapping range ΔK correlates with $K_{\mathrm{Ic}}/K_{\mathrm{G}}$-1, which is used as an alternative formulation of the lattice trapping effect.

To find a quantitative prediction of the lattice trapping range based on the properties of the interatomic potential, we come back to the qualitative prediction, that soft and long-range potentials show a low lattice trapping. Let us further assume, the softness of the potential is described by its maximum effective force F_{max} and the long-range character by the cutoff radius r_{cut}. When comparing the corresponding values provided in Table 7.1 for the studied potentials, it is obvious that the Chamati potential for Fe has both the lowest F_{max} and the highest r_{cut} and does indeed show the lowest lattice trapping range ($\Delta K = 0.27$). At the same time, the potentials with the highest ΔK values, the V-ATFS and the Fe-Chiesa potentials, have the smallest cutoff radii. On the other hand, their maximum forces are only of intermediate ranks. This indicates that the influence of the cutoff radius on the lattice trapping range might be stronger than the influence of the maximum force.

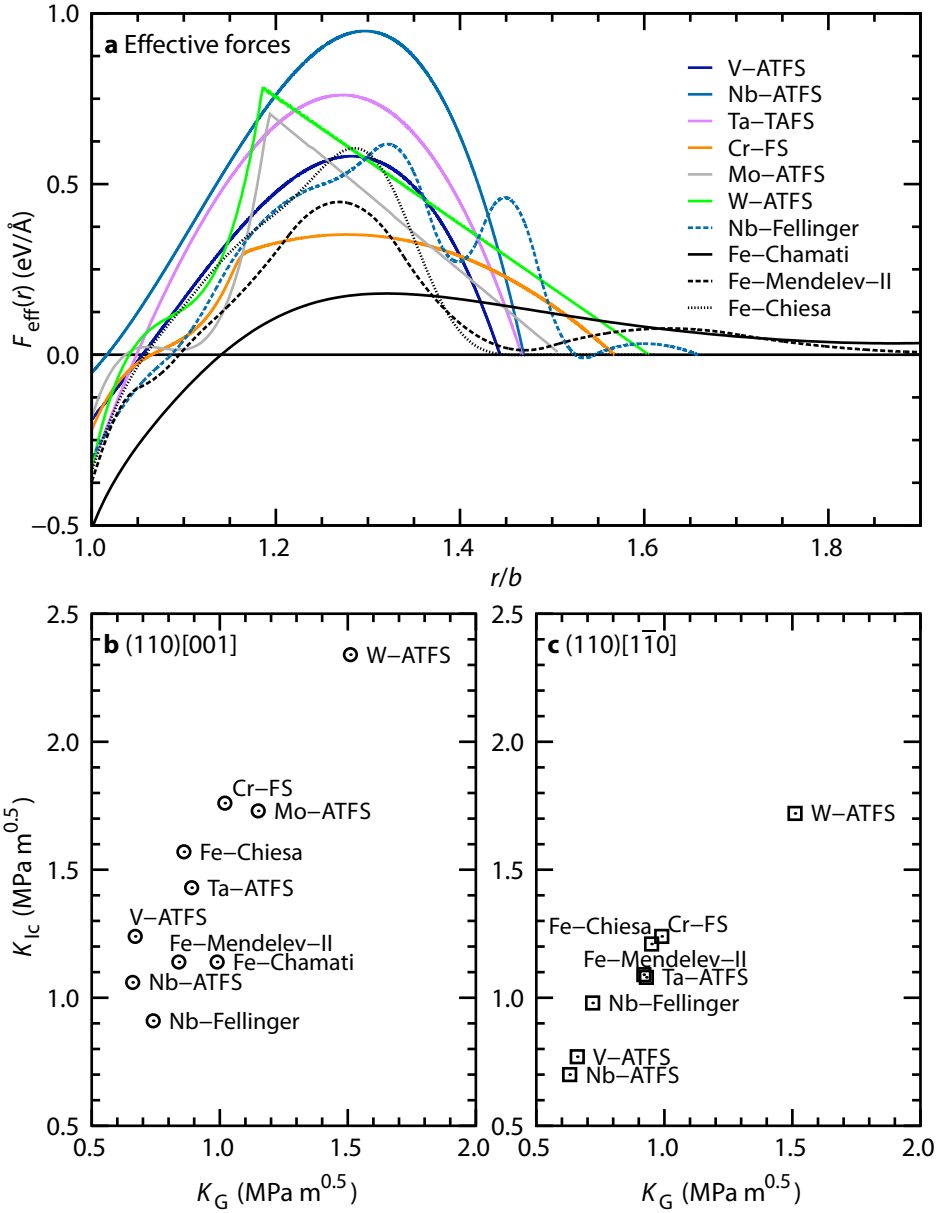

Figure 7.6: Comparison of effective pair forces and fracture toughness K_{Ic} of selected bcc potentials. **a**: effective pair force, i.e., first derivative of effective pair potential [361]; **b**: (110)[001] crack system, no simple correlation between K_{Ic} and K_G; **c**: (110)[1$\bar{1}$0], nearly linear proportionality of K_{Ic} and K_G.

Table 7.1: Comparison of characteristic distances r and effective forces $F(r)$ of different bcc potentials (ordered from low to high lattice trapping range $\Delta K_{[001]}$ on the (110) plane). Units of distances and forces are Å and eV/Å. $N_{\max}$: number of neighbors within the cutoff radius.

Potential	$N_{\max}$	$r(F{=}0)$	$r(F_{\max})$	r_{cut}	$F(b)$	$F(a_0)$	$F_{\max}$	$\Delta K_{[001]}$	$\Delta K_{[1\bar{1}0]}$
Fe-Chamati	4	2.831	3.276	5.670	-0.510	0.031	0.179	0.27	—
Fe-Mendelev-II	4	2.708	3.137	5.300	-0.371	0.160	0.448	0.61	0.35
Mo-ATFS	2	2.824	3.250	4.115	-0.184	0.209	0.712	0.80	—
W-ATFS	2	2.853	3.251	4.400	-0.335	0.386	0.784	0.89	0.22
Cr-FS	2	2.659	3.192	3.916	-0.218	0.251	0.353	0.95	0.46
Nb-Fellinger	3	3.113	3.786	4.750	-0.300	0.286	0.622	1.00	1.60
Ta-ATFS	2	3.002	3.641	4.200	-0.327	0.535	0.763	1.14	0.46
Nb-ATFS	2	2.905	3.703	3.915	-0.053	0.581	0.951	1.22	0.52
Fe-Chiesa	2	2.628	3.192	4.000	-0.343	0.312	0.605	1.55	0.67
V-ATFS	2	2.778	3.378	3.800	-0.187	0.351	0.584	1.64	0.64

In the original work by Sinclair [418], the terms 'soft' and 'long-range' clearly defined the shapes of the effective force functions, which were compared; since the potentials were all fitted to match the equilibrium properties of Si, they did not differ in e.g. the small-strain behavior, but only in their long-range character. In the present case, however, we compare potentials for metals which strongly vary in their equilibrium properties, such as lattice and elastic constants as well as surface energies, cf. Tables 3.2 and 3.3. For this reason, the characteristics of the potentials have to be seen in respect to their corresponding equilibrium properties before we can properly compare the character of the effective force functions in Fig. 7.6a.

To obtain a relative estimate Δk for the lattice trapping range ΔK, we estimate the energy to separate two atoms form their equilibrium position b to $r(F_{\max})$ as $W = {}^1\!/_2[F_{\max} - F(b)][r(F_{\max}) - b]$. The energy W is further related to the energy of a created fracture surface, which has to be proportional to $2\gamma b^2$. Finally, the normalized cutoff radius, i.e., the influence of the long-range character of the interaction force, is used as weighting factor $(b/r_{\text{cut}})^n$ where n can be arbitrarily chosen. In summary, Δk takes on the following general (unitless) form:

$$\Delta k \quad = \quad \left(\frac{b}{r_{\text{cut}}}\right)^n \frac{[F_{\max} - F(b)][r(F_{\max}) - b]}{4\gamma b^2}. \tag{7.9}$$

As stated before, the factor n can in principle be chosen arbitrarily. In Fig. 7.7b, the dependency of the determined ΔK on the predicted Δk is shown for $n = 2$. Given the large number of approximations made to obtain Δk, the agreement with ΔK is surprisingly good for the $[0\,0\,1]$ crack front, where ΔK is on average in the range of $(13 \pm 0.9)\Delta k$. In case of the $[1\bar{1}0]$ crack front direction, the number and character of bonds that contribute to the fracture toughness is much higher; the effect of lattice trapping can therefore not be estimated by simply considering the range between b and $r(F_{\max})$. On the other hand, for $[1\bar{1}0]$ crack front directions the lattice trapping effect is relatively small and K_{Ic} can be sufficiently well estimated already by calculating K_{G}.

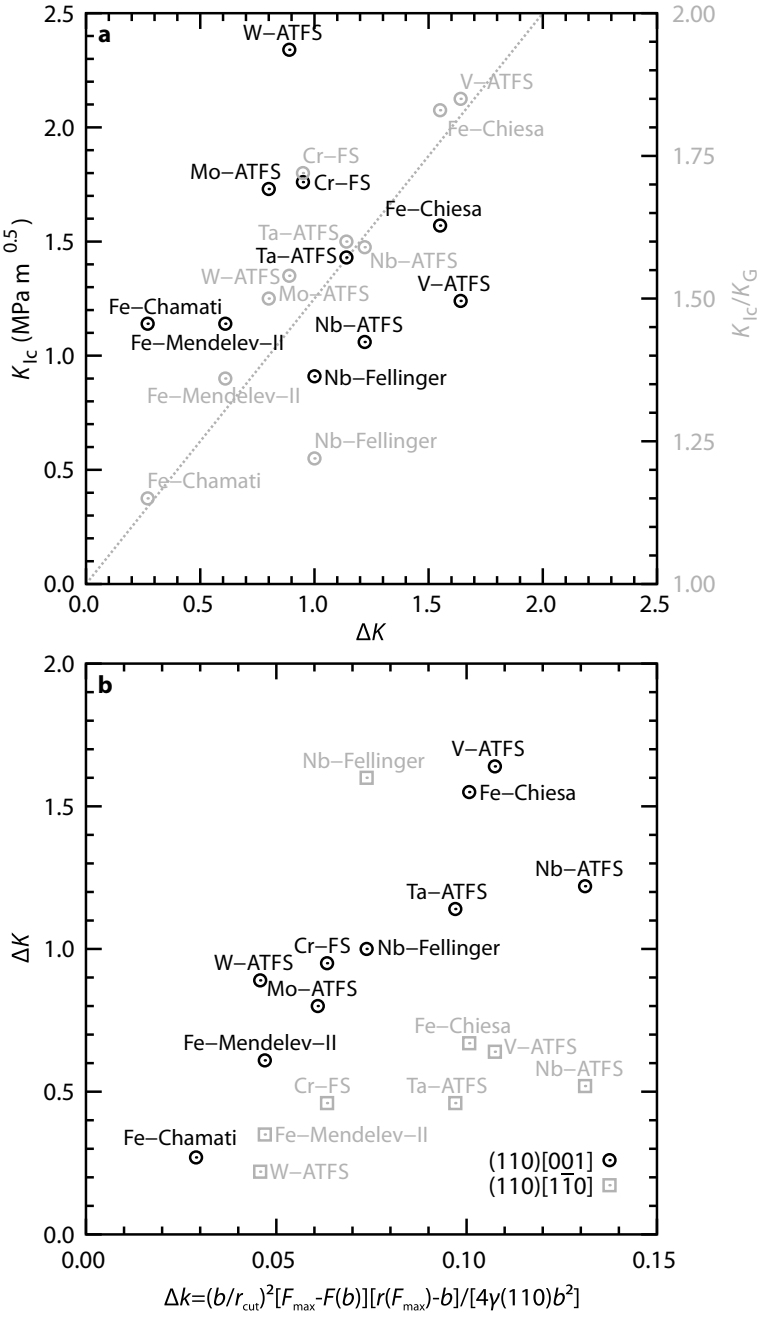

Figure 7.7: Predictions for ΔK based on potential properties. **a**: (110)[001] crack system, large scatter in lattice trapping range ΔK for almost equal K_{Ic} values; nearly linear relationship between K_{Ic}/K_G and ΔK except for the Nb-Fellinger and Cr-FS potentials; **b**: prediction of ΔK based on the function Δk, Eq. (7.9). See text for details.

In summary, I can make the following important statements for the development of future EAM potentials designed for fracture in bcc metals: for ⟨110⟩ crack front directions, the fracture toughness K_{Ic} is most likely in the range of 1.1-1.2K_G; in the (110)[001] crack system, the lattice trapping range ΔK can be estimated as $(13 \pm 0.9)\Delta k(n{=}2)$. In conjunction with a small difference between the (100) and (110) surface energies, these criteria should lead to an overall better agreement with the experimental data. The $(1\,0\,0)[0\,0\,1]$ crack system was excluded here as nearly all potentials showed unreliable values for K_{Ic} as a result of crack-tip transformations. These transformations will be the topic of the following paragraphs.

Formation of {110} planar faults

The majority of the tested potentials shows the formation of $\{1\,1\,0\}$ planar faults at crack tips in the $(1\,0\,0)[0\,0\,1]$ crack system, see Fig. 4.1. Most results and parts of the following discussion have been published in Ref. [122]. The planar defects are produced by shearing of adjacent ±45°-inclined $\{1\,1\,0\}$ planes along a $\langle 1\bar{1}\,0\rangle$ direction. In case of the Marinica potentials, the structural transformations at the $(1\,0\,0)[0\,0\,1]$ crack tips are more complex. As mentioned before, these potentials are, however, excluded from this discussion since they show unphysical structural transformations in almost all orientations. When planar faults were present at the crack tip, this resulted in the final kinking of the crack onto an inclined $\{1\,1\,0\}$ plane, see Fig. 4.1a and e. Here, the Chamati potential displays the only exception as it shows neither the formation of $\{1\,1\,0\}$ planar faults nor fracture along an inclined plane. Instead, only a small region ahead of the crack tip is structurally transformed and the fracture proceeds along the $(1\,0\,0)$ crack plane, see Fig. 4.1c. It is important to note that the occurrence of $\{1\,1\,0\}$ planar faults is independent of simulation setup and loading conditions, see Fig. 4.2. Their formation can furthermore not be attributed to the use of PBCs along the straight crack front, as they are also present at curved crack fronts, cf. Fig. 4.3 and Refs. [164, 201].

In the literature, the same structural transformation in front of $(1\,0\,0)[0\,0\,1]$ cracks are discussed in terms of bcc to fcc phase transformation [164, 197–199, 297]. For this reason, possible fcc unit cells are extracted from the crack tip structures and compared to the perfect fcc structures in terms of $\langle 1\,1\,0\rangle_{fcc}$ bond angles in Fig. 7.8. This comparison shows that only the defect structure at the crack tip of the Chamati potential is in agreement with the fcc lattice, see Fig. 7.8e and g. In this case, the maximum deviation from the perfect fcc bond angles is less than 2°. This observation is explained by the classical tension-induced inverse Bain path [419] to transform bcc to fcc: the bcc unit cell is strained parallel to one of the $\langle 1\,0\,0\rangle$ axes to reach the fcc structure. Such a transformation is likely to happen in the highly stressed regions around the crack tip. To visualize this, the lengths of adjacent $[1\,0\,0]$ bonds are marked in Fig. 7.8a for different distances to the crack tip.

For the remaining potentials (represented by the Mendelev-II potential), the identification as fcc is due to an incomplete analysis of the structure in front of the crack. In these cases, the usually employed CNA identifies a stacking of multiple $\{1\,1\,0\}$ planar faults as fcc structure. As it can be seen in Fig. 7.8h, the highest deviation of the bond angles from

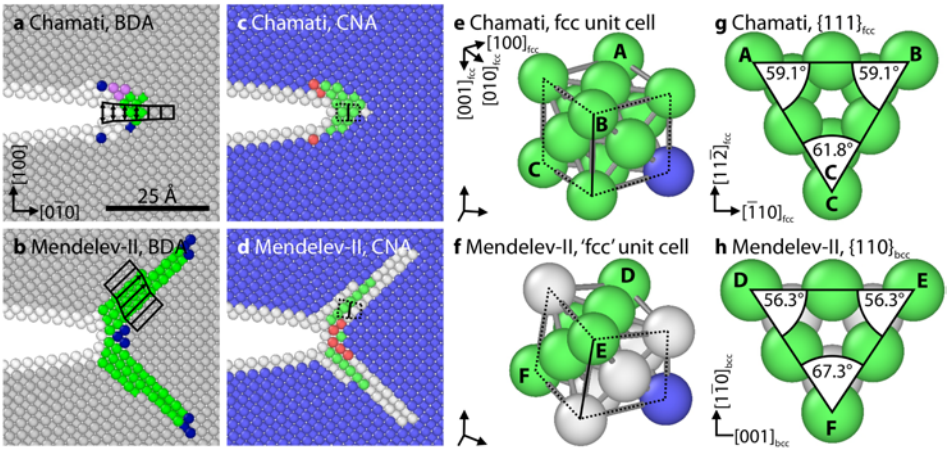

Figure 7.8: Atomistic configurations in the (100)[001] system showing the formation of {110} planar faults and fcc-structured regions at the crack tip. Upper subfigures: Chamati potential; lower subfigures: Mendelev-II potential; **a**: Chamati configuration at $K_I = 1.24$ MPa$\sqrt{\text{m}}$ in BDA coloring (grey: bulk; white: surface; green: {110} planar faults; blue: non-screw dislocation); **b**: Mendelev-II configuration at $K_I = 1.38$ MPa$\sqrt{\text{m}}$ in BDA coloring: deformations that are mainly responsible for the observed defect structures are marked in **a** (tension in [100] direction) and **b** (shear in the $[1\bar{1}0]$ direction on adjacent (110) planes); **c**,**d**: same configurations as in **a** and **b** in CNA coloring (blue: bcc; green: fcc; red: hcp; white: other); **e**,**f**: possible fcc unit cells extracted from the marked regions in **c** and **d**; **g**,**h**: top views on possible $\{111\}_{\text{fcc}}$ planes extracted from the unit cells in **e** and **f**; same atoms in **e**-**h** are marked with same capital latin letters A-F; the characteristic angles between possible $\langle 110\rangle_{\text{fcc}}$ bonds in $\{111\}_{\text{fcc}}$ planes are marked in **g** and **h**; for the Chamati potential, the maximum deviation is less than 2° from the ideal fcc angles ($\sphericalangle$ ABC = $\sphericalangle$ BCA = $\sphericalangle$ CAB = 60°); for the Mendelev-II potential, the maximum deviation from the fcc angles is higher than 7°; in this case, the measured angles are still closer to the ideal bcc values ($\sphericalangle$ DEF = $\sphericalangle$ FDE ≈ 54.7°, $\sphericalangle$ EFD ≈ 70.5°), where the maximum deviation is less than 4°.

the fcc values is more than 7°. On the other hand, the deviation from the bcc values is still less than 4°. This indicates that the observed defect structure is still in the bcc phase.

A comparison to the theoretical shear-induced bcc to fcc transformation path after Cohen, Bogers and Burgers [415, 420] gives a second indication that the observed defect structures are unlikely fcc:

$$\text{bcc} + {}^{a_{\text{bcc}}}/_{8}[1\bar{1}0]_{\text{bcc}}(110)_{\text{bcc}} + {}^{a_{\text{fcc}}}/_{18}[1\bar{1}2]_{\text{fcc}}(1\bar{1}\bar{1})_{\text{fcc}} \rightarrow \text{fcc}\,. \tag{7.10}$$

This means that a shear on the $(1\bar{1}\bar{1})_{\text{fcc}}$ plane is necessary to complete the bcc to fcc transformation in addition to the observed shear on the $(1\,1\,0)_{\text{bcc}}$ plane. The $(1\bar{1}\bar{1})_{\text{fcc}}$ plane corresponds to the plane spanned by the atoms E, F, and the blue atom in Fig. 7.8f. This plane, however, lies oblique to the crack front (vector between atoms D and E). In the presence of periodic boundary conditions, which are used in the majority of the aforementioned reports, this transformation is therefore simply not possible. This consideration further

supports that the observed defect structures are unlikely fcc and instead best described by the term '$\{1\,1\,0\}$ planar faults'.

As with all plastic crack tip processes, the generation of planar faults is a way to relief shear stress in front of a crack tip. Like dislocation processes the shear of adjacent planes can be related to the generalized stacking fault energy (GSFE) surface (γ surface) [61]. Fig. 7.9 shows the $\gamma(1\,1\,0)$ surface for the Mendelev-II potential and cross sectional views (γ lines) along the $[1\bar{1}0]$ and $[1\bar{1}1]$ direction. The $[1\bar{1}0]$ direction is the detected direction in which shearing leads to the observed $\{1\,1\,0\}$ planar faults while the $[1\bar{1}1]$ direction is the conventional Burgers vector direction. The γ lines are also plotted for the Chamati and Chiesa potentials as well as using density functional theory (DFT) calculations. Fig. 7.10 presents the corresponding $\gamma(1\,1\,0)$ lines for the remaining bcc potentials.

It can be seen in Fig. 7.9a, that small rigid-body displacements across the (110) plane create configurations with lower energies in $[1\bar{1}0]$ direction than in the $[1\bar{1}1]$ direction. However, for normalized shifts in $[1\bar{1}0]$ direction larger than approximately 0.25, the $[1\bar{1}1]$ direction becomes favorable. The γ surfaces were also calculated for applied uniaxial and equi-biaxial strains of 7.5 % and 5 %, respectively. These conditions are more representative for the situation in front of the crack tip than the strain-free situation discussed thus far. The corresponding plots are shown in Fig. 7.9b and c. Under these conditions, the overall magnitudes of the energies decrease for all potentials. More remarkably, a local minimum occurs at a normalized shift in $[1\bar{1}0]$ direction of approximately 0.18 in the case of the Mendelev-II potential under uniaxial and biaxial conditions. The same behavior can be observed in case of the Chiesa potential under biaxial strain. These local minima indicate that under tension a stable stacking fault (SSF) can be formed by a partial dislocation on the (110) plane. The positions of the local minima match nicely the shear vectors observed in the fracture simulations, see Ref. [122]. Therefore the occurrence of $\{1\,1\,0\}$ planar faults can be traced back to the stabilization of stacking faults under high strain conditions close to the crack tip. Their existence is, however, not limited to Fe as similar simulations in the remaining bcc potentials show, see Fig. 7.10. Only for Cr a local GSFE minimum is not observed in the studied strain range up to 10 % applied biaxial strains with an important consequence for the crack path: Similar to the behavior observed for the Chamati potential for Fe, the crack remains on its original $(1\,0\,0)$ plane in case of Cr, cf. Table 4.2.

Theoretically, partial dislocations on the $(1\,1\,0)$ plane with a $a_0/s[1\bar{1}0]$ Burgers vector have been proposed by Crussard [421, 422] and Cohen *et al.* [415]. Whereas Crussard proposed a fixed value of $s = 8$, our simulations suggest that the actual value of s depends on the details of the stacking fault energy curve. The data shown in Fig. 7.9, however, shows that the occurrence of local minima in the γ surface is highly potential dependent. Neither the Chamati (for Fe) and FS (for Cr) potentials nor the corresponding DFT calculations exhibit local minima, even if the applied strains are increased up to 10 %. This indicates that planar faults are most likely an artifact of many EAM potentials for bcc metals and do not occur in nature. From an experimental point of view, the existence of $\{1\,1\,0\}$ stacking faults is also questionable as only Smith and Gallot [423] report on a dissociated $\{1\,1\,0\}$ dislocation in Fe. Contrary to them, Rothman and Cohen [424] found $\{1\,1\,0\}$ stacking faults only for Nb, but not for Fe.

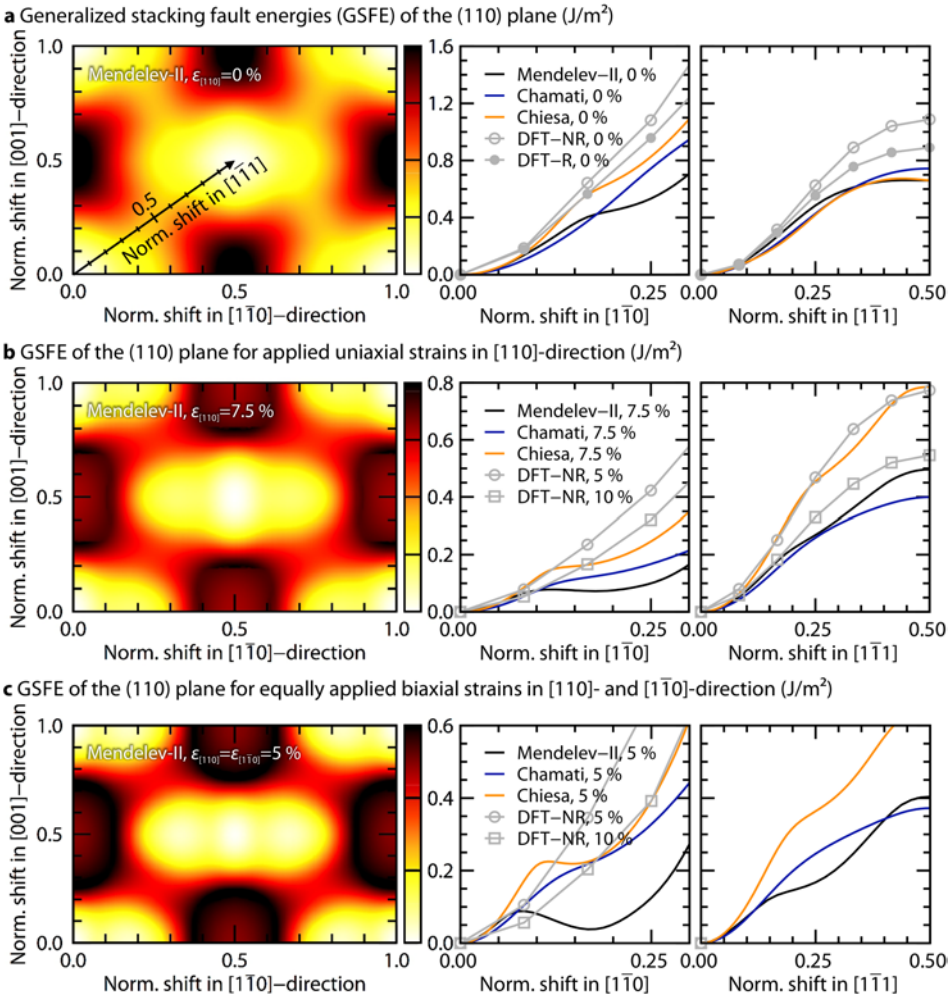

Figure 7.9: γ surfaces and line profiles of the (110) slip plane under varying external loads. The shifts in [001], [1$\bar{1}$0], and [1$\bar{1}$1] directions are normalized, i.e., divided by the corresponding periodicity distances a_0, $\sqrt{2}a_0$, and $\sqrt{3}/2a_0$. The γ surfaces are shown for the Mendelev-II potential. The γ line profiles in [1$\bar{1}$0] and [1$\bar{1}$1] directions are shown for the Mendelev-II, Chamati, and Chiesa potentials as well as for DFT calculations. **a**: no external load; **b**: external uni-axial strain $\varepsilon = 7.5$ %; **c**: external equi-biaxial strain $\varepsilon = 5$ %. The Mendelev-II and Chiesa potentials tend to exhibit local minima along the [1$\bar{1}$0] direction under external strain (**b**,**c**); this behavior is not observed for the Chamati potential and the DFT method.

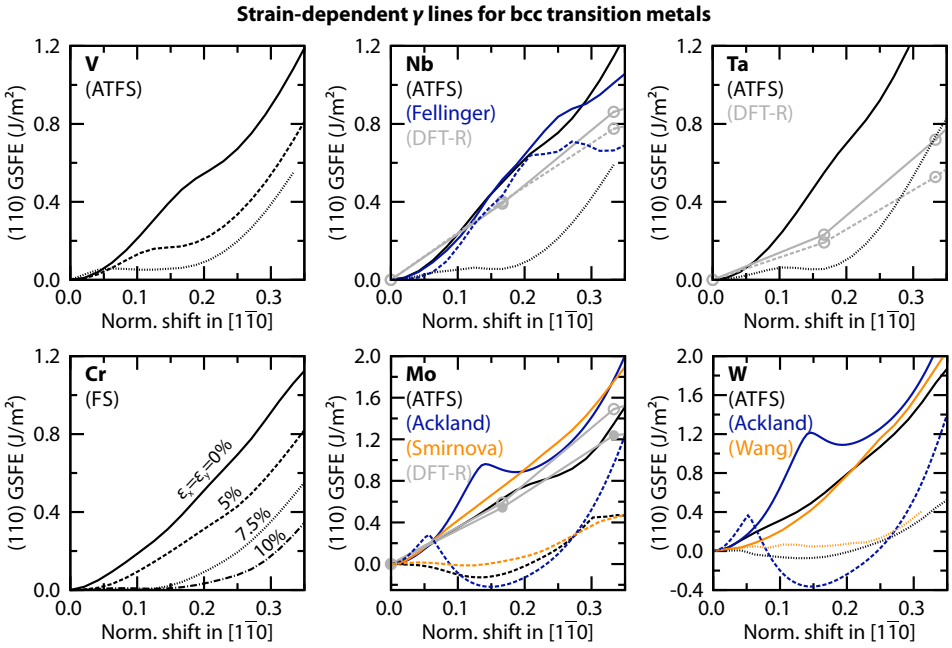

Figure 7.10: Strain-dependent γ lines of various EAM potentials for the bcc metals V, Nb, Ta, Cr, Mo, and W. The GSFE data is plotted for 0 % (solid lines), 5 % (dashed), 7.5 % (dotted), and 10 % (dashed-dotted) applied equi-biaxial strain parallel to both the (110) plane normal and the $[1\bar{1}0]$ shearing direction. The shift in $[1\bar{1}0]$ direction is normalized, i.e., divided by the corresponding periodicity distance $\sqrt{2}a_0$. Relaxed stacking fault energies for Nb, Ta, and Mo were additionally calculated using DFT. Only the FS potential for Cr does not exhibit a local GSFE minimum in the studied strain range.

In summary, the occurrence of {110} planar faults, and with this the crack kinking from {100} to {110} planes in {100}⟨001⟩ crack systems, is linked to the existence of an unexpected local minimum in the γ{110} surface in ⟨110⟩ directions under tensile and biaxial strains. As such a minimum is not predicted by DFT calculations, it is most likely an artifact of many EAM potentials; determining the strain-dependent γ{110} surface is therefore a useful test scenario for the development of new potentials.

Concluding assessment of bcc potentials for fracture simulations

The different Fe potentials are compared in terms of fracture behavior and relative order of fracture toughness values for different crack fronts within the same crack plane and trends of K_{Ic} for different planes in Table 7.2, which has been published in Ref. [122] along with parts of the following paragraphs. In addition, the presence of an artifact-free crack-tip structure and the steadiness of the $\gamma_{\mathrm{usf}}(\varepsilon)$ and $\gamma_{\mathrm{ut}}(\varepsilon)$ is used to further classify the potentials. If a potential is not fully reproducing the experimental behavior it is indicated in the table as 'partial agreement' with an explanatory footnote.

Table 7.2: Comparison of EAM potentials to experimental data for fracture in Fe. The simulation results are compared to the experimentally observed fracture behavior, trends in fracture toughness K_{Ic}, and artifact-free crack-tip structures; the potentials are evaluated in dependence of crack front orientation in a given crack plane as well as among the different planes (●: full agreement, ◐: partial agreement, ○: disagreement). Please note, that the simulation results are not compared with experiments for the {111} crack planes since no experimental studies are reported for these crack systems; the results are further not compared for the (110)[1$\bar{1}$0] crack system since the simulation setup does not allow the experimentally observed behavior (crack kinking onto {100} planes). The highlighted Mendelev-II and Chiesa potentials show the best agreement between simulation results and experimental data.

	(Crack plane)	MFS	Simonelli	Chamati	**Mendelev-II**	Gordon	Marinica07	Marinica11	**Chiesa**
Agreement with	(100)	◐[d]	◐[d]	●	●	◐[d]	◐[e]	◐[e]	●
experimental behavior	(110)	○[f]	○[f]	○[f]	○[f]	○[f]	○[f]	○[f]	○[f]
Agreement with	(100)	●	●	●	●	●	●	○	●
trends in experimental	(110)	●	●	○	●	●	●	○	●
fracture toughness	(110)/(100)	●	◐[g]	○	○	○	◐[g]	○	◐[g]
Artifact-free	(100)	◐[a]	◐[a]	◐[b]	◐[a]	◐[a]	○	○	◐[a]
crack-tip	(110)	●	●	●	●	●	○	○	●
structure	(111)	◐[c]	●	●	●	●	◐[c]	○	●
Steadiness of $\gamma_{usf}(\varepsilon)$		●	○	●	●	●	○	○	●
Steadiness of $\gamma_{ut}(\varepsilon)$		●	●	●	●	●	●	○	●

[a] {110} planar fault formation in the (100)[001] crack system

[b] fcc formation in the (100)[001] crack system

[c] structural transformations in the (111)[11$\bar{2}$] crack system

[d] in the (100)[001] crack system, the crack directly kinks out onto the inclined {1$\bar{1}$0} plane at K_{Ic}

[e] in the (100)[001] crack system, no clear cleavage plane can be determined

[f] experiments show kinking onto {100} planes; simulations predict {1$\bar{1}$0}-cleavage

[g] the (110)[001] and the (100)[011] crack systems show the highest and lowest K_{Ic} values, respectively

It can be seen in the table, that the most recent Marinica11 potential exhibits the highest inconsistencies with the experimental data. This is due to the predominance of large-scale structural transformations ahead of the crack tip, see Figs. 4.1-4.10. These transformations complicate the determination of both a unique K_{Ic} and a distinct fracture behavior. Among all studied potentials, the Mendelev-II and Chiesa potentials for Fe show the overall best agreement with the experimental data. Among the remaining bcc potentials, the ATFS and FS potentials show overall reasonable fracture behavior and do generally not exhibit artifical transformations at the crack tip with exception of the formation of $\{1\,1\,0\}$ planar faults discussed in the previous subsection. Based on the results presented in the Tables 4.2 and 4.4, it is not recommended to use the Ackland, Smirnova, and Wang potentials for fracture simulations. They all show structural transformations at the crack tip, which are most probably linked to the potential parametrization as it was similarly observed for the Marinica potentials. The Fellinger potential for Nb could in principle be used for cracks on $\{1\,1\,0\}$ planes, but shows non-convergent relaxation behavior for cracks (and surfaces in general) on $\{1\,0\,0\}$ planes.

This comparison should, however, not be used by itself when choosing a Fe potential for a specific simulation study. It should rather be used in combination with the Tables 3.1 and 3.2, in order to take into account the properties of all the defects which are relevant for a given scientific question.

In summary, potentials based on the classical FS formulation—also including the Chiesa potential for Fe—are generally usable for fracture simulations; the widely-used Mendelev-II potential for Fe shows also artifact-free crack tip structures and a good agreement with experimental data; for simulations of cracks propagating on the $\{1\,0\,0\}$ plane, only the Chamati potential for Fe and the FS potential for Cr should be used. Many recent potentials, however, are not reliable as they show structural transformations at the crack tip, which are most likely caused by strong fluctuations in the interatomic forces at larger separation distances.

After having tested a total number of 19 EAM potentials for bcc metals, it can therefore be concluded that simpler potentials based on the classical FS potentials, which are not exclusively fitted to only a limited number of certain DFT configurations, are better adapted for atomistic fracture simulations.

7.2 Effects of crack front curvature

To determine the general influence of crack front curvature on the competition between brittle fracture and crack tip plasticity is of fundamental interest for the development of 3D meso-scale models of fracture, which allow for local re-arrangements of the crack front due to e.g. crack pinning at obstacles. For the purpose of laying the foundations for the development of such larger-scale models, the fracture behavior of penny-shaped cracks, which are used as model systems for curved cracks, are compared to theoretical predictions and the behavior of perfectly straight cracks, in subsection 7.2.1. Thereafter, curvature effects on lattice trapping and a possible influence of crack line tension is briefly discussed in subsec-

tion 7.2.2. Finally, fundamental characteristics of crack tip plasticity at curved crack fronts are described in subsection 7.2.3. Parts of the following discussion have been published in Ref. [201].

7.2.1 Fracture behavior

The crack tip response of most penny-shaped cracks was found to be predominantly ductile independent of loading conditions, crack radius, crack plane, crack tip sharpness and interatomic potential. Plastic deformation frequently initiated by the nucleation of dislocations or twins on $\{112\}$ planes. Twins formed by the emission of multiple $a_0/6\langle 111\rangle\{112\}$ twinning dislocations on adjacent twin planes. The favored nucleation sites for dislocations and twins were crack front segments that were locally parallel to $\langle 110\rangle$ directions. In the following, the observed fracture behavior is compared to theoretical predictions and the fracture behavior initiated at straight crack fronts on the same plane.

Comparison with theory

To predict the fracture behavior, the sample-dependent ε_0 should is used as criterion for brittle fracture instead of the theoretical Griffith criterion G_G, see Eq. (2.3), or the corresponding ε_G, which do not account for non-linearity effects as well as boundary conditions. It is remarkable that the discrepancy between ε_0 and ε_G was on average below 10 % for straight crack setups whereas ε_0 exceeds ε_G by approximately 60 % in case of penny-shaped crack setups. From a given ε_0 the corresponding G_0 can be calculated assuming linear elasticity, as given by Eq. (3.5). This means, that brittle fracture is expected if $G_0 < G_e$ (for dislocation emission) and $G_0 < G_t$ (for twin formation). Correspondingly, crack tip plasticity is predicted if $G_0 > G_{e,t}$.

Fig. 7.11a compares the lowest criterion for crack tip plasticity $G_{e,t}$ to the criterion for brittle fracture G_0. According to the G_0-$G_{e,t}$ data, crack tip plasticity is expected for all studied cracks except the $\Sigma 7$ and $\Sigma 49$ GB cracks. Both indeed propagated initially brittle, see Fig. 5.9. The $\Sigma 3$ GB crack, on the other hand, showed initial brittle behavior even though $G_0 = 10.4\ \mathrm{J/m^2}$ was higher than $G_t = 7.1\ \mathrm{J/m^2}$. A possible explanation for this exception might be the extraordinary high GB energy ($\gamma_{GB} = 2.35\ \mathrm{J/m^2}$), which makes it not only thermodynamically less stable, but also kinetically. An indication for this hypothesis is that the crack at the $\Sigma 3$ STGB shows a very low lattice trapping range, cf. Table 5.2. The crack at the $\Sigma 3$ GB, however, remains the only exception.

Unlike at straight crack fronts, the Rice criterion G_e for dislocation nucleation and G_t for twin formation at penny-shaped crack tips has to be evaluated for every combination of the crack plane and all possible slip systems. In other words, the angles φ and θ in Eq. (2.14) have to be calculated for a given crack plane and every crack front direction which is part of the crack plane *and* a possible $\{110\}$ or $\{112\}$ slip plane.

Fig. 7.11b compares the two criteria G_e and G_t to the observed deformation behavior. Among the 13 different combinations of crack planes and interatomic potentials, the observed slip/twin systems are consistent with the lowest calculated G_e or G_t values for penny-

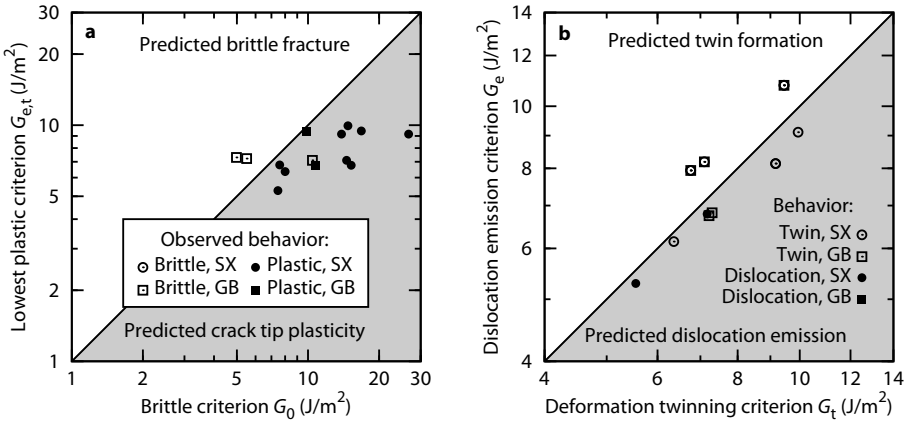

Figure 7.11: Comparison between observed and predicted fracture behavior for penny-shaped cracks in SX and at GBs. **a**: criteria for brittle vs. ductile fracture events in comparison to the observed fracture event (open symbols: brittle; closed symbols: ductile); the Griffith criterion for brittle fracture G_G is compared to the threshold value G_0; **b**: criteria for twin formation vs. dislocation emission in comparison to the observed plastic events (open symbols: twin; closed symbols: dislocation). The fracture behavior is correctly predicted for 13 out of 14 cases using the G_0 criterion; the predicted deformation mode is only correct in eight out of 14 situations.

shaped cracks on the (110), (111), (114), (710) planes as well as at the Σ3, Σ9, and Σ25 GBs. It is interesting to note that this evaluation even correctly predicts the different plastic events at the penny-shaped (111) crack for two different materials: dislocation emission is predicted for the Fe (Mendelev-II potential) whereas twin formation is predicted for W (ATFS potential) on the (111) plane since the twinning tendency $T = \sqrt{\gamma_{usf}(110)/\gamma_{ut}(112)}$ [323], see section 2.3.2, is higher than unity for W and lower for Fe (Mendelev-II). In case of the (010) crack plane, the first activated twin systems have $G_t = 9.2$ J/m^2. This value is higher than for the $a_0/2\langle\bar{1}11\rangle\{110\}$ systems ($G_e = 8.1$ J/m^2). Deformation started, however, by planar fault formation on $\{110\}$ planes, but in $\langle\bar{1}10\rangle$ directions. The corresponding G_e values in these systems would be even smaller since the energy barrier is drastically decreased, see Fig. 7.9. Taking this into account, the theoretical prediction is also correct for the (010) crack in case of the Mendelev-II potential. For the Chamati potential, on the other hand, $a_0/2\langle\bar{1}11\rangle\{110\}$ dislocation emission would be expected ($G_e = 9.1$ J/m^2) rather than the observed twin formation on $\{112\}$ twin planes ($G_t = 9.9$ J/m^2). It can be seen from the tension-shear coupling curves in Fig. 7.1 that twinning becomes favored over $\{110\}$ dislocations for the Chamati potential only at applied strains higher than 7 %. This effect alone can therefore not explain the observation of twin formation in this case. It should, however, not be forgotten that both γ_{usf} and γ_{ut} are only estimates of the actual nucleation barrier as originally proposed by Rice [16]. It cannot be excluded that the barrier to *nucleate* twins is significantly lower than for dislocations. Furthermore, twin formation was observed to occur favorably under dynamic conditions, see Fig. 4.3. In these quasi-2D simulations,

however, $\{112\}$ dislocations are emitted instead of twins in case of the Chamati potential. This indicates that the nucleation barrier for twins might be even smaller under fully-3D conditions where the $\langle 111\rangle$-oriented incoherent twin boundaries play an additional role.

For the remaining penny-shaped cracks, which were all modeled with the Chiesa potential, the Rice criterion always predicts the activation of $a_0/2\langle 111\rangle\{1\bar{1}0\}$ slip systems rather than the observed twin formation on $\{112\}$ planes. On the (112) plane, G_e = 6.2 J/m^2 for $\{10\bar{1}\}$ dislocation emission at $\langle 1\bar{3}1\rangle$ crack fronts and G_t = 6.4 J/m^2 for twin formation at $\langle 1\bar{1}0\rangle$ crack fronts. At the $\Sigma 7$ GB, G_e equals 6.8 J/m^2 for $\{110\}$ dislocation emission at $\langle\bar{5}5\overline{12}\rangle$ crack fronts and G_e = 6.7 J/m^2 at $\langle\bar{2}2\bar{5}\rangle$ crack fronts at the $\Sigma 49$ GB. The observed twin formation at $\langle\bar{4}21\overline{13}\rangle$ and $\langle\bar{3}17\,\overline{11}\rangle$ crack fronts has energy barriers of G_t = 7.3 and 7.2 J/m^2, respectively. On average, the observed G_t values are 6 % higher than the predicted values for dislocation emission. Taking into account the effect of tension-shear coupling, the decrease of the corresponding unstable twinning energy is much stronger as for the unstable stacking fault energy on the (110) plane, see Fig. 7.1. At an applied strain of ε = 5 %, γ_{ut} is reduced by 27 % whereas $\gamma_{usf}(110)$ is still at 90 % of its initial value. This indicates that the preference of twin formation in these cases can be explained by the stronger effect of tension-shear coupling on γ_{ut} than on $\gamma_{usf}(110)$.

In summary, the fracture behavior of penny-shaped cracks is correctly predicted for 13 out of 14 crack configurations by comparing the theoretical criteria for brittle fracture and the lowest criterion for crack tip plasticity. The preferred twin formation at most penny-shaped crack fronts is not predicted theoretically, but can be understood by taking into account the effect of tension-shear coupling, which shows a stronger decrease of the unstable twinning energy than for the unstable stacking fault energy.

Comparison with straight cracks

The fracture behavior and critical strains of penny-shaped and straight cracks in single crystals are compared in Table 7.3. All penny-shaped cracks showed an overall ductile response whereas most straight cracks propagated in a brittle manner. This higher preference of ductile crack-tip deformation was first reported by Ersland *et al.* [164] who compared penny-shaped cracks on the (010), (110), and (111) planes to straight central cracks in Fe [226]. The authors found that the combinations of crack plane and crack front orientations which show certain plastic events, i.e., twinning, dislocation emission, or planar faults, in quasi-2D simulations correspond to the local crack front orientations of the penny-shaped cracks where the same processes are observed.

In agreement with the observation of Ersland *et al.*, penny-shaped cracks on the (010) (using the Mendelev-II potential), (110), (111), (112), and (114) planes exhibited the same elementary deformation processes that were found at straight crack fronts, see Table 7.3. In case of the straight (010) cracks, however, plasticity was only observed after the crack has already propagated for a certain distance, cf. Fig. 4.2d,f. When using the Chamati potential, a deformation twin initially formed at the penny-shaped crack front on the (010) plane. The $\langle 110\rangle$-oriented straight crack front, see Fig. 4.2h, emits a dislocation.

Table 7.3: Comparison of the fracture behavior of penny-shaped and straight cracks. If not mentioned otherwise, the following simulation parameters were used: penny-shaped crack with $a = 100$ Å; quasi-2D edge crack with $a = 1000$ Å; dynamic loading with $\dot{\varepsilon} = 10^8$ s^{-1}; '—' means that no fracture event was *initiated* at the corresponding crack front.

Plane	Potential	Crack tip	Front	Penny-shaped crack	Straight cracks
(010)	Fe (Mendelev-II)	sharp	<001>	PF formation	Brittle after PF formation
			<101>	Twin formation	Brittle, then twin formation
(010)	Fe (Mendelev-II)	blunted	<001>	PF formation	Brittle after PF formation
			<101>	Twin formation	Brittle, then twin formation
(010)	Fe (Chamati)	blunted	<001>	—	Brittle
			<101>	Twin formation	Dislocation emission
(110)	Fe (Chiesa)	sharp	<001>	—	Brittle, then arrest
			<110>	Dislocation emission	Brittle, then arrest
			<111>	—	Brittle
			<112>	—	Brittle
(111)	Fe (Mendelev-II)	sharp	<110>	—	Twin formation
			<112>	Dislocation emission	Dislocation emission
(111)	W (ATFS)	blunted	<110>	Twin formation	Twin formation
			<112>	—	Twin formation
(112)	Fe (Chiesa)	sharp	<110>	Twin formation[a]	Twin formation
			<111>	—	Brittle
(114)	W (ATFS)	blunted	<110>	Twin formation	Twin formation[b]
(710)	W (ATFS)	blunted	<179>	Twin formation	—
			<001>	—	Brittle[b]

[a] radius of penny-shaped crack: $a = 60$ Å

[b] *K*-controlled setup

The agreement with the overall ductile response reported by Ersland *et al.* shows that the fracture behavior of penny-shaped cracks does not depend on the artifical stabilization of the crack by the 'screening' method, which was used by Ersland *et al.* Furthermore, the artificial blunting of some penny-shaped cracks, where one circular atomic layer was removed, does neither alter the fracture behavior nor the critical fracture strains, see Table 7.3.

The lack of brittle fracture of penny-shaped cracks is therefore most probably caused by the multitude of different crack front orientations, which are possible for curved cracks. This makes it possible to activate slip systems, which are not possible or very unfavorable at infinitely straight crack fronts. On the $(7\,1\,0)$ plane, for instance, the deformation twins initiate at $\langle 1\,7\,9\rangle$-oriented crack fronts. This unconventional crack front direction has not been investigated by means of quasi-2D simulations. In other words, one would need to study a multitude of different crack systems to cover all possible crack front directions that

are present at a circular crack front. Furthermore, dislocation half loops can be emitted from the crack tip only under fully 3D conditions, see Fig. 4.6d. The emission of such half loops should be energetically favored over the emission of straight quasi-2D dislocation lines [62]. In addition, plastic deformation can effectively unload the penny-shaped crack thereby preventing brittle cleavage. This requires, however, that the crack tip plasticity does not remain confined to its origin. It is therefore important to note that the cross slip of dislocations along the curved crack front, whereby the formerly sharp crack tip is blunted, is one of the characteristic features observed at penny-shaped cracks, see section 7.2.3. Since this process happens repeatedly, the crack tip becomes more and more blunted, which should generally lead to a decrease of the stress concentration at the crack tip.

Furthermore, the stress distributions around short and long cracks can be significantly different, as discussed in section 7.1.4. The tendency to emit a dislocation in the $(110)[1\bar{1}0]$ crack system increased with decreasing crack length due to higher resolved shear stresses on the inclined $(11\bar{2})$ plane as compared to a long crack. In this context, it is important to recall that the globally applied strains are much higher for small cracks than for large cracks, cf. e.g. Fig. 4.3. As shown in Fig. 7.1, high tensile strains reduce the unstable stacking fault and unstable twinning energies and it is therefore not surprising that small penny-shaped cracks behave on average more ductile than cracks with long, straight crack fronts. An indication for this trend can be found if cracks on the (110) plane with different radii are compared. For the crack radius a = 60 and 100 Å, the crack was stable until the initiation of crack tip plasticity. The crack with a = 200 Å, on the other hand, initially propagated by limited bond breaking processes prior to dislocation emission.

In summary, the higher preference of crack tip plasticity at penny-shaped crack fronts is explained with the higher number of available slip systems in comparison to infinitely long straight cracks. This tendency will be generally smaller for larger crack radii with longer and more straight crack front segments.

7.2.2 Fracture toughness and lattice/bond trapping

The influence of crack front curvature on the fracture toughness and on the lattice trapping effect is presented here for cracks on the (110) plane and at the $\Sigma3(111)_1/(11\bar{1})_2$ 70.5°/$[1\bar{1}0]$ STGB. For comparison with the results for straight central cracks, the critical strains for three different radii are converted to the corresponding stress intensity factors K^*_{Ic} using the linear-elastic fracture mechanics solution in Eq. (2.6) see Table 7.4. Note that K^*_{Ic} is used here to distinguish it from the 'true' fracture toughness K_{Ic} as determined in the K-controlled setup. It can be seen that K^*_{Ic} of central cracks strongly varies in the studied range of crack lengths, which indicates the influence of higher-order terms in the crack length range around $a_{\mathrm{t}} \approx L_{\mathrm{y}}/(2\pi) \approx 160$ Å, see Eq. (7.8) in section 7.1.4 for details; for penny-shaped cracks, on the other hand, the relative critical stress intensity factor was around $(1.07\pm0.02)K_{\mathrm{G}}$ for the single crystal *and* the $\Sigma3$ GB. This indicates that the the effect of higher-order terms is either less important for the stress distribution around penny-shaped cracks or that for them the transition to the crack length independent regime occurs

Table 7.4: Comparison of critical conditions for cracks with equal crack lengths/radii a and box sizes. Conversion of critical strains ε_c to the critical stress intensity factor K^*_{Ic} with Eq. (2.6), where $Y = 2/\sqrt{\pi}$ and $Y = \sqrt{\pi}$ for the penny-shaped and central cracks, respectively. (110) cracks: $L_x \approx L_y \approx 1000$ Å; $E = 229$ GPa; $K_G = 0.95$; $K_{Ic} = 1.21$ and $\Delta K = 0.67$ (in K-controlled setup); Σ3 STGB cracks: $L_x \approx L_y \approx 900$ Å; $E = 345$ GPa; $K_G = 1.38$; $K_{Ic} = 1.47$ and $\Delta K = 0.13$ (in K-controlled setup); for penny-shaped cracks: $L_z \approx L_x$; all values for K in units of MPa$\sqrt{\text{m}}$.

a (Å)	ε_c (%)	$\Delta\varepsilon$	K^*_{Ic}	ε_c (%)	$\Delta\varepsilon$	K^*_{Ic}
	Penny-shaped (110) cracks			*Quasi-2D central (110)[1$\bar{1}$0] cracks*		
60[a]	5.09	—	1.02	—	—	—
60	5.10	0.24	1.02	3.67	0.63	1.15
100	3.85	0.22	0.99	3.01	0.64	1.22
200	2.84	0.26	1.04	2.52	0.65	1.44
	Penny-shaped Σ3 GB cracks			*Quasi-2D central Σ3 GB cracks, x = [11$\bar{2}$]$_1$*		
100	3.81	0.17	1.48	2.38	0.06	1.48
150	3.10	0.19	1.48	2.14	0.11	1.63
200	2.64	0.24	1.46	2.06	0.11	1.81

[a] $L_x \approx L_y \approx L_z \approx 600$ Å

at larger crack radii. The second assumption is additionally strengthened if the transition crack length a_t, see Eq. (7.8), is calculated for penny-shaped cracks, i.e. using the geometry factor $Y = 2/\sqrt{\pi}$ in Eq. (2.6): $a_t \approx L_y\pi/8 \approx 390$ Å for a box length of $L_y \approx 1000$ Å.

The determined critical strains for the penny-shaped cracks are are plotted in comparison to the values for the Σ9 GB in Fig. 7.12a; the calculated K^*_{Ic} values are plotted in subfigure b. The lattice trapping ranges were $\Delta\varepsilon = 0.24\pm0.02$ for the (110) crack and around $\Delta\varepsilon = 0.20\pm0.04$ for the Σ3 crack. The corresponding ranges for central cracks are significantly higher for the (110) crack (around 0.64) and lower for the GB crack (between 0.06 and 0.11), which are both in the same range as for the K-controlled setup (0.67 and 0.13).

In case of a brittle propagating penny-shaped crack, i.e., the Σ3 GB crack, K^*_{Ic} is nearly constant and agrees well with K_{Ic} as determined in the K-controlled setup, see Fig. 7.12a. At the same time, the bond trapping range $\Delta\varepsilon$ increases with increasing crack radius. This contradicts to work on cracks in Si and fcc Cu [58, 65, 425], which predict a lower contribution of lattice trapping to the fracture toughness in the presence of crack front kinks. In such scenarios, the propagation of kinks leads to the extension of the crack. The simulation results, however, indicate that the critical step for brittle propagation is not the *propagation* of crack front kinks: at curved crack fronts, kinks are inherently present, but did not lead to an earlier extension of the crack as compared to a perfectly straight crack front. Instead, the *formation* of kinks might be the controlling factor for both straight and curved crack fronts. Alternatively, a smaller contribution of bond trapping to the fracture toughness of a curved crack could be offset by the effect of crack line tension [73, 75]. In this case, the value of $\Delta\varepsilon$, which is a measure for the stability of the crack at its original position, would

mainly include the effect of crack line tension instead of bond trapping. While the bond trapping effect might be reduced, crack line tension might increase the necessary fracture energy to propagate a curved crack, see Eq. (2.17). The observation that $\Delta\varepsilon$ is nearly equal for the penny-shaped cracks in the single crystal and at the GB could be an indication for this hypothesis: whereas bond trapping strongly varies with material, interatomic potential, and crystal orientation, crack line tension might rather depend on other factors, which are currently not known and need to be further investigated in the future. It is therefore not possible to make a final conclusion on the contribution of crack line tension at the current stage as it cannot not be ruled out that the agreement between the different penny-shaped cracks is a coincidence. Additionally, the crack in the single crystal did not initiate brittle fracture, but crack tip plasticity. The determined value for $\Delta\varepsilon$ does therefore only represent a lower limit for the 'real' contribution of bond trapping. For these reasons, future studies on this topic should be performed for additional materials, crack planes, and also for triaxial ellipsoidal cracks, where all three ellipsoidal semi-axes are distinct and the degree of curvature is varied in comparison to penny-shaped, i.e., bi-axial ellipsoidal, cracks.

At the penny-shaped crack front in the single crystal, crack tip plasticity initiated while brittle fracture is predicted in the K-controlled setup. At the same time, the critical stress intensity factor K_{Ic}^{*} is lower for penny-shaped cracks. Similar behavior can be found for the $\Sigma 9$ GB, see Fig. 7.12b. The decrease of K_{Ic}^{*} with decreasing crack radii can be attributed to the effects of T-stress and tension-shear coupling for small crack lengths as discussed in section 7.1.4; the T-stress increases the resolved shear stress whereas tension-shear coupling decreases the energy barrier for dislocation nucleation and twin formation. In addition, imperfections along curved crack fronts and the lower energy barrier for dislocation nucleation in 3D [62] might further decrease K_{Ic}^{*}. Indications for the decrease of the energy barrier for dislocation nucleation in presence of crack tip ledges can be found in the literature [67, 163]. To the author's knowledge, the role of crack front kinks for dislocation nucleation has not yet been studied and might therefore be an important topic of future studies.

It is finally important to note that the effects of both T-stress and tension-shear coupling are *not* exclusively caused by the small box size in the atomistic configurations and the correspondingly large applied strains. Although both effects are increasingly important under such conditions, they will also be present at crack tips under experimental conditions, particularly for very small crack lengths and specimen dimensions [31] as e.g. in micro electro-mechanical systems (MEMS), and when the stress at the crack tip is close to the theoretical strength.

In summary, the fracture toughness of penny-shaped cracks with different crack radii was determined here for the first time by means of atomistic simulations. The results suggest that (i) the fracture toughness for brittle crack propagation is insensitive to crack front curvature; and that (ii) the critical stress intensity factor for crack tip plasticity at curved cracks is generally reduced as an effect of T-stress and tension-shear coupling.

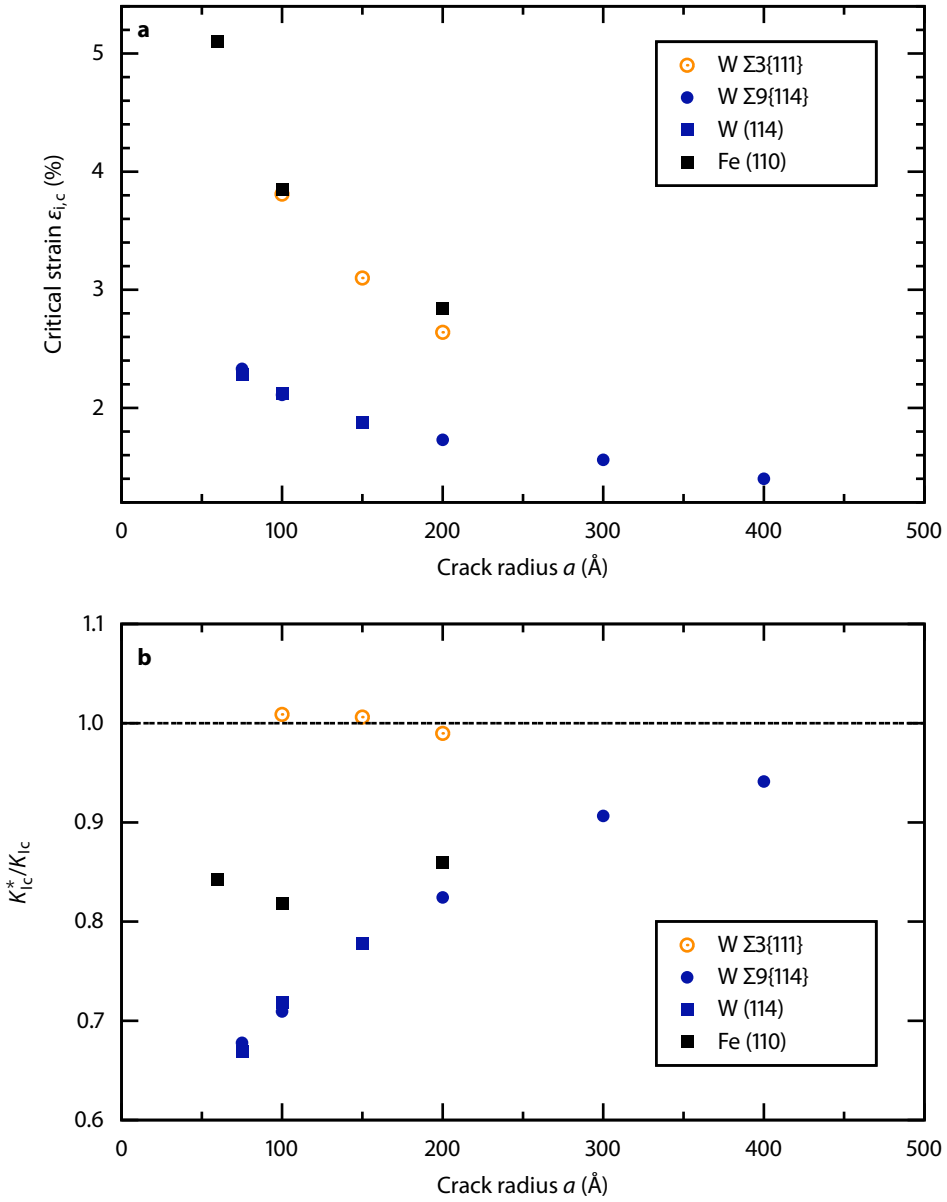

Figure 7.12: Crack length dependence of the critical conditions for different penny-shaped cracks. **a**: determined critical strain $\varepsilon_{i,c}$; **b**: calculated critical stress intensity factors K^*_{Ic}, see Eq. (2.6); K^*_{Ic} is divided by K_{Ic} as determined in the K-controlled setup for comparison; open symbols: brittle fracture; filled symbols: crack tip plasticity.

7.2.3 Crack tip plasticity

Eight out of eleven studied crack systems showed initial plastic deformation at curved crack fronts, which was frequently initiated by the formation of mechanical twins rather than by emission of perfect dislocations. For cracks in single crystals the prevalence of crack tip plasticity was even more pronounced as it occurred in all six studied orientations. Selected simulation results and parts of the following discussion for penny-shaped cracks in single crystals have been published in Ref. [201].

Initial twin formation was frequently observed and took place by successive emission of $a_0/6\langle 111\rangle\{112\}$ twinning dislocations on adjacent twin planes. During the extension of the twins, the screw components of the twinning dislocations remained connected to the crack front. Screw segments of the twinning partial dislocations then cross slipped onto a common plane leading to the formation of perfect screw dislocations. This process is analyzed in more detail in section 7.5.2. The emission of screw dislocations from deformation twins was often accompanied by the shrinkage of the twin in $\langle 110\rangle$ directions. The released $a_0/2\langle 111\rangle$-type screw dislocations were then able to cross slip along the curved crack front and to interact with other dislocations and/or twins. This process is observed for cracks on the (110), (111), and (710) plane, see Fig. 7.13. In case of GB cracks, most nucleated dislocations were observed to slip along or to penetrate through the GB, see section 7.3.3 for further details. In single crystals, however, multiple successive cross slip events on $\{110\}$ and $\{112\}$ planes allow the screw dislocations to account for the crack front curvature. This process is a very efficient way to blunt the crack tip, see e.g., the formation of prismatic dislocation loops with Burgers vector parallel to the crack plane normal in Figs. 4.11 and 5.4a.

Additionally, the emitted screw dislocations can intersect the crack surface. This is however only the case when the dislocation loop bows around the crack plane comparable to a Frank-Read source. The two arms can then annihilate with each other, leaving behind a perfect dislocation glide loop around the crack on an inclined plane. This process is observed for the (010) crack modeled with the Chamati potential, see Fig. 4.3c, and for the (114) crack, see Fig. 5.5a.

Unlike straight cracks, penny-shaped cracks allow for the interaction of dislocations and/or twins, which were nucleated at differently oriented crack front segments and on different glide systems, leading to the formation of dislocation junctions. This was in particular observed for cracks on the (110) and (710) planes. In both cases, two twins intersect along a common $\langle 120\rangle$ direction, see Figs. 4.5e and 5.7a, which does not involve dislocation reactions. The twins can just grow through each other, as marked with 5 in Fig. 5.7a.

A common feature of this junction type is that it forms where the crack front is oriented parallel to a $\langle 100\rangle$ direction. These crack front directions are not part of any active slip or twin plane but lie exactly between two slip systems with different Burgers vectors, which are activated at the same time. Whether one or multiple slip systems are simultaneously activated strongly correlates with the inclination angle between possible slip directions and the crack plane, i.e., the resolved shear stress on the particular slip system. For purely

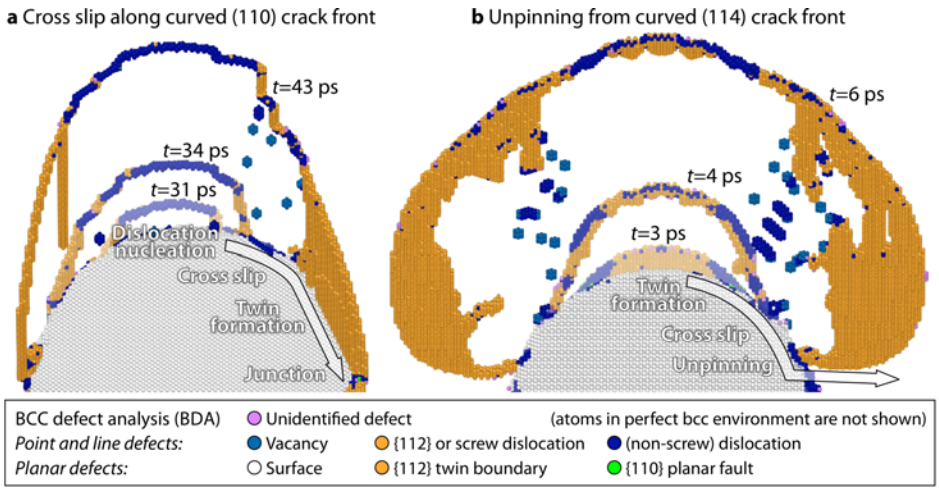

Figure 7.13: Pronounced cross slip vs. unpinning events at penny-shaped cracks. **a**: dislocation nucleation, subsequent cross slip and junction formation at the penny-shaped (110) crack in Fe; **b**: twin formation, subsequent cross slip and unpinning of the dislocation/twin from the penny-shaped (114) crack in W. Three different snapshots overlap in each subfigure to visualize the dynamics.

geometric reasons, curved cracks on planes that contain a $\langle 1\,0\,0 \rangle$ crack front must have equal resolved shear stress on at least two slip systems. Such cracks thus tend to show junction formation in the vicinity of the crack front.

The pronounced crack tip plasticity is a direct consequence of the increasing probability to find favorably oriented crack front segments for dislocation emission or twinning with increasing crack front curvature. With the exception of slip planes lying parallel to the crack plane, all slip planes of the crystal share a common direction with at least one segment of a penny-shaped crack front. In other words, oblique slip planes at one part of the crack become inclined, i.e., more favorably oriented for dislocation emission, at another part.

Due to the small size and the curvature of the crack, even those parts of the crack which are oriented favorably for cleavage show a reduced tendency to fracture in a brittle manner. Dislocations that are nucleated at one part of the crack efficiently shield and even blunt the crack front at other parts of the penny-shaped crack.

Besides the emission of dislocations or twins, none of the characteristic features of crack tip plasticity is possible or even predictable by resorting to quasi-2D setup geometries of infinitely long and straight crack fronts. This highlights the importance of fully 3D studies to investigate the fracture and deformation behavior at highly curved very small cracks.

In summary, the observed mechanisms of crack tip plasticity are all caused by the specific geometry and crystallography of curved cracks in bcc crystals; it can therefore be assumed that crack tip plasticity should be dominant at small highly curved cracks in bcc metals and that the tendency to fracture by cleavage is lower than for cracks with long, straight crack fronts.

7.3 Characteristics of grain boundary fracture

The fracture behaviors and trends in relative critical strains of the Σ3 and Σ9 STGBs were identical to the results obtained in the *K*-controlled setup, cf. Tables 5.2 and 5.3. For the Σ25 STGB, see Table 5.4, on the contrary, the *K*-controlled setups predicts completely brittle fracture whereas in the strain-controlled setup emission of an extended dislocation-like deformation pattern is observed from crack tip position 2, see Fig. 5.6d and e. This observation was also confirmed in quasi-static simulations and is therefore probably an effect of the higher 'background stress' in the strain-controlled setup. In this situation, remote tensile loads are applied to the configuration, which results in the stress distribution schematically shown in Fig. 2.2a. Unlike the *K*-controlled setup, the stresses behind the crack tip do not tend to zero but to a fixed value $\sigma = E_y \varepsilon$. This effect in combination with the extremely high bond trapping at crack tip position 2 might have increased the resolved shear stresses around the crack tip in such a way that dislocation emission became possible.

The usual thermodynamic description of brittle GB fracture assumes that the fracture energy of GBs equals the energy of the created surfaces *minus* the energy of the GB [241], cf. Eq. (2.22). This implies that the fracture toughness of symmetric GBs is lower than the fracture toughness of perfect single crystals in the same orientation. Furthermore, the fracture toughness does not depend on the crack tip position within the GB or on the crack propagation direction from the viewpoint of thermodynamics. The presented simulation results clearly show that these assumptions can no longer be used at the atomic length scale: by comparing the fracture toughness of single crystals and GBs in Fig. 5.2a it is clear that a number of symmetric GBs have a significantly higher fracture toughness than the cracks on the same crack plane in a single crystal [94].

These atomistic aspects can be explained by extending the well-known lattice trapping concept [10] to bond trapping of GB cracks, see section 7.3.1. The occurrence of direction-dependent fracture behavior and slip transmission, especially in case of curved cracks, is discussed in sections 7.3.2 and 7.3.3; section 7.3.4 is focused on the effect of absorbed dislocations on the fracture resistance.

7.3.1 Bond trapping

Similar to the lattice trapping effect, the deviation of the fracture toughness from the thermodynamic prediction $K_{G,GB}$ can be understood by the discrete nature of the atomic bonds at GBs. Bond trapping of GB cracks, however, does not only explain the deviation from the thermodynamic prediction, but also the higher fracture toughness of GBs as compared to SX as well as its direction and position dependence. The results for *K*-controlled GB cracks and parts of the corresponding discussions have been published in Ref. [94].

Higher fracture toughness of GBs than in single crystals

The increased fracture resistance of the Σ3T and the Σ25 GBs is correlated with an increased bond trapping range compared to the lattice trapping range in the single crystal.

This is exemplarily shown for the Σ3T grain boundary in Fig. 7.14 by comparing the dependency of the distances of the crack tip atoms on the applied stress intensity factor for the GB crack and the corresponding single crystal.

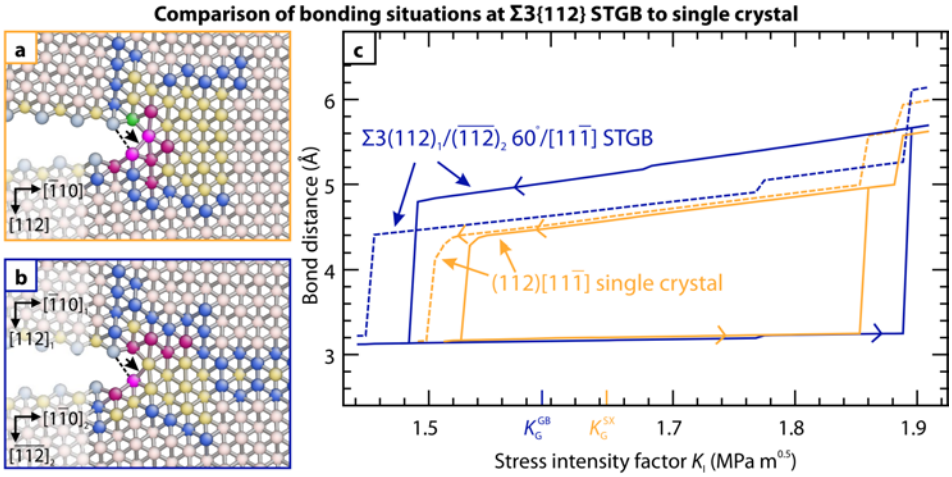

Figure 7.14: Exemplary comparison of the bonding situations at GBs and equally oriented single crystals. **a**: (112)[11$\bar{1}$] single crystal, K_I = 1.66 MPa$\sqrt{m}$; **b**: $\Sigma3(112)_1/(\bar{1}\bar{1}\bar{2})_2$ 60°/[11$\bar{1}$] STGB, K_I = 1.66 MPa$\sqrt{m}$; atomic colors: coordination number (grey: 8, pink: 9, green: 9, red: 11, yellow: 12, blue 13, white: 14); the critical crack-tip bonds are indicated with an arrow. **c**: length of the critical bonds as function of the applied stress intensity factor for loading (→) and unloading (←); dashed lines indicate the bond lengths of the first created bonds due to crack closure upon unloading, see the atoms connected by dashed lines in **a** and **b**.

Several factors can contribute to the increased toughness, e.g., shorter bond lengths in the GB (which are correlated with local compressive regions), increased number of neighbors in the GB (i.e. more bonds need to be broken) or different load sharing of the atoms at the crack tip in the GB compared to the single crystal crack. It is important to note, that in case of K-controlled cracks at the Σ3T and Σ25 GBs, fracture took place in a perfectly brittle manner, and the differences in fracture toughness was not caused by plasticity. As shown in Fig. 5.2a, these GBs can also be tougher than perfect single crystals oriented for fracture on the primary cleavage plane, cf. Table 4.2. A large number of such tough GBs could therefore favor transgranular over intergranular fracture. In this context it is important to note that the increased fracture toughness, i.e., a significantly higher K_{Ic} than the corresponding $K_{G,GB}$, cf. Eq. (2.23), is not correlated with the GB energy. E.g., the Σ25 GB has a significantly higher fracture toughness than the lower energy Σ3 and Σ9 GBs, cf. Tables 5.2 and 5.3.

Direction and position dependence of fracture resistance

Forward-backward asymmetry of the fracture resistance, i.e., different K_{Ic} values in opposite $\pm[h\,k\,l]$ directions, was observed for the cracks at the Σ7, Σ25, and Σ49 GBs. Position-dependent K_{Ic} values were seen in particular for those GBs that have comparably large structural units, i.e., the Σ7 and Σ25 GBs. For both GBs, the quasi-statically determined fracture resistances in the K- and strain-controlled setups are summarized in Fig. 7.15a and b as functions of the crack tip position and the crack extension direction. In the strain-controlled setup, however, only the Σ7 GB crack propagated in a completely brittle manner, see Fig. 5.8. The Σ25 GB crack, on the contrary, ultimately initiated dislocation-like deformation patterns, see Fig. 5.6. Since such structures were not observed in the fully 3D simulations of a penny-shaped crack at this GB, they are most likely artifacts caused by the short crack front length (PBC in crack front direction) and the higher 'background stress' in the strain-controlled quasi-2D setup in combination with the extremely high bond trapping at pos. 2, see Fig. 7.15a. For this reason, the further discussion is focused on the Σ7 GB crack.

Fig. 7.15b shows the necessary increase in energy release rate, ΔG, to propagate the crack by a certain distance Δx through the Σ7 GB. The data for the plot is obtained by quasi-statically straining configurations with the crack tips originally placed at position 2 in both propagation directions, cf. Table 5.5. At this position the stability ranges differ by almost a factor of two for the opposite propagation directions. In $-[\bar{1}\,1\,0]$ direction, the crack stops at several further positions after the bond at position 2 is broken. In the opposite $+[\bar{1}\,1\,0]$ direction, the crack only stops at two other positions, at which the absolute critical strain is significantly higher than in the $-[\bar{1}\,1\,0]$ direction.

Extension of the lattice trapping concept

Based on the possibility of higher bond trapping ranges as well as direction and position dependence, the lattice trapping concept [11], see Fig. 2.2f, is extended to include GBs. Fig. 7.15c shows a schematic comparison of the increase in surface energy by crack advance in a perfect crystal lattice [10], at a GB, and the corresponding linear continuum limits, see Eqs. (2.3) and (2.22). This concept was derived for K-controlled GB cracks and has been published in Ref. [94] along with parts of the following discussion. Unlike in common continuum descriptions [9, 241], the resistance of the crystal against crack propagation is not a constant value, but is high at single atomic bonds and zero inbetween. Locally varying bond strengths across the GB plane can immensely increase and decrease the trapping magnitudes, which results in a position dependence of the fracture toughness K_{Ic}. For this reason, the fracture toughness of a symmetric GB can locally exceed that of a single crystal for the equivalent crack plane. Furthermore, structural GB units are generally asymmetric with respect to the crack propagation direction, which leads to a forward-backward dependence of K_{Ic}.

Although GBs show regions with low fracture toughness, it is the region with the highest K_{Ic} which ultimately determines the crack initiation toughness of a GB. This is clearly shown in Fig. 5.8: under quasi-static loading, the crack tips initially located at weak spots

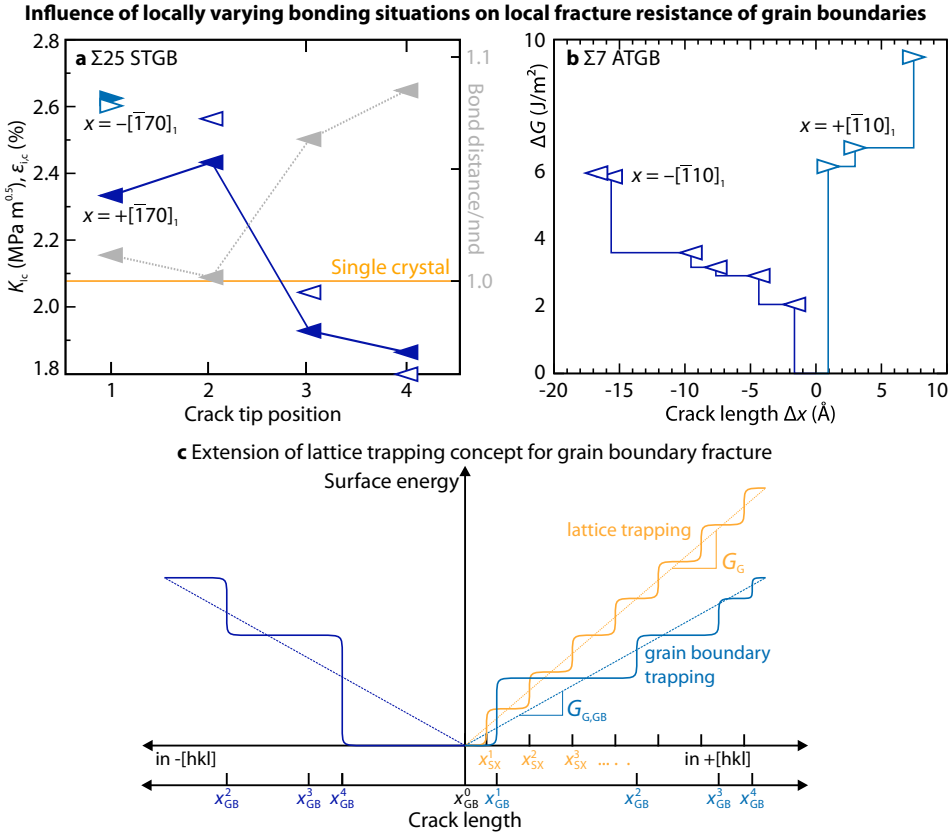

Figure 7.15: Position and direction dependence of the resistance against GB fracture. **a**: K_{Ic} (filled symbols) and critical strains (open symbols) for cracks in the Σ25 STGB; grey symbols: the equilibrium bond distances of the corresponding crack tip bonds; **b**: necessary increase in energy release rate ΔG to propagate the crack by a certain distance Δx through the Σ7 ATGB; triangles pointing in different directions indicate opposite propagation directions within the GB; note that the crack is only stable at the indicated crack tip positions for both GBs. **c**: extended lattice trapping concept for GB fracture; the increase in surface energy by the advance of a crack is compared for a crack in a perfect crystal lattice (orange, according to Ref. [10]), GBs (blue and petrol) and the corresponding linear continuum limits after Refs. [9, 241]; see text for explanation.

of the GB just propagated by breaking one bond and arrested at the next, stronger unit. Only if the crack tip was positioned at the strongest bond, the crack propagated through all GB units. This was observed under both quasi-static and dynamic loading conditions, cf. Table 5.5.

The thermodynamic relation between critical energy release rate and the energy of the surfaces and GBs should of course still hold, however only when averaged over a certain number of broken bonds. I.e., the average slope of the surface energy vs. crack length graph

for the GB, Fig. 7.15c, has to correspond to Eq. (2.22), and consequently has to be lower than for the single crystal. Locally, the required energy release rate for crack advance can however be larger in the GB than for a crack in a single crystal.

Experimental validation of this effect will be challenging as controlled experiments on GB cracks are very difficult to perform [279]. The presence of GB defects like steps or absorbed dislocations, segregated atoms, and the often non-planar nature of GBs and curved crack fronts, as well as the presence of dislocations in the grains, make a direct comparison between the simulation results and experiments nearly impossible. Recent developments in nanomechanical testing however now allow the determination of the fracture toughness of interfaces from in-situ bending tests of notched cantilever beams [426]. Such tests could be performed with well-characterized GBs in polycrystalline materials, avoiding the difficulties in preparing bicrystal specimens. In the simulations, the difference of the GB fracture toughness for different crack propagation directions is rather small, see Fig. 5.2, and will therefore most probably not be detectable in experiments. However, according to our simulations, the determined fracture toughness for brittle fracture can deviate from the thermodynamic prediction according to Eq. (2.23) by up to 90%, e.g., for the Σ25 GB. Comparing the experimentally determined GB fracture toughness in an inherently brittle material with the corresponding theoretical prediction or with a numerical calculation using a CZ model, see section 2.4, could thus allow to reveal the influence of bond trapping on GB fracture toughness. In fact, bond trapping might be one of the underlying reasons for the reported extraordinary high tensile strengths of some GBs [274, 276, 279, 280, 282], in particular when they are not directly correlated with the GB energy [280, 281] or otherwise not directly predictable [279].

Most of the commonly used CZ models, which are parameterized by atomistic simulations, derive their information, e.g., the tensile GB strength or the work of separation, from MD [286, 340, 344, 345] or DFT calculations [21]. Approaches, which do not directly model the crack tip and instead use stess-strain data from tensile test of GBs [21, 340] are, however, averaging over the atomic structure of GBs. As a consequence, continuum simulations with CZ parameters derived in this way fail to reproduce the atomistic simulation results [341]. Simple CZ models are furthermore not able to properly describe the direction dependence of the fracture toughness of GBs. Here, theories like quantized fracture mechanics [427], which take into account lattice trapping, could be extended to include bond trapping of GB cracks. Ultimately, however, parameterized GB CZ models would need to be validated using fracture experiments on defined GBs. To the author's knowledge, such direct comparisons are currently still lacking.

Although the used ATFS potential for W might not exactly model the energies and forces of atoms in real GBs, the observed behavior should be generally valid: the bonding situation in GBs can vary largely from the bonding in single crystals, including the possibility of local GB bonds which are stronger than regular bonds in the single crystals. The observations that for brittle fracture on the same plane GBs can be tougher than single crystals and that the GB fracture toughness depends on the crack tip position and crack front direction should therefore be independent of the details of the atomic interaction model. The deviations from the thermodynamic description of GB fracture in a continuum framework

are caused by the atomic nature of GBs, and should therefore be generalizable and relevant for GB fracture in brittle and semi-brittle materials. In this context it is also interesting to note that atomistic simulations of graphene showed an increased yield strength of sheets containing GBs compared to defect-free graphene [428].

A deeper understanding of GB fracture on the atomic level and improved meso-scale models would be particularly useful for the study of microstructurally short cracks or fracture of nanosized structures, such as micro electro-mechanical systems (MEMS), where the influence of individual GBs on the fracture behavior is particularly important. Taking bond trapping effects into account could also be helpful in the context of grain boundary engineering of fracture-resistant materials and for predicting trans- vs. intergranular fracture.

Three-dimensional aspects

Similar to most studies on lattice trapping [29, 97], most of the presented results are limited to quasi-static calculations in a quasi-2D setup [94]. Temperature effects and the presence of kinks on the crack front are therefore often neglected. In the past, such quasi-2D simulations on lattice trapping were, however, able to explain the macroscopically observed fracture behavior, e.g., the occurrence of primary $\{1\,0\,0\}$ cleavage planes in W [14], or the anisotropy with respect to the propagation direction along different crystallographic directions within the same fracture plane in Si [97]. Similarly, bond trapping of GB cracks could have macroscopic implications e.g. on the selection of the transgranular mode of fracture over intergranular fracture as speculated in Refs. [12, 429].

To determine the influence of three-dimensional aspects, such as the crack front curvature, on bond trapping of GB cracks, the fracture toughness K^*_{Ic} is calculated for three crack radii $a = 100, 150$, and 200 Å at the $\Sigma 3$ GB, see Table 7.4. Here, K^*_{Ic} denotes the fracture toughness as calculated from the critical strains ε_{i} or ε_{c} from Eq. (2.6) to distinguish it from the 'true' fracture toughness K_{Ic} as determined in the K-controlled setup. The increased lattice trapping range $\Delta\varepsilon$ for the penny-shaped GB cracks in comparison to straight GB cracks is most probably rooted in (i) crack line tension, see the discussion in section 7.2.2; or (ii) the particular structure of the GB or the crystal itself. An increased $\Delta\varepsilon$ for curved cracks could indicate an increasing effect of bond trapping for penny-shaped cracks and under 3D conditions in general. Under such conditions, local rearrangements at disordered GB crack fronts might result in even stronger bonding situations and thereby lead to a more efficient pinning of the crack front. It can, however, not be finally concluded whether crack line tension or GB bond trapping causes the lattice trapping ratio of the penny-shaped crack to increase. This question should, however, be investigated more closely in the future by comparing penny-shaped cracks with e.g. tri-axial ellipsoidal cracks where all three ellipsoidal semi-axes are distinct.

In addition, it is striking that the lattice trapping range in single crystals vary only slightly between $a = 60$ and 200 Å whereas the trapping ranges of GB cracks vary strongly for doubled crack lengths a in case of both quasi-2D central (factor 2) and penny-shaped cracks (factor 1.5). This can be understood by taking into account that in case of GB cracks, the

strain and stress distribution in the configuration is not only concentrated at the crack tip, but also at the GB. As the load level increases with decreasing crack radius, the concentration of the stresses in the GB must similarly increase. As a result, the additional amount of stress, which can be applied to the GB bonds before they rupture, behaves not nearly proportional to the applied load as it would be in the single crystal. Instead, it decreases and so does the bond trapping range.

An important consequence of the presented quasi-2D simulations of GB fracture is that a crack, which is located at a weak position, will only propagate until the next stronger bond is reached. At this position, it will remain until K_{Ic} of the current bond is reached and so forth. In other words, the highest K_{Ic} value in a certain propagation direction will determine the overall fracture resistance of the GB in this direction, see Fig. 7.15b. To test this proposition under 3D conditions, I performed strain-controlled crack propagation simulations with an increased box size $L_z \approx 1000$ Å for the Σ25 and Σ7 GBs, see Tables 5.4 and 5.5. Under such fully 3D conditions, cracks at the comparable weak positions 3 ($+[\bar{1}\,7\,0]_1$ direction, Σ25 STGB) and 0 ($+[\bar{1}\,1\,0]_1$, Σ7 ATGB) propagated only until the next stronger GB bond was reached. In case of the Σ7 GB, this was additionally confirmed by performing both dynamic and quasi-static simulations and by minimizing the energy of dynamic snapshots after crack arrest at $\varepsilon = 2.16$ and 2.52 %. Although the crack front of the later two configurations was strongly disturbed, the crack was stable at its position during energy minimization. Even configurations with crack tips located at the strongest crack tip bonds of the Σ7 GB, i.e. positions 1 and 4, were stable during energy minimization. In both cases, however, a small excitation (starting temperature $T_0 = 10$ K) initiated crack propagation during dynamic NVE simulations.

These observations indicate that even if the strongest GB bonds (in case of a perfectly straight crack) can be overcome under 3D conditions, the ultimate strength of a GB is not determined by its weakest bonds. Instead, the GB fracture toughness depends on its medium-strength bonds, where the bond trapping is still too high to be overcome by 3D processes, such as kink propagation, or thermal effects. It should be noted that for the Σ7 ATGB, the critical strains to break these medium strength bonds under fully 3D conditions were still much higher than predicted by the thermodynamic theory.

In summary, locally varying bond strengths at GBs explain (i) the superior fracture toughness of symmetrical GBs as compared to single crystals as frequently observed in our simulations; and (ii) the direction and position dependence of the fracture toughness for brittle fracture. As a result, the fracture resistance of a GB is *not* determined by its weakest bond; instead, stronger GB bonds can act as effective barriers for crack propagation. It is assumed here, that this statement can be made even for non-perfect, defective crack fronts.

7.3.2 Direction-dependent fracture behavior

Direction-dependent fracture behavior, e.g., in case of the straight cracks at Σ3 and Σ9 STGBs, see Fig. 5.3, is usually explained with the asymmetric arrangement of slip planes with respect to the crack propagation direction. As a result, the preference to initiate crack tip plasticity might exist only in one direction whilst brittle fracture is favored in the other. This is a direct consequence of the Rice-Thomson model for GB fracture [15, 93, 292] and has already been reported for experiments [93] and simulations [284] on Cu bicrystals. The purely geometric Rice-Thomson model, however, neglects crystallographic effects, such as the twinning/anti-twinning asymmetry of the bcc lattice [48, 74] as it is observable for the Σ3 GB. In this case, the $\{1\,1\,2\}$ twin planes are inclined by $\theta = \pm 90°$ in both $\pm[1\,1\,\bar{2}]_1$ propagation directions, but activated only in one of the two directions.

For penny-shaped cracks, on the other hand, direction-dependent fracture behavior occurred less frequently and has not yet been reported in the literature. Fig. 7.16 shows top views of characteristic configurations of the Σ3, Σ7, and Σ49 GBs. In all cases, the crack initially propagated in a brittle manner and showed delayed crack tip plasticity.

At the Σ7 and Σ49 GBs, the deformation twins prevent crack propagation at the corresponding crack fronts by efficiently blunting the crack tip, see Fig. 7.16b and c. At the Σ7 GB, a twin forms on the 57.4°-inclined $(2\,1\,1)_2$ twin plane at a crack front that lies at an angle of approximately 8.5° to the $[1\,\bar{9}\,4]_2$ axis. This observation indicates that the twin is emitted at a $[4\,\bar{2}\,1\,13]_2$ crack front for which the Rice criterion, see Eq. (2.14), predicts $G_e = 8.2\ \mathrm{J/m^2}$. At the opposite $[\bar{4}\,21\,\bar{13}]_2$ crack front, no equally-inclined $[1\,\bar{1}\,\bar{1}]_1(2\,1\,1)_1$ twin system is available in grain 1 due to the GB. Instead, the $(2\,1\,1)_2$ twin plane is now inclined by 122.6° and

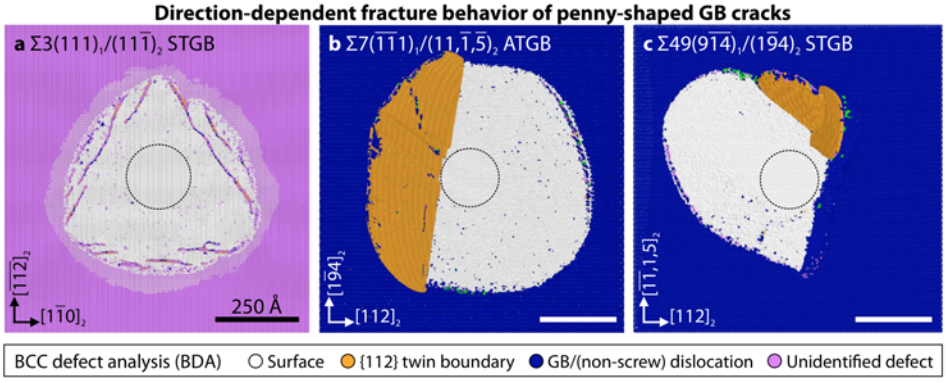

Figure 7.16: Direction-dependent fracture behavior of penny-shaped GB cracks; **a**: Σ3 STGB ($\varepsilon = 4.54\%$, $t = 100$ ps), the twin systems that are activated during brittle crack propagation take on a threefold symmetry; **b**: Σ7 ATGB ($\varepsilon = 4.26\%$, $t = 170$ ps), formation of one large twin in grain 2 completely prevents crack propagation at the corresponding crack front; **c**: Σ49 STGB ($\varepsilon = 4.77\%$, $t = 170$ ps), activation of one twin system per grain leads to the continuation of crack propagation only within an angle of approximately 110°; in all cases, crack tip plasticity is favored only for certain crack front directions; in case of the Σ3 GB, propagation happens too fast and the crack tip plasticity cannot sufficiently unload the crack tip to prevent this.

the Rice criterion increases to G_e = 27.1 J/m^2. This high value explains why twin formation is only observed in one direction and not in the opposite. The same argumentation is used to explain the direction dependence of fracture for the Σ49 GB. Here, twins form at the $[3\,\overline{17}\,11]_1$ and the $[\overline{17}\,\overline{5}\,\overline{7}]_2$ crack fronts, respectively. It is important to note that in both cases the activated twin systems are not those systems with the maximum Schmid factor under uniaxial loads (m = 0.5).

The crack at the Σ3 GB, on the other hand, continues to propagate even though multiple twins and dislocations were subsequently emitted from ⟨1 1 0⟩-oriented crack fronts, see Fig. 7.16a. Due to the twinning/anti-twinning asymmetry of the bcc lattice [48, 74], only three of the six possible {1 1 2} twin planes are oriented in twinning direction, which explains the observed threefold symmetry of plasticity in case of the Σ3 GB. The emitted twins and dislocations were, however, not able to effectively blunt the crack before it propagated further. On the one hand, this is an indication for the inherent brittleness of the Σ3 GB due to its high GB energy, see Table 5.1. On the other hand, one could speculate that the plasticity might cause decelerated crack growth and possibly crack arrest if the simulated time and box size would be significantly increased. Under such conditions, pronounced reoriented crack fronts might observable, which are similar to the situations for the Σ7 and Σ49 GBs in Fig. 7.16b and c.

In case of the Σ9 GB, direction-dependent fracture behavior is expected from the results for straight cracks, but not observed for the penny-shaped crack shown in Fig. 5.5b. In this case, G_t = 6.8 J/m^2 for the observed twin system whereas G_0 = 10.8 J/m^2 for brittle fracture in the opposite crack propagation direction. For small crack radii, see Fig. 7.17a-c for a = 75 Å, the emitted dislocations can reach these parts before the critical conditions for brittle bond breaking are reached. As a consequence, the local crack front segment is unloaded resulting in a decreased driving force for brittle crack propagation. If, however, the crack radius is increased to a = 300 Å, bond breaking can be observed at these parts of

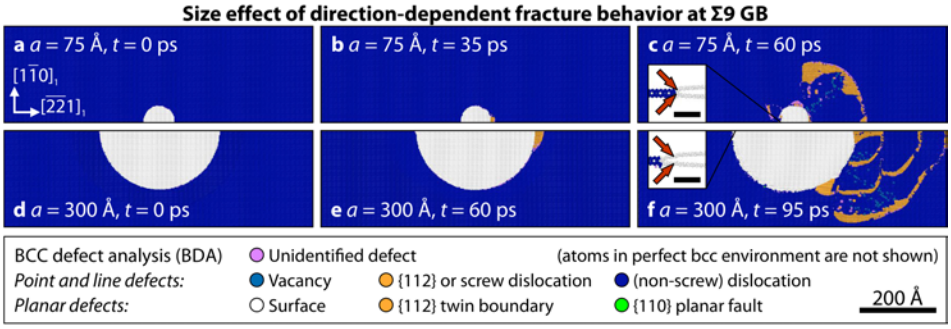

Figure 7.17: Size effect in direction-dependent fracture behavior of penny-shaped GB cracks (Σ9 STGB in W; ATFS potential; $L_x \approx 1600$ Å; $L_y \approx 2000$ Å; $\dot{\varepsilon} = 10^8$ s^{-1}). **a-c**: a = 75 Å; the initiated crack tip plasticity reaches the opposite side of the crack before brittle fracture can start; **d-f**: a = 300 Å; the opposite side of the crack is too far away to be reached by the dislocations in time; brittle fracture initiates (see inset figure; scale bar: 30 Å).

the penny-shaped crack. In this case, the distance is too long for the dislocations to reach the 'brittle' parts in time and to prevent brittle fracture, see Fig. 7.17d-f.

In summary, direction-dependent fracture behavior of small GB cracks is generally expected if (i) the energy barrier for the initiation of brittle fracture and crack tip plasticity are almost equal; or if (ii) the crack radius is large enough to prevent the crack tip from being blunted by cross slipping dislocations that were nucleated at other parts of the curved crack front.

7.3.3 Slip transmission

Slip transmission through grain boundaries plays an important role in materials deformation and has been studied both experimentally, see e.g. Ref. [430], and in computer simulations [431–433] since many years. Typical atomistic simulations of slip transmission often use quasi-2D setups and straight dislocation lines. Furthermore, dislocations are inserted artificially in such setups. In the presented simulations of penny-shaped GB cracks at the Σ9 and Σ25 STGBs, however, dislocations nucleate and move as a product of crack tip stresses, see Figs. 5.5b and 5.7b.

Theoretically, dislocation transmission is expected when the misorientation between the incoming and outgoing slip systems is small and the resolved shear stresses on the outgoing slip system are sufficiently high [241]. The so-called residual Burgers vector $\underline{b}_\mathrm{r}$, on the other hand, is a measure for the connectivity of the two slip systems across the GB. It is defined as the connecting vector between the outgoing and incoming Burgers vectors, $\underline{b}_2$ and $\underline{b}_1$, respectively [241]:

$$\underline{b}_1 \quad = \quad \underline{b}_2 + \underline{b}_\mathrm{r}. \tag{7.11}$$

This vector is required for the conservation of the total Burgers vector. It can be seen as an additional step that is left at the grain boundary after the dislocation was transmitted.

In Fig. 7.18, both criteria are evaluated for the two Σ9 and Σ25 GBs. In case of the Σ9 GB, both slip planes intersect the GB along the same direction, which results in a good connectivity of the two slip systems. The calculated residual Burgers vectors are, as follows:

$$\underline{b}_{1\mathrm{r}} = \underline{b}_{11} - \underline{b}_{12} = a_0/2[1\bar{1}1]_1 - a_0/2[1\bar{1}1]_2 = a_0/9[\bar{2}\,\bar{2}1]_1 \text{ and} \tag{7.12}$$

$$\underline{b}_{2\mathrm{r}} = \underline{b}_{21} - \underline{b}_{22} = a_0/2[1\bar{1}\bar{1}]_1 - a_0/2[1\bar{1}\bar{1}]_2 = a_0/9[2\,2\bar{1}]_1 \tag{7.13}$$

Here, the first subscript identifies the dislocation and the second the corresponding coordinate system, see Fig. 7.18a. In case of the Σ25 GB, see Fig. 5.5b, the $(\bar{2}11)_1$ twin is transmitted through the GB onto the equivalent $(\bar{2}11)_2$ twin plane. The calculated residual Burgers vector between $\underline{b}_{11} = [\bar{1}\bar{1}\bar{1}]_1$ and $\underline{b}_{12} = [\bar{1}\bar{1}\bar{1}]_2$ is $\underline{b}_{1\mathrm{r}} = a_0/25[\bar{4}\,3\,0]_1$. Here, incoming and outgoing planes are misaligned by approximately 16.5°, see Fig. 7.18b. As a consequence, the dislocation that is transmitted into grain 2 cross slips to remain connected to the intersection of the GB and the twin in grain 1. This observation indicates that slip transmission is highly facilitated in cases of easy cross slip of screw dislocation segments. In such cases,

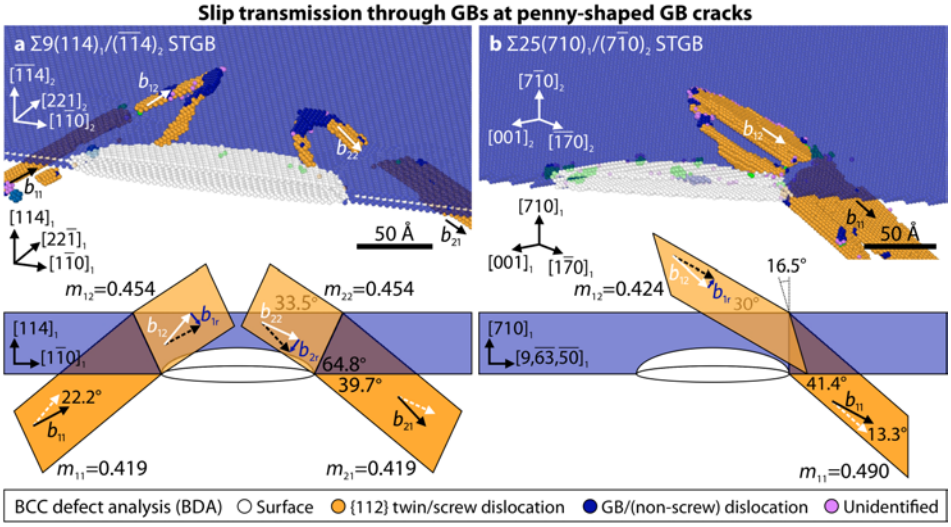

Figure 7.18: Slip transmission through GBs at penny-shaped GB cracks in W; **a**: transmission of two $\{112\}_1$ dislocations through the Σ9 STGB onto $\{110\}_2$ planes; $\varepsilon = 2.55\%$, $t = 55$ ps; **b**: transmission of a $(\bar{2}11)_1$ twin through the Σ25 STGB into the same twin system in grain 2; $\varepsilon = 2.46\%$, $t = 45$ ps. Burgers vectors $\underline{b}_{ij}$, slip planes, Schmid factors m, inclination and misorientation angles are shown schematically in the lower subfigures. Burgers vector nomenclature: i: dislocation identifier, j: grain identifier; both GBs are identified as (non-screw) dislocations.

the misorientation of the glide planes at the grain boundary should generally be of secondary importance for the occurrence of slip transmission. It can therefore be expected that slip transmission occurs frequently at the tips of curved GB cracks, where the edge components are emitted and the screw components remain attached to the crack front.

In summary, crack tip plasticity at GBs might not be limited to the grain, in which it was initiated, but be transferred to its neighboring grain by slip transmission. In this context, the misorientation of the incoming and outgoing glide planes at the grain boundary should be of secondary importance as a possible mismatch can be easily accommodated by cross-slipping screw dislocation segments. Meso-scale models of GB fracture should account for this possibility.

7.3.4 Effects of absorbed dislocations

Thus far we have only discussed perfectly planar grain boundaries without defects like steps, impurities, vacancies, or absorbed dislocations. Grain boundaries in realistic microstructures, however, contain a multitude of such defects making them probably weaker and sometimes stronger obstacles for crack propagation. If and how the presence of GB defects alters the propagation behavior of GB cracks, is therefore interesting to study from a fundamental point of view. As we have seen in section 6.3, absorbed dislocations did not lead to qualitatively different fracture behavior since the inclined $\{110\}$ slip planes are ori-

ented very unfavorable ($\theta_1 \approx 135°$ and $\theta_2 \approx 90°$). The critical strains for crack propagation were, however, markedly affected. Whether the critical strains to fracture the first structural unit, ε_1^{λ}, were lower or higher than the corresponding values in the dislocation-free configuration depended on the details of the inserted dislocation. In general, the insertion of a dislocation has a twofold influence on the driving force for crack propagation: first, the dislocation influences the stress distribution around the dislocation core and thereby also the crack tip stress field; second, the globally applied strain depends on whether the dislocation was inserted by adding or removing an atomic half plane. The actual driving force on the crack is therefore a combination of both factors: one realistic (dislocation stress field) and one due to the setup (by adding or removing an atomic half plane).

Fig. 7.19 qualitatively compares the theoretical isotropic linear-elastic σ_{xx} and σ_{yy} stress distributions, see Eqs. (2.24-2.26), for the dislocation-free case and for the two opposite Burgers vectors $\underline{b}^- = -a_0/2[11\bar{1}]$ and $\underline{b}^+ = +a_0/2[11\bar{1}]$. In presence of an absorbed dislocation, both σ_{xx} and σ_{yy} stress fields become asymmetric with respect to the GB plane. The σ_{yy} stress distributions for the two opposite Burgers vectors are equal to each other when mirrored at the GB plane, cf. Fig. 7.19c and e. The influence on the σ_{xx} component, however, strongly differs for the two Burgers vectors. For $\underline{b}^-$, the highly stressed region around

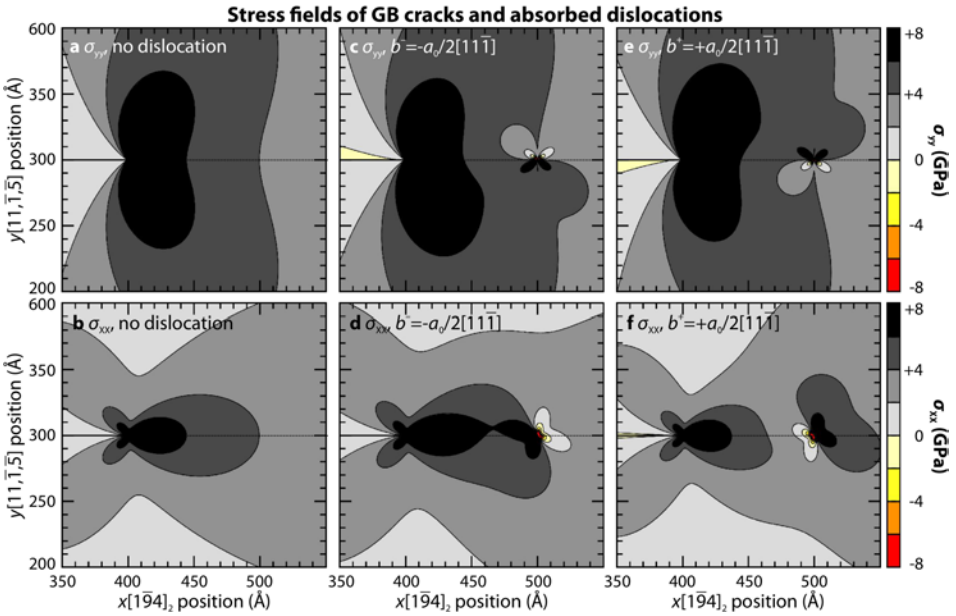

Figure 7.19: Comparison of theoretical stress fields of Σ7 ATGB cracks in absence and presence of absorbed dislocations; **a**,**b**: without absorbed dislocation; **c**,**d**: with absorbed $\underline{b}^-$ dislocation; **e**,**f**: with absorbed $\underline{b}^+$ dislocation; upper figures: σ_{yy} stress distribution; lower figures: σ_{xx} stress distribution. Note that the regions of high σ_{xx} stresses are largest for $\underline{b}^-$ and lowest for $\underline{b}^+$; the influence on σ_{yy} stresses is visible, but shows a less clear trend. The isotropic solutions for crack tip and dislocation stress fields, see Eqs. (2.24-2.26), were used for qualitative comparison with the following parameters: $K_I = 1\,\mathrm{MPa}\sqrt{\mathrm{m}}$; $\mu = 52.5$ GPa; $\nu = 0.3$.

the crack tip is larger than in the dislocation-free case and takes on an asymmetric shape with respect to the GB plane. An asymmetric stress distribution causes a mixed-mode situation, which in turn leads to lower fracture strains, see e.g. Refs. [199]. In the present case, the stress state at the crack tip becomes even more critical by the larger high-σ_{xx} regions. The crack tip bonds are generally not only loaded in y direction, but also in x and z direction. For this reason, higher strains in these directions additionally favor premature bond breaking, as it is also shown in Fig. 7.27. For $\underline{b}^+$, on the contrary, the region of highest σ_{xx} stresses shrinks and its approximately mirror-symmetric shape is mostly maintained.

As mentioned earlier, the globally acting strain ε is a function of the position in x direction in presence of absorbed dislocations. In the region, where an atomic half plane (HP) was removed, the corresponding part of the crystal is displaced by approximately $u'_y = a_0/\sqrt{2}[\bar{1}10]$. This leads to an increase in applied strain of $\Delta\varepsilon^- = u'_y/L_y \approx 0.24$ % and hence an increase in the driving force for crack propagation. For an inserted HP, the applied strain is decreased by only $\Delta\varepsilon^+ \approx -0.24$ %. This contribution is rather small in comparison to determined differences up to 0.92 % ($\underline{b}^+$, added HP)

The comparison between these two considerations and the observed critical strains and propagation distances, see Table 6.3, indicates that the local influence of the dislocation stress field is more pronounced than the effect of the globally applied strain. The critical strain ε_i^λ is higher and Δx is lower for the decreased high-σ_{xx} regions in case of $\underline{b}^+$ than for the increased and more asymmetric stress distribution when the Burgers vector is $\underline{b}^-$. For equal Burgers vectors, which have the same local stress distributions, global strain variations only determine the order of the two insertion methods.

In summary, even the presence of only one individual absorbed dislocations can markedly affect the fracture resistance of a GB. This highlights the need for future simulations of non-perfect GBs, with e.g. steps, voids, and curvature, for the development of more realistic meso-scale models for GB fracture.

7.4 Mechanisms of crack tip blunting by crack-dislocation interactions

As only an atomically sharp crack tip can propagate by brittle fracture, mechanisms that lead to crack tip blunting are highly relevant for the development of new microstructure-sensitive meso-scale models [339, 434] for the prediction of the influence of e.g. pre-deformation on the fracture resistance. We first focus on 'classical' crack tip blunting by the emission of (edge or mixed) dislocations in section 7.4.1; thereafter, I describe a number of mechanisms leading to crack tip blunting by the interaction of cracks with pre-existing dislocations in section 7.4.2. Even though the study of crack-dislocation interactions in this thesis is only of exemplary nature, the fundamental features should not depend strongly on the setup or the interatomic potential; instead they can be mainly traced back to the behavior of dislocations in the stress fields of cracks and to fundamental properties of bcc crystals and might therefore be generally valid.

7.4.1 Emitted dislocations

The blunting of a straight crack front by the emission of an edge dislocation is well studied by analytical work, continuum studies, and atomistic simulations, see e.g. Refs. [16], [119], and [62], respectively. Such studies, however, usually consider the nucleation of an edge dislocation at an infinitely long straight crack front. If the crack front is aligned in such a way that a crack system is favorably oriented according to the Rice criterion [16], dislocation emission is likely. The results of this thesis, however, present a further possibility how crack fronts can be blunted even if they are unfavorably oriented for direct dislocation emission. This can be seen e.g. for the crack located on the (1 1 0) plane, which is predicted to fracture in a completely brittle manner according to the quasi-2D simulations, see Table 4.3 and Fig. 4.5a-d. At a curved crack front, on the other hand, the passing screw segments of dislocations, which were emitted at other parts of a curved crack front, successively cross slip on $\{1\,1\,0\}$ and $\{1\,1\,2\}$ planes, cf. Fig. 4.5e. These cross slip events allow the screw dislocation to follow the crack front curvature, cf. Fig. 7.13, and to efficiently blunt the crack tip, see also the formation of prismatic dislocation loops with Burgers vector parallel to the crack plane normal in Fig. 4.10.

In general, the blunting by cross-slipping screw components of emitted dislocations should not be a process that is limited to the artificial scenario of a perfectly penny-shaped cracks. In reality, it can for example occur at a long and straight propagating crack, which is facing an obstacle and is therefore locally slightly curved; furthermore, freshly initiated crack nuclei will inevitably exhibit a certain degree of curvature as long as their dimensions are comparable to the grain size.

7.4.2 Pre-existing dislocations

The presented simulation results show that pre-existing dislocations can cause (i) the emission of blunting dislocations as a result of the indirect interaction of the crack tip and dislocation stress fields; and (ii) the blunting of the crack tip by direct crack-dislocation interactions. Examples for both possibilities were presented in section 6 and briefly reviewed in the following paragraphs; furthermore, their possible relevance for larger-scale models is pointed out.

Indirect interaction between stress fields

The indirect interaction of cracks and dislocations by their stress fields was shown in section 6.1, where dislocations led to decreased critical strains and a higher tendency for crack tip plasticity as compared to the dislocation-free situations. Both observations can be explained with the changed distribution of stresses around the crack tip when a dislocation is present. The theoretical isotropic linear-elastic stress distributions, see Eqs. (2.24-2.26), are qualitatively compared in Fig. 7.20 for both the absence and presence of dislocations. Whereas the influence of an edge dislocation on the σ_{yy} stresses is marginal, cf. subfigures a and b, it becomes more significant for the σ_{xx} and σ_{xy} stresses, cf. subfigures c to f. The

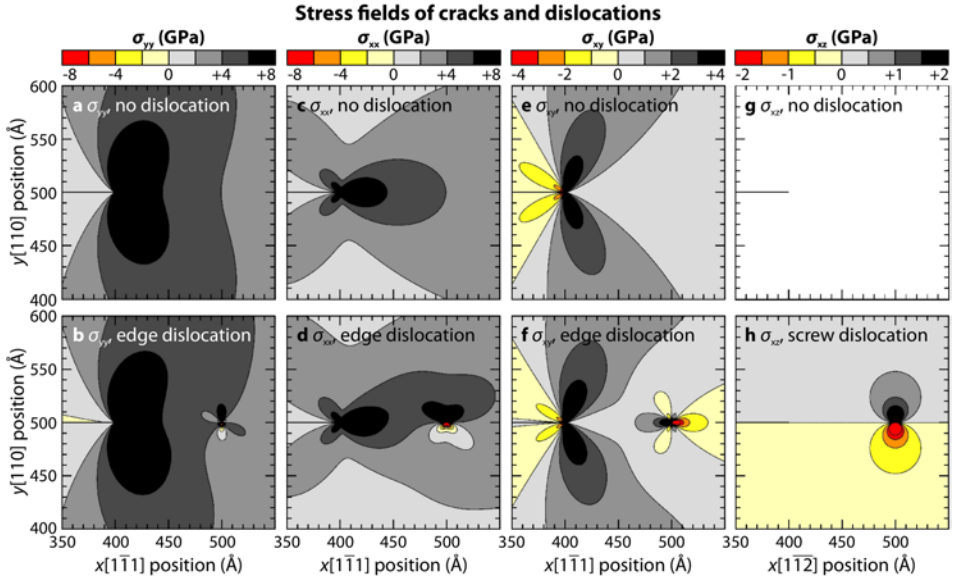

Figure 7.20: Comparison of theoretical stress fields σ_{ij} of cracks in absence and presence of pre-existing dislocations; **a**,**b**: σ_{yy} for [$\bar{1}$12] crack front (edge orientation); **c**,**d**: σ_{xx} in edge orientation; **e**,**f**: σ_{xy} in edge orientation; **g**,**h**: σ_{xz} for [1$\bar{1}$1] crack front (screw orientation); upper figures: reference without dislocation; lower figures: in presence of a dislocation. Note the qualitatively higher shear stresses in presence of pre-existing dislocations (**f**,**h**) in comparison to their absence (**e**,**g**). The isotropic solutions for crack tip and dislocation stress fields, see Eqs. (2.24-2.26), were used for qualitative comparison with the following parameters: $K_I = 1\,\mathrm{MPa}\sqrt{\mathrm{m}}$; $\mu = 52.5$ GPa; $\nu = 0.3$.

distribution of the σ_{xx} component becomes highly asymmetric as it decreases in the crystal half where the half plane was inserted to create a dislocation. In the other half crystal, the σ_{xx} stress component increases. Such an asymmetric situation leads to an additional mode II (in-plane shearing) component of the crack tip stress intensity. The presence of a screw dislocation, on the other hand, does not influence the aforementioned stress fields since $\sigma_{xx} = \sigma_{yy} = \sigma_{xy} = 0$ for screw dislocations. In this case, σ_{xz} stresses occur, cf. Fig. 7.20g and h, leading to an additional mode III (out-of-plane shearing) component of the stress intensity at the crack tip. Vatne *et al.*[199] showed for four different Fe crack systems that the effective stress intensity factor $K_{\mathrm{eff,c}} = \sqrt{K_I^2 + K_{II}^2 + (1+\nu)/(1-\nu^2)K_{III}^2}$ can decrease under both mixed mode I/II and I/III conditions. This indicates that the lower critical strains observed here can be explained by additional mixed-mode components in the presence of dislocations.

The second implication of the increased σ_{xy} and σ_{xz} components, cf. Fig. 7.20e,f and g,h, is the increased driving force for dislocation emission. The resulting resolved shear stresses (τ_{rss}) on the observed ($\bar{1}\,3\,\bar{2}$) and (0 1 1) slip planes are compared in Fig. 7.21. In this context, it is important to note that the unstable stacking fault energy of the Chiesa potential for {1 2 3} planes ($\gamma_{\mathrm{usf}} = 1.023\ \mathrm{J/m^2}$) is in the same range as compared to {1 1 2} planes; from

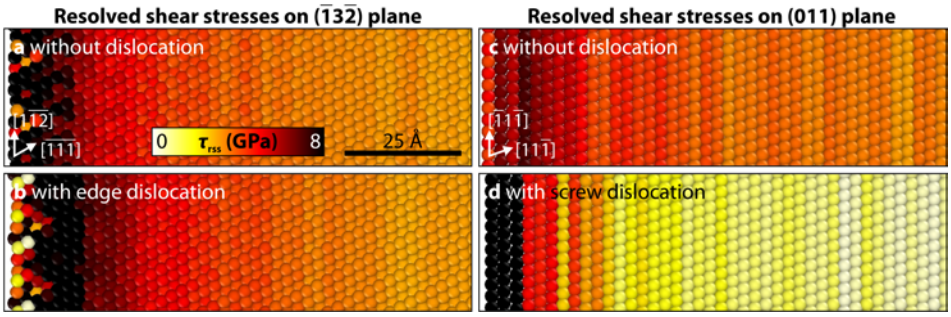

Figure 7.21: Comparison of resolved shear stresses (τ_{rss}) in absence and presence of pre-existing dislocations at $\varepsilon = 2.40$ % applied strain, see Fig. 6.1. **a**,**b**: τ_{rss} on the $(\bar{1}3\bar{2})$ plane in $[\bar{1}\bar{1}\bar{1}]$ direction; $t = 4$ ps; **c**,**d**: τ_{rss} on the (011) plane in $[11\bar{1}]$ direction; $t = 6$ ps; upper figures: reference without dislocations; lower figures: in presence of a dislocation, shortly before dislocation emission; in both cases, the regions of high resolved shear stresses and the maximum resolved shear stresses (τ_{mrss}) are larger if a dislocation is present in front of the crack. The distance from the crack tip to the dislocation position was 80 Å and 60 Å in **a**,**b** and **c**,**d**, respectively.

this point of view, dislocation emission on the $(\bar{1}\,3\,\bar{2})$ plane is therefore not unexpected. In both cases, the regions of highest τ_{rss} values are larger for pre-existing dislocations than in the dislocation-free configurations. This qualitative observation is further strengthened by a comparison of the maximum resolved shear stresses τ_{mrss} as determined in the vicinity of the crack tip. In presence of an edge dislocation, $\tau_{\mathrm{mrss}} \approx 11$ GPa whereas it is 10 GPa without a pre-existing dislocation. In screw orientation, this difference is even more pronounced as $\tau_{\mathrm{mrss}} \approx 17$ GPa with and only $\tau_{\mathrm{mrss}} \approx 7$ GPa without dislocation.

In summary, the indirect interaction of a crack with the stress fields of pre-existing dislocations can lead to mixed-mode situations at the crack tip; under these circumstances, the emission of blunting dislocations can be more favorable as in a dislocation-free scenario. The interaction of cracks with dislocations on the same crystallographic plane are relevant in cases where the crack was initiated on a slip plane, e.g., under fatigue (cyclic loading) conditions, and/or emitted the dislocation beforehand, e.g. under prior shear loading.

Direct crack-dislocation interactions

Direct interactions between cracks and pre-existing dislocations on oblique slip planes are shown in Figs. 6.4-6.6. In these cases, blunting occurred either by (i) the cross slip of screw segments after contact with the crack front, see e.g. in Figs. 6.5 and 6.6, or by (ii) partial crack closure until the surface steps at the crack face were reached, which were created by dislocation cutting beforehand, e.g., in Fig. 6.4.

Following the work by Bitzek [155, 214, 215], the initial movements of the dislocations can be understood by calculating the glide components of the Peach-Koehler forces acting on dislocations segments of unit length [48, 435]:

$$F_{\mathrm{PK}} = \frac{[(\underline{b}\cdot\underline{\underline{\sigma}})\times\underline{l}]\cdot[\underline{l}\times(\underline{b}\times\underline{l})]}{\|\underline{b}\times\underline{l}\|}, \tag{7.14}$$

where $\underline{b}$ is the Burgers vector, $\underline{l}$ the dislocation line direction, and $\underline{\underline{\sigma}}$ the stress tensor, which can be either calculated theoretically or determined from the simulation output, see section 3.5. In case of screw dislocations, where $\underline{b}$ and $\underline{l}$ are parallel, it is sufficient to calculate:

$$F_{\mathrm{PK}}^{\mathrm{screw}} = (\underline{b}\cdot\underline{\underline{\sigma}})\cdot\underline{n}, \tag{7.15}$$

where $\underline{n}$ is the normal to the slip plane of interest. Fig. 7.22 shows the corresponding driving forces on the dislocations for selected scenarios.

In case of the $\underline{b}_1$ dislocation, see Fig. 6.4, one part of the dislocation line is attracted by the crack, see the yellow regions above the crack tip in Fig. 7.22a; the other part of the dislocation is dragged towards the boundaries. As a result of this opposite motion of the dislocation line, a screw segment forms in between, see Fig. 6.4c. As it is pinned by the edge segments that cuts along the crack face, it cannot move away from the crack tip; instead, it cross slips in the system shown in Fig. 7.22b, where it also cuts along the crack face and moves away from the point of initial contact with the crack.

Fig. 7.22c shows the driving force on the $\underline{b}_2$ dislocation, which is dragged towards the crack tip by the overall attractive interaction force ahead of the crack tip. Upon contact of the dislocation with the crack tip, a $\underline{b}_{\mathrm{e1}}$ dislocation nucleates in the system shown in Fig. 7.22d, which then experiences a force away from the crack tip, see Fig. 6.5c.

It is worth noting that so far the stimulated emission of dislocations was observed in experiments in Si [318, 319] and atomistic simulations in fcc Ni [155, 214], but not in bcc crystals. In Si, stimulated emission is believed to cause a softer brittle-ductile transition in presence of pre-existing dislocations as compared to dislocation-free crystals [318]. To further elucidate the role of stimulated emission for the crack tip plasticity in bcc crystals, more systematic and in-depth studies are needed under variation of the crack systems and dislocation types.

In case of the $\underline{b}_{\mathrm{j}}$ dislocation junction, cf. Fig. 6.6, the junction experiences a positive driving force towards the crack tip on both the $(0\,1\,\bar{1})$ and $(0\,1\,1)$ plane (not shown). At the same time, the $\underline{b}_2$ segment is attracted by the crack, see Fig. 7.22e; all other screw segments are pushed away from it towards the boundaries. The $\underline{b}_1$ segment, however, experiences a stronger force in the $(\bar{1}\,\bar{1}\,2)$ cross slip plane shown in Fig. 7.22f. Here, it is also pulled away from the crack, but as it is pinned at the intersection with the $\underline{b}_2$ segment and the $\underline{b}_{\mathrm{j}}$ junction, it bows out and finally comes in contact with the crack tip, cf. Fig. 6.6c.

For all three cases of cracks interacting with dislocations on oblique slip planes, the further reactions involve a multitude of cross slip events and interactions that are too complex to be visualized by a stress field analysis. In the following, I therefore focus on a general statements on the fundamental importance of cross slipping screw segments in the vicinity

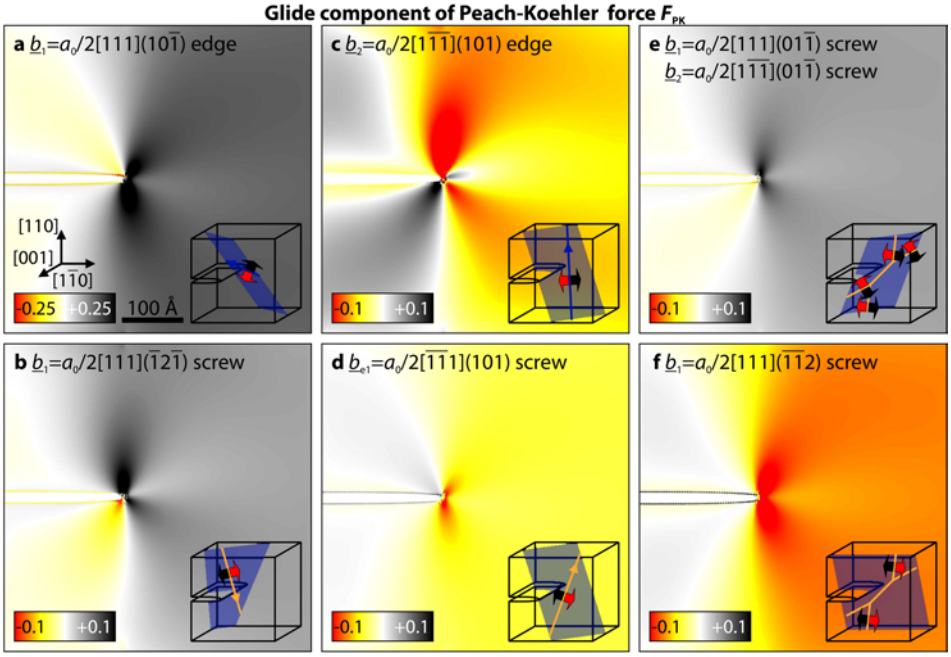

Figure 7.22: Magnitude and sign of the glide component of the Peach-Koehler forces on various dislocations as determined from the atomistic stress state according to Eqs. (7.14-7.15). (110)[001] crack system; $\varepsilon = 2.50$ %; see section 6.2 for the setup. The positive and negative directions are indicated for selected dislocations in the inset panels. **a**: local varying driving force on $\underline{b}_1$ edge dislocation leading to partial attraction and repulsion, cf. Fig. 6.4b; **b**: cross slip system of $\underline{b}_1$ dislocation after formation of the screw segment between the repelled and attracted dislocation segments, cf. Fig. 6.4c; **c**: local varying driving force on $\underline{b}_2$ edge dislocation leading to attraction and emission of the $\underline{b}_{e1}$ dislocation; **d**: emitted $\underline{b}_{e1}$ dislocation, cf. Fig. 6.5c, repelled; **e**: $\underline{b}_1$ and $\underline{b}_2$ screw segment of $\underline{b}_j$ junction; only the lower $\underline{b}_2$ segment is attracted towards the crack face, cf. Fig. 6.6b. **f**: cross slip system of lower $\underline{b}_1$ segment, cf. Fig. 6.6b; although the force is highly repulsive in this case, the pinning of the dislocation segments leads to its bow out and to the direct interaction with the crack, cf. Fig. 6.6c.

of the crack. In the $\underline{b}_1$ case, the dislocation leaves its initially oblique glide plane after contact with the crack front and proceeds to slip on an inclined plane in a direction parallel to the crack front. A similar process is observed for the newly nucleated $\underline{b}_{e1}$ dislocation in Fig. 6.5d and for the $\underline{b}_1$ screw segment initially forming the dislocation junction, see Fig. 6.6c. The dislocations slip along the crack front—and thereby blunt it—at least for some distance before they again cross slip on another plane, on which they glide along the crack face whereby surface steps are created. Such surface steps are the reason for crack tip blunting in the scenario, where the $\underline{b}_1$ dislocations first cut along the crack face and the crack reorients accordingly only thereafter, see Fig. 6.4d. It is finally interesting to note, that the $\underline{b}_2$ segment of the dislocation junction, see Fig. 6.6d, cuts along the crack face but leaves no step as its $a_0/2[1\bar{1}\bar{1}]$ Burgers vector lies within the (110) crack plane.

Despite of possible inaccuracies of the interaction potentials and the typical limitations of MD simulations (small length and time scales), the key features of the observed processes should be generally valid. The described events are mainly linked to high stresses, highly curved dislocation lines, and multiple cross slip events; these characteristics should be undoubtedly present also at real crack tips independent of the shortcomings of atomistic simulations. At the same time, the important role of cross-slipping screw segments for crack tip blunting makes the presented observations typical for bcc metals as cross slip should occur generally more frequently than in the fcc structure, where (i) a dissociated dislocation has to contract before it can cross slip; and (ii) a dislocation can glide on only two independent slip planes (in comparison to four $\{110\}$ and four $\{112\}$ slip planes in bcc crystals).

In summary, it is expected that the interaction of cracks with pre-existing dislocations frequently causes crack tip blunting in bcc metals. The stimulated emission of dislocations, which was seen before in experiments in Si [318, 319] and atomistic simulations in fcc Ni [155, 214], was observed here for the first time in a bcc crystal.

7.5 Dynamic instabilities

Two types of dynamic instabilities were frequently observed during the simulations of cracks in bcc metals: (i) the arrest of a formerly propagating crack during dynamic loading; (ii) the emission of dislocations from propagating twins. Both effects were observed under quasi-2D and fully 3D conditions and in case of dislocation emission from twin tips even for different materials. In the following, I address the question of the underlying reasons for both instabilities and speculate about possible consequences.

7.5.1 Crack arrest

The main difference between quasi-static and dynamic loading of atomically sharp cracks was their qualitatively different propagation behavior. This becomes in particular interesting for the $(110)[1\bar{1}0]$ crack system, where initial brittle fracture events were observed for both quasi-static and dynamic loading conditions. Thereafter, the cracks continued to propagate under quasi-static conditions, see Fig. 4.8c; all dynamically loaded cracks, on the other hand, arrested after a certain period of propagation, cf. Table 4.3. In certain cases, formerly brittle propagating cracks emitted dislocations from the arrested crack tips under dynamic loading conditions, see e.g. Fig. 4.6b and d. These observations were found independent of the (strain-controlled) simulation setup.

Unexpected events at brittle propagating cracks can often be explained by elastic waves that have been emitted by the breaking of the first bond. When such a wave propagates to the fixed boundaries, it is reflected back to the propagating crack tip and might cause artificial events. This issue led to the development of damping boundary conditions, which reduce the intensity of the reflected waves [162]. In the present study, on the other hand, the problem is tackled by making the box dimensions so large that the propagation distances

of emitted elastic waves lie in the range of several hundred Å. For Fe, the longitudinal wave speed c_l lies in the range of approximately 4.2 km/s in $\langle 0\,0\,1\rangle$ direction and 6.2 km/s in $\langle 1\,1\,1\rangle$ direction, cf. Eq. (2.9). In case of the quasi-2D simulation geometry with $L_x \times L_y \approx 3000 \times 1000$ Å^2 and crack length $a = 1000$ Å, for instance, the first elastic wave needs $\Delta t \approx 18$ ps to return to the crack tip. The crack tip, however, arrested after a propagation period of less than 10 ps, cf. Table 4.3 and Fig. 4.6d. Similarly, the dislocation shown in Fig. 4.6b, was emitted after less than 5 ps of crack propagation; the corresponding elastic wave would have needed approximately 16 ps to return to the crack tip. These comparisons undoubtedly show that the multiple observed arrest events in the $(1\,1\,0)[1\bar{1}\,0]$ crack system cannot be attributed to elastic waves that have returned to the crack tip. The same statement can be made for the arrested crack tips in $(1\,1\,0)[0\,0\,1]$, $(1\,1\,\bar{2})[\bar{1}\,1\,0]$, and $(1\,1\,\bar{2})[1\,1\,1]$ orientations, see Fig. 4.5a-d and Fig. 4.12a,b. The following discussion will, however, only focus on the $(1\,1\,0)[1\bar{1}\,0]$ system as an in-depth analysis of crack arrest is beyond the scope of this study.

Another possible explanation for crack arrest could be rooted in the dynamic loading of the crack. With the presented dynamic simulation technique, the strain rate $\dot{\varepsilon}$ is held constant. This allows to rapidly determine ε_i, but might also result in a strongly accelerated crack tip that could cause nonphysical events. For this reason, the displacement fields of the relaxed configurations at ε_{in} were scaled to $\varepsilon = \varepsilon_i$ to perform additional simulations at constant strain. To test their *local* stability, the crack tip structures before and after crack arrest were subsequently relaxed using the MIK relaxator, see section 3.1. The corresponding snapshots after 120,000 steps are shown in Fig. 7.23a and b, respectively. It can be seen in subfigure b that the crack tip atoms are slightly rearranged leading to a characteristic pentagonal structure. This pentagonal structure is also seen for simulations at a constant strain rate, see the inset panel in Fig. 4.6d. Crack arrest is therefore not caused by the dynamic loading technique used here.

Another explanation could be that the applied driving force at $\varepsilon = \varepsilon_i$ is enough to initiate crack propagation, but too small for steady crack growth [41]. Such a situation is schematically shown in Fig. 2.2e. Fig. 7.23c, however, shows that the crack arrested even at an overload of $\varepsilon = 1.1\varepsilon_i$. In this case, two characteristic pentagonal structures can be observed below and above the arrested crack tip.

These comparisons show that the occurrence of crack arrest can be explained by atomic rearrangements at the crack tip during crack propagation. The initial structure is called the 'mobile' structure in the following since it is present at the propagating crack tip until it arrests, see Fig. 7.23a. The pentagonal arrangements at the arrested crack tips in Fig. 7.23b and c characterize the 'immobile' structures since brittle re-initiation has never been observed for these configurations until the first emitted elastic wave returned to the crack tip.

Importance and consequences of the two competing structures become visible when the crack tip configurations of other potentials are analyzed. The mobile structure observed for the Chiesa potential is also present at the sub-critical crack tip, i.e., at $K<K_{Ic}$, modeled with the Mendelev-II potential, see Fig. 7.23e. On the other hand, the immobile structures of the Chiesa potential are equal to the relaxed sub-critical crack tip structures of the Simonelli, Chamati, and Gordon potentials. The corresponding configurations of the Gordon and Chamati potentials are shown in Fig. 7.23f and g, respectively. Upon further

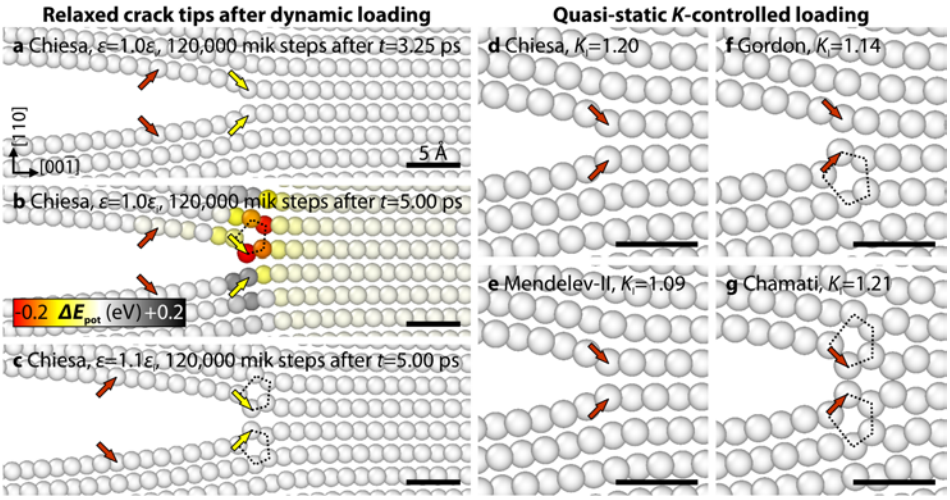

Figure 7.23: Comparison of arrested crack tips under dynamic loading and sub-critical crack tip structures under quasi-static loading; **a**-**c**: configurations after 120,000 relaxation steps of formerly propagating cracks under constant strain (Chiesa potential); **a**: $\varepsilon = \varepsilon_i$, at the end of the propagation period slightly before crack arrest; **b**: $\varepsilon = \varepsilon_i$, arrested crack tip structure at the same applied strain as in **a**; atoms in **b** are colored according to their energy difference ΔE_{pot} to the configuration shown in **a**; **c**: $\varepsilon = 1.1\varepsilon_i$, arrested crack tip structure; **d**-**g**: crack tip configurations at $K_I = K_{Ic}$-ΔK_I for different potentials. In case of the Chiesa potential, different crack tip structures exist under dynamic conditions: (i) the mobile structure shown in **a**, which is equal to the quasi-static structures of both the Chiesa and the Mendelev-II potentials, see **d** and **e**; (ii) the immobile structures shown in **b** and **c**, where either one or two characteristic pentagonal atomic arrangements are present at the crack tip (marked with dotted black lines); both immobile structures are similar to the sub-critical crack tip configurations of the Gordon and Chamati potentials in **f** and **g**, respectively; in case of immobile structures dislocation emission was observed at K_{Ic} whereas mobile structures led to purely brittle fracture under quasi-static loading conditions. The total energy difference between the mobile structure shown in **a** and the immobile structure in **b** is ΔE_{pot}^{tot} = -0.65 eV; this indicates that the immobile structure is the lower energy configuration for this situation. Red arrows: original crack tip atoms; yellow arrows: atoms at the arrested crack tip; unit of K_I: MPa$\sqrt{\text{m}}$.

loading, different crack tip structures result in qualitatively different fracture behaviors: whereas the Simonelli, Chamati, and Gordon potentials show dislocation emission from the initial crack tip at K_{Ic}, the Mendelev-II and Chiesa potentials exhibit brittle fracture, see Table 4.3 and Fig. 4.4d and f. This comparison explains why dislocation emission is observed only from arrested crack tips in case of the Chiesa potential. It further emphasizes the importance of the atomic-scale details at the crack tip for the final fracture behavior.

Gumbsch [161] reported on a related effect for dynamically propagating cracks in the $(1\,0\,0)[0\,0\,1]$ crack system in Ni, where even highly overloaded cracks showed comparably low terminal velocities of $v \approx 0.4c_R$. This was explained with the non-linearity of the atomic interactions, which strengthen in compression and weaken in tension. When freshly sepa-

rated atoms, which are then just behind the crack tip, impact into the surface, their neighbors are pushed with strong forces into the crystal. The resulting weak coupling to the crack tip atoms then reduces the velocity of information passing and could hence be responsible for the rather low terminal speed. In the present study, the occurrence of the arrested, immobile crack tip structure strongly depended on the interatomic potential. This finding further indicates that the crack arrest can be understood with the non-linearity of atomic interactions, which are defined by the interatomic potential. Gumbsch's explanation might thus equally apply here even though he did not observe the complete arrest of a formerly propagating crack as it happened in the present study. In this context, it is important to note that non-linear atomic interactions were also made responsible for dynamical instabilities during fracture in Si [160].

The energy difference of the immobile and mobile structures in Fig. 7.23a and b is $\Delta E_{\mathrm{pot}}^{\mathrm{tot}} = -0.65$ eV. This clearly shows that the immobile structure is the preferred configuration also for the Chiesa potential. The fact that this structure was not created during the initial energy minimization indicates that the energy barrier between the mobile and immobile structures must be higher in case of the Chiesa potential than for the Simonelli, Chamati, and Gordon potentials. At the tip of a propagating crack, however, the kinetic energy of the atoms is very high and it is therefore highly likely that this barrier can be overcome by thermal vibrations. Which of the two possible structures is present at a crack tip therefore not only depends on the details of the used interatomic potential, but can also be triggered by dynamic loading of the crack.

With the present EAM-type potentials it is, however, not possible to determine which of the two competing crack tip structures would occur in reality. To identify the 'true' crack tip structure, future studies are therefore needed with more accurate descriptions of the atomic interactions, e.g. by using BOPs or DFT calculations.

In summary, crack arrest in the {110}⟨110⟩ crack systems is explained with the dynamic formation of an 'immobile' structure at the crack tip, which often leads to dislocation emission in the following. It can be speculated that this inhibition of easy crack propagation on {110} planes leads to the experimentally observed preference of {100} cleavage [28].

7.5.2 Dislocation emission from propagating twins

One key process of the observed crack tip plasticity is the emission of dislocations from propagating deformation twins. This is of particular importance as dislocations were emitted directly from the crack tip only for the (110) and (111) cracks modeled with the Mendelev-II potential. In all remaining cases, dislocations were nucleated from growing twins that formed at the crack tip. The twins have a half-lenticular shape with main propagation direction parallel to the Burgers vector (edge orientation) and pointing away from the crack front. In this direction, $a_0/6\langle 111\rangle$ twinning dislocations can simply glide away from the crack front on adjacent $\{112\}$ planes whereby the twinned region grows. The twin segments that are attached to the crack front are in 'screw' orientation, i.e., they have a line

direction parallel to a ⟨111⟩ direction. Without exception, the emission of dislocations from growing twins took place from such ⟨111⟩-oriented segments. Similar observations were made by Alcalá *et al.* who performed MD simulations of nano-indentation in Ta and reported on dislocation emission from twins and subsequent twin annihilation [436].

Experimental observations of the emission of dislocations from deformation twins in Fe (containing 3 % Si) were first reported by Hull [437]. He explained the formation of a full dislocation at the twin tip by the combination of three twinning dislocations that cross-slipped on the same {110} plane:

$$a_0/6\langle 111\rangle_{\{112\}} + a_0/6\langle 111\rangle_{\{112\}} + a_0/6\langle 111\rangle_{\{112\}} \rightarrow a_0/2\langle 111\rangle_{\{110\}}. \tag{7.16}$$

Sleeswyk proposed an alternative, more comprehensive, model in which a $a_0/2\langle 111\rangle$ dislocation can be emitted by the following dissociation of every third twinning dislocation [438, 439]:

$$a_0/6\langle 111\rangle_{\{112\}} \rightarrow a_0/3\langle \bar{1}\bar{1}\bar{1}\rangle_{\{112\}} + a_0/2\langle 111\rangle_{\{112\}}. \tag{7.17}$$

Later, Mahajan reported on dislocations emitted from deformation twins in a Mo-35%Re alloy [440]. He concluded that Hull's model is more likely to occur than Sleeswyk's dissociation reaction because the former is "energetically less unfavorable" [440]. Even though the phenomenon of dislocation emission from twins has been known for over 50 years, there is still only little understanding of how and why it takes place. It is particularly unclear, which atomic-scale processes lead to dislocation emission and if they are consistent with one of the proposed models. Besides a mechanistic understanding of how the emission proceeds, it is also desirable to identify the underlying reasons.

To determine the relevant mechanisms at the twin tip, additional simulations were performed. The setup used for this purpose is shown in Fig. E.1 in the appendix. Here, dynamic NVE simulation were performed with the ATFS potential for W and different system sizes of cross sectional dimensions between 300×100 and 1200×400 Å^2 containing twins of four to eight layers; the shear rate was varied between $\dot{\tau} = \pm0.0783$ and ±15.7 MPa/ps. Unlike the setups for fracture simulations, the twin already exists *a priori* in this case and the applied loads can be controlled precisely. Differential displacement (DD) maps [441] are used to visualize the emission process, which takes place where the twin boundary is parallel to the Burgers vector of the twinning dislocations (TDs). With this visualization technique, the relative shift of two atoms perpendicular to the plane of paper is indicated by the arrows between them.

Fig. 7.24 compares the paths of the twinning dislocations that lead to stable twin growth and dislocation emission from the twin tip of a four-layer twin. Here, the cross sectional box size was 600×200 Å^2 and the applied shear was held constant at $\tau = \pm1.37$ GPa. Sequential snapshots of the two processes are presented in higher time resolution in Fig. E.2 in the appendix. Before and after stable twin growth, the two leading twinning dislocations are located at equivalent crystal sites, cf. Fig. 7.24a and b. The resulting $a_0/3[11\bar{1}]$ partial dislocation core dissociates on the inclined $(0\,1\,1)$ plane.

The process of stable twin growth is schematically shown in Fig. 7.24c. To propagate the twin by a distance of $a_0[\bar{1}10]$, the first two TDs take different paths to reach their next

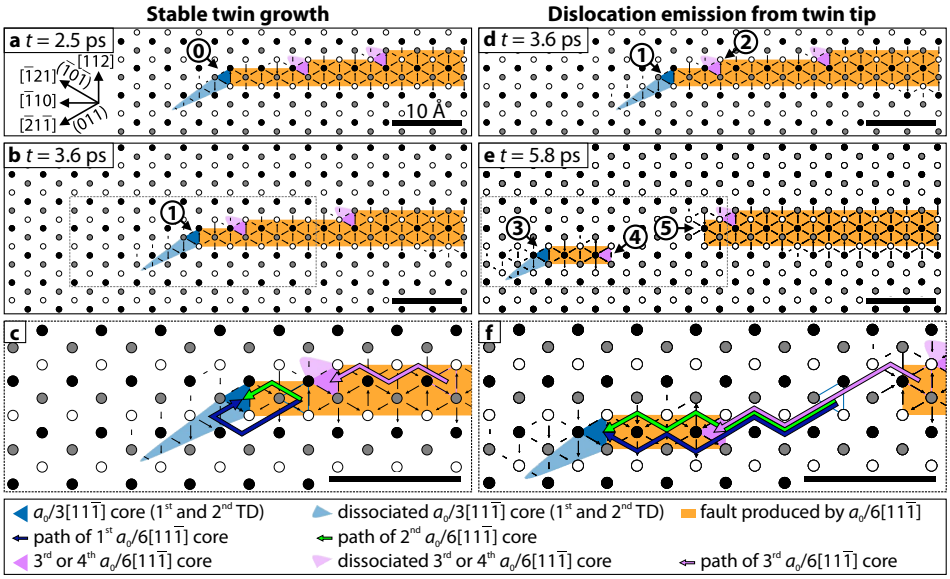

Figure 7.24: Differential displacement maps of stable twin growth and dislocation emission from a propagating deformation twin. ATFS potential for W; box size: 600×200 Å^2; $\tau = \pm 1.37$ GPa; the relative shift of two atoms perpendicular to the plane of paper, i.e., the $[11\bar{1}]$ direction, is indicated by the arrows between them; **a**: four-layer $[11\bar{1}](112)$ twin before propagation; the first and second twinning dislocations (TD) are initially located at the same position (⓪); this $a_0/3[11\bar{1}]$ core dissociates on the (011) plane; **b**: twin tip after propagation by a distance of $a_0[\bar{1}10]$ (①) **c**: magnification of the dashed region in **b** with schematic trajectories of the first three TDs during stable twin growth; **d**: twin tip configuration before dislocation emission; note that the third TD (②) is closer to the twin tip (①) as compared to the situation shown in **a**; **e**: twin tip and emitted dislocation; the former two leading TDs are now leading the emitted dislocation (③) while the third TD is trailing (④); this emission results in an immobile configuration at the twin tip (⑤); **f**: magnification of the dashed region in **e** with schematic trajectories of the first three TDs during dislocation emission.

position. At the same time, the third TD glides in a zig-zag fashion on the two-layer twin produced by the first two TDs. Compared to the necessary splitting, separated motion, and re-union of the first two TDs, the path of the third TD is comparably easy. As a result, the third TD propagates faster than the two leading TDs. This is visible by e.g., comparing Fig. 7.24a and b. The traveled net distance of the third TD was twice the glide distance of the two leading TDs. For all above mentioned variations of box size, loading rate, and twin thickness, the third TD propagated faster than the leading two TDs, which showed constant average velocities in the range of 5.1±0.6 Å/ps, see Table E.1 in the appendix. The higher velocity of a TD on an existing twin can be qualitatively understood by the relatively small additional energy that is needed to further increase the number of twin layers once a twin nucleus exists, cf. Fig. 7.1e and the DFT calculations for Mo by Ogata *et al.* [442].

The higher velocity of the third TD leads to the configuration shown in Fig. 7.24d. The third TD has nearly reached the twin tip. In the following, the two leading TDs both slip on the same $(0\,1\,1)$ plane thereby producing a $a_0/3[11\bar{1}](0\,1\,1)$ fault. To overcome this unfavorable state, cf. Fig. 7.1c, the third TD follows the leading TDs to complete the slip by $a_0/2[11\bar{1}]$ on the $(0\,1\,1)$ plane. Thus, the third TD has become the trailing partial dislocation of the emitted $a_0/2[11\bar{1}]$ dislocation and the region between the third TD and the twin tip returns to the perfect stacking sequence. Fig. 7.24e shows the final state of this process. The corresponding paths of the TDs are indicated in subfigure f.

Although the used EAM-type potentials might not fully represent the precise characteristics of twin growth in bcc metals, the identified key process of cross-slipping screw-oriented twinning partial dislocations can be expected to occur also in reality. The process itself is only linked to the crystallography of the bcc structure and has been rationalized before [437]. The different velocities of the twin tip and the third twinning dislocation, on the other hand, might additionally depend on the material and its chemical composition; in general, they should, however, follow the trend suggested by the calculated energy barriers, see Ref. [442] for DFT calculations and Fig. 7.1c for EAM simulations. The fact, that the observation of dislocation emission from twin tips was observed independent of material and simulation setup, cf. Ref. [436] for nano-indentation in Ta and Ref. [201] for penny-shaped cracks in Fe and W, and interatomic potential, cf. Fig. 4.3 for two different Fe potentials, further strengthens the assumption that it is not a simulation artifact. It is therefore expected that the identified process for dislocation emission from twin tips can occur also in real materials.

In summary, the presented simulations indicate that dislocation emission from twins is caused by cross-slipping twinning dislocations on a common slip plane, in agreement with the model proposed by Hull [437] and the energetic considerations of Mahajan [440]. Possible consequences of the twin growth instability are (i) that the immobile configurations, which remain after dislocation emission, might act as preferred crack nucleation sites due to high coherency stresses between the twin and the surrounding matrix; and (ii) that twins are only able to carry comparable small amounts of plastic deformation in bcc crystals thereby favoring their overall brittle response [443].

7.6 Influence of simulation parameters

The influences of several simulation-related parameters on the fracture behavior and critical strains were presented in section 4.2 for the $(1\,1\,0)[1\bar{1}\,0]$ crack system modeled with the Chiesa potential for Fe. The influences of the crack length and the interatomic potential, were discussed in sections 7.1.4 and 7.1.5. Loading conditions, crack tip sharpness, box size, and aspect ratio have only minor influence or can be understood by theories, cf. e.g. Eq. (3.3) for the box size dependence. The focus is therefore on the remaining parameters, i.e., the effect of simulation setup, strain rate, and lateral straining.

Setup geometry

Although the simulation setup did neither influence the fracture behavior nor the critical strain in case of the strain-controlled setups, the precise mechanisms of crack tip plasticity, however, were different as the comparison between the quasi-2D and 3D edge crack in Fig. 4.6 shows: in case of the quasi-2D edge crack a straight dislocation is nucleated with a dislocation line parallel to the crack front; when the box dimension in crack front direction becomes larger, as for the 3D edge crack, dislocation emission takes place by the nucleation of dislocation half loops and their subsequent coalescence to an almost straight dislocation. The nucleation of such dislocation half loops prior to the formation of straight dislocations was shown to be energetically favorable compared to the immediate formation of a straight dislocation [62]. In case of the quasi-2D edge crack, the formation of dislocation half loops is prohibited by the small box dimension and the use of PBCs in crack front direction. To investigate the exact details of crack tip plasticity, it is therefore necessary to use 3D setups since important crack tip mechanisms might remain unrevealed if quasi-2D setups are used.

Strain rate

The influence of the applied strain rate $\dot{\varepsilon}$ on the fracture behavior and initiation strain ε_i is plotted in Fig. 4.9b for $\dot{\varepsilon} = 10^6$ to 10^9 s^{-1}. While the initial fracture process was brittle bond breaking for all investigated strain rates, the initiation strain was similar to the quasi-static fracture strain $\varepsilon_\mathrm{c} = 2.47$ % only until $\dot{\varepsilon} = 10^8$ s^{-1}. At $\dot{\varepsilon} = 10^9$ s^{-1}, the critical strain increased to $\varepsilon_\mathrm{i} = 2.70$ %.

Fig. 7.25 compares the bond length directly at the crack tip in dependence on the applied strain for three different strain rates. The linearly extrapolated crack tip bond distance at ε_in and the corresponding data points in case of quasi-static loading are plotted for comparison. It can be clearly seen that the quasi-statically determined crack tip bond distances increase with a higher slope than the linear extrapolation. The reason for this behavior is that the atomic strain increments are homogeneously distributed in a configuration containing a highly *inhomogeneous* deformation state: only the uncracked part of the system behaves similar to a homogeneously strained body, but not the already cracked part. Large regions in this part are thus mainly strain free and behave similar to rigidly separated bodies upon straining. At the crack tip, these two different parts meet each other leading to a highly localized and complex strain state. The real displacements per strain increment are thus much higher than predicted by linear scaling. Particularly near $\varepsilon = \varepsilon_\mathrm{i}$ non-linearity effects play a role as it can be clearly seen in the figure. The bond distances in case of $\dot{\varepsilon} = 10^7$ and 10^8 s^{-1} oscillate around the quasi-static reference and therefore lead to the same critical strain. In case of $\dot{\varepsilon} = 10^9$ s^{-1}, on the other hand, the system has not enough time to adjust the atomic positions properly and the bond distance starts to follow the linear scaling function for rather long time. Only at higher strains, the deviation from the linear scaling becomes more pronounced, but is still too small to result in the same critical strain as determined by quasi-static loading as well as by using lower strain rates. It is therefore concluded, that the

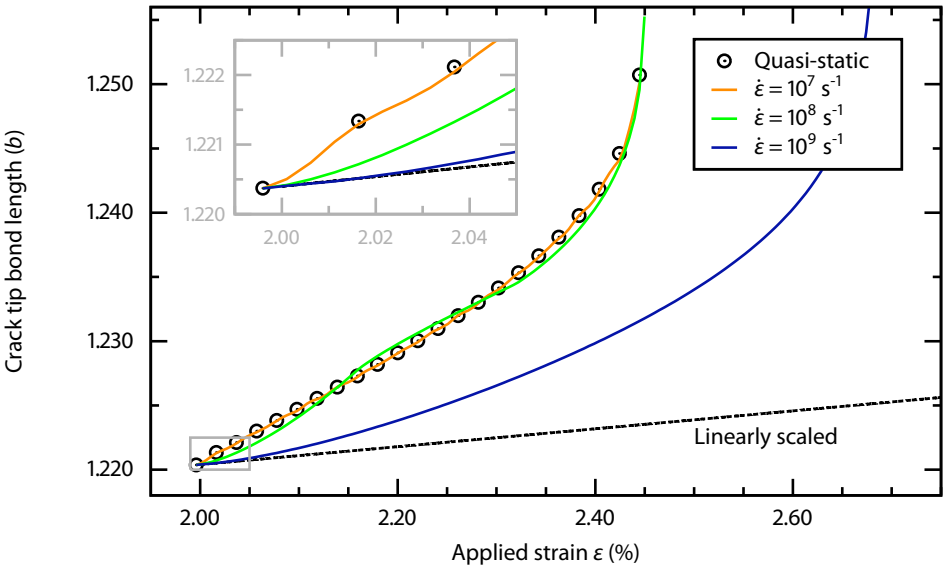

Figure 7.25: Comparison of crack tip bond distances for different strain rates $\dot{\varepsilon}$ and quasi-static loading; box dimensions: L_x = 3000 Å, L_y = 1000 Å; length of the edge crack: a = 1000 Å; the critical strains are $\varepsilon_c = \varepsilon_i = (2.46 \pm 0.01)$ % for $\dot{\varepsilon} = 10^7$ s^{-1} and 10^8 s^{-1} and $\varepsilon_i = 2.70$ % for $\dot{\varepsilon} = 10^9$ s^{-1}; the dashed line indicates the extrapolation of the bond distance by linear scaling of the initial distance at ε_{in}.

homogeneous scaling of an inhomogeneously deformed configuration causes the increase of ε_i for strain rates $\dot{\varepsilon} > 10^8$ s^{-1}.

The magnitude of the mismatch between the applied homogeneous deformation and the heterogeneous strain and stress distribution in the body generally depends on the specific setup geometry. In case of an edge crack, for instance, the highest mismatch will occur where the crack face meets the box boundaries. Here, the applied displacement, $u_y = \dot{\varepsilon}\Delta t y$, will cause the lower surface to move upwards and the upper surface to move downwards with respect to the new box length $L_y = (1 + \dot{\varepsilon}\Delta t)L_y$; to recover its previous (and correct) stress-free state, the applied deformation has to be undone. With a box size of L_y = 1000 Å, the mismatch u_y during 1 ps of deformation will be in the range of 0.05 Å for $\dot{\varepsilon} = 10^8$ s^{-1} and around 0.5 Å for $\dot{\varepsilon} = 10^9$ s^{-1}. The time spent to regain the stress-free state would on principle scale with $L_y/(2c_l)$ with c_l being the longitudinal wave speed, see Eq. (2.9). At the same time, the information about this mismatch would need to be transferred to the crack tip by a surface wave propagating along the crack face. The time spent for this process should generally scale with a/c_R with c_R being the Rayleigh wave speed, Eq. (2.11). The difference between ε_i and ε_c would therefore be linked to a combination of these effects:

$$\varepsilon_i - \varepsilon_c = (t_y + t_a)\dot{\varepsilon} = \left(f_y \frac{L_y}{2c_l} + f_a \frac{a}{c_R}\right)\dot{\varepsilon}, \tag{7.18}$$

with f_y and f_a being unknown factors describing the interplay of the decaying oscillations in y direction and between surface waves originated at different locations along the crack face. By comparing the different critical strains for varying L_y, a, and $\dot{\varepsilon}$ in Table 4.3, it can be seen that this assumption is qualitatively rational: the difference between ε_i and the quasi-static reference ε_c increased with increasing crack length, box size, and strain rate. In other words, the strain rate needs to decrease if the box length L_y increases to ensure that ε_i is not affected by the strain rate.

The given explanation, however, does not provide a quantitative prediction, which would require a broader parametric study in the future; in such a study, the temperature and the interatomic potential should be additionally varied to include or exclude further influencing factors.

Method of lateral straining

The influence of different methods to take into account lateral straining was tested for the quasi-2D edge crack with sample dimensions L_x = 3000 Å, L_y = 1000 Å, and crack length a = 1000 Å. The corresponding simulation results are plotted in Fig. 4.9d. The lateral straining method has a marked influence on the sample-dependent predicted fracture strain ε_0 as well as the determined critical strains ε_c (quasi-static loading) and ε_i (dynamic loading). These values are highest using the ε^{pre} method while the ε^{zero} method causes the lowest values.

The influence of the lateral straining on the theoretical fracture strain ε_0 can be seen by comparing the corresponding energy-strain dependencies that are used to define ε_0, cf. Eq. (3.4) in section 3.3. The different curves are plotted in Fig. 7.26 for the ε^{zero}, σ^{min}, and ε^{pre} methods. The potential energies E_{pot} of the configurations at different strains ε were used to calculate the corresponding energy release rates G, as follows:

$$G(\varepsilon) = \frac{\sum_{i=0}^{N} E_{pot}(\varepsilon) - \sum_{i=0}^{N} E_{pot}(\varepsilon = 0)}{L_x L_z} \tag{7.19}$$

where N is the number of atoms in the configuration. The theoretical threshold strain ε_0 is then defined as the intersection of the $G(\varepsilon)$-ε curves of 'uncut' and 'cut' configurations, cf. Eq. (3.4).

In all cases, the determined G curves are proportional to ε^2 meaning that the acting stresses increase linearly with the applied strains. Since the lateral box sizes are not adjusted if the ε^{zero} method is used, the increasing strains generate lateral stresses in the system. This results in a stronger increase in the energy of the 'uncut' configuration than for the other two methods. Both the σ^{min} and the ε^{pre} methods aim to reduce the lateral stresses. In the present case, the $G(\varepsilon)$-ε curves of both methods lie on top of each other. It is important to note that this observation has not to be true in general. If and how strong they differ depends on the (non-)linear elastic response of the potential. The Chiesa potential used in this study shows nearly perfect linear-elastic behavior up to applied strains ε = 3 %. As a result, the difference in the $G(\varepsilon)$-ε of the 'uncut' configurations is marginal.

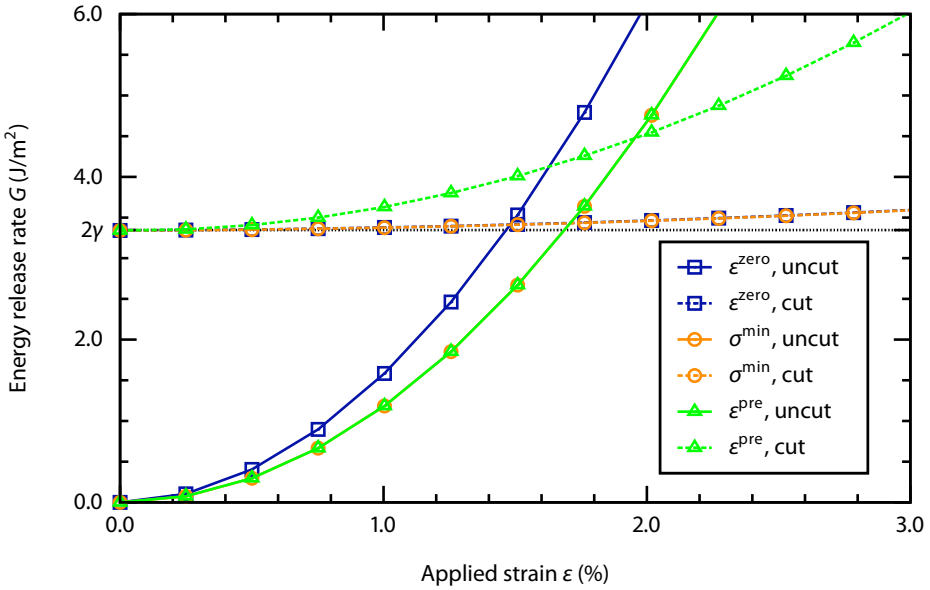

Figure 7.26: Plot of energy release rate G over applied strain for different methods of lateral straining in the quasi-2D edge crack setup. $G=[E_{pot}(\varepsilon)-E_{pot}(\varepsilon=0)]/(L_xL_z)$, where E_{pot} is the sum of the potential energy of all atoms in the configuration; the strain-independent surface energy is indicated by the dotted line for comparison; the 'cut' samples model configurations after the crack has virtually propagated through the whole system; the theoretical threshold strain ε_0 is defined as the intersection of the curves of 'cut' and 'uncut' samples, cf. Eq. (3.4) in section 3.3.

All 'cut' configurations, which model the situation after the crack virtually propagated through the whole system, start at the Griffith value, i.e., $G = 2\gamma$. As the applied strain increases, the energy release rate increases only slightly for the ε^{zero} and σ^{min} methods. In both cases, the two separated parts of the configuration are mainly stress free and only the fixed displacements in the boundary regions contribute to the small energy increase. In contrast, the energy increase is rather high when using the ε^{pre} method. In this case, the lateral box sizes of the 'cut' configuration are equally adjusted as for the 'uncut' configuration. Since the strain in y direction is zero for the 'cut' configurations, this results in high lateral stresses.

When the predicted ε_0 values are compared to the determined critical strains ε_c, it is striking that the ε^{zero} and ε^{pre} methods exhibit the same relative value of $\varepsilon_c = 1.26\varepsilon_0$. In both cases, the lateral strains at a given strain ε are the same for the 'cut' and 'uncut' configurations as well as for the configuration containing the crack: $\varepsilon_{xx} = \varepsilon_{zz} = 0$ for the ε^{zero} method; $\varepsilon_{xx} = \nu_{xy}\varepsilon_{yy}$ and $\varepsilon_{zz} = \nu_{zy}\varepsilon_{yy}$ for the ε^{pre} method. The σ^{min} method, on the other hand, adjusts the lateral box sizes to minimize the lateral stresses for each configuration separately. As a result, the energies of configurations under completely different conditions are compared to determine ε_0. This method results inevitably in the worst predictability of ε_c ($\varepsilon_c = 1.32\varepsilon_0$).

Fig. 7.27 compares the crack tip stress fields for the three different methods. It can clearly be seen that the zones of $\sigma_{yy} > 8$ GPa and $\sigma_{zz} > 2$ GPa are largest in case of the ε^{zero} method and smallest for the ε^{pre} method. It is not surprising that this observation is inverse proportional to the ordering of the determined critical strains, which are lowest for the ε^{zero} ($\varepsilon_c = 1.86$ %) and highest for the ε^{pre} method ($\varepsilon_c = 2.47$ %). In case of the σ^{min} method, ε_c is 2.26 %. This large difference shows that the method of lateral straining has by far the highest influence on the critical strains in the crack-length-independent regime. It further shows that the ε^{pre} method produces the highest critical strains. Furthermore, with the ε^{pre} method the critical strains are slightly higher than predicted by $\varepsilon_{p,large}(K_{Ic})$, cf. Eq. (7.6) in section 7.1.4, which is explained by the presence of higher-order terms in the crack tip stress field. This shows that the other methods cause artificially high stress levels at the crack tip leading to lower critical strains when compared to the K-controlled setup. For reasons of comparability between the different setups, the ε^{pre} method should therefore be used.

As mentioned before, it should be kept in mind that the accuracy of the ε^{pre} method strongly correlates with the (non-)linear elastic behavior of the used interatomic potential. With this method the change in the lateral box sizes is prescribed by fixed Poisson ratios ν_{xy} and ν_{zy}. The calculation of ν_{xy} and ν_{zy} is done under the assumption of linear-elastic

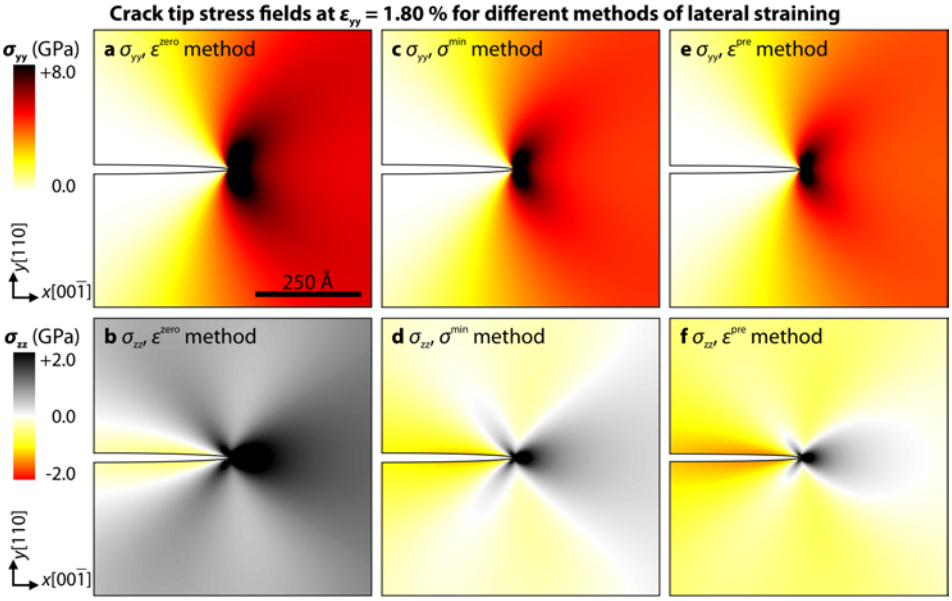

Figure 7.27: Comparison of crack tip stress fields at $\varepsilon = 1.80$ % for different methods of lateral straining in the quasi-2D edge crack setup. **a,c,e**: σ_{yy} stresses in crack plane normal direction; **b,d,f**: σ_{zz} stresses in crack front direction. Both σ_{yy} and σ_{zz} stresses are highest using the ε^{zero} method (**a** and **b**) and lowest for the ε^{pre} method (**e**,**f**); the stresses in case of the σ^{min} methods (**c**,**d**) lie between both extrema.

behavior. The stress-strain relationships of many potentials, however, deviate from linear elastic behavior at higher strains. In such cases, additional σ_{xx} and σ_{zz} stresses might evolve at higher strains resulting in lower critical strains than predicted by e.g. $\varepsilon_{p,large}(K_{Ic})$, cf. Eq. (7.6). This issue can be overcome when the strain-dependence of the Poisson ratios is determined beforehand in a perfect bulk crystal. In this manner, the lateral strains can then be prescribed as functions of the applied strain during the fracture simulation.

Best practices for atomistic fracture simulations

The systematic variation of several simulation parameters finally allows to suggest a number of best practices for future atomistic simulations of fracture. The recommended simulation setup strongly depends on the focus of study and the scientific question to be addressed. For this reason, simulation parameters, typical box sizes, and crack lengths, as well as estimates for the conversion of the corresponding critical values are given in Table 7.5. Similarly, an effect of the crack length should be most likely excluded if a is larger than $0.4L_x$. At the same time, the crack length should not be too large to prevent interaction with the boundaries, i.e., below $L_x/4$ for central and penny-shaped cracks and below $L_x/2$ for edge cracks As discussed before, the effect of the strain rate will generally increase with larger crack lengths and larger box sizes.

The independence of the results from box size, crack length, and strain rate should, however, always be tested in any atomistic study; more actionable recommendations are, on the other hand, the suggested boundary conditions, lateral straining methods, and loading conditions.

In the future, concurrent multi-scale simulations of fracture, i.e., by coupling atomistic and FE methods, see e.g. Refs. [198, 199], will become increasingly important. Such simulation techniques will allow to drastically decrease the necessary level of applied strains; it will therefore be possible to study crack propagation under more realistic conditions as currently reached with purely atomistic methods.

Table 7.5: Overview of setups for different focuses of fracture studies. t_b: propagation time of an elastic wave emitted at the crack tip to reach the boundaries, see Eq. (2.12); c_l: longitudinal wave speed, see Eq. (2.9); c_R: Rayleigh surface wave speed, see Eq. (2.11); K_{Ic}^*: critical stress intensity factor as determined from strain-controlled simulations (always slightly affected by higher-order terms due to effects from the small box size and boundary conditions); E_y: sample-dependent elastic modulus in crack plane normal direction; parentheses indicate less practicable loading conditions or alternative lateral strain methods (if the suggested method is not applicable). The suggested crack lengths are chosen such that the determined critical strains can be predicted using the corresponding equations for ε_p.

Focus of study	Fracture toughness, fracture behavior	2D crack propagation, fracture behavior	Crack tip plasticity, 3D crack propagation, crack-defect interactions	Crack curvature effects
Geometry	*K*-controlled crack	Qu.-2D edge/central crack	3D edge crack	Penny-shaped crack
	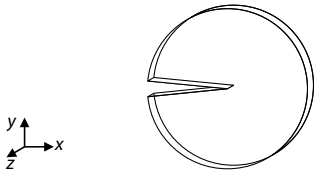	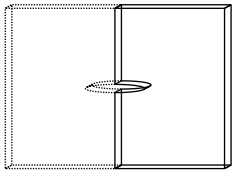	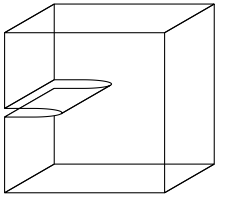	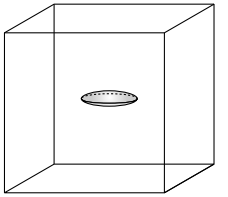
Box size	$R \approx 50a_0$	$L_y \approx 2/3L_x > 2c_l t_b$ (edge) $L_y \approx 1/3L_x > 2c_l b_p$ (central)	$L_x \approx L_y \approx L_z > 2c_l t_b$	$L_x \approx L_y \approx L_z > 2c_l t_b$
Boundary conditions	fixed	*y*: fixed in *y* *x*: fixed in *x* (edge) *x*: fixed in *xy* (central)	*y*: fixed in *y* *x*: fixed in *x*	fixed
Crack length/radius	—	$a > L_y/2$	$a > 0.4L_x$	$a < L_x/4$
Lateral straining	—	ε^{pre} (ε^{zero})	ε^{pre} (ε^{zero})	ε^{pre} (ε^{zero})
Loading conditions	quasi-static	quasi-static or dynamic	dynamic (quasi-static)	dynamic (quasi-static)
Predicted critical strain	—	$\varepsilon_p = \sqrt{L_y/2}K_{Ic}/E_y$	$\varepsilon_p = \sqrt{L_y/2}K_{Ic}/E_y$	$\varepsilon_p = K_{Ic}/(2E_y)\sqrt{\pi/a}$
Critical conditions	K_{Ic}	$K_{Ic}^* \approx \sqrt{L_y/2}\varepsilon_{c/i}E_y$	$K_{Ic}^* \approx \sqrt{L_y/2}\varepsilon_{c/i}E_y$	$K_{Ic}^* \approx 2\varepsilon_{c/i}E_y\sqrt{a/\pi}$

8 Summary

The objective of this thesis was to obtain a better understanding of crack-microstructure interactions at the atomic scale and to lay the foundations for the development of new microstructure-sensitive meso-scale models for bcc-based materials that include important crack-defect interactions. For this purpose, I first determined the fracture properties of perfectly straight cracks in defect-free bcc single crystals to obtain a reference data set. Thereafter, the effects of crack front curvature, grain boundary structure, and pre-existing dislocations were studied for selected single crystal and bicrystal configurations in the bcc metals Fe and W. This systematic approach allowed to address the key questions raised in section 2.5:

What is the general influence of crack front curvature on the competition between brittle fracture and crack tip plasticity? This question was investigated in the first systematic study of penny-shaped cracks in Fe and W by means of large-scale molecular dynamics and statics simulations. Based on the presented simulation results, the following statements can be made:

- As a result of the higher number of possible slip systems, curved crack fronts exhibited a generally higher tendency for crack tip plasticity than perfectly straight cracks. This finding is expected to be particularly relevant for small freshly nucleated cracks or long cracks, that locally exhibit a certain degree of curvature, e.g., due to crack pinning at obstacles. The overall ductile response was often correctly predicted by theory if the criteria for twin formation and dislocation emission were evaluated for all possible crack front orientations.

- For small cracks, crack tip plasticity was facilitated by the decrease of the criteria for twin formation and dislocation emission due to the effects of T-stress and tension-shear coupling [411]. Both effects were increased—but not solely caused—by the high strains in the small atomistic configurations; it is therefore expected that they are also important for the fracture criteria of cracks under realistic conditions, i.e., if the crack and specimen sizes are small and the crack tip stresses are in the range of the theoretical strength.

- The growth of deformation twins was often limited by the emission of dislocations from the incoherent twin boundaries oriented in $\langle 111 \rangle$ directions, which has been observed before in experiments [437]; the corresponding process was identified here as correlated cross slip of three twinning partial dislocations onto a common $\{110\}$ plane. The underlying reason, i.e., the different velocities of the twin tip and the third twinning partial dislocation, is expected to be mainly caused by the crystal structure and might therefore occur similarly in nature.

How do locally different bonding situations influence the propagation behavior of grain boundary cracks? To address this question, various tilt grain boundaries in Fe and W were studied in different simulation setups under variation of the misorientation, plane, and symmetry of the grain boundary. In summary, a number of statements can be made, which are mainly caused by the atomic (discrete) nature of grain boundaries and should therefore be relevant for grain boundary fracture in brittle and semi-brittle materials:

- Locally varying bonding situations in GBs lead to the dependence of the fracture resistance on the precise crack tip position and its extension direction. In our simulations, the ultimate fracture toughness of straight GB cracks is therefore mainly determined by the highest bond strength within the GB. As a result, the critical stress intensity factor of GBs was frequently higher than predicted by the thermodynamic Griffith theory; for symmetrical GBs, it can even exceed the fracture resistance of single crystals in the same crystallographic orientation. In reality, it is expected that these strongest propagation barriers can, however, be overcome by thermally activated processes, such as crack front kink propagation.

- The simulations further indicate that bond trapping of curved cracks at GBs could be higher than for straight cracks, which might be either an effect of crack line tension or of the multitude of different, possibly stronger, bonding situations along a curved crack front. Nevertheless, it is generally expected that the bond trapping barrier in case of dynamic loading, thermal activation, or defective crack fronts should be lower than for perfectly straight GB cracks.

- The asymmetric orientation between crack propagation direction and possible slip planes led to direction-dependent fracture behavior of GB cracks, i.e., brittle propagation in one direction and crack tip plasticity in the opposite. Whereas this was already observed in experiments [93] and atomistic simulations [156] for straight cracks in fcc Cu, the presented simulations further indicated that small, circular cracks might also show such a behavior if (i) the corresponding fracture criteria are almost equal; or if (ii) the crack radius is large enough to prevent the crack tip from being blunted by cross slipping dislocations that were nucleated at other parts of the curved crack front.

How do cracks interact with pre-existing dislocations? This question was studied by exemplary simulations of crack-dislocation interactions in bcc Fe in selected single crystal and bicrystal configurations. Although future studies on this topic are needed to further elucidate the role of pre-existing dislocations, the following statements can already be made:

- Crack interactions with pre-existing dislocations frequently led to mixed-mode conditions caused by the interaction of the crack-tip and dislocation stress fields. Not only can this result in lower fracture criteria [199], but also in increased resolved shear stresses on inclined slip planes thereby favoring the emission of dislocations as compared to the dislocation-free scenarios.

- If the dislocations glide on oblique slip planes with respect to the crack plane, their direct interaction with the crack front was observed to cause local crack tip blunting. Under such conditions, stimulated dislocation emission, which was seen before in experiments in Si [318, 319] and atomistic simulations in fcc Ni [155, 214], was observed here for the first time in a bcc crystal.

- The sign of the Burgers vector determined whether absorbed (edge) dislocations had either a marginal effect on the driving force for brittle propagation of GB cracks or if they markedly slowed down the crack velocity. It can be speculated that if, for instance, cracks and dislocations both originate from the specimen surface under cyclic loading conditions, dislocations nucleated under compression will not significantly alter the growth behavior; dislocations nucleated under tension, however, could have a beneficial effect on the fracture resistance of the GB.

Furthermore, recommendations were given for specific bcc potentials, which can on principle be used for fracture studies. It was found that simpler potentials based on the classical Finnis-Sinclair (FS) potentials [307] are generally better adapted for atomistic fracture simulations than many recent potentials. A semi-empirical equation was derived to estimate the potential-dependent lattice trapping ratio based on the characteristics of its effective force function; this equation can be directly used for the development of new potentials, which come closer to the experimentally observed fracture properties.

The occurrence of planar faults on $\{1\,1\,0\}$ planes, which caused crack kinking from $\{1\,0\,0\}$ onto $\{1\,1\,0\}$ planes, was shown to be a result of local minima in the generalized stacking fault energy (γ) surface [61] of $\{1\,1\,0\}$ planes under applied tensile strains for many EAM-type potentials. As such minima are not predicted by DFT calculations, it was suggested that their occurrence is used as exclusion criterion during the development of new bcc potentials.

In addition, a novel technique for analyzing bcc crystal structures was introduced, which enables the unambiguous identification of the most common lattice defects in this crystal structure; finally, a number of best practices was provided for future studies of fracture by means of atomistic simulations.

9 Outlook

In the future, atomistic simulations will become increasingly important for the development of fully 3D micostructure-sensitive meso-scale models for fracture in metallic polycrystals. Large-scale molecular dynamics and statics simulations of cracks-microstructure interactions are, however, still in their infancy. This thesis represents only a first step towards a better understanding of a number of aspects relevant in this context, i.e., the effects of crack front curvature, grain boundary structure, and pre-existing dislocations. Some of the conclusions, e.g., the higher tendency for plasticity at curved crack fronts or the direction dependence of GB cracks, could on principle directly be used to improve current meso-scale models. Other observations should be investigated in more detail to provide actionable information for larger-scale models. Some ideas for future research activities are listed in the following.

The effect of crack front curvature should be further investigated using 'toy' potentials with tuned lattice trapping ratios; this allows to systematically address the question how the lattice trapping ratio of straight cracks influences the lattice trapping effect in case of curved cracks. In the context of crack tip plasticity at curved crack fronts, it is particularly interesting how and if nucleated dislocations can slip along the curved crack front in fcc metals, where cross slip is generally less favorable. The higher tendency for crack tip plasticity at curved crack fronts could be investigated experimentally by producing cracks with different degrees of curvature with the focused ion beam (FIB) technique; the produced cracks could then be loaded in a micro-cantilever beam setting to determine the curvature-dependent fracture toughness. It would be further interesting to investigate the effect of locally curved crack front segments in an otherwise straight cleavage crack. Can the dislocations generated at the curved segments reach the straight and 'brittle' parts? If so, does this result in a higher fracture toughness due to massive crack tip blunting?

Studies on crack-microstructure interactions should focus on the general influence of defects, e.g, steps, GB curvature, voids, and secondary phases, on the propagation behavior of GB cracks. Determining the barrier effect of certain GBs, on the other hand, can always be only of exemplary nature as the parameter space of possible GBs is simply too large. Furthermore, the interaction of pre-existing dislocations with cracks in cleavage systems of bcc metals should be studied more systematically, i.e., under variation of the Burgers vector, line direction, and initial distance to the crack tip, as well as for propagating cracks. Can the crack tip blunting by cross-slipped screw dislocations effectively stop the crack growth? In this context, the interaction with several other material defects, e.g, voids, impurity atoms, phase boundaries, and particles, might also be interesting. For comparison with experiments, the FIB technique could be used to insert cracks with different extension directions in one well-defined GB. The importance of cross slip for crack tip blunting in

bcc metals could be studied experimentally by *in situ* TEM studies on dislocation motion in pre-notched foils.

Developing more reliable interatomic potentials, particularly for bcc metals, is crucially important for better comparability with experiments. First of all, future potentials for fracture in bcc metals should not exhibit local minima in the strain-dependent $\gamma\{1\,1\,0\}$ surface; they should further be of relatively simple functional form and have a minimal difference between the $\{1\,0\,0\}$ and $\{1\,1\,0\}$ surface energies (as predicted by DFT calculations).

Appendix

A Slip systems for selected cracks

Table A.1: Overview of (110) and (112) slip systems available for dislocation emission in selected crack systems; θ: angle between slip and crack plane, φ: angle between the slip direction and the vector normal to the crack front in the slip plane, see Fig. 2.1a.

Crack plane	Crack front	Slip plane(s)	Slip direction(s)	θ (°)	φ (°)
(100)	[001]	±(110)	± $[1\bar{1}1]$ and ± $[1\bar{1}\bar{1}]$	45	± 35.26
		±(1$\bar{1}$0)	± [111] and ± $[11\bar{1}]$	-45	± 35.26
	[011]	± (0$\bar{1}$1)	± [111] and ± $[\bar{1}11]$	± 90	± 54.74
		± (2$\bar{1}$1) or ± (21$\bar{1}$)	± $[11\bar{1}]$ or ± $[\bar{1}1\bar{1}]$	± 35.26	0
(110)	[001]	± (1$\bar{1}$0)	± [111] and ± $[11\bar{1}]$	± 90	± 35.26
	$[1\bar{1}0]$	±(112) or ± (11$\bar{2}$)	± $[11\bar{1}]$ or ± [111]	± 54.74	± 0
	$[1\bar{1}1]$	±(10$\bar{1}$) or ±(011)	± [111] or ± $[1\bar{1}1]$	± 60	± 19.47
		±(10$\bar{1}$) or ±(011)	± $[1\bar{1}1]$	± 60	± 90
		±(1$\bar{1}$2)	± $[\bar{1}11]$	± 90	± 90
		±(121) or ±(21$\bar{1}$)	± $[\bar{1}1\bar{1}]$	± 30	± 90
(111)	$[1\bar{1}0]$	±(110)	± $[1\bar{1}1]$ and ± $[1\bar{1}\bar{1}]$	35.26	± 54.74
		±(112)	± $[11\bar{1}]$	19.47	0
		±(11$\bar{2}$)	± [111]	± 90	0
	$[11\bar{2}]$	±(1$\bar{1}$0)	± [111]	± 90	0
			± $[11\bar{1}]$	± 90	± 70.53
(112)	$[1\bar{1}0]$	(11$\bar{2}$)	±[111]	-70.53	0
	$[11\bar{1}]$	±(1$\bar{1}$0)	±[111]	90	-19.47

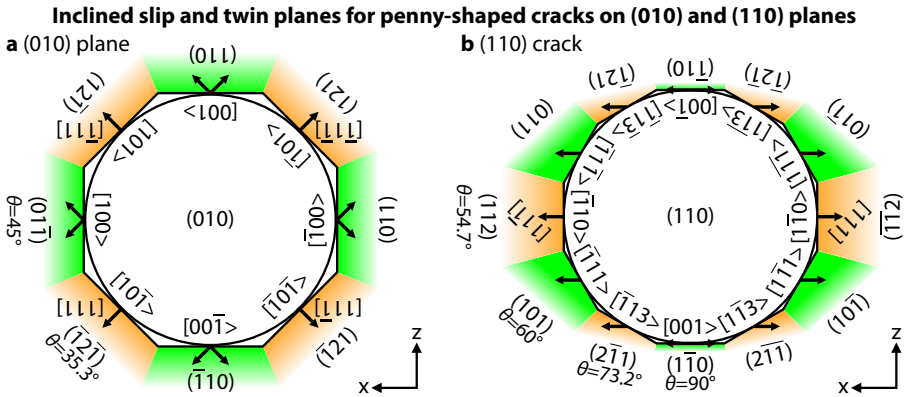

Figure A.1: Possible inclined {110} slip (green) and {112} twin planes (orange), which contain local crack front segments. **a**: (010) plane; **b**: (110) plane; black arrows: possible Burgers vectors; colored slip plane areas are inversely proportional to their inclination angle θ.

B Twinning tendency T for bcc metals

According to Eq. (30) in Ref. [323], the so-called normalized nucleation load for fcc metals λ_{crit} can be written as:

$$\lambda_{\mathrm{crit}} = \frac{(\eta - r)\kappa + \eta\sqrt{\kappa^2 + gr(2\eta - r)}}{r(2\eta - r)}, \tag{B.1}$$

where $g = \gamma_{\mathrm{sf}}/\gamma_{\mathrm{usf}}$ is the ratio between stable and unstable stacking fault energy and κ is the ratio between the stress intensity factors for nucleation of the trailing partial B and leading partial dislocation A, K^*_{Bcrit} and K_{Acrit}, respectively. For fcc materials, r, η, and κ depend on the angles ϕ_{A} and ϕ_{B}, which characterize the inclination of the leading partial and the trailing partial dislocation with respect to the crack front normal in the slip plane. Unlike in fcc, different partial (twinning) dislocations have equal Burgers vectors in bcc metals and the angle-dependent terms r, η, and κ evolve, as follows:

$$r = \frac{\cos(\phi_{\mathrm{B}} - \alpha)}{\cos(\phi_{\mathrm{A}} - \alpha)} = 1 \tag{B.2}$$

$$\eta = \frac{\cos\phi_{\mathrm{A}}\cos\phi_{\mathrm{B}} + (1-\nu)\sin\phi_{\mathrm{A}}\sin\phi_{\mathrm{B}}}{\cos^2\phi_{\mathrm{A}} + (1-\nu)\sin^2\phi_{\mathrm{A}}} = 1 \tag{B.3}$$

$$\kappa = \sqrt{\frac{2\mu/(1-\nu)\left[\cos^2\phi_{\mathrm{B}} + (1-\nu)\sin^2\phi_{\mathrm{B}}\right](\gamma_{\mathrm{usf}} - \gamma_{\mathrm{sf}})}{2\mu/(1-\nu)\left[\cos^2\phi_{\mathrm{A}} + (1-\nu)\sin^2\phi_{\mathrm{A}}\right]\gamma_{\mathrm{usf}}}} = \sqrt{\frac{\gamma_{\mathrm{usf}} - \gamma_{\mathrm{sf}}}{\gamma_{\mathrm{usf}}}}, \tag{B.4}$$

where α characterizes the inclination angle of an external mixed-mode stress intensity factor K within the slip plane ($\alpha = 0$ for pure mode-I loading).

With this, Eq. (B.1) can be rewritten as:

$$\lambda_{\mathrm{crit}} = \sqrt{\kappa + g} = \sqrt{\frac{\gamma_{\mathrm{usf}} - \gamma_{\mathrm{sf}}}{\gamma_{\mathrm{usf}}} + \frac{\gamma_{\mathrm{sf}}}{\gamma_{\mathrm{usf}}}} = 1 \tag{B.5}$$

and the twinning tendency according to Eq. (33) in [323] takes on the form:

$$T = \sqrt{\frac{\gamma_{\mathrm{usf}}}{\gamma_{\mathrm{ut}}}}. \tag{B.6}$$

C Crack-tip displacement fields

K-controlled cracks

According to Sih & Liebowitz [46, 47], the crack-tip displacement field in orthotropic materials depends on the applied stress intensity factor K_I, as follows [47]:

$$u_\mathrm{x} = \frac{K_\mathrm{I}\sqrt{2r}}{\sqrt{\pi}}\mathrm{Re}\left[\frac{1}{s_1 - s_2}\left(s_1 p_2\sqrt{\cos\theta + s_2\sin\theta} - s_2 p_1\sqrt{\cos\theta + s_1\sin\theta}\right)\right], \quad \text{(C.1)}$$

$$u_\mathrm{y} = \frac{K_\mathrm{I}\sqrt{2r}}{\sqrt{\pi}}\mathrm{Re}\left[\frac{1}{s_1 - s_2}\left(s_1 q_2\sqrt{\cos\theta + s_2\sin\theta} - s_2 q_1\sqrt{\cos\theta + s_1\sin\theta}\right)\right], \quad \text{(C.2)}$$

where r is the distance between crack tip and the present position and θ is the angle between the crack plane and the vector connecting the present position with the crack tip, see Fig. 2.1. The complex parameters p_1, p_2, q_1 and q_2 are given by Eq. (4.13) in Ref. [47] while s_1 and s_2 are either complex or purely imaginary [444] and solve Eq. (4.8) in Ref. [47].

Under plane strain conditions ($u_z = 0$), the connection between K_I and G is given by Eq. (2.5) where the elastic modulus is determined as [47]:

$$E^* = \left[\frac{b_{11}b_{22}}{2}\left(\sqrt{\frac{b_{22}}{b_{11}}} + \frac{2b_{12} + b_{66}}{2b_{11}}\right)\right]^{-0.5} \quad \text{(C.3)}$$

where the reduced plane strain moduli b_ij are obtained from the elastic compliances a_ij [46, 445]:

$$b_{11} = \frac{a_{11}a_{33} - a_{13}^2}{a_{33}}, \qquad b_{22} = \frac{a_{22}a_{33} - a_{23}^2}{a_{33}},$$
$$b_{12} = \frac{a_{12}a_{33} - a_{13}a_{23}}{a_{33}}, \qquad b_{66} = \frac{a_{66}a_{33} - a_{26}^2}{a_{33}}, \quad \text{(C.4)}$$

and have to be calculated for each coordinate system separately. An analytical solution for this problem can be found in Ref. [446]. The present work uses a numerical solution method to calculate b_ij, see Ref. [447].

Strain-controlled edge cracks

With the crack located at $(c_x, L_y/2)$, the different regions A, B, and C, cf. Fig. 3.3, are defined as follows:

A: $0 \leq x < c_x/2$,
B: $c_x/2 \leq x < c_x$, and
C: $c_x \leq x < L_x$.

The following displacement field is independent of the box length L_z and equally applies to the quasi-2D and 3D edge crack setups. For a given initial strain ε_{in}, which lies around the threshold strain ε_0, the atomic displacements are [214]:

$$u_y^A = \begin{cases} 0 & \text{if } y < c_y, \\ L_y \varepsilon_{in} & \text{if } y > c_y, \end{cases} \tag{C.5}$$

$$u_y^B = \begin{cases} \left[y - y\sqrt{1 - \frac{4(x-c_x/2)^2}{c_x^2}} \right] \varepsilon_{in} & \text{if } y < c_y, \\ \left[y - (y - L_y)\sqrt{1 - \frac{4(x-c_x/2)^2}{c_x^2}} \right] \varepsilon_{in} & \text{if } y > c_y, \text{ and} \end{cases} \tag{C.6}$$

$$u_y^C = y\varepsilon_{in}. \tag{C.7}$$

Strain-controlled quasi-2D central cracks

For central cracks, the displacements u_y^B and u_y^C are symmetrically applied with the symmetry plane being the yz-plane at $x = L_y/2$ and a being the longer half axis of the ellipse:

$$u_y = \begin{cases} y\varepsilon_{in} & \text{if } \|x - L_x/2\| \geq a, \\ \left[y - y\sqrt{1 - \frac{(x-L_x/2)^2}{a^2}} \right] \varepsilon_{in} & \text{if } \|x - L_x/2\| < a \text{ and } y < L_y/2, \\ \left[y - (y - L_y)\sqrt{1 - \frac{(x-L_x/2)^2}{a^2}} \right] \varepsilon_{in} & \text{if } \|x - L_x/2\| < a \text{ and } y > L_y/2. \end{cases} \tag{C.8}$$

Strain-controlled penny-shaped cracks

The penny-shaped crack is inserted by displacing the atoms in the configuration according to the following linear-elastic solution for the displacement field around a penny-shaped crack [393]:

$$u_r = -\frac{\varepsilon r(1+\nu)}{2}\left[(1-2\nu)\left(\frac{(1+2\nu)(1-\nu)}{(1-2\nu)(1+\nu)} - \frac{2}{\pi}\arctan\frac{\sqrt{\eta}}{a}\right) - \frac{2\beta a\sqrt{\eta}}{\pi\alpha(a^2+\eta)}\right] \quad \text{(C.9)}$$

$$u_y = \varepsilon y(1+\nu)\left[(1-2\nu)\left(\frac{\nu(1+2\nu)}{(1-2\nu)(1+\nu)} + \frac{2}{\pi}\arctan\frac{\sqrt{\eta}}{a}\right) + \right.$$
$$\left. + \frac{2a(\beta - y^2a^2(a^2+\eta^2))}{\pi\alpha\sqrt{\eta}}\right] \quad \text{(C.10)}$$

where $r = \sqrt{x^2+z^2}$ is the radial distance from the crack center and ν is the isotropic Poisson's ratio. The numbers α, β, and η are defined as follows:

$$\alpha = r^2\eta^2 + y^2(a^2+\eta^2) \quad \text{(C.11)}$$

$$\beta = (1-2\nu)(y^2+r^2)\eta^2 + 4(1-\nu)\eta y^2a^2 + (3-2\nu)y^2a^4 \quad \text{(C.12)}$$

$$\eta = \frac{1}{2}(y^2+r^2-a^2)\frac{1}{2}\sqrt{(y^2+r^2+a^2)^2 - 4a^2r^2} \quad \text{(C.13)}$$

Giordiano *et al.* [393] developed these equations for isotropic linear-elastic materials. To use them for anisotropic materials, Eq. (C.9) is rescaled with the correct Poisson ratios ν_{xy} and ν_{zy} to obtain the displacements in x and z direction. At the same time, the average Poisson ratio $0.5(\nu_{xy} + \nu_{zy})$ is used instead of ν in Eqs. (C.10-C.13). This method ensured that the change of the box lengths L_x and L_z behaved as required by the respective Poisson ratios.

D BCC defect analysis (BDA)

The bcc defect analysis (BDA) compares the common neighbor analysis (CNA), coordination number (CN), and centrosymmetry parameter (CSP) of each atom to typical values for certain crystal defects. Fig. D.1 shows a schematic overview of the basic steps of the BDA. The typical values for CN and CSP were identified for the known bcc defects by evaluating a number of different ideal (in an energetic minimum) and excited systems (during dynamic simulations). The known defects were the $(1\,0\,0)$, $(1\,1\,0)$, $(1\,1\,1)$, and $(1\,1\,2)$ surfaces, mono- and di-vacancies as well as vacancy rows, twin boundaries on $\{1\,1\,2\}$ planes, planar faults on $\{1\,1\,0\}$ planes, screw dislocations, and edge dislocations on $\{1\,1\,0\}$ and $\{1\,1\,2\}$ planes.

Each non-bcc atom is first pre-characterized according to its values for the CNA, CN, and CSP. Thereafter, the occurrences of certain combinations of CN and CSP are evaluated for all neighbor atoms, which are not classified as bcc according to the adaptive CNA (a-CNA) [396]. An identified defect is finally assigned to an atom if the defect represents the relative majority of all defects in the atom's neighborhood. This final optimization of the results is done in an iterative manner until the number of identified defects reaches a steady state.

In essence, the BDA method consists of the following steps:

1. Calculate a-CNA [396], CSP [404], and CN (with cutoff radius $r_c = (1+\sqrt{2})/2a_0$ to include also next-nearest neighbors) for all atoms.
2. Generate list of non-bcc neighbors, i.e., with a-CNA≠bcc or CN≠14, for each atom.
3. For defects in Table D.1: test for the given criteria and proceed with no. 5 in case of positive match. In this context, it is important to test for the different defects in the ordering as they are presented in Table D.1.
4. Append atoms, for which no match was found, to the list of unidentified defects.
5. If the identified defect is not representing the relative majority of the defects in its neighborhood (excluding unidentified atoms) or occurs less than two times: append atom to list of unidentified defects.
6. For all atoms in the list of unidentified defects: assign the defect, which represents the relative majority of all neighbors' defects and occurs more than two times, to the atom; remove the atom from the list of unidentified atoms.
7. Repeat no. 6 until the number of unidentified atoms is smaller than a threshold value or does not change upon further repetition.

The detailed criteria for CN and CSP are presented in Table D.1. The significant advantage of the BDA method becomes evident when the different techniques are compared for a configuration that contains a large number of different defects. Such an example is provided in Fig. D.2, which shows the complex plastic zone that forms around a penny-shaped crack on the $(0\,1\,0)$ plane in Fe, see Refs. [95, 201] for details. For instance, both

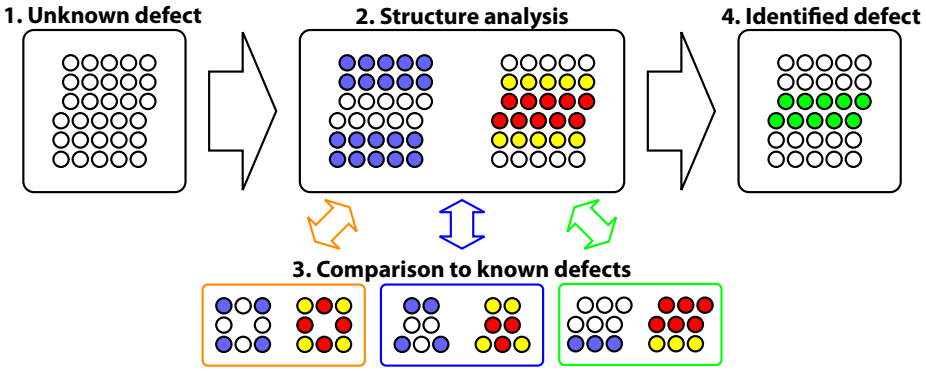

Figure D.1: Simplified overview of the basic steps during the BCC Defect Analysis.

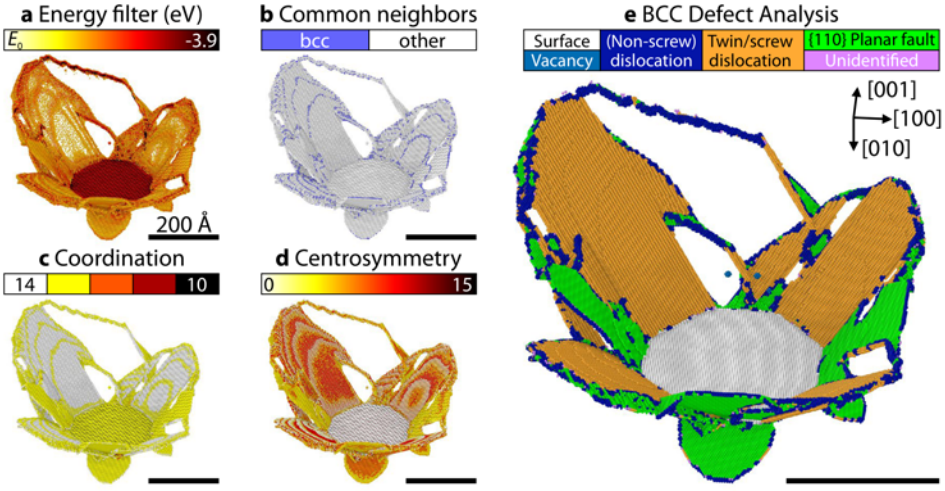

Figure D.2: Comparison of different analysis techniques for the penny-shaped crack on the (010) plane in Fe. Atomic interactions: Mendelev-II potential [225]; All subfigures show the same snapshot after $t = 38$ ps, at $\varepsilon = 5.73$ % ; Atoms are only shown in subfigures **b**-**d**, if they are not classified as bcc due to CNA *and* do not exhibit a coordination number of 14. **a**: energy filtered configuration where atoms with a potential energy lower than –4.05 eV are not shown; **b**: a-CNA [396]; **c**: CN including next-nearest neighbors; **d**: CSP [404]; **e**: the newly developed bcc defect analysis (BDA); with the BDA, all relevant defects are robustly identified even if it was originally developed for the Chiesa potential; the other methods (**a**-**d**), on the other hand, are not able to uniquely distinguish between all the different defect types.

edge-oriented dislocations and surfaces fall into the same energy range with the energy filtering method (a). At the same time, atoms in the interior of a twin exhibit the same energy as the perfect structure and the twin therefore appears semi-transparent in the figure. The CNA, on the other hand, reliably detects all defects, but is not able to distinguish between them (b). The (010) surface and the dislocations have the same CN (c). Likewise, twins and {110} planar faults exhibit similar CSP (d). The new BDA method, however, clearly distinguishes between surfaces, planar faults, twins, dislocations, and vacancies (d).

The recommended color scheme to visualize the output data of the BDA is given in Table D.2. It is based on the 'cubehelix' approach [448] and yields images where the different defects can be distinguished even if printed with most B/W printers.

BDA at high temperatures

To demonstrate the applicability of the BDA also at elevated temperatures, NVE simulations of selected defect structures were performed and analyzed for $T = 1000$ K, which is approximately 50 % of the melting temperature. Fig. D.3 shows the high-temperature configurations of the mono-vacancy and the edge dislocation after $t = 20$ ps of equilibration. The figure further compares the well-established CNA to the newly developed BDA technique. While the CNA detects a multitude of non-bcc atoms, the BDA correctly identifies the vacancy and the edge dislocation even at $T = 1000$ K. Most other non-bcc atoms are not assigned to any other defect type with the exception of spurious atomic clusters that were erroneously identified as screw dislocations or twins (orange). The zero-dimensionality of these clusters, however, clearly contradicts to such defect types, which have to be either one- or two-dimensional.

At high temperatures, the BDA can even be used to reduce the thermal noise. This is shown in the right subfigures of Fig. D.3, where unidentified atoms are not printed. In this manner, those atoms are not visualized, which deviate from the bcc structure only as a result of thermal vibrations. The resulting pictures mainly contain the introduced defects, do not suffer from confusing thermal noise, and may thus help to clearly convey a scientific message.

Table D.1: Overview of criteria for common bcc defects in the bcc defect analysis (BDA). $N_d(c)$ is the number of non-bcc (CNA≠bcc) neighbors fulfilling the criterion c; N_p is the number of neighbors in a perfect bcc environment (CNA=bcc and CN=14).

Surface (S)								
CNA	**CN**	**CSP**	N_p	N_d(CN<12)				
≠bcc	<12	—	—	—				
≠bcc	<14	—	—	>3				
Vacancy and vacancy row (V)								
CNA	**CN**	**CSP**	N_p	N_d(CN=12,CSP<1)	N_d(CN=12,CSP>4)	N_d(CN=13,CSP<1)	N_d(CN=13,CSP>4)	N_d(CN=13)
≠bcc	=12	<1	6	—	2	—	4	—
≠bcc	=12	>4	3	2	1	2	4	—
≠bcc	=13	<1	9	— —	— 2	— —	4 2	— —
≠bcc	=13	>4	7	— 2 —	— 2 —	3 1 —	3 1 —	— — 6
			>7	—	—	—	4	—
Twin boundary and screw dislocation (T)								
CNA	**CN**	**CSP**	N_p	N_d(CN=13)	N_d(CN=14)	N_d(CN=14,CSP>8)		
≠bcc	=13	<1	—	—	—	4		
≠bcc	=13	>4.5	6	5	2	—		
—	=14	—	[6..9]	— 4	>3 2	— —		
—	=14	>8	<9	—	—	—		

{110} planar fault (P)						
CNA	**CN**	**CSP**	N_p	N_d(CN=12)	N_d(CN=13)	N_d(11<CN<14)
≠bcc	=12	—	0	>8 [3..6] >5	— [7..9] >2	— — —
≠bcc	=13	—	— 4 >5 <4	— 3 <2 <5	>6 6 6 >6	9 — — —
(Non-screw) dislocation (D)						
CNA	**CN**	**CSP**	N_p	N_d(CN>11,CN≠14)	N_d(CN≠14)	N_d(CN=14)
≠bcc	>11,≠14	—	—	—	>N_d(CN=14)	<N_d(CN≠14)
≠bcc	=14	—	<5	>3	—	<7

Table D.2: Recommend color scheme for the BCC Defect Analysis (BDA).

(Defect) structure	RGB color scheme	CMYK color scheme
Perfect bcc crystal	(179,179,179)	#B3B3B3
Surface	(255,255,255)	#FFFFFF
Mono- and di-vacancy, vacancy row	(0,109,179)	#006DB3
Twin boundary, screw dislocation	(255,170,51)	#FFAA33
{110} Planar fault	(0,255,0)	#00FF00
(Non-screw) Dislocation	(4,20,168)	#0414A8
Unidentified defect	(223,133,255)	#DF85FF

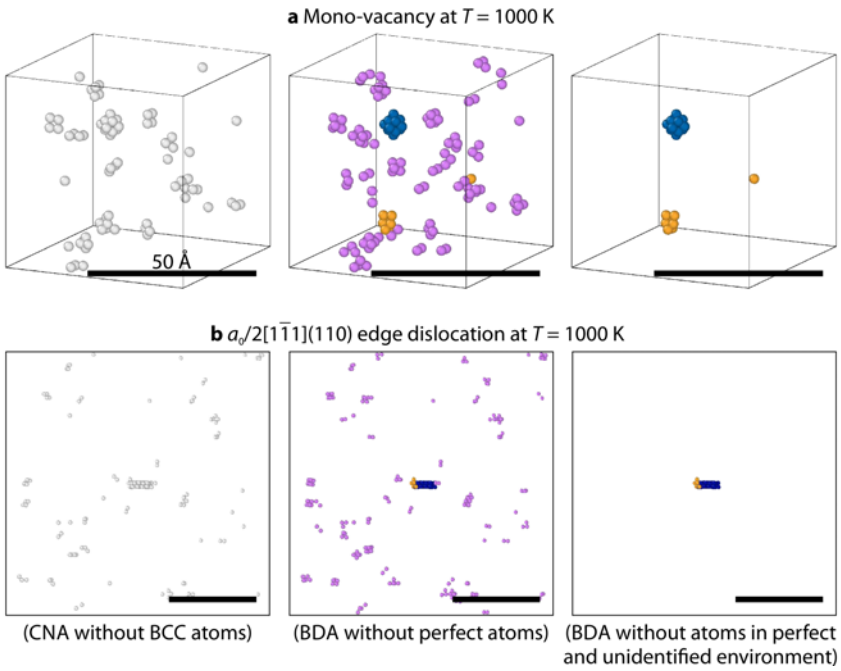

Figure D.3: Comparison of the CNA and BDA techniques for defect structures at high-temperature (T = 1000 K). **a**: mono-vacancy; **b**: edge dislocation; the CNA encounters a multitude of non-bcc atoms, which makes it difficult to separate the thermal noise from the actual defect (left subfigures); the BDA, on the contrary, correctly detects both the vacancy and the edge dislocation even at 1000 K (center subfigures); when unidentified defects are not shown (right subfigures), the BDA can also be used to significantly reduce the thermal noise.

E Dislocation emission from propagating twins

For the atomic interactions of tungsten, the Finnis-Sinclair potential [307] in the modified version of Ackland and Thetford [367] was used. The setup for the simulation of deformation twin (DT) growth is shown in Fig. E.1, where the crystal is oriented such that the shearing direction is parallel to the direction of the Burgers vector and the twin tip line. The initial atomistic configuration of the stationary twin tip structure is created by insertion of partial twinning dislocations with Burgers vector $\underline{b}_t = a_0/6[11\bar{1}]$ on eight adjacent $(11\,2)$ planes, where the generated twin faults are of different lengths thereby leading to a wedge-like shape if viewed along the dislocation line direction. The created structure is then relaxed under varied applied shear stresses τ until a stationary structure is held, where the twin is neither propagating nor annihilating. Starting with the relaxed structure, quasistatic simulations with stepwise increasing shear stresses τ are performed to determine the instability point of the stationary structure. From the last stable configuration, subsequent NVE simulations were performed to observe the DT growth behavior; the rate of the applied shear stress was varied between $\dot{\tau} = \pm 0.0783$ and ± 15.7 MPa/ps for a system size of cross sectional dimensions $L_z \times L_y \approx 1200 \times 400$ Å^2, see Table E.1.

The results shown in Fig. E.2 are for an eight-layer twin in a simulation box of $L_z \times L_y \approx 600 \times 200$ Å^2 (approx. 81,000 atoms) at a constant shear stress level of $\tau = \pm 1.37$ GPa.

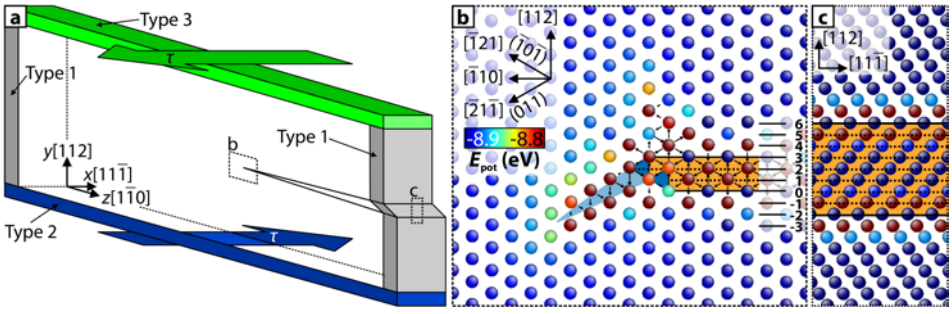

Figure E.1: Simulation setup for investigating the dislocation emission from a propagating twin. **a**: general setup; **b**: view at the twin tip along the $[11\bar{1}]$ direction (incoherent twin boundary); atomic out-of-plane shifts in $[11\bar{1}]$ direction are visualized by differential displacement; **c**: view on the twin along the $[\bar{1}10]$ direction; twinned regions are indicated by orange regions in **b** and **c**. Note the distribution of the two twinning partial dislocations at the twin tip on the inclined (011) plane. Boundary conditions: free in xy (type 1); free in xz (types 2 and 3). The applied shear stress is $\tau = \pm 1.33$ GPa.

Table E.1: Critical conditions for dislocation emission from propagating twins for different shear rates $\dot{\tau}$; τ_{in}: initial shear stress; t_{crit}: time of dislocation emission; Δx: propagation distance of twin after t_{crit}; v_{tip}: velocity of twin tip; v_{3rd}: velocity of third twinning partial.

τ_{in} (GPa)	$\dot{\tau}$ (MPa/ps)	t_{crit} (ps)	Δx (Å)	v_{tip} (Å/ps)	v_{3rd} (Å/ps)
±1.33	±0.0783	380	223.9	5.71	6.28
±1.33	±0.157	220	201.6	4.99	5.94
±1.33	±0.783	89	194.8	4.47	4.72
±1.33	±1.57	58	118.7	4.55	5.90
±1.33	±7.83	32.4	78.4	4.78	4.97
±1.33	±15.7	25.4	62.8	5.97	6.96

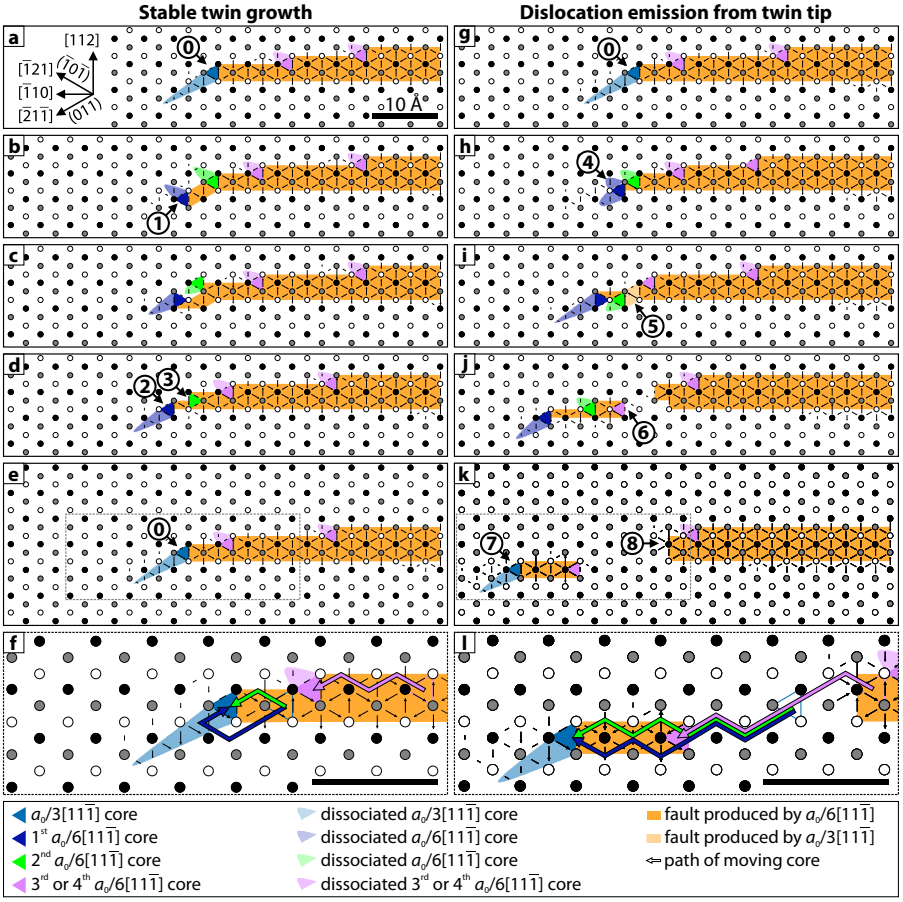

Figure E.2: DD maps showing stable twin growth and dislocation emission from a propagating twin. **a**-**e**: positions of twinning dislocation (TD) cores during stable twin growth; **g**-**k**: positions of TD cores during emission of a dislocation from the twin tip; **f**,**l**: schematic illustrations of both pathways.

References

[1] R. P. Reed, J. H. Smith, and B. W. Christ, *The economic effects of fracture in the United States. Part 1 - A Synopsis of the September 30, 1982 Report to NBS by Battelle Columbus Laboratories* (National Bureau of Standards Special Publication 647-1, 1983).

[2] J. J. Duga, W. H. Fisher, R. W. Buxbaum, A. R. Rosenfild, A. R. B. E. J. Honton, and S. C. McMillan, *The economic effects of fracture in the United States. Part 2 - A report to NBS by Batelle Columbus Laboratories* (National Bureau of Standards Special Publication 647-2, 1983).

[3] L. Faria, *Tech. Rep. Study Contract NO. 32105, Comm. Eur. Comunities*, Tech. Rep. (Technical Report Study Contract NO. 32105, Commission of the European Comunities, 1991).

[4] R. Razvan, in *ASMCSS'09 Proc. 3rd Int. Conf. Appl. Math. Simulation, Model. Circuits, Syst. Signals* (2009) pp. 122–131.

[5] M. A. Meyers and K. K. Chawla, *Mechanical Behavior of Materials* (Cambridge University Press, 2009).

[6] A. Needleman and E. van der Giessen, Mater. Res. Bull. **26**, 211 (2001).

[7] S. Kumar and W. A. Curtin, Mater. Today **10**, 34 (2007).

[8] S. Suresh, *Fatigue of Materials*, 2nd ed. (Cambridge Univ. Press, 2001).

[9] A. A. Griffith, Phil. Trans. Roy. Soc. London A **221**, 163 (1921).

[10] B. Lawn, *Fracture of Brittle Solids*, edited by E. A. Davis and I. M. Ward (Cambridge Solid State Science Series, 1993).

[11] R. Thomson, C. Hsieh, and V. Rana, J. Appl. Phys. **42**, 3154 (1971).

[12] P. Gumbsch and R. M. Cannon, Mater. Res. Bull. **25**, 15 (2000).

[13] M. Marder, Int. J. Fract. **130**, 517 (2004).

[14] J. Riedle, P. Gumbsch, and H. F. Fischmeister, Phys. Rev. Lett. **76**, 3594 (1996).

[15] J. R. Rice and R. Thomson, Philos. Mag. **29**, 73 (1974).

[16] J. R. Rice, J. Mech. Phys. Solids **40**, 239 (1992).

[17] A. D. Rollett, G. S. Rohrer, and R. M. Suter, MRS Bull. **40**, 951 (2015).

[18] A. Needleman, J. Mech. Phys. Solids **38**, 289 (1990).

[19] L. P. Kubin, G. Canova, M. Condat, B. Devincre, V. Pontikis, and Y. Bréchet, Solid State Phenom. **23-24**, 455 (1992).

[20] V. Yamakov, E. Saether, D. R. Phillips, and E. H. Glaessgen, J. Mech. Phys. Solids **54**, 1899 (2006).

[21] R. Janisch, N. Ahmed, and A. Hartmaier, Phys. Rev. B **81**, 184108 (2010).

[22] C. Sommer, H. Mughrabi, and D. Lochner, Acta Mater. **46**, 1537 (1998).

[23] U. Krupp, *Mikrostrukturelle Aspekte der Rissinitiierung und -ausbreitung in metallischen Werkstoffen* (2004).

[24] H. Mughrabi, Phil. Trans. R. Soc. A **373**, 1 (2014).

[25] C. Gandhi and M. F. Ashby, Acta Metall. **27**, 1565 (1979).

[26] H. J. Frost and M. F. Ashby, *Deformation-Mechanism Maps - The Plasticity and Creep of Metals and Ceramics* (Pergamon Press, Oxford, 1982).

[27] P. Gumbsch, J. Riedle, A. Hartmaier, and H. F. Fischmeister, Science **13**, 1293 (1998).

[28] M. L. Hribernik, *Cleavage Oriented Iron Single Crystal Fracture Toughness*, Ph.D. thesis, University of Santa Barbara (2006).

[29] S. Kohlhoff, P. Gumbsch, and H. F. Fischmeister, Phil. Mag. A **64**, 851 (1991).
[30] P. A. Gordon, T. Neeraj, M. J. Luton, and D. Farkas, Met. Mater. Trans. A **38**, 2191 (2007).
[31] K. B. Broberg, *Cracks and Fracture* (Academic Press, Burlington, 1999).
[32] T. L. Anderson, *Fracture Mechanics - Fundamentals and Applications* (Taylor & Francis, 2005).
[33] D. Gross and T. Seelig, *Fracture Mechanics - With an Introduction to Micromechanics* (Springer, Berlin, 2006).
[34] C. E. Inglis, Trans. Inst. Nav. Archit. , 219 (1913).
[35] E. Orowan, Reports Prog. Phys. **12**, 185 (1948).
[36] G. R. Irwin, Trans. Am. Soc. Met. **40A**, 147 (1948).
[37] H. M. Westergaard, J. Appl. Mech. **6**, A49 (1939).
[38] I. N. Sneddon, Proc. R. Soc. Lond. A **187**, 229 (1946).
[39] M. L. Williams, J. Appl. Mech. **24**, 109 (1957).
[40] G. R. Irwin, J. Appl. Mech. **24**, 361 (1957).
[41] L. B. Freund, *Dynamic Fracture Mechanics* (Cambridge University Press, 1990).
[42] S. G. Larsson and A. J. Carlsson, J. Mech. Phys. Solids **21**, 263 (1973).
[43] B. L. Karihaloo and Q. Z. Xiao, Int. J. Fract. **112**, 111 (2001).
[44] B. L. Karihaloo and Q. Z. Xiao, in *Struct. Integr. Fract.* (A.V. Dyskin and X. Hu and E. Sahouryeh, 2002) pp. 49–58.
[45] F. Berto and P. Lazzarin, Int. J. Fract. **161**, 221 (2010).
[46] G. C. Sih, P. C. Paris, and G. R. Irwin, Int. J. Fract. **1**, 189 (1965).
[47] G. C. Sih and H. Liebowitz, in *Fracture* (Academic Press, New York, 1968).
[48] J. P. Hirth and J. Lothe, *Theory of Dislocations, 2nd Edition* (John Wiley and Sons, 1982).
[49] Y. Murakami, *Stress Intensity Factors Handbook Vol. 1*, edited by Y. Murakami (Pergamon Press, Oxford, 1990).
[50] Y. Murakami, *Stress Factors Intensity Handbook Vol. 2*, edited by Y. Murakami (Pergamon Press, Oxford, 1990).
[51] H. Tada, P. C. Paris, and G. R. Irwin, *The Stress Analysis of Cracks Handbook* (ASME Press, New York, 2000).
[52] "ASTM Standard E 399-90: Standard Test Method for Plane-Strain Fracture Toughness of Metallic Materials," (1997).
[53] P. Gumbsch, "Computer Simulation in Materials Science: Nano/Meso/Macroscopic Space and Time Scales," (Kluwer Academic, Netherlands, 1996) p. 227.
[54] K. Ravi-Chandar, *Dynamic fracture* (Elsevier Ltd., 2004).
[55] G. R. Irwin, in *Handb. der Phys.*, Vol. 6, edited by H. Geiger (Springer, Berlin, 1958).
[56] P. Gumbsch, *Atomistische Modellierung zweidimensionaler Defekte in Metallen: Risse, Phasengrenzflächen* (Dissertation, Universität Stuttgart, 1991).
[57] R. Thomson, in *Solid State Phys.*, Vol. 39, edited by H. Ehrenreich and D. Turnbull (Academic Press, 1986) pp. 2–129.
[58] J. R. Kermode, A. Gleizer, G. Kovel, L. Pastewka, G. Csányi, D. Sherman, and A. De Vita, Phys. Rev. Lett. **115**, 135501 (2015).
[59] R. Peierls, Proc. Phys. Soc. **52**, 34 (1940).
[60] F. Nabarro, Proc. Phys. Soc. **59**, 256 (1947).
[61] V. Vítek, Philos. Mag. **18**, 773 (1968).
[62] T. Zhu, J. Li, and S. Yip, Phys. Rev. Lett. **93**, 25503 (2004).
[63] J. Riedle, *Bruchwiderstand in Wolfram Einkristallen: Einfluß der kristallographischen Orientierung, der Temperatur und der Lastrate* (Dissertation, Universität Stuttgart, 1995).

[64] J. R. Kermode, T. Albaret, D. Sherman, N. Bernstein, P. Gumbsch, M. C. Payne, G. Csanyi, and A. D. Vita, Nature **455**, 1224 (2008).
[65] T. Zhu, J. Li, and S. Yip, Proc. R. Soc. A **462**, 1741 (2006).
[66] S. J. Zhou, D. M. Beazley, P. S. Lomdahl, and B. L. Holian, Phys. Rev. Lett. **78**, 479 (1997).
[67] P. A. Gordon, T. Neeraj, and M. J. Luton, Modelling Simul. Mater. Sci. Eng. **17**, 25005 (2009).
[68] H. Gao and J. R. Rice, J. Appl. Mech. **56**, 828 (1989).
[69] A. S. Argon, J. Eng. Mater. Technol. **123**, 1 (2001).
[70] R. A. Sack, Proc. Phys. Soc. **58**, 729 (1946).
[71] J. R. Willis, Quart. J. Mech. Appl. Math. **25**, 367 (1971).
[72] M. Kachanov and J.-P. Laures, Int. J. Fract. **41**, 289 (1989).
[73] F. F. Lange, Philos. Mag. **22**, 0983 (1970).
[74] D. Hull and D. J. Bacon, *Introduction to Dislocations, 4th Edition* (Buttlerworth-Heinemann, Oxford, 2001).
[75] B. Cotterell, *Fracture and Life* (World Scientific, 2010).
[76] A. G. Evans, Philos. Mag. **26**, 1327 (1972).
[77] B. Cotterell and J. R. Rice, Int. J. Fract. **16**, 155 (1980).
[78] K. P. Meade and L. M. Keer, Int. J. Elast. **14**, 79 (1984).
[79] J. R. Rice, J. Appl. Mech. **52**, 571 (1985).
[80] H. Gao and J. R. Rice, J. Appl. Mech. **53**, 774 (1986).
[81] H. Gao and J. R. Rice, Int. J. Fract. **33**, 155 (1987).
[82] P. Krysl and T. Belytschko, Int. J. Numer. Methods Eng. **44**, 767 (1999).
[83] P. A. J. M. Steenkamp, in *Fract. Mech. Eighteenth Symp.*, edited by D. T. Read and R. P. Reed (American Society for Testing and Materials, 1988) pp. 583–610.
[84] E. Pan and F. G. Yuan, Int. J. Numer. Meth. Engng. **48**, 211 (2000).
[85] M. Gosz and B. Moran, Eng. Fract. Mech. **69**, 299 (2002).
[86] J. H. Chang and D. J. Wu, Int. J. Solids. Struct. **44**, 371 (2007).
[87] N. Sukumar, N. Moës, B. Moran, and T. Belytschko, Int. J. Numer. Meth. Engng. **48**, 1549 (2000).
[88] N. Moës, J. Dolbow, and T. Belytschko, Int. J. Numer. Meth. Engng. **46**, 131 (1999).
[89] N. Sukumar, D. L. Chopp, and B. Moran, Eng. Fract. Mech. **70**, 29 (2003).
[90] H. L. Zhang, P. Z. Huang, J. Sun, and H. Gao, Appl. Phys. Lett. **85**, 1143 (2004).
[91] Y. Umakoshi, T. Nakano, and B. Ogawa, Scr. Mater. **34**, 1161 (1996).
[92] F. Ebrahimi and L. Kalwani, Mater. Sci. Eng. A **268**, 116 (1999).
[93] J.-S. Wang and P. M. Anderson, Acta Metall. Mater. **39**, 779 (1991).
[94] J. J. Möller and E. Bitzek, Acta Mater. **73**, 1 (2014).
[95] E. Bitzek, J. R. Kermode, and P. Gumbsch, Int. J. Fract. **191**, 13 (2015).
[96] E. R. Fuller and R. Thomson, in *Fract. 1977 Proc. 4th Int. Conf. Fract.*, edited by D. M. R. Taplin (University of Waterloo Press, Canada, 1977) pp. 387–394.
[97] R. Pérez and P. Gumbsch, Phys. Rev. Lett. **84**, 5347 (2000).
[98] A. A. Johnson, Philos. Mag. **7**, 177 (1962).
[99] A. Giannattasio and S. G. Roberts, Philos. Mag. **87**, 2589 (2007).
[100] A. S. Wronski and A. A. Johnson, Philos. Mag. **7**, 213 (1962).
[101] L. C. Lim and T. Watanabe, Acta Metall. Mater. **38**, 2507 (1990).
[102] M. F. Ashby and J. D. Embury, Scr. Metall. **19**, 557 (1985).
[103] B. A. Wilcox, N. D. Veigel, and A. H. Clauer, Metall. Trans. **3**, 273 (1972).
[104] L. A. Norström and O. Vingsbo, Met. Sci. **13**, 677 (1979).

[105] A. V. Samant and J. J. Lewandowski, Metall. Mater. Trans. A Phys. Metall. Mater. Sci. **28**, 2297 (1997).
[106] T. L. Johnston, R. G. Davies, and N. S. Stoloff, Philos. Mag. **12**, 305 (1965).
[107] P. Cotterill, Prog. Mater. Sci. **9**, 205 (1961).
[108] M. M. Farahani, F. Attia, and K. Salama, Met. Trans. A **12**, 631 (1981).
[109] S. Fariabi, L. W. Collins, and K. Salama, Metall. Trans. A **14**, 701 (1983).
[110] B. A. Loomis and N. Carlson, *Ames Lab. Iowa State Coll.*, Tech. Rep. March (1958).
[111] M. Tanaka, E. Tarleton, and S. G. Roberts, Acta Mater. **56**, 5123 (2008).
[112] A. Y. Krasovskii and V. A. Vainshtok, Probl. Prochnosti **9**, 65 (1977).
[113] M. Ellis, *Ph.D. thesis* (University of Oxford, 1991).
[114] S. G. Roberts, P. B. Hirsch, a. S. Booth, M. Ellis, and F. C. Serbena, Phys. Scr. **T49B**, 420 (1993).
[115] T. D. Joseph, M. Tanaka, A. J. Wilkinson, and S. G. Roberts, J. Nucl. Mater. **367-370**, 637 (2007).
[116] N. J. Petch, Philos. Mag. **3**, 1089 (1958).
[117] A. N. Stroh, Adv. Phys. **6**, 418 (1957).
[118] H. Huang and W. W. Gerberich, Acta Metall. Mater. **42**, 639 (1994).
[119] A. Hartmaier and P. Gumbsch, Phys. Rev. B **71**, 24108 (2005).
[120] J. J. Möller, *Atomistic Simulations of Crack Propagation in α-Fe* (Studienarbeit, Friedrich-Alexander-Universität Erlangen-Nürnberg, 2011).
[121] J. J. Möller, *Atomistic Simulations on Grain Boundary Fracture in Tungsten Bicrystals* (Diplomarbeit, Friedrich-Alexander-Universität Erlangen-Nürnberg, 2011).
[122] J. J. Möller and E. Bitzek, Modelling Simul. Mater. Sci. Eng. **22**, 45002 (2014).
[123] U. E. Wolff, Trans. Met. Soc. AIME **224**, 327 (1962).
[124] P. Beardmore and D. Hull, J. Less-Common Met. **9**, 168 (1965).
[125] A. S. Argon and S. R. Maloof, Acta Metall. **14**, 1463 (1966).
[126] D. Hull, P. Beardmore, and A. P. Valintine, Philos. Mag. **12**, 1021 (1965).
[127] J. E. Cordwell and D. Hull, Philos. Mag. **19**, 951 (1969).
[128] J. E. Cordwell and D. Hull, Philos. Mag. **26**, 215 (1972).
[129] J. E. Cordwell and D. Hull, Philos. Mag. **27**, 1183 (1973).
[130] J. Liu and J. C. Bilello, Phil. Mag. **35**, 1453 (1977).
[131] H. W. Paxton and A. T. Churchman, Acta Metall. **1**, 473 (1953).
[132] H. W. Paxton, Acta Metall. **1**, 141 (1953).
[133] N. P. Allen, B. E. Hopkins, and J. E. McLennan, Proc. Roy. Soc. A **234**, 221 (1956).
[134] W. D. Biggs and P. L. Pratt, Acta Metall. Mater. **6**, 694 (1958).
[135] J. Harding, Proc. Roy. Soc. A **299**, 464 (1967).
[136] K. Kitajima, Y. Aono, H. Abe, and E. Kuramoto, Scr. Met. **13**, 1033 (1979).
[137] E. Kuramoto, Y. Aono, and K. Kitajima, Scr. Met. **13**, 1039 (1979).
[138] D. Hull, Philos. Mag. **3**, 1468 (1958).
[139] D. Hull, Proc. Roy. Soc. A **274**, 5 (1963).
[140] M. Gell, Acta Metall. **14**, 1625 (1966).
[141] R. K. Govila, Acta Metall. **17**, 1209 (1969).
[142] K. F. Ha, C. Yang, and J. S. Bao, Scr. Met. Mater. **39**, 1065 (1994).
[143] T. W. Shield and K. S. Kim, J. Mech. Phys. Solids **42**, 845 (1994).
[144] L. Zhang, T. Ohmura, K. Seikido, K. Nakajima, T. Hara, and K. Tsuzaki, Scr. Mater. **64**, 919 (2011).
[145] S. M. Ohr, Mat. Sci. Eng. **72**, 1 (1986).

[146] S. M. Ohr, H. Saka, Y. Zhu, and T. Imura, Phil. Mag. A **57**, 677 (1988).
[147] A. S. Tetelman and W. D. Robertson, Acta Metall. **11**, 415 (1963).
[148] M. Gell and W. D. Robertson, Acta Metall. **12**, 108 (1964).
[149] M. Landa, A. Machová, Z. Prevorovský, and J. Cerv, Czech. J. Phys. **48**, 1589 (1998).
[150] A. Spielmannová, M. Landa, A. Machová, P. Hausild, and P. Lejcek, Mater. Charact. **58**, 892 (2007).
[151] S. Kobayashi and S. M. Ohr, Phil. Mag. A **42**, 763 (1980).
[152] C. St. John, Philos. Mag. **32**, 1193 (1975).
[153] R. J. Fields, T. Weerasooriya, and M. F. Ashby, Met. Trans. A **11**, 333 (1980).
[154] D. Sen, C. Thaulow, S. V. Schieffer, A. Cohen, and M. J. Buehler, Phys. Rev. Lett. **104**, 235502 (2010).
[155] E. Bitzek and P. Gumbsch, Acta Mater. **61**, 1394 (2013).
[156] Y. Cheng, Z. H. Jin, Y. W. Zhang, and H. Gao, Acta Mater. **58**, 2293 (2010).
[157] R. Chang, Int. J. Fract. Mech. **6**, 111 (1970).
[158] S. Hai and E. B. Tadmor, Acta Mater. **51**, 117 (2003).
[159] F. Cleri, S. Yip, D. Wolf, and S. R. Phillpot, Phys. Rev. Lett. **79**, 1309 (1997).
[160] M. J. Buehler and H. Gao, Nature **439**, 307 (2006).
[161] P. Gumbsch, Z. Metallkd. **87**, 341 (1996).
[162] P. Gumbsch, S. J. Zhou, and B. L. Holian, Phys. Rev. B **55**, 3445 (1997).
[163] C. Thaulow, D. Sen, and M. J. Buehler, Mater. Sci. Eng. A **528**, 4357 (2011).
[164] C. H. Ersland, I. R. Vatne, and C. Thaulow, Modelling Simul. Mater. Sci. Eng. **20**, 75004 (2012).
[165] A. Latapie and D. Farkas, Phys. Rev. B **69**, 134110 (2004).
[166] D. Farkas, M. Willemann, and B. Hyde, Phys. Rev. Lett. **94**, 165502 (2005).
[167] S. A. Kotrechko, A. V. Filatov, and A. V. Ovsjannikov, Theor. Appl. Fract. Mec. **45**, 92 (2006).
[168] A. Cao and Y. Wei, Phys. Rev. B **76**, 24113 (2007).
[169] K. Nishimura and N. Miyazaki, Comp. Mat. Sci. **31**, 269 (2004).
[170] M. F. Horstemeyer, D. Farkas, S. Kim, T. Tang, and G. Potirniche, Int. J. Fatigue **32**, 1473 (2010).
[171] H. Van Swygenhoven and J. R. Weertman, Mater. Today **9**, 24 (2006).
[172] M. Klesnil and P. Lukás, *Fatigue of Metallic Materials* (Elsevier, 1992).
[173] Y. Cheng, M. Mrovec, and P. Gumbsch, Mater. Sci. Eng. A. **483**, 329 (2008).
[174] A. J. Markworth, L. R. Kahn, P. C. Gehlen, and G. T. Hahn, Bull. Am. Phys. Soc. **24**, 528 (1979).
[175] A. J. Markworth and J. P. Hirth, J. Mater. Sci. **16**, 3405 (1981).
[176] A. J. Markworth, L. R. Kahn, P. C. Gehlen, and G. T. Hahn, Res. Mech. **2**, 141 (1981).
[177] M. Mullins and M. A. Dokainish, Phil. Mag. A **46**, 771 (1982).
[178] B. DeCelis, A. S. Argon, and S. Yip, J, Appl. Phys. **54**, 4864 (1983).
[179] M. Mullins, Acta Metall. **32**, 381 (1984).
[180] K. Cheung and S. Yip, Modelling Simul. Mater. Sci. Eng. **2**, 865 (1994).
[181] V. Shastry and D. Farkas, Modelling Simul. Mater. Sci. Eng. **4**, 473 (1996).
[182] A. Machová, G. E. Beltz, and M. Chang, Modelling Simul. Mater. Sci. Eng. **7**, 949 (1999).
[183] Z. Hu, S. Fukuyama, K. Yokogawa, and S. Okamoto, Modelling Simul. Mater. Sci. Eng. **7**, 541 (1999).
[184] Y. Guo, C. Wang, and D. Zhao, Mater. Sci. Eng. A **349**, 29 (2003).
[185] G. E. Beltz and A. Machová, Scr. Mater. **50**, 483 (2004).
[186] A. Machová and G. E. Beltz, Mater. Sci. Eng. A **387-389**, 414 (2004).
[187] D. Farkas, Philos. Mag. **85**, 387 (2005).
[188] L.-X. Cao and C.-Y. Wang, J. Mater. Res. **21**, 2542 (2006).

[189] V. Pelikán, P. Hora, A. Machová, and M. Landa, in *Proc. 16th Eur. Conf. Fract.*, edited by E. E. Gdoutos (Alexandroupolis, Greece, 2006).
[190] Y. Guo, Y. Wang, and D. Zhao, Acta Mater. **55**, 401 (2007).
[191] Y. Guo and D. Zhao, Mater. Sci. Eng. A **448**, 281 (2007).
[192] Y. Guo and C. Wang, Comp. Mat. Sci. **40**, 376 (2007).
[193] P. Hora, V. Pelikán, A. Machová, A. Spielmannová, J. Prahl, M. Landa, and O. Cervená, Eng. Fract. Mech. **75**, 3612 (2008).
[194] A. Spielmannová, A. Machová, and P. Hora, Acta Mater. **57**, 4065 (2009).
[195] A. Spielmannová, A. Machová, and P. Hora, Comp. Mat. Sci. **48**, 296 (2010).
[196] N. Miyazaki, IACM Expressions **28**, 6 (2010).
[197] V. A. Borodin and P. V. Vladimirov, J. Nucl. Mater. **415**, 320 (2011).
[198] I. R. Vatne, E. Østby, C. Thaulow, and D. Farkas, Mater. Sci. Eng. A **528**, 5122 (2011).
[199] I. R. Vatne, E. Østby, and C. Thaulow, Modelling Simul. Mater. Sci. Eng. **19**, 85006 (2011).
[200] C. H. Ersland, C. Thaulow, I. R. Vatne, and E. Østby, Eng. Fract. Mech. **79**, 180 (2012).
[201] J. J. Möller and E. Bitzek, Eng. Fract. Mech. **150**, 197 (2015).
[202] Y. Furuya, N. Noguchi, and S. Schmauder, Int. J. Fract. **107**, 139 (2001).
[203] S. L. Frederiksen, K. W. Jacobsen, and J. Schiøtz, Acta Mater. **52**, 5019 (2004).
[204] W.-S. Ko, J. B. Jeon, J.-H. Shim, and B.-J. Lee, Int. J. Hydrogen Energy **37**, 13583 (2012).
[205] Z. L. Pan, Y. L. Li, and Q. Wei, Acta Mater. **56**, 3470 (2008).
[206] J. Mei, Y. Ni, and J. Li, Int. J. Solids Struct. **48**, 3054 (2011).
[207] R. E. Rudd, Philos. Mag. **89**, 3133 (2009).
[208] K. Cheung, R. J. Harrison, and S. Yip, J. Appl. Phys. **71**, 4009 (1992).
[209] C. Hsieh and R. Thomson, J. Appl. Phys. **44**, 2051 (1973).
[210] E. B. Tadmor and R. E. Miller, *Modeling Materials: Continuum, Atomistic and Multiscale Techniques* (Cambridge University Press, 2011).
[211] D. G. Pettifor, Phys. Rev. Lett. **63**, 2480 (1989).
[212] M. I. Baskes, Phys. Rev. B **46**, 2727 (1992).
[213] Y. Mishin, M. J. Mehl, and D. A. Papaconstantopoulos, Acta Mater. **53**, 4029 (2005).
[214] E. Bitzek, *Atomistic Simulation of Dislocation Motion and Interaction with Crack Tips and Voids* (Dissertation, Universität Karlsruhe, 2006).
[215] E. Bitzek and P. Gumbsch, J. Solid Mech. Mater. Eng. **2**, 1348 (2008).
[216] M. S. Daw and M. I. Baskes, Phys. Rev. B **29**, 6443 (1984).
[217] P. A. Gordon, T. Neeraj, and M. I. Mendelev, Philos. Mag. **91**, 3931 (2011).
[218] L. Proville, D. Rodney, and M. C. Marinica, Nat. Mater. **11**, 845 (2012).
[219] L. Malerba, M. C. Marinica, N. Anento, C. Björkas, H. Nguyen, C. Domain, F. Djurabekova, P. Olsson, K. Nordlund, A. Serra, D. Terentyev, F. Willaime, and C. S. Becquart, J. Nucl. Mater. **406**, 19 (2010).
[220] S. L. Dudarev and P. M. Derlet, J. Phys. Condens. Matter **17**, 7097 (2005).
[221] S. Chiesa, P. M. Derlet, S. L. Dudarev, and H. Van Swygenhoven, J. Phys. Condens. Matter **23**, 206001 (2011).
[222] J. J. Cox and G. T. Horne, Trans. Am. Soc. Met. **49**, 118 (1957).
[223] G. Simonelli, R. Pasianot, and E. J. Savino, Mater. Res. Soc. Symp. Proc. **291**, 567 (1993).
[224] G. J. Ackland, D. J. Bacon, A. F. Calder, and T. Harry, Phil. Mag. A **75**, 713 (1997).
[225] M. I. Mendelev, S. Han, D. J. Srolovitz, G. J. Ackland, D. Y. Sun, and M. Asta, Philos. Mag. **83**, 3977 (2003).

[226] G. J. Ackland, M. I. Mendelev, D. J. Srolovitz, S. Han, and A. Barashev, J. Phys. Condens. Matter **16**, S2629 (2004).
[227] H. Chamati, N. I. Papanicolaou, Y. Mishin, and D. A. Papaconstantopoulos, Surf. Sci. **600**, 1793 (2006).
[228] A. Machová and G. J. Ackland, Modelling Simul. Mater. Sci. Eng. **6**, 521 (1998).
[229] F. F. Abraham, R. Walkup, H. Gao, M. Duchaineau, T. Diaz De La Rubia, and M. Seager, Proc. Nat. Acad. Sci. USA **99**, 5783 (2002).
[230] J. Knap and K. Sieradzki, Phys. Rev. Lett. **82**, 1700 (1999).
[231] V. Yamakov, E. Saether, D. R. Phillips, and E. H. Glaessgen, Phys. Rev. Lett. **95**, 15502 (2005).
[232] D. Terentyev and F. Gao, Mater. Sci. Eng. A **576**, 231 (2013).
[233] P. Gumbsch, J. Mater. Res. **10**, 2897 (1995).
[234] P. L. Sun, C. Y. Yu, P. W. Kao, and C. P. Chang, Scr. Mater. **52**, 265 (2005).
[235] T. Kawabata and O. Izumi, J. Mater. Sci. **13**, 945 (1978).
[236] T. Kim, K. T. Hong, and K. S. Lee, Intermetallics **11**, 33 (2003).
[237] W. Blum, Y. J. Li, and K. Durst, Acta Mater. **57**, 5207 (2009).
[238] H. W. Höppel, L. May, M. Prell, and M. Göken, Int. J. Fatigue **33**, 10 (2011).
[239] D. Wolf and S. Yip, eds., *Materials Interfaces: Atomic-level structure and properties* (Chapman & Hall, London, 1992).
[240] J. M. Howe, *Interfaces in Materials* (John Wiley & Sons, New York, 1997).
[241] A. P. Sutton and R. W. Balluffi, *Interfaces in Crystalline Materials* (Clarendon Press, Oxford, 2006).
[242] R. C. Pond and V. Vítek, Proc. R. Soc. Lond. A **357**, 453 (1977).
[243] V. Randle, *The Measurement of Grain Boundary Geometry* (Institute of Physics Publishing, Bristol & Philadelphia, 1993).
[244] V. Vítek, D. A. Smith, and R. C. Pond, Phil. Mag. A **41**, 649 (1980).
[245] H. K. Chang and R. S. Weidman, Surf. Sci. **144**, 224 (1984).
[246] D. Farkas, Phil. Mag. Lett. **80**, 229 (2000).
[247] D. L. Olmsted, S. M. Foiles, and E. A. Holm, Acta Mater. **57**, 3694 (2009).
[248] T. Honglai and Y. Wei, Acta Mech. Sin. **10**, 150 (1994).
[249] S. Dorfman, V. Liubich, D. Fuks, and K. C. Mundim, J. Phys. Condens. Matter **13**, 6719 (2001).
[250] R. W. Smith, Comput. Phys. Commun. **71**, 134 (1992).
[251] M. Keser and S. Stupp, Comput. Methods Appl. Mech. Eng. **186**, 373 (2000).
[252] A. P. Sutton and V. Vítek, Phil. Trans. R. Soc. A **309**, 1 (1983).
[253] A. P. Sutton and V. Vítek, Phil. Trans. R. Soc. A **309**, 37 (1983).
[254] A. P. Sutton and V. Vítek, Phil. Trans. R. Soc. A **309**, 55 (1983).
[255] G. H. Bishop and B. Chalmers, Scr. Met. **2**, 133 (1968).
[256] M. Weins, B. Chalmers, H. Gleiter, and M. F. Ashby, Scr. Met. **3**, 601 (1969).
[257] A. P. Sutton, Phil. Mag. Lett. **59**, 53 (1989).
[258] R. C. Pond, Proc. R. Soc. Lond. A **357**, 471 (1977).
[259] V. Vítek, Scr. Met. **4**, 725 (1970).
[260] P. Bristowe and A. G. Crocker, Philos. Mag. **31**, 503 (1975).
[261] Y. Mishin, M. Asta, and J. Li, Acta Mater. **58**, 1117 (2010).
[262] W. E. King, G. Campbell, T. Gonis, G. Henshall, D. Lesuera, E. Zywicz, and S. Foiles, Mater. Sci. Eng. A **191**, 1 (1995).
[263] V. Y. Gertsman and K. Tangri, Acta Metall. Mater. **43**, 2317 (1995).
[264] D. Wolf, Phil. Mag. B **59**, 667 (1989).

[265] D. Wolf, Phil. Mag. A **62**, 447 (1990).
[266] D. Wolf, J. Appl. Phys. **69**, 185 (1991).
[267] D. L. Olmsted, E. A. Holm, and S. M. Foiles, Acta Mater. **57**, 3704 (2009).
[268] M. Rühle and A. G. Evans, Mater. Sci. Eng. A **107**, 187 (1989).
[269] M. Lane, Annu. Rev. Mater. Res **33**, 29 (2003).
[270] T. Watanabe and S. Tsurekawa, Acta Mater. **47**, 4171 (1999).
[271] T. Watanabe, Mater. Sci. Eng. A **387-389**, 447 (2004).
[272] J. M. Liu and B. W. Shen, Met. Trans. A **15**, 1289 (1984).
[273] H. Vehoff, P. Ochmann, M. Göken, and M. G. Gehling, Mater. Sci. Eng. A **239-240**, 378 (1997).
[274] I. M. Mikhailovskij, T. I. Mazilova, V. N. Voyevodin, and A. A. Mazilov, Phys. Rev. B **83**, 134115 (2011).
[275] J. B. Brosse, R. Fillit, and M. Biscondi, Scr. Mater. **15**, 619 (1981).
[276] H. Kurishita, A. Oishi, H. Kubo, and H. Yoshinaga, T. Jpn. I. Met. **26**, 341 (1985).
[277] H. Kimura, T. Jpn. I. Met. **29**, 521 (1988).
[278] K. Ikeda, K. Morita, H. Nakashima, and H. Abe, J. Japan Inst. Met. **63**, 179 (1999).
[279] J.-Q. Su, M. Demura, and T. Hirano, Phil. Mag. A **82**, 1541 (2002).
[280] J.-Q. Su, M. Demura, and T. Hirano, Acta Mater. **51**, 2505 (2003).
[281] A. Suzuki, M. F. X. Gigliotti, and P. R. Subramanian, Scr. Mater. **64**, 1063 (2011).
[282] K. Sato, H. Miyazaki, Y. Ikushara, H. Kurishita, and H. Yoshinaga, Mater. T. JIM **31**, 865 (1990).
[283] S. Yip and D. Wolf, Mater. Sci. Forum **46**, 77 (1989).
[284] F. Cleri, S. R. Phillpot, and D. Wolf, Interface Sci. **7**, 45 (1999).
[285] P. Gumbsch, Mater. Sci. Eng. A **260**, 72 (1999).
[286] V. Yamakov, E. Saether, and E. H. Glaessgen, J. Mater. Sci. **43**, 7488 (2008).
[287] Y. Ishida, M. Mori, and M. Hashimoto, Surf. Sci. **144**, 253 (1984).
[288] M. Grujicic, H. Zhao, and G. L. Krasko, Int. J. Refract. Met. Hard Mater. **15**, 341 (1997).
[289] M. Grujicic, H. Zhao, and G. L. Krasko, *Atomistic Simulation of Σ3(111) Grain Boundary Fracture in Tungsten Containing Various Impurities*, Tech. Rep. (Army Research Laboratory, 1999).
[290] D. Farkas, Phil. Mag. A **80**, 1423 (2000).
[291] V. Yamakov, E. Saether, D. R. Phillips, and E. H. Glaessgen, J. Mater. Sci. **42**, 1466 (2007).
[292] P. M. Anderson and J. R. Rice, Scr. Met. **20**, 1467 (1986).
[293] J.-S. Wang and G. E. Beltz, Mat. Res. Soc. Symp. Proc. **238**, 405 (1992).
[294] D. E. Spearot, M. A. Tschopp, K. I. Jacob, and D. L. McDowell, Acta Mater. **55**, 705 (2007).
[295] D. Farkas, R. Nogueira, M. Ruda, and B. Hyde, Met. Mater. Trans. A **36A**, 2067 (2005).
[296] K. Nishimura and N. Miyazaki, Comput. Model. Eng. Sci. **2**, 143 (2001).
[297] A. Latapie and D. Farkas, Modelling Simul. Mater. Sci. Eng. **11**, 745 (2003).
[298] A. H. Cottrell, Proc. R. Soc. A **276**, 1 (1963).
[299] E. Smith and J. T. Barnby, Met. Sci. J. **14**, 56 (1967).
[300] E. Schmid and W. Boas, *Kristallplastizität - Mit Besonderer Berücksichtigung der Metalle* (Springer, Berlin, 1935).
[301] S. J. Zhou, A. E. Carlsson, and R. Thomson, Phys. Rev. Lett. **72**, 852 (1994).
[302] V. Vítek, Philos. Mag. **21**, 1275 (1970).
[303] V. Vítek, Cryst. Latt. Def. **5**, 1 (1974).
[304] V. Vítek and V. Paidar, in *Dislocations in Solids*, Vol. 14, edited by J. P. Hirth (Elsevier B. V., 2008) Chap. 87.
[305] G. Gottstein, *Physikalische Grundlagen der Materialkunde* (Springer, Berlin, 2007).
[306] C. R. Weinberger, B. L. Boyle, and C. C. Battaile, Int. Mater. Rev. **58**, 296 (2013).

[307] M. W. Finnis and J. E. Sinclair, Phil. Mag. A **50**, 45 (1984).
[308] M. Marchese, G. Jacucci, and C. P. Flynn, Phil. Mag. Lett. **57**, 25 (1988).
[309] T. Dümmer, J. C. Lasalvia, G. Ravichandran, and M. A. Meyers, Acta Mater. **46**, 6267 (1998).
[310] V. Vítek and F. Kroupa, Phys. Stat. Sol. **18**, 703 (1966).
[311] T. Takeuchi, R. Honda, K. Iwayama, and T. Taoka, Jpn. J. Appl. Phys. **6**, 1282 (1967).
[312] J. W. Christian, Met. Mater. Trans. A **14**, 1237 (1983).
[313] S. Ismail-Beigi and T. A. Arias, Phys. Rev. Lett. **84**, 1499 (2000).
[314] C. Woodward and S. I. Rao, Phil. Mag. A **81**, 1305 (2001).
[315] C. Woodward and S. I. Rao, Phys. Rev. Lett. **88**, 216402 (2002).
[316] A. George and G. Michot, Mater. Sci. Eng., A **164**, 118 (1993).
[317] B. J. Gally and A. S. Argon, Phil. Mag. A **81**, 699 (2001).
[318] G. Michot, M. A. Loyola de Oliveira, and H. Koizumi, J. Phys. IV Fr. **8**, Pr4145 (1998).
[319] C. Scandian, H. Azzouzi, N. Maloufi, and G. Michot, Phys. Stat. Sol. **171**, 67 (1999).
[320] G. Michot, Acta Mater. **59**, 3864 (2011).
[321] M. Tanaka, S. Sadamatsu, H. Nakamura, and K. Higashida, Mater. Trans. **52**, 352 (2011).
[322] J. Rösler, H. Harders, and M. Bäker, *Mechanisches Verhalten der Werkstoffe* (Vieweg+Teubner, Wiesbaden, 2008).
[323] E. B. Tadmor and S. Hai, J. Mech. Phys. Solids **51**, 765 (2003).
[324] A. G. Crocker, P. E. J. Flewitt, and G. E. Smith, Int. Mater. Rev. **50**, 99 (2005).
[325] D. S. Dugdale, J. Mech. Phys. Solids **8**, 100 (1960).
[326] G. I. Barenblatt, Adv. Appl. Mech. **7**, 55 (1962).
[327] N. Chandra, H. Li, C. Shet, and H. Ghonem, Int. J. Solids Struct. **39**, 2837 (2002).
[328] H. D. Espinosa and P. D. Zavattieri, Mech. Mater. **35**, 333 (2003).
[329] Y. J. Wei and L. Anand, J. Mech. Phys. Solids **52**, 2587 (2004).
[330] D. H. Warner and J. F. Molinari, Acta Mater. **54**, 5135 (2006).
[331] R. H. Kraft, J. F. Molinari, K. T. Ramesh, and D. H. Warner, J. Mech. Phys. Solids **56**, 2618 (2008).
[332] T. Luther and C. Könke, Eng. Fract. Mech. **76**, 2332 (2009).
[333] Z. Shabir, E. Van der Giessen, C. A. Duarte, and A. Simone, Modelling Simul. Mater. Sci. Eng. **19**, 35006 (2011).
[334] J. Qian and S. Li, J. Eng. Mater. Technol. **133**, 11010 (2011).
[335] L. Lin, X. Wang, and X. Zeng, Int. J. Damage Mech. **0**, 1 (2015).
[336] H. H. M. Cleveringa, E. V. der Giessen, and A. Needleman, J. Mech. Phys. Solids **48**, 1133 (2000).
[337] S. Liang, M. Huang, and Z. Li, Int. J. Solids Struct. **56-57**, 209 (2015).
[338] B. Devincre and S. G. Roberts, Acta Mater. **44**, 2891 (1996).
[339] G. V. P. Reddy, C. Robertson, C. Deprés, and M. Fivel, Acta Mater. **61**, 5300 (2013).
[340] V. R. Coffman, J. P. Sethna, G. Heber, M. Liu, A. Ingraffea, N. P. Bailey, and E. I. Barker, Modelling Simul. Mater. Sci. Eng. **16**, 65008 (2008).
[341] V. R. Coffman, J. P. Saetna, A. R. Ingraffea, J. E. Bozek, N. P. Bailey, E. I. Barker, J. Sethna, A. R. Ingraffea, J. E. Bozek, N. P. Bailey, and E. I. Barker, Strain **47**, 99 (2011).
[342] A. M. Tahir, R. Janisch, and A. Hartmaier, Modelling Simul. Mater. Sci. Eng. **21**, 16 (2013).
[343] X. W. Zhou, J. A. Zimmerman, E. D. Reedy Jr., and N. R. Moody, Mech. Mater. **40**, 832 (2008).
[344] J. T. Lloyd, J. A. Zimmerman, R. E. Jones, X. W. Zhou, and D. L. McDowell, Modelling Simul. Mater. Sci. Eng. **19**, 65007 (2011).
[345] B. Paliwal and M. Cherkaoui, Int. J. Solids Struct. **50**, 3346 (2013).

[346] M. Ortiz and A. Pandolfi, Int. J. Numer. Meth. Engng. **44**, 1267 (1999).
[347] H. M. Jensen, in *Proc. Crack Paths (CP 2006), Parma, Italy* (2006).
[348] D. Raabe, *Computational Materials Science* (Wiley-VCH, Weinheim, 1998).
[349] S. Yip, *Handbook of materials modelling* (Springer, Berlin, 2005).
[350] D. C. Rapaport, *The art of molecular dynamics simulation* (Cambridge Univ. Press, 1995).
[351] D. Frenkel and B. Smit, *Understanding Molecular Simulation, Second Edition: From Algorithms to Applications* (Academic Press, 2001).
[352] M. P. Allen and D. J. Tildesley, *Computer simulation of liquids* (Clarendon Press, Oxford, 1996).
[353] J. Stadler, R. Mikulla, and H.-R. Trebin, Int. J. Mod. Phys. C **8**, 1131 (1997).
[354] J. Roth, in *High Perform. Comput. Sci. Eng. 1999*, edited by E. Krause and W. Jäger (Springer, Berlin, 2000) pp. 72–81.
[355] E. Bitzek, F. Gähler, J. Hahn, C. Kohler, G. Krdzalic, J. Roth, C. Rudhart, G. Schaaf, J. Stadler, and H.-R. Trebin, in *High Perform. Comput. Sci. Eng. 2000*, edited by E. Krause and W. Jäger (Springer, Heidelberg, 2001).
[356] IMD, *http://imd.itap.physik.uni-stuttgart.de*.
[357] J. R. Beeler, *Radiation Effects Computer Experiments*, edited by S. Amelinckx, R. Gevers, and J. Nihoul (North-Holland, Amsterdam, 1983).
[358] E. Bitzek, P. Koskinen, F. Gähler, M. Moseler, and P. Gumbsch, Phys. Rev. Lett. **97**, 170201 (2006).
[359] M. S. Daw, Phys. Rev. B **39**, 7441 (1989).
[360] M. S. Daw, S. M. Foiles, and M. I. Baskes, Mat. Sci. Reports **9**, 251 (1993).
[361] R. A. Johnson, Phys. Rev. B **39**, 12554 (1989).
[362] P. M. Morse, Phys. Rev. **34**, 57 (1929).
[363] L. a. Girifalco and V. G. Weizer, Phys. Rev. **114**, 687 (1959).
[364] J. P. Biersack and J. F. Ziegler, Nucl. Instrum. Methods **194**, 93 (1982).
[365] E. C. Stoner, Proc. R. Soc. A **169**, 339 (1939).
[366] W. B. Pearson, *A Handbook of Lattice Spacings and Structures of Metals and Alloys* (Pergamon Press, Oxford, 1967).
[367] G. J. Ackland and R. Thetford, Phil. Mag. A **56**, 15 (1987).
[368] M. R. Fellinger, H. Park, and J. W. Wilkins, Phys. Rev. B **81**, 1 (2010).
[369] G. J. Ackland, "http://www.homepages.ed.ac.uk/gja/moldy/AMISH.txt," (2009).
[370] S. Han, L. A. Zepeda-Ruiz, G. J. Ackland, R. Car, and D. J. Srolovitz, J. Appl. Phys. **93**, 3328 (2003).
[371] D. E. Smirnova, A. Y. Kuksin, S. V. Starikov, V. V. Stegailov, Z. Insepov, J. Rest, and A. M. Yacout, Modelling Simul. Mater. Sci. Eng. **21**, 35011 (2013).
[372] J. Wang, Y. L. Zhou, M. Li, and Q. Hou, Modelling Simul. Mater. Sci. Eng. **22**, 15004 (2014).
[373] C. Kittel, *Introduction to Solid State Physics* (John Wiley & Sons, New York, 1996).
[374] W. P. Mason, *Piezoelectric Crystals and Their Application to Ultrasonics* (Van Nostrand, New York, 1950).
[375] W. R. Tyson and W. A. Miller, Surf. Sci. **62**, 267 (1977).
[376] P. Blonski and A. Kiejna, Surf. Sci. **601**, 123 (2007).
[377] L. Ventelon and F. Willaime, Philos. Mag. **90**, 1063 (2010).
[378] A. E. Carlsson, in *Solid State Phys.*, Vol. 43, edited by H. Ehrenreich and D. Turnbull (Academic Press, 1990) pp. 1–91.
[379] P. Hohenberg, Phys. Rev. **136**, B864 (1964).
[380] W. Kohn and L. J. Sham, Phys. Rev. **140**, A1133 (1965).

[381] D. Sholl and J. A. Steckel, *Density Functional Theory: A Practical Introduction* (John Wiley & Sons, Inc., 2009).
[382] F. Giustino, *Materials Modelling using Density Functional Theory: Properties and Predictions* (Oxford University Press, 2014).
[383] P. Giannozzi, S. Baroni, N. Bonini, M. Calandra, R. Car, C. Cavazzoni, D. Ceresoli, G. Chiarotti, M. Cococcioni, I. Dabo, A. Dal Corso, S. de Gironcoli, S. Fabris, G. Fratesi, R. Gebauer, U. Gerstmann, C. Gougoussis, A. Kokalj, M. Lazzeri, L. Martin-Samos, N. Marzari, F. Mauri, R. Mazzarello, S. Paolini, A. Pasquarello, L. Paulatto, C. Sbraccia, S. Scandolo, G. Sclauzero, A. P. Seitsonen, A. Smogunov, P. Umari, and R. M. Wentzcovitch, J. Phys. Condens. Matter **21**, 395502 (19pp) (2009).
[384] Quantum ESPRESSO, "http://www.quantum-espresso.org/," .
[385] J. P. Perdew, K. Burke, and M. Ernzerhof, Phys. Rev. Lett. **77**, 3865 (1996).
[386] D. Vanderbilt, Phys. Rev. B **41**, 7892 (1990).
[387] B. Meyer, "Private communication," (2014).
[388] H. J. Monkhorst and J. D. Pack, Phys. Rev. B **13**, 5188 (1976).
[389] C. L. Fu and K. M. Ho, Phys. Rev. B **28**, 5480 (1983).
[390] W. H. Press, *Numerical Recipes 3rd Edition: The Art of Scientific Computing* (Cambridge University Press, 2007) p. 1235.
[391] R. Golesorkhtabar, P. Pavone, J. Spitaler, P. Puschnig, and C. Draxl, Comput. Phys. Commun. **184**, 1861 (2013).
[392] ElaStic, "http://exciting-code.org/elastic," .
[393] S. Giordano, A. Mattoni, and L. Colombo, "Brittle Fracture: From Elasticity Theory to Atomistic Simulations," in *Rev. Comput. Chem.*, Vol. 27, edited by K. B. Lipkowitz (John Wiley & Sons, 2011) Chap. 1, pp. 1–84.
[394] P. A. Gordon, T. Neeraj, Y. Li, and J. Li, Modelling Simul. Mater. Sci. Eng. **18**, 85008 (2010).
[395] A. Stukowski, Modelling Simul. Mater. Sci. Eng. **18**, 15012 (2010).
[396] A. Stukowski, Modelling Simul. Mater. Sci. Eng. **20**, 45021 (2012).
[397] OVITO, *http://ovito.org*.
[398] M. Zhou, Proc. R. Soc. Lond. A **459**, 2347 (2003).
[399] R. Clausius, Philos. Mag. **40**, 122 (1870).
[400] W. Brostow, J. P. Dussault, and B. L. Fox, J. Comput. Phys **29**, 81 (1978).
[401] H. Van Swygenhoven and P. Derlet, in *Dislocations in Solids*, Dislocations in Solids, Vol. 14 (Elsevier, 2008) pp. 1–42.
[402] J. D. Honeycutt and H. C. Andersen, J. Phys. Chem. **91**, 4950 (1987).
[403] B.-J. Lee, M. I. Baskes, H. Kim, and Y. K. Cho, Phys. Rev. B **64**, 184102 (2001).
[404] C. L. Kelchner, S. J. Plimpton, and J. C. Hamilton, Phys. Rev. B **58**, 11085 (1998).
[405] D. Weygand, M. Mrovec, T. Hochrainer, and P. Gumbsch, Annu. Rev. Mater. Res. **45**, 369 (2015).
[406] D. J. Bacon, Y. N. Osetsky, and D. Rodney, in *Dislocations in Solids*, Vol. 15, edited by J. P. Hirth and L. Kubin (Elsevier B. V., 2009) Chap. 88.
[407] J. J. Möller and E. Bitzek, Methods X **3**, 279 (2016).
[408] BDA, *http://jomoeller.github.io/bda*.
[409] A. Stukowski, "Private communication," (2015).
[410] J. Bach, J. J. Möller, M. Göken, E. Bitzek, and H. Höppel, Int. J. Fatigue **93**, 281 (2016).
[411] Y. Sun, G. E. Beltz, and J. R. Rice, Mater. Sci. Eng. A **170**, 67 (1993).
[412] I. Bleskov, "Private communciation," (2014).

[413] D.-S. Xu, J. P. Chang, J. Li, R. Yang, D. Li, and S. Yip, Mater. Sci. Eng. A **387-389**, 840 (2004).
[414] M. Müller, P. Erhart, and K. Albe, J. Phys. Condens. Matter **19**, 326220 (2007).
[415] J. B. Cohen, R. Hinton, K. Lay, and S. Sass, Acta Mater. **10**, 894 (1962).
[416] E. H. Glaessgen, E. Saether, D. R. Phillips, and V. Yamakov, in *Proc. 47th AIAA/ASME/ASCE/AHS/ASC Struct. Struct. Dyn. Mater. Conf.* (2006).
[417] W. Nöhring, J. J. Möller, Z. Xie, and E. Bitzek, Extrem. Mech. Lett. **8**, 140 (2016).
[418] J. E. Sinclair, Philos. Mag. **31**, 647 (1975).
[419] E. C. Bain, Trans. AIME Steel Div. **70**, 25 (1924).
[420] A. J. Bogers and W. G. Burgers, Acta Mater. **12**, 255 (1964).
[421] C. Crussard, C. R. Acad. Sci. Paris **252**, 273 (1961).
[422] C. Crussard, Acta Mater. **10**, 749 (1962).
[423] D. A. Smith and J. Gallot, Met. Sci. J. **3**, 79 (1969).
[424] R. L. Rothman and J. B. Cohen, J. Appl. Phys. **42**, 971 (1971).
[425] T. Zhu, J. Li, and S. Yip, Phys. Rev. Lett. **93**, 1 (2004).
[426] J. Schaufler, C. Schmid, K. Durst, and M. Göken, Thin Solid Films **522**, 480 (2012).
[427] N. M. Pugno and R. S. Ruoff, Philos. Mag. **84**, 2845 (2004).
[428] R. Grantab, V. Shenoy, and R. S. Ruoff, Science **330**, 946 (2010).
[429] R. M. Cannon, in *Adv. Ceram. Struct. Prop. MgO Al2O3 Ceram.*, Vol. 10, edited by W. D. Kingery (The American Ceramics Society, Inc. Columbus, Ohio, 1984) pp. 818–838.
[430] T. C. Lee, I. M. Robertson, and H. K. Birnbaum, Phil. Mag. A **62**, 131 (1990).
[431] E. Arzt, G. Dehm, P. Gumbsch, O. Kraft, and D. Weiss, Prog. Mater. Sci. **46**, 283 (2001).
[432] B. von Blanckenhagen, E. Arzt, and P. Gumbsch, Acta Mater. **52**, 773 (2004).
[433] D. V. Bachurin, D. Weygand, and P. Gumbsch, Acta Mater. **58**, 52232 (2010).
[434] C. Déprés, G. V. Prasad Reddy, C. Robertson, and M. Fivel, Philos. Mag. **94**, 4115 (2014).
[435] M. Peach and J. S. Koehler, Phys. Rev. **80**, 436 (1950).
[436] J. Alcalá, R. Dalmau, O. Franke, M. Biener, J. Biener, and A. Hodge, Phys. Rev. Lett. **109**, 75502 (2012).
[437] D. Hull, Acta Metall. **9**, 909 (1961).
[438] A. W. Sleeswyk, Acta Metall. **10**, 705 (1962).
[439] A. W. Sleeswyk, J. Phys. F Met. Phys. **2**, L93 (1972).
[440] S. Mahajan, J. Phys. F Met. Phys. **2**, 19 (1972).
[441] R. Gröger, *http://groger.ipm.cz/download/ddplot/ddplot.html*.
[442] S. Ogata, J. Li, and S. Yip, Phys. Rev. B **71**, 224102 (2005).
[443] C. N. Reid, Metall. Trans. A **12**, 371 (1981).
[444] S. G. Lekhnitskii, *Theory of Elasticity of an Anisotropic Elastic Body* (Holdenday, San Francisco, 1963).
[445] M. H. Sadd, *Elasticity - Theory, Applications, and Numerics* (Academic Press, Burlington, 2009).
[446] D. S. Liebermann and S. Zirinsky, Acta Cryst. **9**, 431 (1956).
[447] J. J. Möller, *https://bitbucket.org/snippets/jomoeller/qE5aK* (2010).
[448] D. A. Green, Bull. Astr. Soc. India **39**, 289 (2011).

The resistance against crack propagation is undoubtedly one of the most important properties of metallic materials. Particularly in the early stage of their existence, the growth of cracks is influenced by interactions with the surrounding microstructure, e.g., grain boundaries and dislocations. In this context, atomistic simulations play an important role in providing valuable information about fundamental crack tip processes, which can be used for the development of larger-scale models to predict crack propagation in realistic microstructures.

The present thesis contributes to this development by systematically determining the influences of crack front curvature and grain boundary (GB) structure on the competition between brittle fracture and crack tip plasticity in body-centered cubic (bcc) metals. For this purpose, multi-million atom molecular statics and dynamics simulations of perfectly straight and penny-shaped cracks were performed in defect-free single crystals and for the first time at GBs. Crack-dislocation interactions were exemplarily investigated for selected crack and slip systems.

At curved crack fronts, many slip planes intersect parts of the crack front and the tendency for crack tip plasticity is consequently higher than for infinitely long and straight crack fronts. At GBs, locally varying bonding situations lead to the dependence of the fracture resistance on the crack tip position and crack propagation direction. Crack-dislocation interactions are dominated by dislocation cross slip and subsequent glide along the crack front leading to local crack tip blunting.

ISBN 978-3-96147-007-5

FAU UNIVERSITY PRESS 2017